Research supported by the
National Science Foundation
under grant #ATM-0071371

QUASI-TWO-DIMENSIONAL CONVECTIVE LINES WITH LEADING PRECIPITATION: DYNAMICS INFERRED FROM IDEALIZED NUMERICAL SIMULATIONS

by

Matthew D. Parker

Richard H. Johnson, P.I.

Colorado State University

DEPARTMENT OF ATMOSPHERIC SCIENCE

PAPER NO. 726

QUASI-TWO-DIMENSIONAL CONVECTIVE LINES WITH LEADING PRECIPITATION: DYNAMICS INFERRED FROM IDEALIZED NUMERICAL SIMULATIONS

by

Matthew D. Parker

Department of Atmospheric Science
Colorado State University
Fort Collins, CO 80523-1371

Summer 2002

Atmospheric Science Paper # 726

ABSTRACT

QUASI–TWO–DIMENSIONAL CONVECTIVE LINES WITH LEADING PRECIPITATION: DYNAMICS INFERRED FROM IDEALIZED NUMERICAL SIMULATIONS

Recent work has identified three types of linear mesoscale convective systems (MCSs): those with convective lines and either trailing (TS), leading (LS), or parallel (PS) stratiform precipitation, the latter two of which have received comparatively little study. This publication describes a study in which the author used idealized numerical simulations to investigate the basic structures of convective lines with leading precipitation, and addresses the dynamics governing individual air parcels' accelerations within them. It appears that, although unconventional, systems with inflow passing through their line-leading precipitation can be stable and long–lived. Lower tropospheric inflowing air in the simulations is destabilized by lifting and by the vertical profile of evaporation and melting within the pre–line precipitation. This air then ascends, overturns in deep updrafts, and subsequently carries its water content forward from the convective line, where it gives rise to the leading precipitation region. Although relatively strong wind shear in the middle and upper troposphere accounts for a component of the downshear acceleration, and hence overturning, of air parcels in the simulated updrafts, a mature system with leading precipitation also renders both persistent and periodic pressure anomalies that contribute just as much. Many of these accelerations, which govern the overall system structure, are largely transient and are lost when averaged over multiple convective cycles. This publication explains the dynamics that govern the transient updrafts and downdrafts within the systems, including a precipitation cut–off mechanism that governs their multicellular periods. The text also addresses the applicability of several theoretical squall

line models to convective lines with leading precipitation, and briefly documents the simulations' sensitivities and the basic evolutions between convective modes produced in the model.

Matthew David Parker
Department of Atmospheric Science
Colorado State University
Fort Collins, Colorado 80523-1371
Summer 2002

ACKNOWLEDGEMENTS

I gratefully ackowledge the guidance of my doctoral committee at Colorado State University (CSU), Bogusz Bienkiewicz, Bill Cotton, and Steve Rutledge, and especially the support of my advisor, Dick Johnson. Hearty thanks are also due to Gail Cordova and Rick Taft of CSU, who have always taken care of my administrative and computing needs. Many of my fledgling ideas were hatched during discussions with Jason Knievel of CSU and NSSL, and Mitch Moncrieff and Morris Weisman of NCAR also provided many excellent suggestions for this work. Discussions about the ice phase with Bob Maddox of Tucson, AZ also helped to augment my thoughts on the destabilization problem. The simulations in this study were made using the Advanced Regional Prediction System (ARPS) developed by the Center for Analysis and Prediction of Storms (CAPS), University of Oklahoma. CAPS is supported by the National Science Foundation and the Federal Aviation Administration through combined grant ATM92-20009. Stefan Tulich and Zach Eitzen of CSU frequently favored me with words of wisdom and caution about the ARPS model, and Stefan provided the code that I used to compute trajectories during the simulations. Rob Fovell of UCLA also enthusiatically offered insight into some numerical problems. The National Center for Atmospheric Research (NCAR) provided supercomputer facilities and computational time for many of the simulations in this study, and the Scientific Computing Division (SCD) at NCAR, especially Dick Valent of SCD, was of great assistance to me in getting the model to compile and run on the NCAR supercomputers. Finally, I owe a great debt of gratitude to Kerri Brown Parker, who supported me throughout my time at CSU. The National Science Foundation funded this research under grant ATM–0071371.

DEDICATION

That all people might live in the Peace that surpasses understanding.

CONTENTS

FIGURES

TABLES

Chapter 1

INTRODUCTION

1.1 Motivation and focus of this study

Mesoscale convective systems (MCSs) account for a disproportionate number of flash floods (Johnson and Parker 2001), and the degree to which they cause flooding is related to their organizational modes and motion vectors (Doswell et al. 1996). Parker and Johnson (2000) investigated base scan reflectivity data from the central United States and catalogued 88 linear MCSs (that is, convective systems possessing a convective line) that occurred over the course of two months. They found that, although the well–known convective line with trailing stratiform precipitation (TS) archetype accounted for roughly 60% of their study population, about 20% of the systems best corresponded to a convective line with leading stratiform precipitation (LS) archetype, and about 20% of the systems best corresponded to a convective line with parallel stratiform precipitation (PS) archetype. These archetypes are represented schematically in Fig. 1.1. As discussed by Parker and Johnson (2000), the LS and PS modes have received very little attention to this point. Therefore, their dynamics and possibly unique internal structures are heretofore unexplored, which is surprising given their relevance to the flash flood forecast problem [Doswell et al. (1996) and Johnson and Parker (2001)].

Given our lack of knowledge about them, the LS and PS systems are obvious candidates for more detailed research. Numerical modeling techniques are desirable for attacking this problem owing to the paucity of high–resolution observations (e.g. dual–Doppler wind fields) available for in–depth case studies. Hane (1973) put it well: "mesoscale networks of surface and radiosonde

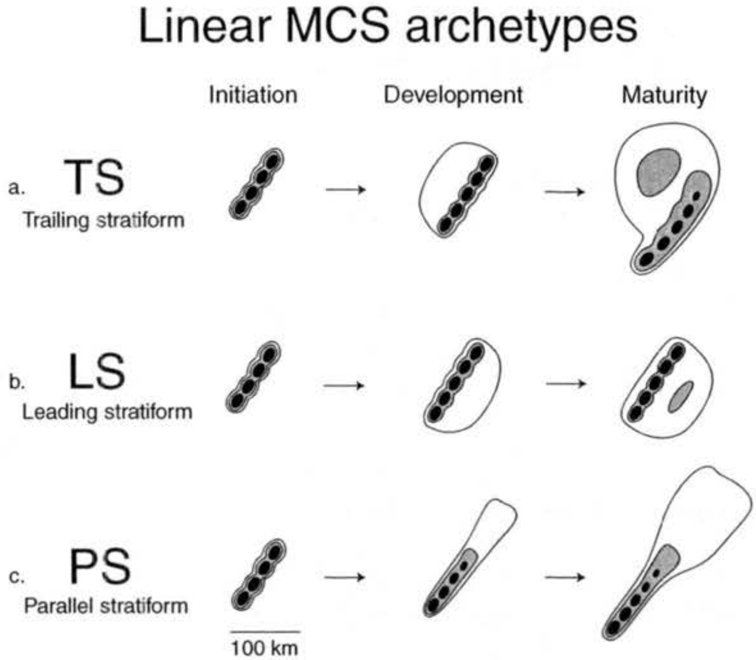

Figure 1.1: Schematic reflectivity drawing of idealized life cycles for three linear MCS archetypes from Parker and Johnson (2000): (a) leading line trailing stratiform (TS), (b) convective line with leading stratiform (LS), (c) convective line with parallel stratiform (PS). Approximate time interval between phases: for TS 3–4 h; for LS 2–3 h; for PS 2–3 h. Levels of shading roughly correspond to 20, 40, and 50 dBZ.

stations which now operate (or have operated) are not (or were not) designed for resolving scales within even large clouds... It seems reasonable, therefore, to turn to numerical modeling of these systems, using the environmental data which now exist as a guide in specifying initial and boundary conditions." This was the basic philosophy of the present work, which focused on convective lines with leading precipitation. Unfortunately, PS systems presented a much larger demand for computer resources owing to their decidedly 3D structure: both line perpendicular and line–parallel inhomogeneities and flow fields are essential to their existence, which thereby excludes the possibilities for affordable 2D and/or periodic–3D simulations. On the other hand, an LS system is *quasi–2D*, meaning that toward its center the along–line derivatives are small and its flow almost exclusively lies in line–perpendicular planes. This made feasible numerous 2D and periodic–3D simulations of LS systems (the possible drawbacks to this approach are discussed in Chapter 2).

Convective lines with leading precipitation pose several interesting questions that this publication addresses. Firstly, given their "mirror–image similarity" to convective lines with trailing precipitation, it is obvious to ask: just how similar are LS systems to TS systems dynamically and kinematically? Parker and Johnson (2000) and Pettet (2001) found in case studies that at least some of the LS systems in the central U.S. are sustained by inflow of high–θ_e air from behind the system (i.e. they were "rear–fed"). However, the mean wind profiles computed by Parker and Johnson (2000) revealed that, on average, the LS systems in their study were chiefly "front–fed"[1] (Fig. 1.2). On reinvestigating the cases compiled by Parker and Johnson (2000) it became clear that, indeed, a significant number of the individual LS systems were front–fed. Hence, the LS reflectivity category proposed by Parker and Johnson (2000) must be understood to comprise at least two kinematic subtypes: front–fed LS ("FFLS") systems as well as rear–fed LS ("RFLS") systems. For completeness, it should be mentioned that all of the TS systems Parker and Johnson (2000) investigated were "front–fed", hence the additional term front–fed TS ("FFTS") MCS is also appropriate.[2] In many ways, RFLS systems do indeed possess "mirror–image similarity" to FFTS systems; there are a few relevant differences, which are discussed in detail toward the end of Chapter 7.

This publication focuses mainly on FFLS systems, which are distinctly different from FFTS systems (later chapters explain how). An important question for these systems is whether the most important factor in their stratiform precipitation distribution is the middle and upper tropospheric wind shear or the middle and upper tropospheric storm–relative flow. Parker and Johnson (2000) found that, for the linear MCSs they studied, "the stratiform precipitation arrangement... was roughly consistent with the advection of hydrometeors implied by the mean middle– and upper–tropospheric storm–relative winds." Similarly, Nachamkin et al. (2000) found in a case study of a system with leading precipitation that, "condensate was... passively [moving] downstream in the mean environmental flow." In contrast, however, Grady and Verlinde (1997) found that strong upper–level shear was very important in establishing the predominantly leading anvil in a system

[1] Although not shown, wind profiles from *behind* LS MCSs in the Parker and Johnson (2000) study also did not reveal mean rear–to–front storm–relative flow. In other words, the Parker and Johnson (2000) LS MCS population was not, on average "rear–fed".

[2] If the reader likes, he/she could devise further acronyms in this way *ad nauseam*.

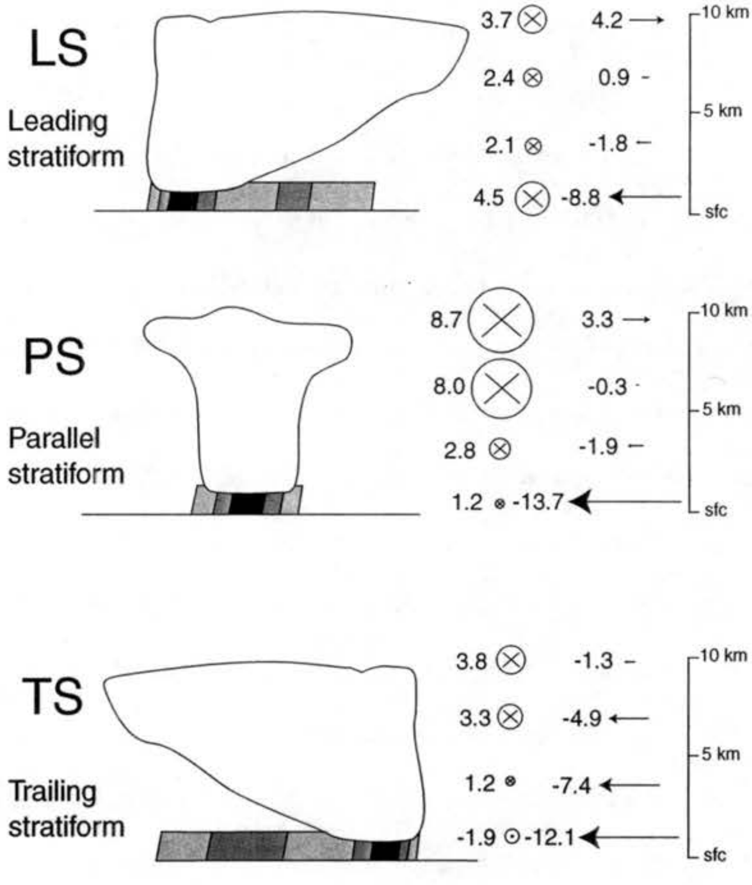

Figure 1.2: Vertical profiles of layer-mean storm-relative pre-MCS winds for linear MCS classes from Parker and Johnson (2000). Wind vectors depicted as line-parallel (⊗) and line-perpendicular (→) components in m s^{-1}. Layers depicted are 0–1 km, 2–4 km, 5–8 km, and 9–10 km. Typical base scan radar reflectivity patterns (shading) and hypothetical cloud outlines are drawn schematically for reference. MCSs' leading edges are to the right.

that they studied. The vertical wind shear did not vary much among the three linear MCS modes that Parker and Johnson (2000) studied (e.g. Fig. 1.2), which made the issue unclear [at least it was unclear to Parker and Johnson (2000)].[3] The present work emphasizes the role of the middle and upper tropospheric wind shear, whose importance becomes very clear when one embraces the parcel perspective endorsed by this publication.

FFLS systems are also interesting from a numerical modeling perspective, because previously published works have documented simulations that lie roughly within the appropriate range of vertical wind shear for FFLS systems, yet in which a long–lived system failed to develop. Simulations that came "close" include those by Hane (1973), Thorpe et al. (1982), Seitter and Kuo (1983), Nicholls et al. (1988), Weisman et al. (1988), and Szeto and Cho (1994). However, as noted by Hane (1973): "some rain tends to fall on the right–hand side of the cloud [which] creates additional difficulty for the regeneration process," and, as noted by Seitter and Kuo (1983), when "large amounts of liquid water were carried forward into the anvil of the storm... the fall of this water into the front of the storm led to excessive loading of the updraft and caused a rapid decay of the storm." Interestingly, Dudhia et al. (1987) claimed that, "no convincing example of steady convection of the pure steering–level [i.e. overturning updraft] type has yet been demonstrated in two dimensions." Some reasons for the prior failures to simulate FFLS systems may include the manner in which those scientists initiated the convection (i.e. using a bubble instead of a cold pool), their exclusion of the ice phase, and/or the possibility that the temperature and humidity profiles in their environments were not appropriate for the destabilization mechanism described in Chapter 4.

Given the scant observational resources for a study of non–classical convective systems, the scarcity of published studies on FFLS systems, and the aforementioned difficulties in simulating them, the present study stands to fill a void in our understanding of linear convective systems. Perhaps not surprisingly, many of the current working dynamical hypotheses for convective systems [e.g. those proposed by Seitter and Kuo (1983), Rotunno et al. (1988), Yang and Houze (1995), Fovell and Tan (1998), and Lin et al. (1998)] were based heavily, if not exclusively, on the FFTS

[3] Notably, the inclusion of RFLS systems in Parker and Johnson (2000)'s averages may have biased the mean vertical shear for LS MCSs downward somewhat.

convective paradigm. Although this publication does not present a new consolidated theory for linear convective systems to replace the old theories, it does offer a somewhat novel approach to the dynamical analysis of a linear convective system, and it presents results for FFLS systems, whose dynamics have heretofore received very little study.

1.2 Background

The rich body of literature concerning squall lines and linear convective systems traces its lineage primarily through significant papers about FFTS systems, especially those by Newton (1950), Ogura and Liou (1980), Smull and Houze (1985), Smull and Houze (1987a), Rutledge et al. (1988), and Houze et al. (1989). These, along with countless others, led to the unifying paper by Houze et al. (1990), in which the authors specified criteria for the FFTS archetype and assessed the degree to which a large population of Oklahoma convective systems met those criteria. In turn, the paper by Houze et al. (1990) was one among several that constitute a lineage of taxonomy papers, including those by Bluestein and Jain (1985), Blanchard (1990), and Schiesser et al. (1995). Standing on the shoulders of these many studies, Parker and Johnson (2000) investigated 88 linear MCSs from the central U.S. and classified them as either TS, LS, or PS [a taxonomy whose strong similarity to that of Schiesser et al. (1995) was duly noted]. In some sense, therefore, the present work about FFLS systems is the latest effort in a string of papers on the structures, kinematics, and dynamics of convective systems—especially FFTS convective systems—that is more than half of a century old.

Meanwhile, as studies of FFTS MCSs were gaining a literary critical mass, other papers that addressed systems with overturning updrafts and leading anvils, if not precipitation, sporadically appeared. Newton and Fankhauser (1964) presented a schematic diagram of a squall line with an extensive leading "downwind" anvil. Houze and Rappaport (1984) analyzed a tropical convective system that, although it primarily produced trailing precipitation, also produced some line–leading precipitation for part of its lifetime (Fig. 1.3). The squall line that Kessinger et al. (1987) studied had a very strong overturning updraft for part of its lifetime, and produced an appreciable leading anvil, even though most of its precipitation fell rearward of the convective line (Fig. 1.4). Similarly, the squall line analyzed by Fankhauser et al. (1992) had a significant overturning updraft and leading anvil with some overhanging precipitaton, although its structure was complicated and most of the surface precipitation occurred to the line's rear (Fig. 1.5). Probably the two best–observed FFLS systems have been recently described by Grady and Verlinde (1997) and Nachamkin et al. (2000).[4] The study by Grady and Verlinde (1997) is quite relevant to the present work: their triple–Doppler radar observations revealed an overturning updraft (Fig. 1.6), rooted some ways behind the surface outflow boundary, which produced a large leading anvil and a small plume of pre–line precipitation (Fig. 1.7). Much as in Chapter 5 of the present work, Grady and Verlinde (1997) emphasized the importance of the strong upper–level vertical shear to the system's structure. The MCS analyzed by Nachamkin et al. (2000) also possessed an overturning updraft (it takes some imagination to infer this from UREL and W in Fig. 1.8), a leading anvil, and a significant region of leading precipitation (the convective line was generally somewhat centered within the low to mid–level reflectivity field, as in Fig. 1.8). Given our present lack of observational data for FFLS systems, any attempt to "verify" these numerical simulations must, of necessity, be a sort of low–order comparison to the analyses of Grady and Verlinde (1997) and Nachamkin et al. (2000).

There also exists a lineage of theoretical work on the basic idealized flow structures of 2D convective lines, advanced largely by Dr. Mitchell Moncrieff. Parker and Johnson (2000) tried with some uncertainty to interpret TS and LS systems in terms of these theoretical models and, as Chapter 6 will show, they have considerable relevance to the quasi–steady FFLS structures in the present study. Thorpe et al. (1982) summarized a 2D numerical simulation with the conceptual model in Fig. 1.9, which comprised an overturning updraft, a rearward–sloping jump updraft, an up–down rearward–flowing airstream (with a possible rotor), and an overturning downdraft. This fit well with an idealized theoretical model that they derived, which is shown in Fig. 1.10 [as redrawn by Moncrieff (1992)]. As shown in Moncrieff (1992)'s Fig. 2 (not reproduced here), the steady state

[4] Interestingly, both the Grady and Verlinde (1997) and Nachamkin et al. (2000) systems were observed over the eastern plains of Colorado during the summer of 1993. The existence of dual/triple–Doppler radar and surface mesonet data from the NCAR RAPS–93 (Realtime Analysis and Prediction of Storms, 1993) field experiment made case studies from that season and region attractive. It's unclear whether or not FFLS systems were unusually common in Colorado during the summer of 1993.

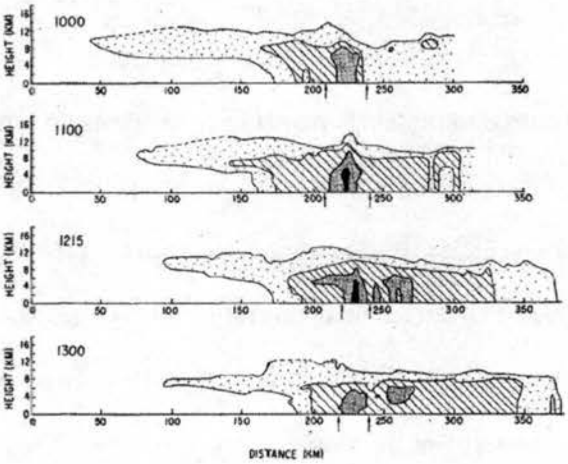

Figure 1.3: Sample of the evolution of vertical reflectivity structure in the squall system from Houze and Rappaport (1984). Cross sections are along the direction of propagation, with motion from right to left. Shading thresholds are for the minimum detectable echo, 24, 34, and 44 dBZ.

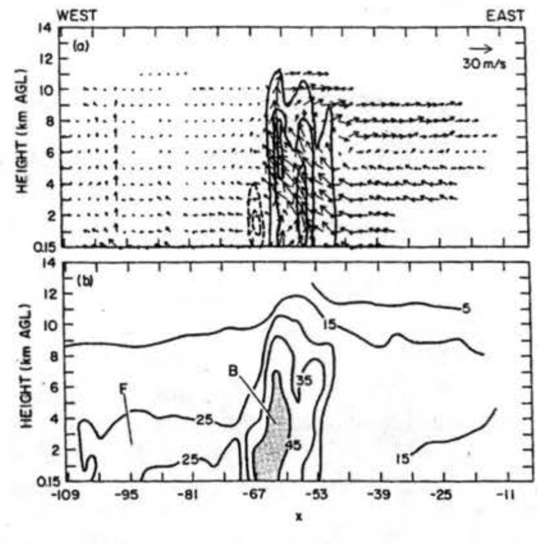

Figure 1.4: East-west vertical cross section through squall line case presented by Kessinger et al. (1987). (a) line-relative winds along the cross section and (b) reflectivity (dbZ$_e$).

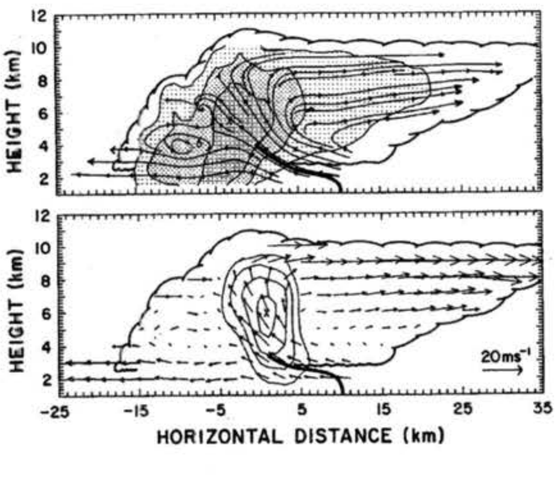

Figure 1.5: Vertical cross section through squall line presented by Fankhauser et al. (1992). (a) streamlines and radar reflectivity (shading thresholds of 5, 20, and 35 dBZ); (b) air motion vectors and vertical velocity contours at 2 m s^{-1} increments. Cloud boundary indicated, along with forward boundary of cold pool (heavy line).

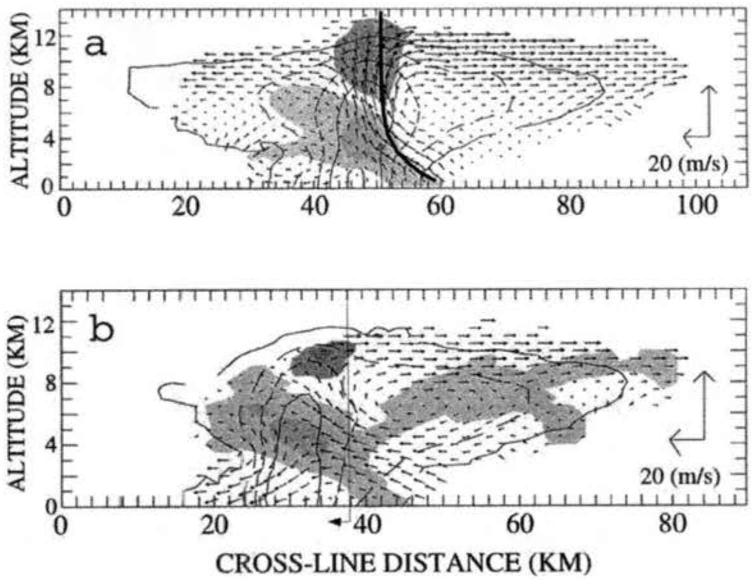

Figure 1.6: Along-line averaged cross sections at two times for squall line from Grady and Verlinde (1997). Reflectivity contours are in 10-dBZ increments beginning with 10 dBZ. Vectors depict line-relative flow. Light shading indicates convergence, dark shading indicates divergence.

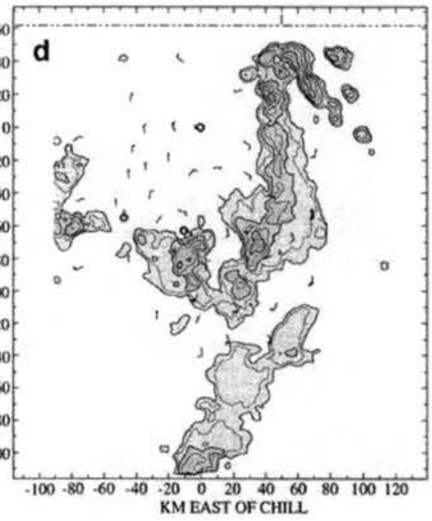

Figure 1.7: Constant altitude map at 3.0 km AGL of the reflectivity field for squall line from Grady and Verlinde (1997). Contours are in 7.5–dBZ increments beginning at 15 dBZ. Shading intervals are 15, 30, and 45 dBZ. Surface winds (full barb = 5 m s^{-1}) are also plotted.

transport properties of any convective line can be idealized by considering slight modifications and asymptotic limits to the basic structure in Fig. 1.10. In the parameter space that Moncrieff (1992) discussed, the jump updraft might be more or less prominent than that shown in Fig. 1.10, and might occur without either an overturning updraft or an overturning downdraft. Later, Liu and Moncrieff (1996) developed similar, derivative models for the flow near density currents, some of which are shown in Fig. 1.11. Including the stagnant region that was added in subfigures (a) and (b), it is clear that these structures share many properties with the Thorpe et al. (1982) and Moncrieff (1992) models in Figs. 1.9 and 1.10. Although Liu and Moncrieff (1996) likely didn't intend for these models to be applied to convective lines, Chapter 6 shows that they are quite relevant to the FFLS systems in the present study.

Finally, there have been numerous numerical studies of convective lines since the advent of high–powered computers. An ongoing question in the field of convective dynamics has been the sensitivity of deep convective clouds and organized convective systems to the environments in which they occur. A great deal of attention has been focused on the influence of vertical wind shear on convective structure and organization, and numerical simulations have provided an ideal frame-

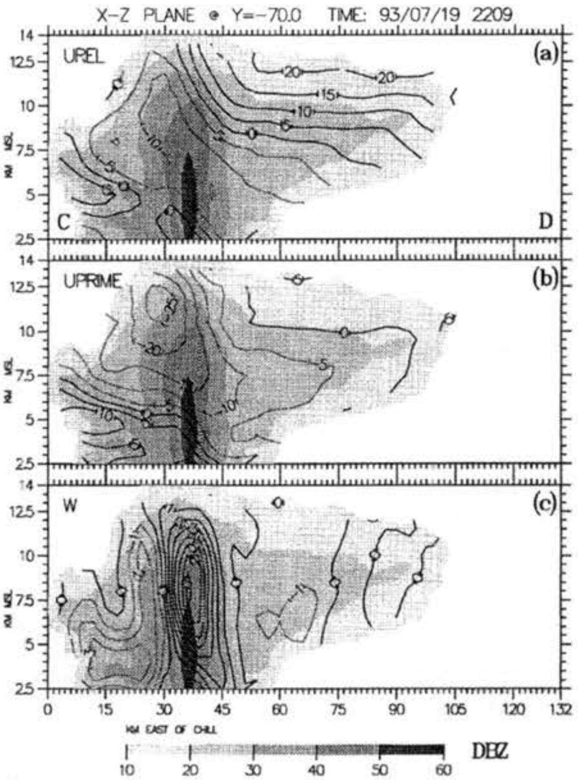

Figure 1.8: Vertical cross sections from Nachamkin et al. (2000). Radar reflectivity is shaded in all plots as defined by the bar. Storm–relative and envirnment–relative u component winds are contoured at 5 m s^{-1} increments in (a) and (b), respectively. (c) Vertical velocity is contoured at 1 m s^{-1} increments.

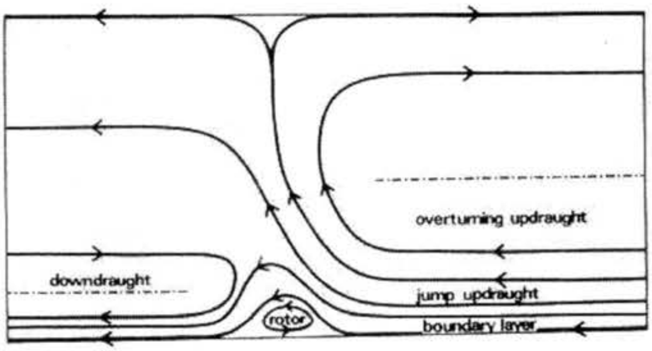

Figure 1.9: Schematic diagram of conceptual model for 2D convection from Thorpe et al. (1982), with individual flows labelled.

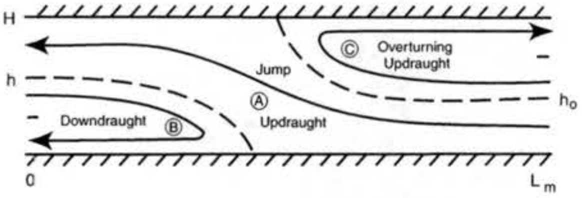

Figure 1.10: Schematic diagram of the airflow in Moncrieff (1992)'s stationary dynamical model for two-dimensional convection.

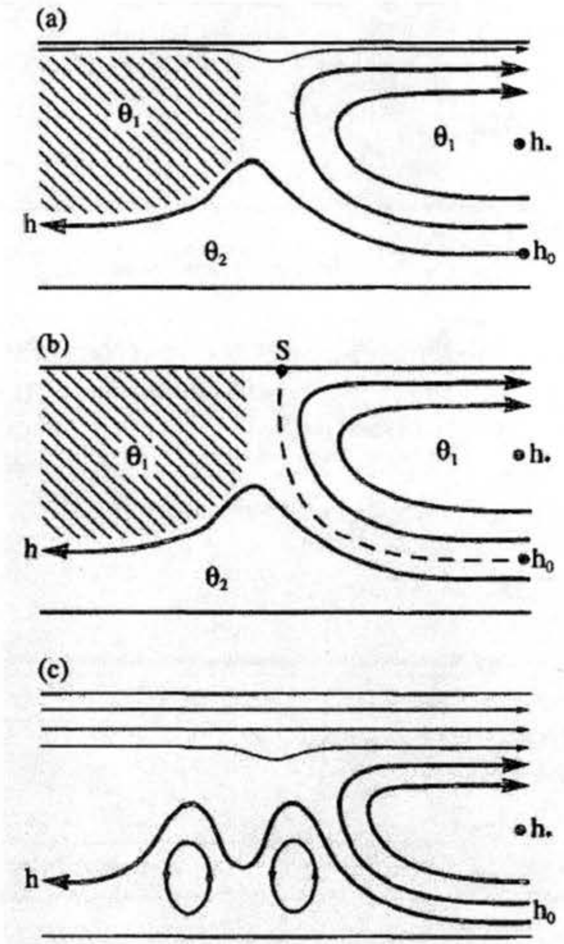

Figure 1.11: Schematic diagram of idealized flow regimes from Liu and Moncrieff (1996): a) Partly blocked jump regime, b) partly blocked jump regime with a separating flow on the upper boundary at the stagnation point, S, c) high shear regime.

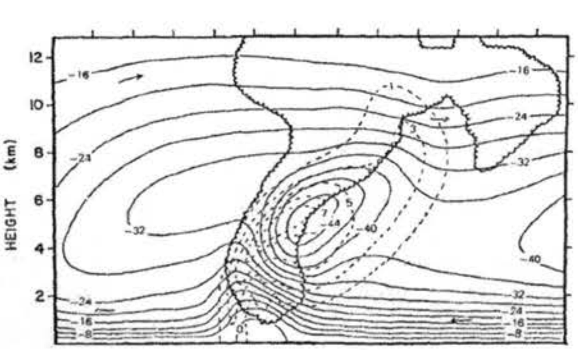

Figure 1.12: Streamfunction (solid lines, 10^3 kg m^{-1} s^{-1}), rainwater mixing ratio (dashed lines, g kg^{-1}), and cloud outline from Hane (1973).

work to test the shear parameter space. For example, Hane (1973), Thorpe et al. (1982), Seitter and Kuo (1983), Dudhia et al. (1987), Nicholls et al. (1988), Weisman et al. (1988), and Szeto and Cho (1994) have performed experiments by varying the wind profiles within numerical models. As mentioned in the previous section, because these studies investigated such a broad spectrum of wind profiles, some of them simulated close relatives of FFLS systems, if not actual FFLS systems. Hane (1973) simulated a 2D system in strong vertical shear that produced an overturning updraft and leading anvil, with some overhanging precipitation (Fig. 1.12). A system simulated by Thorpe et al. (1982) also produced an overturning updraft and leading precipitation (Fig. 1.13), although they noted that when they added middle and upper tropospheric shear to their wind profile (such as in the present study) the simulated systems became unsteady and decayed. Other simulations with overturning updrafts and leading precipitation include those by Seitter and Kuo (1983, Fig. 1.14), Weisman et al. (1988, Fig. 1.15), and Nicholls et al. (1988, as described in words but not shown). In general, these systems did not produce large leading precipitation regions even though their general structures resembled those of the FFLS systems in this publication. As well, many of the quasi–FFLS systems that these authors simulated were not very long–lived.[5] Therefore, although these prior modeling studies have shed some light on the problem of FFLS systems, they have not adequately explained the relatively large, long–lived MCSs observed by Parker and Johnson (2000).

In addition to their suitability for sensitivity experiments, numerical simulations also provide

[5] As mentioned earlier, this may be attributable to their different thermodynamic environments and microphysical parameterizations, whose importance Section 4.2 discusses.

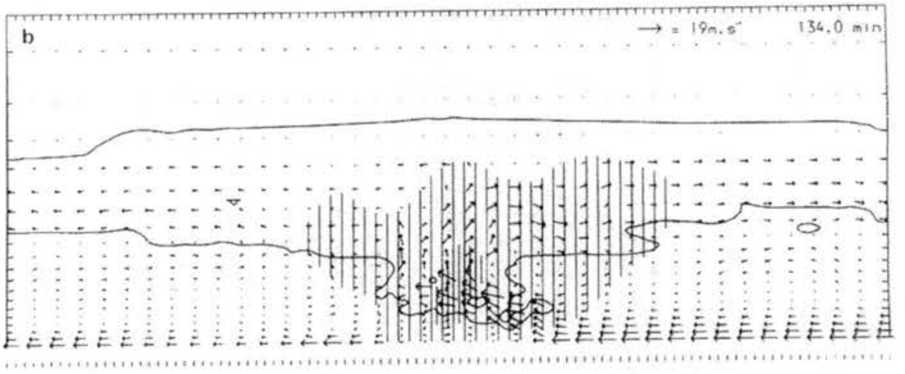

Figure 1.13: Cross section of cloud, rain and velocity vectors from Thorpe et al. (1982). Horizontal ticks every 500 m and vertical ticks every 50 mb.

gridded, high resolution results that represent ideal datasets with which to investigate dynamical hypotheses. In addition to the physical interpretations that Seitter and Kuo (1983), Nicholls et al. (1988), Weisman et al. (1988), and Szeto and Cho (1994) proposed as a result of their sensitivity tests, other authors [e.g. Yang and Houze (1995), Fovell and Tan (1998) and Lin et al. (1998)] have advanced the dynamical understanding of squall lines by performing idealized 2D simulations. The present work is descended from the above ancestries of numerical studies in that it comprises sensitivity tests for simulated convective systems and in that it seeks to learn about convective dynamics by analyzing the high–resolution model output.

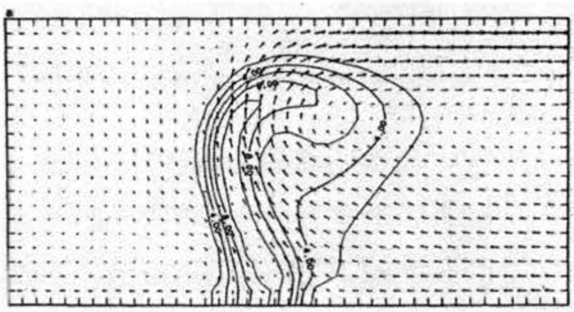

Figure 1.14: Storm relative winds and liquid water (g m^{-3}) distribution from Seitter and Kuo (1983). Storm is moving from left to right.

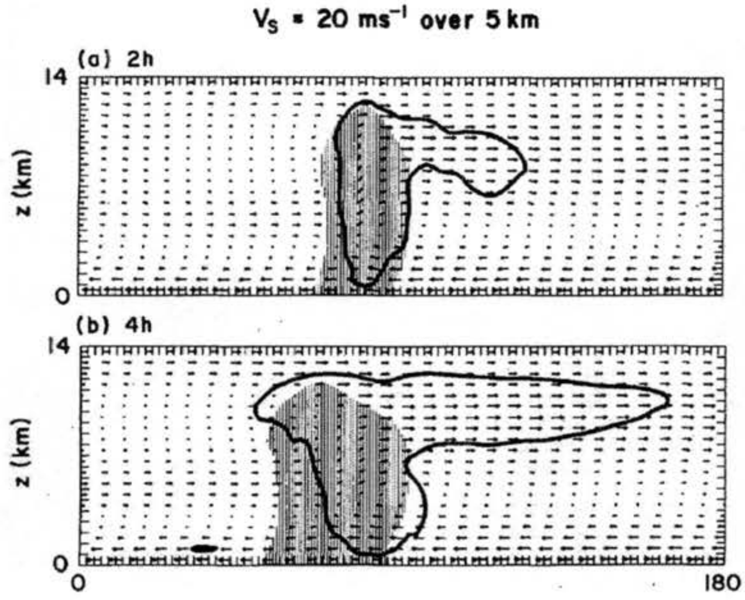

Figure 1.15: Line averaged vertical cross sections of velocity vectors, cloud outline, and rainfall (shaded) from Weisman et al. (1988).

1.3 Structure of this publication

Chapter 2 presents the set–up and details of the numerical model used for this work and discusses the basic scientific principles and philosophies that guided the experiment and analysis. From a broad perspective, Chapters 3– 7 together describe the kinematics and dynamics of the simulated quasi–2D convective systems. Chapter 3 lays out the conceptual framework for interpreting the systems' dynamics. Chapter 4 then describes the basic structures and temporal mean fields of the simulated convective lines with leading precipitation. Chapter 5 goes beyond the mean state and considers the transient updrafts and downdrafts in a mature FFLS system, describing their dynamics from a parcel acceleration perspective. Thereafter, Chapter 6 compares the transient and steady motions to well–known conceptual and theoretical models for squall lines, and discusses how the steady and temporally varying components fit together. Finally, Chapter 7 concludes the body of the text by describing some basic sensitivity tests, paying brief attention to other quasi–2D linear convective modes and evolution toward and among them. Most of this publication is about FFLS systems, although Sections 7.2 and 7.3 do address FFTS and RFLS systems. The crux of the dynamical perspective offered in this publication is in Section 5.1, yet it is only a part of the broader picture of a front–fed convective line with leading precipitation. Chapter 8 closes the text by presenting a consolidated view of the kinematics and dynamics of front–fed systems with leading precipitation, followed by some possibilities for future work and an overall summary.

Chapter 2

METHODS

2.1 Numerical model

This work incorporated both 2D and 3D simulations using the Advanced Regional Prediction System (ARPS), which was developed by the Center for Analysis and Prediction of Storms (CAPS) and the University of Oklahoma. The dynamical framework of the ARPS was described by Xue et al. (1995, 2000, 2001). Among the publicly available nonhydrostatic mesoscale numerical models, the ARPS was ideal for this study because of its ease of use and its suitability for simple, idealized simulations.

2.1.1 Numerical methods

This study utilized the following ARPS finite difference schemes: for momentum advection, the Milne corrector finite difference scheme, which has fourth-order accuracy; for scalar advection, a flux-corrected transport scheme (Zalesak and Ossakow 1980), in which second order centered differences and first-order upstream differences are combined such that negative water and negative temperatures are prohibited; for all other non-advective terms, leapfrog finite differencing, which is second-order accurate. A time splitting technique enabled the simulations to be efficient and yet stable. The forcing terms associated with sound waves were computed on a short timestep that was stable for sound waves; all other forcing terms were computed on a longer timestep that was stable for the fastest wind and inertial-buoyancy wave speeds. Because the vertical grids were spaced more closely than the horizontal grids, the vertical dimension restricted the length of the small timesteps. The use of a trapezoidal implicit (Crank-Nicolson) finite difference for w and p in the vertical dimension also helped to lengthen the short timestep. The vertically implicit scheme is more computationally expensive, but it is unconditionally stable and permits the use of a larger small timestep, whose stability criterion is based on the horizontal (instead of vertical) grid spacing.

The model used a 1.5-order turbulence kinetic energy (TKE) based closure. In this scheme the horizontal and vertical turbulent mixing coefficients are functions of both the length scales of the horizontal and vertical grids, and the local value of TKE. In order to damp very short waves on the domain, the model also included fourth–order computational mixing (the mixing coefficient was 1.0×10^{-3} s^{-1}) and an Asselin time filter (the filter coefficient was 0.10). Finally, the model included divergence damping in order partly to suppress sound waves (the damping coefficient was 0.05).

Both the model's lower and upper boundaries were flat, free–slip plates. The model had a Rayleigh damping layer in the upper third of the domain in order to control reflections off the lid. This technique is appropriate for, and does not does not generally degrade simulations of, MCSs [Gray (2000), Lin and Joyce (2001)]. All fields in the Rayleigh layer were damped toward the base state in 20 timesteps. The model's $\hat{x}$ lateral boundaries (the eastern and western edges) had a wave–radiating (open) boundary condition, as adapted from Orlanski (1976) by Durran and Klemp (1983). Domain–scale pressure detrending prevented the domain–averaged pressure drift that can occur when open lateral boundary conditions are used. The 3D simulations incorporated a periodic boundary condition on the northern and southern edges of the domain (at the line's ends) in order to simulate quasi–2D convective lines. Several preliminary experiments revealed that the central regions of long but finite 3D convective lines behave much like 2D and periodic 3D lines. This is particularly true of cases in the present study, for which the wind profiles were 2D or nearly 2D and convection was initiated with a long linear trigger.

Open boundary conditions in $\hat{y}$ might be important because they remove the quasi–2D constraint upon gravity wave dispersion. However, this constraint likely exists to some degree in the middle sections of long quasi–2D convective lines in the real world because, when heating occurs

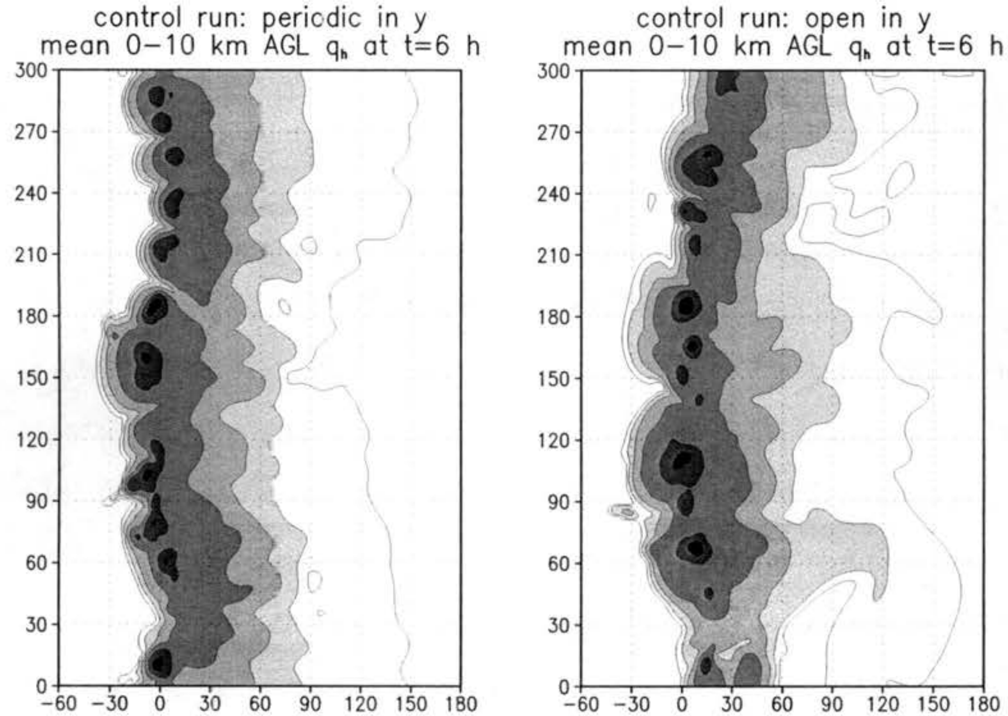

(a)

(b)

Figure 2.1: Mean hydrometeor mixing ratio from 0–10 km AGL at 6 h for: a) 3D control run with periodic $\hat{y}$ boundary condition; b) 3D control run with open $\hat{y}$ boundary condition. Levels of shading are 0.005, 0.02, 0.08, 0.32, 1.28, and 5.12 g kg^{-1}. The initial conditions for the control run are given in § 2.1.4.

over a line's entire length, gravity waves' along–line flux divergences in the center of the line become quite small. Several tests incorporated open boundary conditions on the northern and southern edges of the domain. Overall, the simulated convection's structure and evolution were not affected much by changing the $\hat{y}$ boundary condition (Fig. 2.1), probably because the simulations never developed large v–wind components. Therefore, it appears that the use of a periodic condition in $\hat{y}$ did not overly detract from the results of this study.

The control simulations did not include Coriolis accelerations or radiative effects. Several sensitivity tests, in which the Coriolis parameter (f) was set to 1×10^{-4} s^{-1} (a typical midlatitude value) revealed that the inclusion of planetary rotation had little discernable effect on the simulations during their first 6 hours (the focus for the analyses in this publication). The results of the simulations with Coriolis accelerations are not described in the text. In like manner, a sensitivity test using an infrared radiation parameterization scheme revealed few appreciable differences during the first 6 hours of the simulation.

2.1.2 *Grid configuration and timesteps*

In order to explicitly simulate convective clouds on the domain, the model had a horizontal grid spacing of 2 km in both the $\hat{x}$ and $\hat{y}$ directions. This resolution is adequate to simulate convection in MCSs, as documented by Weisman et al. (1997). For comparison and detailed analysis, other 2D simulations had grid spacings of 1 km. Trial and error revealed that a domain size of 600 km in the across–line dimension (for this study, $\hat{x}$) was large enough to simulate MCSs without having the lateral boundary conditions add appreciable error. The model solutions on smaller grids were dependent upon the grid size, while the solutions did not change much for domain sizes greater than 600 km. In the along–line dimension (for this study, $\hat{y}$) the domain was 300 km long in the 3D simulations. Although this may seem unnecessarily large given the quasi–2D nature of the experiments, it allowed individual convective cells to develop at spacings that were intrinsic to the problem rather than those imposed by a small domain's along–line period. The large along–line extent permitted the modeled convective cells to move and interact with one another more naturally, much as real–world convective cells would when part of a long, quasi–2D line. It also increased the number of convective cells on the domain at any time, allowing computation of a greater variety of air parcel trajectories.

The domain height was 18 km owing to the fact that the tropopause in the averaged midlatitude MCS sounding was near 12 km, and that it was desirable to have a Rayleigh damping layer whose depth composed one third of the domain. Hence, the Rayleigh damping layer existed in the stratospheric part of the model. The vertical grid in the model was stretched, with an averaged spacing of 643 m, ranging from 400 m in the lowest 2 km of the domain to 780 m in the stratosphere. For comparison, the high resolution 2D simulations had an averaged vertical spacing of 499 m, ranging from 250 m in the lowest 2 km of the domain to 730 m in the stratosphere.

For the simulations with horizontal grid spacings of 2 km, the large timestep was 6 seconds and the small (acoustic) timestep was 3 seconds. For the simulations with horizontal grid spacings of 1 km, the large timestep was 3.5 seconds and the small (acoustic) timestep was 1.75 seconds.

2.1.3 Cloud microphysics

The simulations used a 6-category water microphysics scheme, incorporating two categories of liquid water (cloud droplets, q_c, and raindrops, q_r) following the Kessler-like scheme of Klemp and Wilhelmson (1978), and incorporating three categories of solid water (cloud ice, q_i, snow, q_s, and graupel/hail, q_g) as constructed by Tao and Simpson (1993) [who adapted the scheme of Lin et al. (1983)].

For the purposes of sensitivity studies it was useful to modify the strength (density perturbation) of the surface pool of cold outflow. The test included simulations whose environmental profiles of temperature, humidity, and wind were identical, but whose cold pools were different from one another because of the different evaporative chilling rates. This isolated the effects of evaporative chilling and the cold pool's strength on the systems' evolution without fundamentally altering the storms' initial structures and basic processes.

In the microphysical scheme, when cloud droplets enter unsaturated air they evaporate until either the air is saturated or the droplets are exhausted. However, when raindrops enter unsaturated air they evaporate at a rate given by the following equation [whose source can be traced back through similar forms which appear in Klemp and Wilhelmson (1978), Ogura and Takahashi (1971), and Kessler (1969)]:

$$E = \frac{1}{\bar{\rho}} \frac{C\left(1 - q_v/q_{sat}\right)\left(\bar{\rho} q_r\right)^{0.525}}{2.03 \times 10^4 + 9.584 \times 10^6 / \left(p q_{sat}\right)}, \tag{2.1}$$

wherein q_v is the water vapor mixing ratio, q_{sat} is the saturation mixing ratio, $\bar{\rho}$ is the base state density, p is the pressure, and C is the ventilation coefficient, given by:

$$C = 1.6 + 30.3922 \left(\bar{\rho} q_r\right)^{0.2046}, \tag{2.2}$$

with q_r as the rainwater mixing ratio. The sensitivity studies were simple modifications of the rain evaporation rate by a multiplicative factor. Results of these experiments are discussed in Chapter 7. Another sensitivity test involved halving the fallspeeds of graupel in the model; this modification had little effect, as discussed in Chapter 4. And yet a final sensitivity experiement incorporated a different ice microphysics scheme as designed by Schultz (1995).

2.1.4 Initial conditions

The model had a horizontally homogeneous initial condition, which was defined by a single sounding. The virtue of a horizontally homogeneous initial state in an idealized simulation is that the structure, organization, and evolution of convective storms are governed by the mean environment throughout the domain, and are not convoluted by the effects of synoptic-scale variations. In the real world, such variations are undoubtedly important in controlling mesoscale convective organization; however, the philosophy of the present study was to remove all unnecessary complications from the problem in order to gain as much direct insight as possible into the basic dynamics of the convective systems.

In simulations that included the Coriolis acceleration, the horizontal homogeneity necessarily meant that the initial condition was not in geostrophic/thermal wind balance. Such a balance would have required a horizontal temperature gradient, thereby forgoing the benefits of using a homogeneous environment. Instead, the model was configured so that the Coriolis accelerations only applied to the perturbation wind (that is, the part of the wind that is different from the initial state). Using this method, the initial condition is in a pseudo–balanced state: during the simulation, the wind field behaves as if the initial condition were balanced, but the thermodynamic variables retain their initial horizontal homogeneity.

Design of initial soundings

The environmental temperature and humidity soundings for this study were manual interpolations between the mean sounding for 59 warm–sector MCSs from Parker and Johnson (2000) and the mean sounding for 42 classifiable systems from Houze et al. (1990), as shown in their Fig.

15; therefore, they resembled those for midlatitude MCSs. Notably, except for their lowest 2 km, the two mean soundings were nearly identical to one another. In both studies, the soundings utilized were the best available conventional, operational observations, which were not always very close to the convective system in time and/or space. Accordingly, the averaged soundings in both studies, and in the new sounding for the present work, had significant convective inhibition (CIN, whose magnitude was generally ≥ 100 J kg^{-1}) and did not exhibit deep surface mixed–layers. This is likely because many of the soundings were from 1200 UTC (early morning in North America) and had not been destabilized by diurnal heating. Therefore, the present study used an artificial, 1 km deep surface mixed–layer for the mean sounding incorporating the mean sounding's maximal values of θ and q_v from the lowest 1 km. In practice, empirically determined analytic functions [closely following the structure used by Weisman and Klemp (1982)] defined the sounding used in the simulations. This was beneficial because the analytic functions were easy to modify in order to change the sounding systematically. The potential temperature (θ) and relative humidity (r) profiles were as follows, wherein z has units of m:

- if $z \leq z_{trop}$ then:

$$\alpha = 3 - 2\left(\frac{z}{z_{trop}}\right)^{0.1}, \tag{2.3}$$

$$\theta = \theta_{sfc} + (\theta_{trop} - \theta_{sfc})\left(\frac{z}{z_{trop}}\right)^{\alpha}, \tag{2.4}$$

$$\begin{aligned} r &= 1.0 - (1.0 - r_{min})\left(\frac{z}{z_{trop}}\right)^{360/z} \\ &+ (r_{trop} - r_{min})\left[\frac{|z - z_{rmin}| + z - z_{rmin}}{2\,(z_{trop} - z_{rmin})}\right]^{1.5}, \end{aligned} \tag{2.5}$$

subject to the constraint that everywhere $q_v \leq q_{v\,sfc}$.

- if $z > z_{trop}$ then:

$$\theta = \theta_{trop} \exp\left[\frac{g\,(z - z_{trop})}{c_p T_{trop}}\right], \tag{2.6}$$

$$r = r_{trop}. \tag{2.7}$$

Table 2.1: Default values for analytic creation of the mean MCS sounding used in this study. These values are used in (2.3)–(2.7).

variable	description	value
θ_{sfc}	surface potential temperature (K)	305.5
θ_{trop}	tropopause potential temperature (K)	340.0
T_{trop}	tropopause temperature (K)	214.0
z_{trop}	tropopause height (m)	11700
q_{sfc}	surface water vapor mixing ratio	0.015
r_{min}	sounding's minimum relative humidity	0.35
z_{rmin}	height of relative humidity minimum (m)	6000
r_{trop}	tropopause relative humidity	0.65
p_{sfc}	surface pressure (Pa)	95000

The default values for the mean MCS sounding are summarized in Table 2.1. The resulting sounding, as shown in Fig. 2.2, is slightly smoothed but is nevertheless representative of the mean environment for midlatitude linear MCSs. The bulk thermodynamic variables that describe the mean MCS sounding are summarized in Table 2.2. Notably, the convective available potential energy (CAPE) of this mean sounding is on the high end of typical values for midlatitude MCSs as documented by Houze et al. (1990) and Parker and Johnson (2000). However, as discussed above, the original mean sounding had to be modified in order for convection to be initiated and survive in the simulations; presumably, nature also destabilizes the environment (removing CIN and adding CAPE) prior to real world convective initiation.

The base state wind profile for the front–fed LS system control runs was taken as the average wind profile of four archetypal front–fed LS systems (which were among the population of LS MCSs summarized by Parker and Johnson 2000). For simplicity, the wind profile was reduced to

Table 2.2: Bulk thermodynamic variables for the analytic mean MCS sounding. Parcel indices are computed using an un–mixed surface air parcel.

thermodynamic parameter	value
lifting condensation level (hPa)	840
level of free convection (hPa)	795
convective available potential energy (J kg^{-1})	2577
convective inhibition (J kg^{-1})	–34
lifted index (K)	-8.4
precipitable water (cm)	3.20

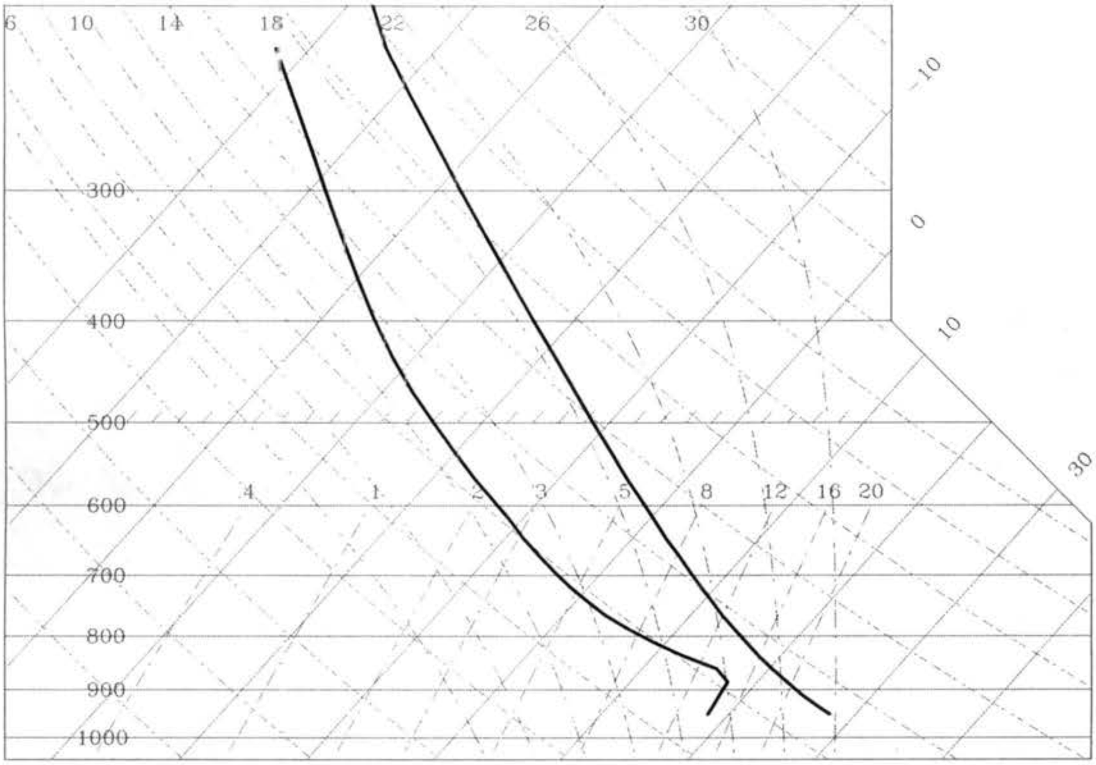

Figure 2.2: Skew-T ln-p diagram of the mean MCS sounding used in this study. Bulk thermodynamic variables for this sounding are given in Table 2.2.

anchor points, and varied linearly between the values at the anchor points. The u–wind values for the control run ("S=16", so called because the 3–10 km vector wind difference was $\approx$ 16 m s^{-1}) are plotted in Fig. 2.3, along with two variations that had weaker wind shear above 3 km AGL ("S=10" and "S=4", which had 3–10 km vector wind differences of $\approx$ 10 and 4 m s^{-1}, respectively). Simulations with weaker wind shear tested the sensitivity of the convection's evolution to the middle and upper tropospheric winds, much has been done in many previous numerical squall line studies [e.g. Hane (1973), Thorpe et al. (1982), Seitter and Kuo (1983), Dudhia et al. (1987), Nicholls et al. (1988), Weisman et al. (1988), and Szeto and Cho (1994)]. An additional experiment (in both 2D and 3D) used the S=10 profile, but with the wind shear below 3 km AGL reduced by half (not shown). The control run's initial state was 2D, and included no v–wind. Sensitivity tests indicated that the inclusion of a realistic v–wind did not substantially affect the structure or evolution of the periodic 3D simulations.

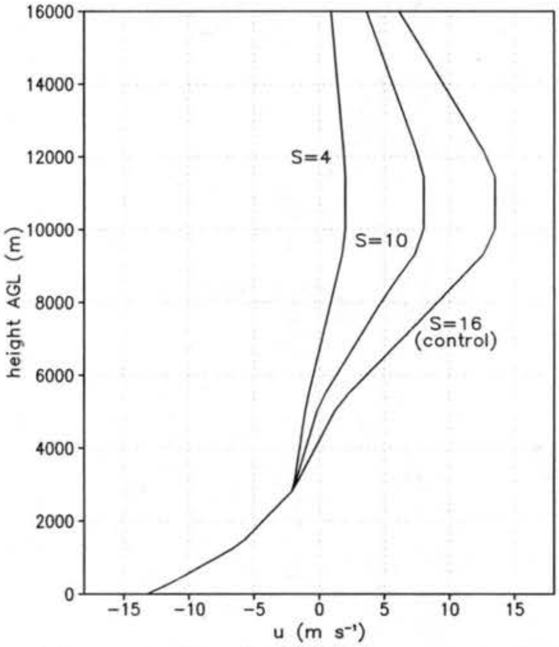

Figure 2.3: Profiles of u–wind used in this study. The mean front–fed LS MCS wind profile is labeled as "S=16" (3–10 km vector wind difference $\approx$ 16 m s^{-1}). "S=10" and "S=4" are modified wind profiles with decreased wind shear above 3 km AGL (3–10 km vector wind differences $\approx$ 10 and 4 m s^{-1}, respectively).

Initiation of convection

Much as Yang and Houze (1995), Weisman et al. (1997), and others have done, in order to initiate convection the model included an initial surface cold box that was 2 km deep and defined by a constant buoyancy of -0.1 m s^{-2} (which corresponds to a potential temperature perturbation of -3.2 K in the BASE sounding). This was the minimal cold pool strength that reliably initiated a long–lived convective system. Because the first round of simulated convection in the model produced much colder surface outflow, the later simulated convection was fairly independent of the initial trigger. For all of the 3–D simulations, the cold box included small ($\leq$ 0.1 K) random fluctuations in order to help 3–D structures develop and amplify. While the initial convection was fairly 2–D, after 2 hours of simulation the convective lines were cellular and remained 3–D for the duration of the simulations. For this study, a cold box was preferable to warm thermals because it mimics the way that convective lines tend to be initiated in the real world: 63 of the 64 linear warm–

sector MCSs studied by Parker and Johnson (2000) occurred at or near a linear surface boundary (e.g. front, pressure trough, dryline, or outflow boundary). In addition, the long linear edge of the cold box was useful in ensuring that the convective line's initial orientation with respect to the wind profile was correct.

2.2 Analysis of model output

2.2.1 Trajectories

To facilitate analysis of air parcels, the model computed particle trajectories during the simulations using the scheme described by Eitzen (2001), generalized to three dimensions. The particles were advected by the grid–scale wind; neither conservation properties nor sub–gridscale mixing were included in their computation. One thousand massless particles were launched at the initial model time, and their new positions owing to advection were computed at each model time step using a Runge–Kutta iterative finite difference scheme. The u, v, and w wind components at any location were determined by tri–linear interpolation for each particle and for each iteration of the Runge–Kutta computation. The values of model variables (e.g. temperature) along the particle trajectories were then computed in post–processing via tri–linear interpolation in space and linear interpolation in time. Post–processing routines computed additional trajectories of interest using tri–linear interpolation for u, v, and w in space, linear interpolation in time, and a Heun iterative finite difference scheme to advect the parcels.

2.2.2 Pressure field decomposition

For the 2D simulations, and for select times in the 3D simulations, it was computationally affordable to solve the diagnostic pressure equation in terms of its dynamic and buoyant components. This section describes the formulation of the diagnostic pressure equation and the method used to solve it.

A diagnostic pressure equation

The prognostic equation for motion in Cartesian coordinates is:

$$\frac{D\mathbf{u}}{Dt} = -\frac{1}{\rho}\boldsymbol{\nabla} p - 2\Omega \times \mathbf{u} - \mathbf{g} + \mathbf{F}. \tag{2.8}$$

Assuming that $|\rho'/\rho_o| \ll 1$ and that the mean state is hydrostatic, the scaled equation of motion is:

$$\frac{D\mathbf{u}}{Dt} = -\frac{1}{\rho_o}\boldsymbol{\nabla} p' - 2\Omega \times \mathbf{u} - \mathbf{g}\left(\frac{\rho'}{\rho_o}\right) + \mathbf{F}. \tag{2.9}$$

The anelastic continuity equation is:

$$\boldsymbol{\nabla} \cdot (\rho_o \mathbf{u}) = 0. \tag{2.10}$$

By combining $\mathbf{u}$(2.10) with ρ_o(2.9), the equation of motion in flux form is:

$$\frac{\partial}{\partial t}(\rho_o \mathbf{u}) + \boldsymbol{\nabla} \cdot (\rho_o \mathbf{u}\mathbf{u}) + \boldsymbol{\nabla} p' - \rho_o \mathbf{B} = 0, \tag{2.11}$$

wherein the Coriolis and frictional accelerations have been omitted, and for brevity of notation $\mathbf{B} \equiv -\mathbf{g}\,\rho'/\rho_o$. By taking $\boldsymbol{\nabla}\cdot$ (2.11), the diagnostic pressure equation is:

$$\frac{\partial}{\partial t}\left[\underbrace{\boldsymbol{\nabla} \cdot (\rho_o \mathbf{u})}_{=0}\right] + \boldsymbol{\nabla} \cdot [\rho_o (\mathbf{u} \cdot \boldsymbol{\nabla})\,\mathbf{u}] + \nabla^2 p' - \frac{\partial}{\partial z}(\rho_o B) = 0, \tag{2.12}$$

or more simply:

$$\nabla^2 p' = -\boldsymbol{\nabla} \cdot [\rho_o (\mathbf{u} \cdot \boldsymbol{\nabla})\,\mathbf{u}] + \frac{\partial}{\partial z}(\rho_o B). \tag{2.13}$$

Separating into buoyant and dynamic parts ($p' = p'_B + p'_D$):

$$\nabla^2 p'_B = \frac{\partial}{\partial z}(\rho_o B); \tag{2.14}$$

$$\nabla^2 p'_D = -\boldsymbol{\nabla} \cdot [\rho_o (\mathbf{u} \cdot \boldsymbol{\nabla})\,\mathbf{u}]. \tag{2.15}$$

Applying the identity $\boldsymbol{\nabla} \cdot (\psi \mathbf{a}) = \mathbf{a} \cdot \boldsymbol{\nabla}\psi + \psi\,(\boldsymbol{\nabla} \cdot \mathbf{a})$, (2.15) becomes:

$$\nabla^2 p'_D = -\left[(\mathbf{u} \cdot \boldsymbol{\nabla})\,w\right]\frac{\partial \rho_o}{\partial z} - \rho_o \boldsymbol{\nabla} \cdot [(\mathbf{u} \cdot \boldsymbol{\nabla})\,\mathbf{u}], \tag{2.16}$$

or:

$$\begin{aligned} \nabla^2 p'_D \;=\;& -\left[(\mathbf{u} \cdot \boldsymbol{\nabla})\,w\right]\frac{\partial \rho_o}{\partial z} - \rho_o\left[\left(\frac{\partial u}{\partial x}\right)^2 + \left(\frac{\partial v}{\partial y}\right)^2 + \left(\frac{\partial w}{\partial z}\right)^2\right] \\ & -2\rho_o\left(\frac{\partial v}{\partial x}\frac{\partial u}{\partial y} + \frac{\partial u}{\partial z}\frac{\partial w}{\partial x} + \frac{\partial v}{\partial z}\frac{\partial w}{\partial y}\right) - \rho_o\left[(\mathbf{u} \cdot \boldsymbol{\nabla})\,(\boldsymbol{\nabla} \cdot \mathbf{u})\right]. \end{aligned} \tag{2.17}$$

From (2.10), $\nabla \cdot \mathbf{u} = -(w/\rho_o)\, \partial\rho_o/\partial z$, so the final term of (2.17) can be rewritten to yield:

$$\begin{aligned}
\nabla^2 p'_D \;=\; & -\frac{\partial \rho_o}{\partial z}\left(u\frac{\partial w}{\partial x} + v\frac{\partial w}{\partial y} + w\frac{\partial w}{\partial z}\right) \\
& -\rho_o\left[\left(\frac{\partial u}{\partial x}\right)^2 + \left(\frac{\partial v}{\partial y}\right)^2 + \left(\frac{\partial w}{\partial z}\right)^2\right] \\
& -2\rho_o\left(\frac{\partial v}{\partial x}\frac{\partial u}{\partial y} + \frac{\partial u}{\partial z}\frac{\partial w}{\partial x} + \frac{\partial v}{\partial z}\frac{\partial w}{\partial y}\right) \\
& +u\frac{\partial \rho_o}{\partial z}\frac{\partial w}{\partial x} + v\frac{\partial \rho_o}{\partial z}\frac{\partial w}{\partial y} + \rho_o w^2 \frac{\partial^2}{\partial z^2}(\ln\rho_o) + w\frac{\partial \rho_o}{\partial z}\frac{\partial w}{\partial z},
\end{aligned} \tag{2.18}$$

or, removing the cancelling terms:

$$\begin{aligned}
\nabla^2 p'_D \;=\; & \underbrace{-\rho_o\left[\left(\frac{\partial u}{\partial x}\right)^2 + \left(\frac{\partial v}{\partial y}\right)^2 + \left(\frac{\partial w}{\partial z}\right)^2 - w^2\frac{\partial^2}{\partial z^2}(\ln\rho_o)\right]}_{\text{fluid extension terms}} \\
& \underbrace{-2\rho_o\left(\frac{\partial v}{\partial x}\frac{\partial u}{\partial y} + \frac{\partial u}{\partial z}\frac{\partial w}{\partial x} + \frac{\partial v}{\partial z}\frac{\partial w}{\partial y}\right)}_{\text{fluid shear terms}}.
\end{aligned} \tag{2.19}$$

Finally, by applying $u = u_o(z) + u'$ and $w = w'$, the linear part of the dynamic pressure perturbation is diagnosed from:

$$\nabla^2 p'_{D\ linear} = -2\rho_o \frac{du_o}{dz}\frac{\partial w}{\partial x}. \tag{2.20}$$

Therefore, the non–linear part of the dynamic pressure perturbation ($p'_{D\ non-linear}$) is simply $p'_D - p'_{D\ linear}$. Basic pressure anomalies in FFLS systems, along with their relationship to the forms in (2.14) and (2.19), are described in Chapter 3.

Method of solution

Model output provides p', ρ_o, B, u, u_o and w. Gauss–Seidel relaxation then provides p'_D and $p'_{D\ lin}$, subject to the following constraints:

- at the top and lateral boundaries, which are far–removed, $p'_D = 0$
- at the bottom boundary, $\partial p'_D/\partial z = 0$
- on all boundaries, $p'_{D\ linear} = 0$

p'_B is then the remainder of the pressure perturbation:

$$p'_B = p' - p'_D. \tag{2.21}$$

Notably, if (2.14) is relaxed to solve for p'_B with suitable boundary conditions, the result is very similar to that from (2.21); in other words, the residual is small.

2.2.3 Momentum equation decomposition and nomenclature

In order to make the discussions and labeling simpler, this publication employs abbreviated names for the terms in the decomposed momentum equation, as shown by brackets below. For inviscid, irrotational flow, (2.9) becomes:

$$\frac{D\mathbf{u}}{Dt} = \underbrace{-\frac{1}{\rho_o}\boldsymbol{\nabla}p' - \mathbf{g}\left(\frac{\rho'}{\rho_o}\right)}_{ACC}. \tag{2.22}$$

Following the analysis in § 2.2.2,

$$\underbrace{p'}_{P'} = \underbrace{p'_B}_{P'B} + \underbrace{p'_{D\ linear}}_{P'DL} + \underbrace{p'_{D\ non-linear}}_{P'DNL}. \tag{2.23}$$

By applying (2.23), regrouping the terms, and explicitly writing the hydrometeor contribution to density, (2.22) becomes:

$$\frac{D\mathbf{u}}{Dt} = \underbrace{-\frac{1}{\rho_o}\boldsymbol{\nabla}p'_B \underbrace{-\mathbf{g}\left(\frac{\rho'_{gas}}{\rho_o}\right)}_{BUOY} \underbrace{-\ \mathbf{g}\, q_h}_{DRAG}}_{ACCB} \underbrace{-\frac{1}{\rho_o}\boldsymbol{\nabla}p'_{D\ linear}}_{ACCDL} \underbrace{-\frac{1}{\rho_o}\boldsymbol{\nabla}p'_{D\ non-linear}}_{ACCDNL}, \tag{2.24}$$

wherein ρ'_{gas} is the density perturbation attributable to the gaseous consituents and q_h is the total hydrometeor mixing ratio. In words, P' is the total pressure perturbation, $P'B$ is the buoyant pressure perturbation, $P'DL$ is the linear part of the dynamic pressure perturbation, $P'DNL$ is the non–linear part of the dynamic pressure perturbation, ACC is the total parcel acceleration, $BUOY$ is the acceleration owing to local buoyancy of humid air, $DRAG$ is the acceleration owing to the weight of hydrometeors suspended in the air, $ACCB$ is the acceleration owing to the combined effects of local buoyancy and the gradient in the buoyant pressure field, $ACCDL$ is the acceleration owing to the gradient in the linear dynamic pressure field, and $ACCDNL$ is the acceleration owing to the gradient in the non–linear dynamic pressure field. These terms appear throughout this publication.

2.2.4 Emphasis on parcel analysis

Conservation equations for the gaseous (q_v), liquid ($q_c + q_r$), and solid ($q_i + q_s + q_g$) water constituents are:

$$\frac{Dq_v}{Dt} = E - C + S - D, \tag{2.25}$$

$$\frac{D}{Dt}(q_c + q_r) = -E + C - F + M - \nabla \cdot (\hat{\mathbf{u}}_r q_r), \tag{2.26}$$

$$\frac{D}{Dt}(q_i + q_s + q_g) = -S + D + F - M - \nabla \cdot (\hat{\mathbf{u}}_s q_s) - \nabla \cdot (\hat{\mathbf{u}}_g q_g), \tag{2.27}$$

wherein E is the evaporation rate, C is the condensation rate, S is the sublimation rate, D is the deposition rate, F is the freezing rate, M is the melting rate, and velocities with hats and subscripts represent the mass–weighted average velocities of each hydrometeor species. Note that, by definition, cloud water and ice (q_c and q_i) follow air parcels and do not move with respect to the flow. The total water mixing ratio, q_t, is:

$$q_t = q_v + q_c + q_r + q_s + q_i + q_g. \tag{2.28}$$

Similarly, the precipitation mixing ratio, q_p is:

$$q_p = q_r + q_s + q_g. \tag{2.29}$$

By summing (2.25)–(2.27) and applying (2.28) and (2.29), the continuity equation for total water substance can be written as:

$$\frac{Dq_t}{Dt} = -\nabla \cdot (\hat{\mathbf{u}}_r q_r) - \nabla \cdot (\hat{\mathbf{u}}_s q_s) - \nabla \cdot (\hat{\mathbf{u}}_g q_g) \approx -\nabla \cdot (\hat{\mathbf{u}}_p q_p) \approx -\frac{\partial}{\partial z}(\hat{w}_p q_p), \tag{2.30}$$

wherein $\hat{\mathbf{u}}_p$ is the mass–weighted average velocity of the precipitation particles and $\hat{w}_p$ is the mass-weighted vertical speed of the precipitation particles. Because the background total water content in the middle and upper troposphere is quite low, air parcels with high water content must be

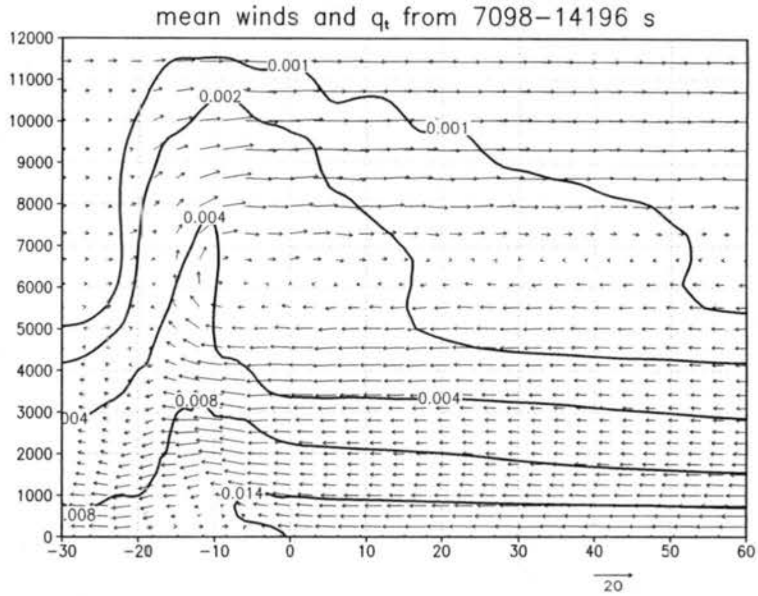

Figure 2.4: Mean wind vectors (m s^{-1}) and total water mixing ratio (q_t, contoured at 0.001, 0.002, 0.004, 0.008, and 0.014) for control (S=16, E=1) simulation from 7098–14196 s.

transported forward from the convective line in order for leading stratiform precipitation to develop, or rearward in order for trailing stratiform precipitation to develop. Both temporally averaged fields (Fig. 2.4) and parcel trajectories (see, e.g., § 5.1) confirm that the water in the leading preciptiation regions of the present simulations is attributable primarily to air parcels that have ascended in the convective updrafts. Plus or minus gains and losses from vertical divergence in the precipitation flux, air parcels from the lower troposphere carry with them their comparatively high total water contents, as in (2.30). Therefore, the most suitable way to analyze the dynamics that generate a leading or trailing stratiform precipitation region is to analyze the dynamics that affect the velocities of individual parcels as they pass through the convective region.

The relevant velocity for this problem is an air parcel's storm–relative velocity as it leaves the main updraft. The x-component of (2.22) is:

$$\frac{Du}{Dt} = -\frac{1}{\rho_o}\frac{\partial p'}{\partial x}. \tag{2.31}$$

A storm–relative velocity is defined via:

$$u_{sr} = u - c, \tag{2.32}$$

wherein c is the translational speed of the updraft. Initially, for an inflowing air parcel,

$$(u_{sr})_i = (u_{env})_i - c, \tag{2.33}$$

wherein u_{env} is the environmental inflow windspeed. Therefore, integrating (2.31) over the course of an air parcel's ascent, a parcel's final storm–relative velocity is given by:

$$(u_{sr})_f = (u_{sr})_i + \int_{t_i}^{t_f} \left(-\frac{1}{\rho_o} \frac{\partial p'}{\partial x} \right) dt. \tag{2.34}$$

This publication describes the total horizontal pressure gradient acceleration along air parcel trajectories and analyzes the buoyant and dynamic pressure contributions as described in Section 2.2.2.

Chapter 3

ACCELERATIONS ON AIR PARCELS IN THE CONVECTIVE REGION

This chapter outlines the basic and higher–order processes that produce pressure anomalies in the vicinity of cold pools and buoyant updrafts in a sheared environment. These pressure anomalies are important because, as shown by (2.24) and (2.34), they determine the horizontal accelerations on air parcels which, in turn, determine whether hydrometeors and water vapor are transported forward or rearward away from the convective updrafts.

3.1 Basic 2D parcel accelerations

This section presents the components of typical pressure perturbations that accompany cold pools and updrafts in vertical wind shear. Figure 3.1 depicts the basic shapes and processes that account for P'B, P'DL, and P'DNL. Before discussing them, it is worthwhile to restate the results of § 2.2.2 for reference. In 2D:

$$\nabla^2 p'_B = \frac{\partial}{\partial z}\left(\rho_o B\right); \tag{3.1}$$

$$\nabla^2 p'_{D\ linear} = -2\rho_o \frac{du_o}{dz}\frac{\partial w}{\partial x}; \tag{3.2}$$

$$\nabla^2 p'_{D\ nonlinear} = -\rho_o\left[\left(\frac{\partial u'}{\partial x}\right)^2 + \left(\frac{\partial w}{\partial z}\right)^2 - w^2\frac{\partial^2}{\partial z^2}\left(\ln\rho_o\right)\right] - 2\rho_o\frac{\partial u'}{\partial z}\frac{\partial w}{\partial x}; \tag{3.3}$$

wherein u' represents the deviation from the base state's $u_o(z)$.

Cold pool P'B

A surface cold pool exhibits relatively high pressure near the surface compared to its top (Fig. 3.1A). Because most cold pools are characterized by $\partial B/\partial z \approx 0$ near the surface with

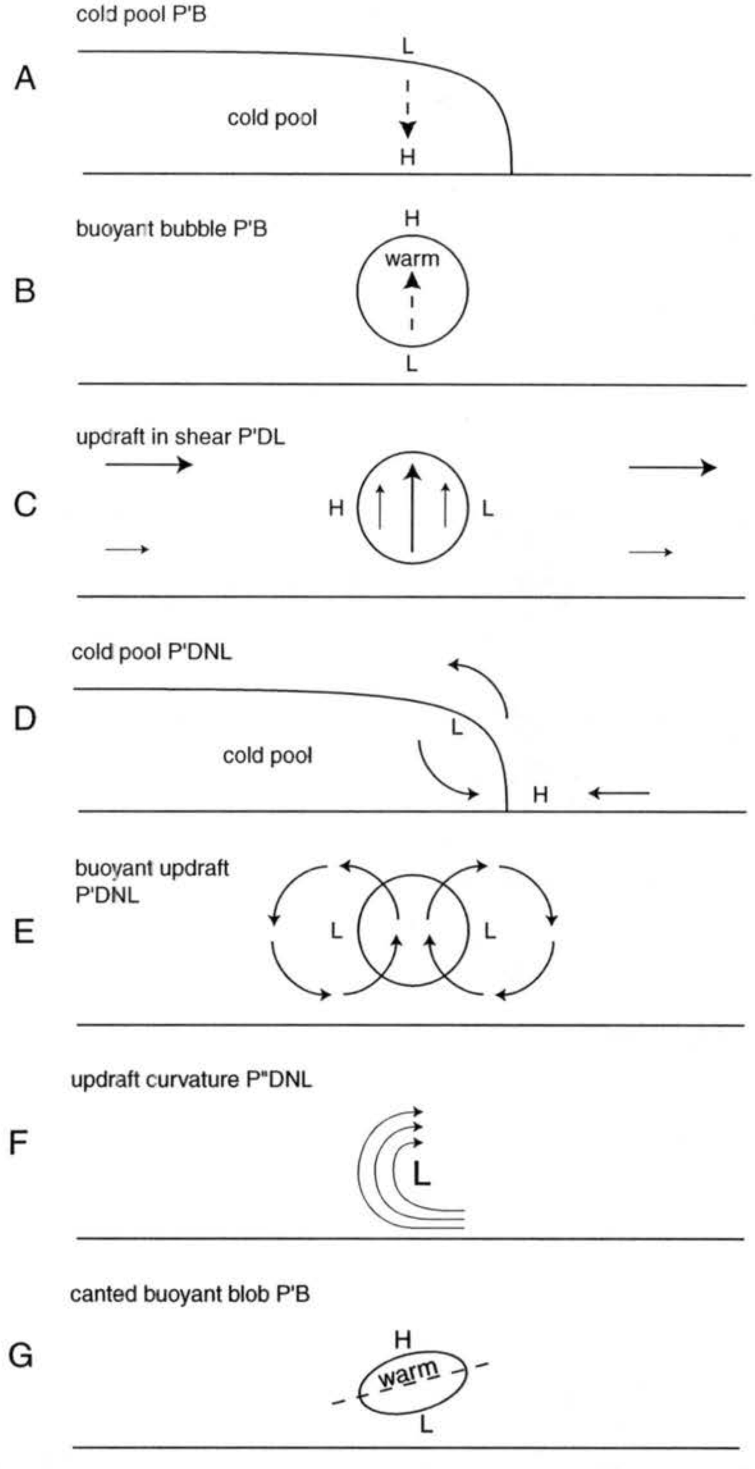

Figure 3.1: Schematic depiction of simple cold pool, updraft, and wind shear configurations that account for components of the perturbed pressure field. Wind streamlines are depicted as solid arrows, buoyant accelerations are depicted as dashed arrows, and pressure maxima and minima are denoted by H and L, respectively. Subfigures are labeled above and are explained in the text. Sizes and magnitudes are not necessarily scaled quantitatively.

$\partial B/\partial z > 0$ in the middle and upper parts of the cold pool, simple consideration of (3.1) implies minimized pressure in their middle and upper reaches. However, the exact values for P'B in this case are heavily dependent upon the far field. As a simplified thought experiment, consider a vertical profile of buoyancy in a cold pool as given by:

$$\rho_o B = -\cos\left(\frac{\pi z}{D}\right), \tag{3.4}$$

wherein D is the top of the cold pool. Now, in the limit of hydrostaticity, $Dw/Dt = 0$ and (2.24) reduces to:

$$\frac{\partial^2 p'_B}{\partial z^2} = \frac{\partial}{\partial z}\left[\rho_o\left(-g\frac{\rho'}{\rho_o}\right)\right], \tag{3.5}$$

or equivalently, in the context of (3.1):

$$\nabla^2 p'_B = \frac{\partial^2 p'_B}{\partial z^2} = \frac{\partial}{\partial z}\left(\rho_o B\right). \tag{3.6}$$

Therefore, for the case of (3.4):

$$p'_B = -\frac{D}{\pi}\sin\left(\frac{\pi z}{D}\right) + \text{constant}. \tag{3.7}$$

The constant of integration is then determined by the boundary conditions. If no perturbations exist on the top boundary of the cold pool then the constant of integration is D/π and the result is a pressure maximum at the surface that decays to zero at the top of the cold pool. However, quite often when convection is present additional patches of positive buoyancy exist in the environment such that the cold pool's top boundary condition is actually $p'_B < 0$; in that case, the constant of integration for (3.7) must be smaller than D/π. In other words, the cold pool's P'B field exhibits both a maximum at the surface and a minimum in the strong gradient in buoyancy in the upper part of the cold pool, as shown in Fig. 3.1A. Without rigorously solving for P'B in each individual case (including the environment above the cold pool), it is impossible to exactly determine whether a cold pool's P'B will locally appear as a surface pressure maximum or as a pressure minimum aloft. Nevertheless, in either case P'B will be comparatively higher at the surface than at the cold pool's top. Additionally, in most circumstances, the P'B field is not hydrostatic. Generally, because the buoyancy field exhibits horizontal structure, P'B also has horizontal structure. In that case, both

a) horizontal accelerations occur, and b) P'B is insufficient to oppose the negative buoyancy in the cold pool; therefore, the dense air descends (as depicted by the dashed arrow in Fig. 3.1A) and the vertical pressure gradient owing to P'B is somewhat less than the hydrostatic value.

Buoyant bubble P'B

A bubble of buoyant air exhibits relatively high pressure above and relatively low pressure below its center (Fig. 3.1B). Buoyancy increases with height in the lower half of the bubble, which is consistent with locally minimized pressure, and decreases with height in the upper half of the bubble, which is consistent with locally maximized pressure.

Updraft in shear P'DL

An updraft in a mean sheared environment exhibits relatively high pressure on its upshear side and relatively low pressure on its downshear side (Fig. 3.1C). On the upshear side of the updraft the local flow is dominated by deformation and du_o/dz and $\partial w/\partial x$ are same–signed, which is consistent with locally maximized pressure. On the downshear side of the updraft the local flow is dominated by rotation and du_o/dz and $\partial w/\partial x$ are opposite–signed, which is consistent with locally minimized pressure.

Cold pool P'DNL

The accelerations due to buoyancy and P'B, as shown in Fig. 3.1A, generate a local circulation that renders relatively high pressure near and ahead of the cold pool's gust front and relatively low pressure in the cold pool's head (Fig. 3.1D). Heavy air in the cold pool descends, as represented by the dashed arrow in Fig. 3.1A, and then is accelerated forward by the horizontal gradient in P'B, accounting for the descending rear–to–front flow branch depicted in Fig. 3.1D. Meanwhile, the vertical gradient in P'B forces air to ascend near and to the right of the cold pool's edge. This occurs because the P'B field is two dimensional; the non–hydrostatic part of P'B extends rightward past the boundary of the cold pool and produces an upward acceleration in regions where there is no negative buoyancy to counteract it. Once air has ascended to near the height of the cold pool's top, it is then accelerated rearward toward the minimum in P'B that is shown in Fig. 3.1A. These processes account for the ascending front–to–rear flow branch depicted in Fig. 3.1D. Away from the cold pool, the environment's wind is unperturbed, as represented by the arrow to the right of the cold pool in Fig. 3.1D. Therefore, the low levels ahead of the cold pool's leading edge are dominated by convergence, which is consistent with locally maximized pressure, whereas the cold pool's head is dominated by rotation, which is consistent with locally minimized pressure.

Buoyant updraft P'DNL

Any updraft in an unpertubed environment necessarily embodies a couplet of positive and negative horizontal vorticity owing to its locally maximized w. In addition, the P'B field associated with a buoyant updraft (Fig. 3.1B) will cause divergence above the updraft, convergence below the updraft, and subsidence to the sides of the updraft, rendering a vortical circulation such as depicted by the arrows in Fig. 3.1E. Therefore, both flanks of the updraft are dominated by rotation, with opposite–signed $\partial u'/\partial z$ and $\partial w/\partial x$, which is consistent with locally minimized pressure.

Updraft curvature P'DNL

Although it is merely a refinement to the P'DNL field associated with a simple buoyant updraft (Fig. 3.1E), for strongly curved flow fields (in this case updrafts), the pressure minimum on the side nearer to the axis of rotation has an increased magnitude, while the pressure minimum on the side farther from the axis of rotation has a decreased magnitude (Fig. 3.1F). On the side of the updraft closer to the axis of rotation (the right hand side of the updraft in Fig. 3.1F), the magnitude of $\partial u'/\partial z$ is greatly increased, which is consistent with more strongly minimized pressure. In contrast, on the side of the updraft that is farther from the axis of rotation (the left side of the updraft in Fig. 3.1F), the magnitude of $\partial u'/\partial z$ is decreased to nearly zero, which thereby implies negligible perturbed dynamic pressure.

Canted buoyant blob P'B

Although it is merely a refinement to the P'B field associated with a simple buoyant bubble (Fig. 3.1B), when a non–spherical blob of buoyant air is tilted off–vertical it yields a horizontal gradient in P'B, and therefore a horizontal acceleration. Provided that the shape of the buoyancy field in the canted blob is well–behaved (i.e. approximately linear, sinusoidal, or Gaussian with respect to its major and minor axes), if its axes are not purely vertical and horizontal, its characteristic pressure maximum and minimum (as in Fig. 3.1B) will not be vertically aligned. This is because the pressure extrema are not located directly above and below the maximum in buoyancy, but rather are located where the vertical gradient in buoyancy is largest. This process, although essentially the same as for a simple buoyant bubble, is unique in that it will produce horizontal accelerations owing to the horizontal gradient in P'B. The process is applicable to a forced updraft at the edge of a surface cold pool (which air parcels generally pass through, carrying buoyancy with them) and to a free deep convective updraft that is tilted, as well as on the larger scale of a broad stratiform cloud.

3.2 Additional 2D parcel accelerations in mature systems

In a mature convective system, quasi–steady perturbed pressure fields exist. Persistent pressure anomalies, in turn, induce persistent mesoscale circulations. After about 2 hours of the control FFLS simulation, it is clear that the mature convective system has had several prominent effects on the local winds (Fig. 3.2). The updrafts during this time interval occur between $x = -15$ and $x = 0$ km. Above 6 km AGL the dynamic and buoyant pressure maxima, which are located above active buoyant updrafts, have rendered mean storm–top divergence. Additionally, in the lowest 1.5 km AGL the buoyant pressure maximum associated with a persistent, quasi–steady surface cold pool has produced mean westerly accelerations which account for westerlies within the cold pool itself and for the deceleration of the easterly inflowing air to the right of $x = 0$ km. Finally, between 2 and 6 km AGL and east of $x = -15$ km, the wind is strongly perturbed into an easterly mid–level jet. Between $x = -15$ and $x = -5$ km, the easterly perturbation is largely a symptom of vertical

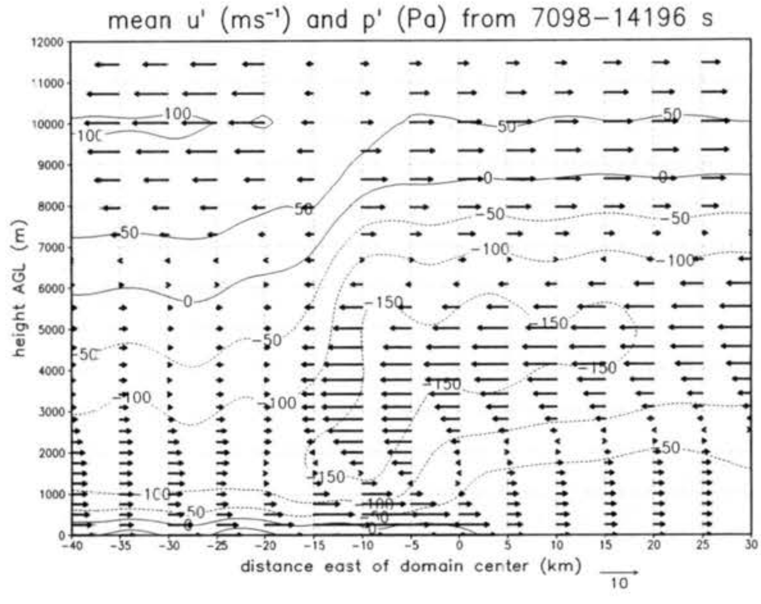

Figure 3.2: Mean perturbation u–wind (vectors, m s^{-1}) and perturbation pressure (contours, Pa) for the control FFLS simulation from 7098–14196 s. As discussed in the text, the pictured u' field is long–lived, but represents a perturbation with respect to the base state.

fluxes of easterly momentum in convective updrafts. Farther east, however, the front–to–rear flow is a response to a mid–level pressure minimum (Fig. 3.2). This mid–level low is primarily from P'B beneath the positively buoyant air exiting the convective cells and forming the leading cloud region, although P'DNL owing to the curved overturning flow contributes non–trivially on the downshear flank of the mean updraft's position (Fig. 6.12). Middle tropospheric pressure minima and attendant front–to–rear inflow jets are known to commonly occur in mature TS MCSs (Smull and Houze 1987b). LeMone (1983) cited hydrostatic adjustment to the buoyancy of the rearward–tilting updrafts and stratiform regions of TS systems as accounting for their mid–level pressure minima, and Szeto and Cho (1994) discussed the additional importance of a dynamic contribution from the vorticity located between the front–to–rear and rear–to–front airstreams in TS systems. In these two respects, there may be a great deal of similarity between the middle tropospheric low pressure anomalies in TS systems and in the FFLS simulations[1] .

[1] However, unlike in TS systems, the front–to–rear inflow jet in the simulated FFLS systems does not appear to descend and add its momentum to the surface cold pool.

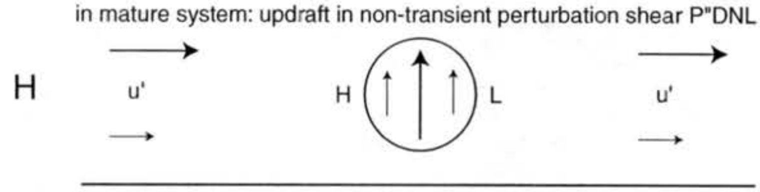

Figure 3.3: Schematic depiction of an updraft and wind shear configuration that accounts for a component of the perturbed pressure field in a mature system. Perturbed wind vectors are depicted as solid arrows and pressure maxima and minima are denoted by H and L, respectively. The figure is labeled "H" for continuity with Fig. 3.1, and is explained in the text. Sizes and magnitudes are not necessarily scaled quantitatively.

Updraft in non–transient perturbation shear P'DNL

Because the convective system perturbs the wind field in a way that changes the vertical shear for long periods of time (i.e. much longer than an individual convective life cycle), updrafts that occur in the local wind profile exhibit additional dynamic pressure anomalies which are attributable to the "updraft in shear" process shown in Fig. 3.1C. However, these pressure anomalies are diagnosed as a part of P'DNL, as in Fig. 3.3H, rather than as a part of P'DL, as in Fig. 3.1C, because even though the wind perturbations are persistent they nevertheless represent deviations (u') from the background state. On the upshear side of the updraft in Fig. 3.3H the perturbed flow is dominated by deformation and $\partial u'/\partial z$ and $\partial w/\partial x$ are same–signed, which is consistent with locally maximized pressure. On the downshear side of the updraft in Fig. 3.3H the perturbed flow is dominated by rotation and $\partial u'/\partial z$ and $\partial w/\partial x$ are opposite–signed, which is consistent with locally minimized pressure. For the mature phase of the simulated FFLS system, the vertical wind shear was decreased (became more easterly) in the lowest 4 km AGL, and was increased (became more westerly) in the 4–10 km AGL layer. From consideration of (3.3) and by analogy to Fig. 3.3H, this should imply a westward ACCDNL for updrafts in the lowest 4 km, and an eastward ACCDNL for updrafts in the 4–10 km layer.

Chapter 4

QUASI–STABLE STRUCTURES FOR SIMULATED CONVECTIVE LINES WITH LEADING PRECIPITATION

Parker and Johnson (2000) identified convective lines with trailing (TS), leading (LS), and parallel (PS) stratiform precipitation. Among these three archetypes, the TS and LS systems exist in environments with quasi–2D wind profiles and can be represented in 2D models. Based on the observational study of Parker and Johnson (2000), three basic and somewhat similar mean flow configurations occur for the TS and LS systems: convective lines with trailing precipitatation that are fed by front–to–rear low–level inflow ("front–fed TS", or FFTS), convective lines with leading precipitation that are fed by front–to–rear low–level inflow ("front–fed LS", or FFLS), and convective lines with leading precipitation that are fed by rear–to–front low–level inflow ("rear–fed LS", or RFLS).[1] The mean flow fields in FFTS systems are well–known, and have been described in numerous studies [e.g. Zipser (1977), Houze et al. (1989), and Biggerstaff and Houze (1991)]. Parker and Johnson (2000) suggested that RFLS and FFTS systems might be very similar to one another dynamically given their mirror–image reflectivity patterns and the approximate symmetry of their storm–relative wind profiles. Although the RFLS/FFTS question is not a major focus of this publication, Section 7.3 does address it briefly. The remainder of this chapter is devoted to describing the *quasi–stable* mature stages of FFLS systems in the 2D and periodic–3D simulations. Section 4.1 is about the basic kinematic and precipitation fields in the 2D and 3D FFLS systems and Section 4.2 is about the importance of the persistent pre–line precipitation in helping to maintain

[1] Although there is no fundamental principle that *prohibits* a "rear–fed TS" configuration, this author knows of no such cases, and the environment necessary for the production of an RFTS system (e.g. strong easterly shear superposed upon the western edge of a cold pool) seems exceedingly unlikely.

FFLS systems.

4.1 Basic system structures

4.1.1 Two–dimensional simulated front–fed LS system

In a 2D simulation using the control sounding (Fig. 2.2) and S=16 wind profile (Fig. 2.3), a long–lived front–fed convective line with leading precipitation occurred (Fig. 4.1). As can be seen in Fig. 4.1, the leading precipitation region developed with time throughout the first 4 hours of the simulation. Deep convection was continually initiated above the surface cold pool in the vicitnity of its outflow boundary and, as can be inferred from Fig. 4.2, each updraft pulse of the multicellular system contributed a patch of enhanced water content to the plume of line–leading hydrometeors. Chapter 5 describes the periodic components of the multicellular system's circulation and analyzes the dynamics that govern them. The present discussion addresses the system's persistent structure and kinematic features. Although this publication emphasizes the transience of the essential dynamics that determine whether updraft parcels feed a leading or trailing stratiform region, the steady part of the structure is also important in that it determines, on average, how the convective system modifies its environment. Additionally, the persistent periodic phase of the FFLS system shown in Fig. 4.2 is of independent interest because it is *quasi–stable*; in other words, despite the chaotic details of the evolving flow, similar behaviors continue to occur periodically over an extended range of time.[2]

On average, during the mature phase of the FFLS system, air below ≈6 km AGL flows westward and passes through a pre-line region of cloud and precipitation on its way to the convective zone (Fig. 4.3). Some of this inflowing air ascends and feeds deep convective updrafts while the remainder does not attain a level of free convection and instead passes through the line's mean position, in some cases being cooled and contributing to the surface cold pool (Fig. 4.3). Notably, it isn't clear from Fig. 4.3 that air below ≈4.5 km AGL ever participates in the deep convective updrafts.

[2] This quasi–stability is a reassuring property. It implies that, as Parker and Johnson (2000) suggested, the FFLS structure is indeed a convective mode (Lorenz might say, "an attractor"), and not merely a transient state in the immense phase space of convective evolution.

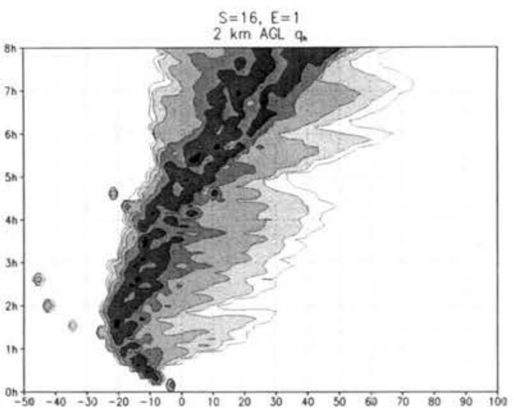

Figure 4.1: Hovmoller diagram depicting 2 km AGL hydrometeor mixing ratio (from t=0–8 h) for 2D FFLS simulation. Levels of shading are 0.005, 0.02, 0.08, 0.32, 1.28, and 5.12 g kg^{-1}.

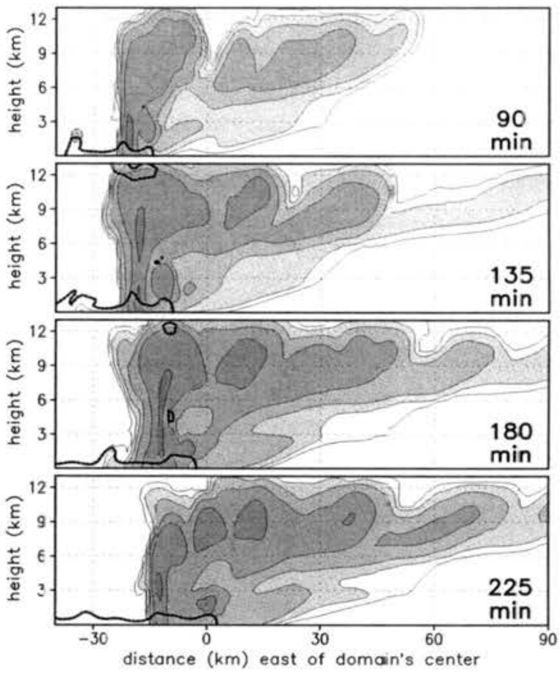

Figure 4.2: Total hydrometeor mixing ratio (q_h) and cold pool location for selected times during the 2D FFLS system's quasi–stable period; q_h thinly contoured and shaded at 0.005, 0.02, 0.08, 0.32, 1.28, and 5.12 g kg^{-1}; general cold pool position indicated by $\theta' = -4$ K isopleths (thick contours).

This is a result of averaging; time–dependent air parcel trajectories such as A–a in Fig. 4.4 do ascend in deep updrafts, but other lower tropospheric inflowing parcels like B–b and C–c in Fig. 4.4 do not. Indeed, the magnitude of w in the convective region after temporal averaging (Fig. 4.3) is quite small below 5 km AGL because this is a zone in which both updrafts (i.e. trajectories A–a and E–e) and downdrafts (i.e. trajectories B–b, C–c, and D–d) are fed by both lower (i.e. A–a, B–b, and C–c) and middle (i.e. D–d and E–e) tropospheric inflow. The updrafts that develop periodically (as sampled in Fig. 4.2 and embodied by trajectory A–a) produce hydrometeors, some of which fall out near the updraft's position (i.e. the vertical plume of enhanced q_h at x = –20 to $x = 0$ km in Fig. 4.3). Additionally, almost all of the updraft trajectories overturn (e.g. A–a and E–e in Fig. 4.4) and are detrained with significant westerly velocities (i.e. above 7 km AGL in Fig. 4.3), carrying at least some of their water content with them and contributing to a persistent leading precipitation region (i.e. east of $x = 0$ km in Fig. 4.3). The mean flow in the middle and upper troposphere to the west of the convective region is weak, having been decelerated (the reasons why are discussed in Chapters 5 and 6). A few air parcels, such as F–f in Fig. 4.4, are entrained into the deep convection or cross over its mean position. However, analysis of the mass fluxes through the convective region (Fig. 4.5) reveals that the the environmental air above 7 km AGL on the system's upshear side contributes relatively little to the mass outflux east of the convective updraft. The storm–relative winds in this region are nearly stagnant, a point that addressed in Section 6.2. Like the trajectories in Fig. 4.4, the mass fluxes in Fig. 4.5 reveal that the predominant flow branch is an overturning updraft that is fed by both the lower and middle tropospheric inflow.

Despite the vigorous convection feeding water vapor and condensate into the line–leading precipitation region, surface rainfall rates > 1 mm h^{-1} extend only 20–25 km ahead of the convective line on average in the simulated FFLS systems (not shown, but can be inferred from Figs. 4.1–4.3). Sensitivity tests in which the ice particle fallspeeds were halved and tests that used an altogether different microphysics parameterization (the Schultz scheme, as mentioned in Section 2.1.3) exhibited leading anvils and precipitation regions of very similar extent and aspect ratio. There appears to be some observational support for this result: in reviewing the Parker and Johnson (2000)

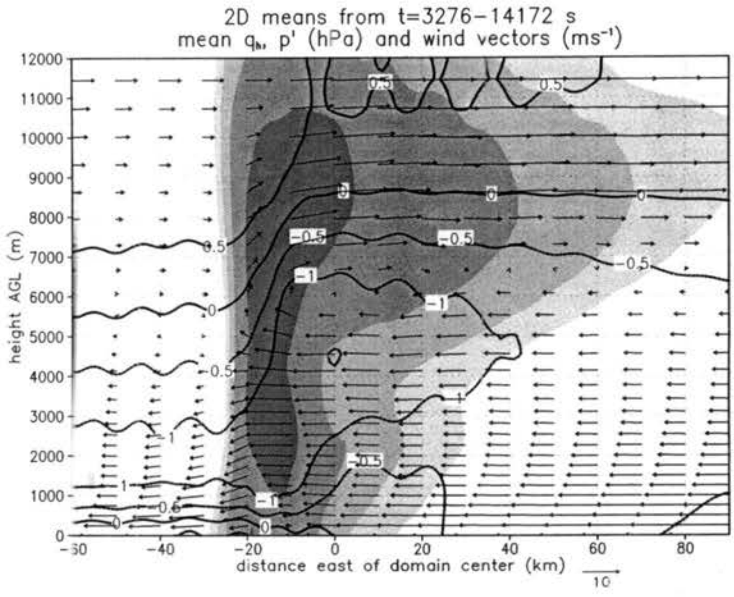

Figure 4.3: Mean total hydrometeor mixing ratio (levels of shading are 0.02, 0.08, 0.32, 1.28, and 5.12 g kg^{-1}), pressure pertubation (contours, hPa), and wind vectors (m s^{-1}, scaled as shown) for 2D FFLS simulation.

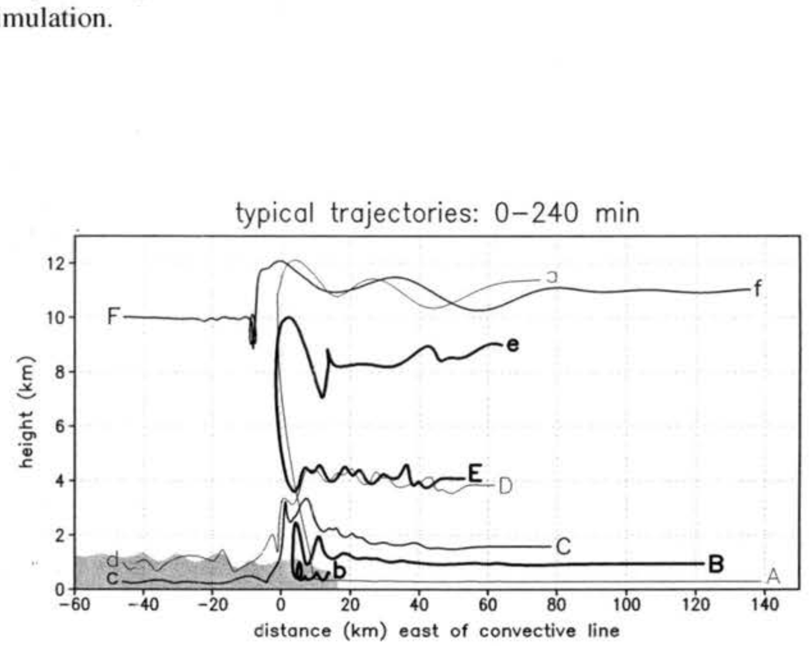

Figure 4.4: Four–hour parcel trajectories typifying commonly observed airstreams for 2D FFLS simulation. Parcels' initial positions (at $t = 0$ min) are indicated by capital letters. Parcels' final positions (at $t = 240$ min) are indicated by lower–case letters. Averaged $\theta' < -2$ K are shaded to indicate the mean position of the surface cold pool during the time period. The trajectories' thicknesses vary in order to assist in differentiating them. The thicknesses have no additional meaning.

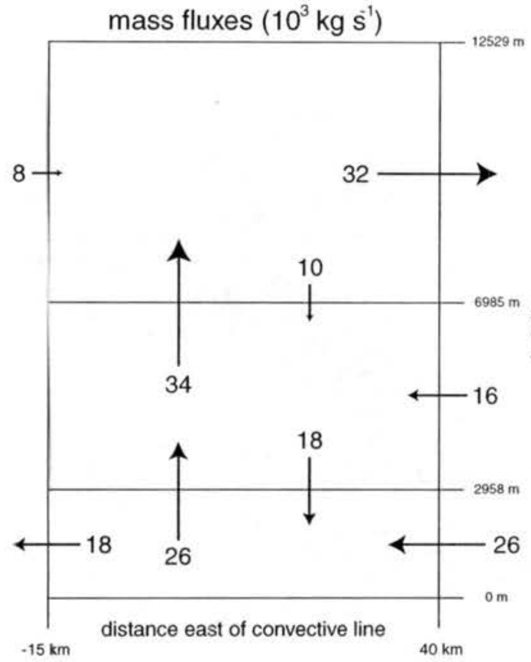

Figure 4.5: Temporally averaged (over the period from 3276–14172 s) mass fluxes (kg s^{-1}) through a region containing the convective line of the 2D FFLS simulation. The values are obtained for an x–z slab that is 1 m wide.

study data, it became clear that many of the observed FFLS cases had comparatively smaller stratiform regions than their RFLS (or FFTS) counterparts. The present study results are consistent with these data in that the simulated RFLS and FFTS systems do indeed have larger regions of stratiform precipitation (rain rates > 1 mm h^{-1} extend approximately 100 km from their convective lines, roughly consistent with their real–world counterparts); these two other archetypes are discussed further in Section 7.3. The physical explanation for the comparatively smaller stratiform precipitation regions in the FFLS simulations is as follows. A variety of liquid and ice particles develop in the convective updrafts and are transported into the downshear part of the convective system. Graupel particles with large terminal speeds fall out very near the line's position, melting as they descend below the 0° level and contributing to a core of moderate rainfall. Other ice and liquid particles that fall into the inflowing airstream are recirculated, eventually develop into larger graupel particles, and also fall out near the convective region. The remainder of the leading anvil in the middle and upper troposphere comprises snow, which falls very gradually over a much broader region. However, as these slowly falling particles descend below approximately 6 km AGL, they encounter a region of significant front–to–rear inflow (see Fig. 4.3) and are advected back toward the convective line, all the while melting and evaporating as they go. In this way, the stratiform precipitation's horizontal extent is limited to a much smaller region than in the simulated RFLS or classical FFTS systems.

On average, the pressure field in the simulated FFLS system was significantly perturbed on both sides of the convective region (Fig. 4.3), which represents a departure from the classical conceptual model for an FFTS system [e.g. as described by Houze et al. (1989)]. A mean surface mesohigh exists to the west of $x = 0$ km in Fig. 4.3, and this is a quasi–hydrostatic response to the surface cold pool. In addition, a middle tropospheric mesolow exists to the east of the convective region (centered at about $x = 0$ km, $z = 4.5$ km AGL). This mesolow is largely a quasi–hydrostatic response to the latent heating and detrained buoyancy in the leading cloud and precipitation region. In this respect, it is analogous to the mesolow described by LeMone (1983). Additionally, as discussed by Szeto and Cho (1994), there is a small dynamic contribution to the persistent mesolow owing to the curvature of the mean flow field. The details of this mesolow and its relevance to system structure are addressed in detail in Section 7.2. The importance of the FFLS system's unique pressure field is that middle tropospheric environmental inflow is accelerated toward the convective line, thereby significantly modifying the near–line wind profile. The dynamical implications of these persistent modifications to the environmental wind profile were discussed in Section 3.2. Additionally, the upward pressure gradient force owing to p' in the pre–line region can be important in providing upward accelerations to inflowing air parcels, whose ascent may help to continually destabilize the near–line environment, as addressed in Section 4.2. Ultimately, this publication concludes by emphasizing the importance of transient processes to the overall dynamics of FFLS systems. However, after reading Chapters 3– 6, it should also be clear to the reader that the quasi–stable structures described above are also important; they reveal, on average, how the convective system modifies the mesoscale environment and, in turn, how these modifications are important to both the steady and transient parts of the system's dynamics. The next part of this section compares the present 2D simulation's quasi–stable characteristics to those of the control periodic–3D simulation.

4.1.2 Periodic three–dimensional simulated front–fed LS system

Although it isn't practical to prepare individual cross sections like those in Fig. 4.2, the plan views of mean tropospheric q_h in Fig. 4.6 reveal that the periodic–3D FFLS simulation also exhibits a quasi–stable behavior. In particular, a line of healthy convection persists, comprising individual convective cells that temporally develop, mature, and decay. Reassuringly, despite the idealized nature of the simulation and the constraint of $\hat{y}$–periodicity, the convective line "segments" shown in Fig. 4.6 are similar to the plan view reflectivity images presented by Parker and Johnson (2000, e.g. their Fig. 6). Even though some of the system's inhomogeneities have mesoscale durations,[3] the periodic–3D system is on average quasi–2D. Evidence for this includes the visually obvious slab symmetry of the structures in Fig. 4.6, the strong similarity of the along–line means in Fig. 4.7 to the temporal means from the 2D simulation in Fig. 4.3, and the strong similarity of the $x-z$ cross section of trajectories from the periodic–3D simulation (Fig. 4.8) to those from the 2D simulation (Fig. 4.4).

The mean fields in the 2D simulation (Fig. 4.3) are slightly more perturbed than those in the periodic–3D simulation (Fig. 4.8), which is to be expected given that the temporally averaged areal coverage of convection in the 3D simulation is somewhat less than in the 2D simulation owing to the spacing of its isolated convective cells (as seen in Fig. 4.6). However, the shapes of the q_h, p', and wind fields correspond quite well between the 2D and periodic–3D systems, and the logic of the physical processes that links them together is unchanged. Of major importance is that, not only are the averaged fields similar, but the trajectories computed in the temporally evolving 3D flow field are quasi–2D and correspond quite well to those from the 2D simulation. The periodic–3D trajectories are quasi–2D in that air parcels' line–parallel motions are minimal (Fig. 4.8), such that to a very high order their basic paths can be described in the $x-z$ plane. The periodic–3D

[3] For example, a region of minimal q_h at $y = 155$ km, $t = 4.5$ h in Fig. 4.6a persists and moves eastward, appearing as a notch in the eastern edge of the q_h field by $t = 5.5$ h in Fig. 4.6c.

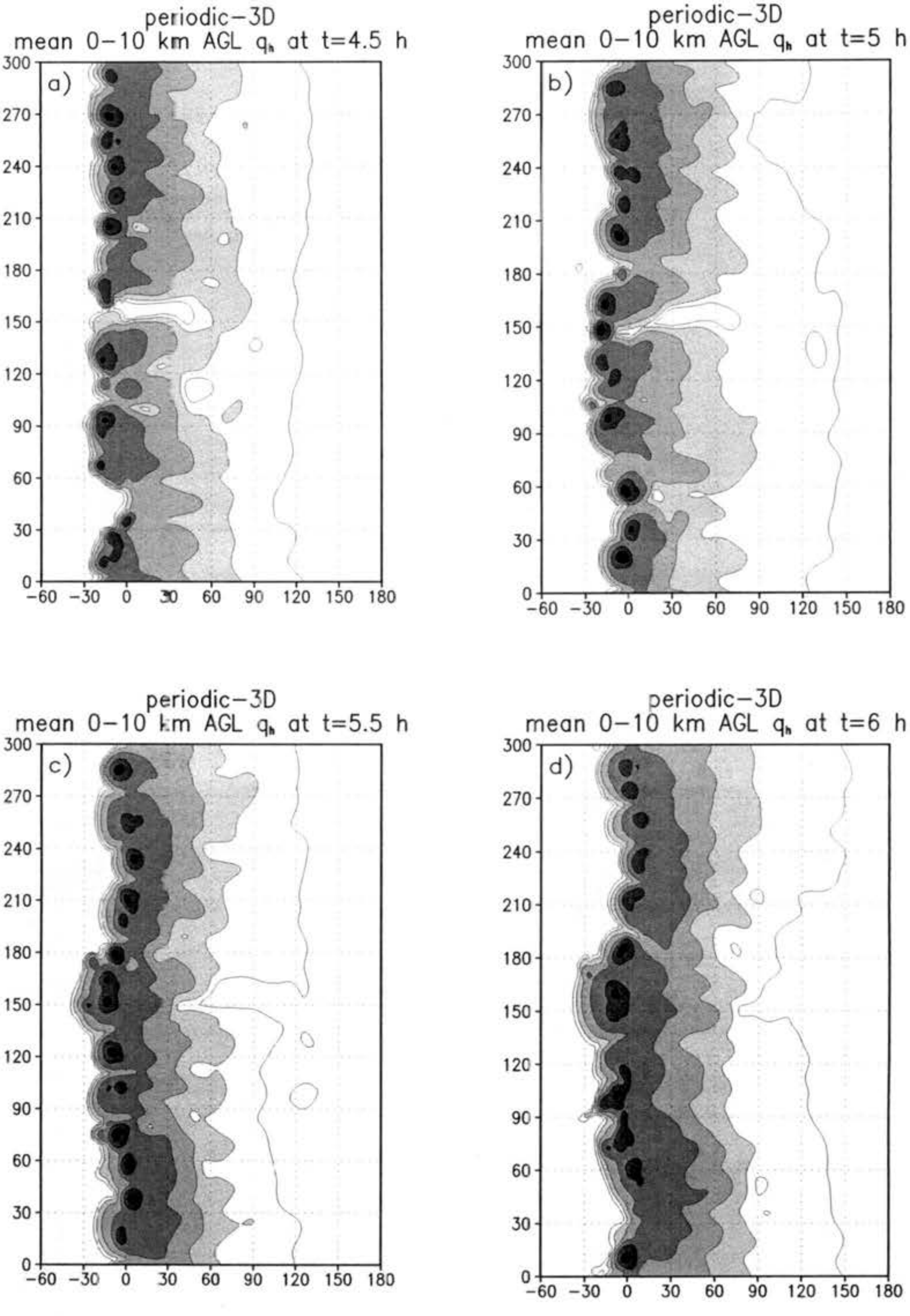

Figure 4.6: Mean hydrometeor mixing ratio from 0–10 km AGL for periodic–3D FFLS simulation: a) at $t = 4.5$ h, b) at $t = 5$ h, c) at $t = 5.5$ h, d) at $t = 6$ h. Levels of shading are 0.005, 0.02, 0.08, 0.32, 1.28, and 5.12 g kg^{-1}.

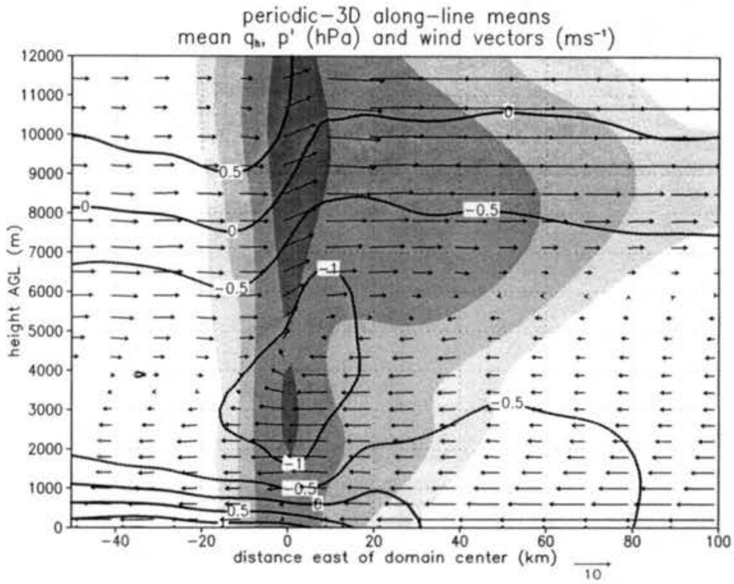

Figure 4.7: Mean total hydrometeor mixing ratio (levels of shading are 0.02, 0.08, 0.32, 1.28, and 5.12 g kg^{-1}), pressure pertubation (contours, hPa), and wind vectors (m s^{-1}, scaled as shown) for periodic–3D FFLS simulation.

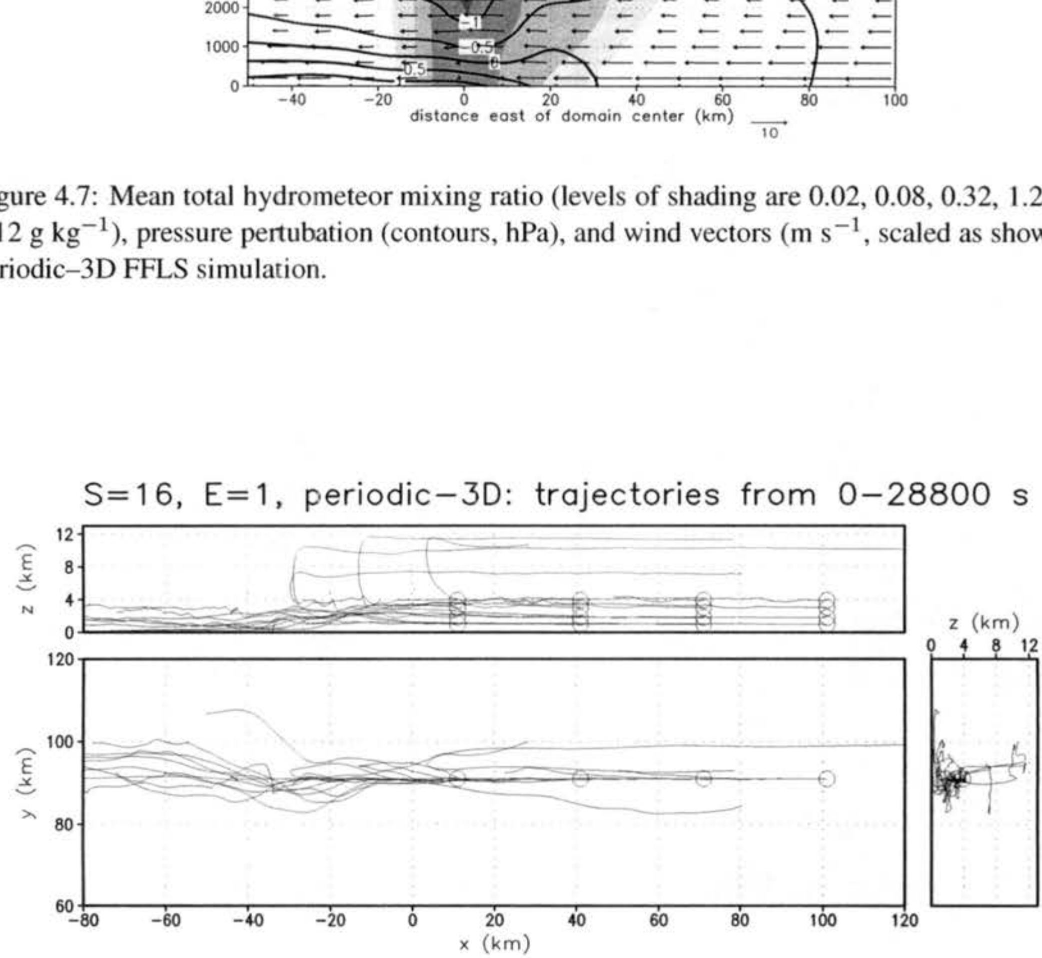

Figure 4.8: "Shadow" depiction of forward trajectories computed for periodic–3D FFLS simulation. The central panel of this figure is an $x - y$ plan view of trajectory positions, the top panel is an $x - z$ cross–section of trajectory positions, and the right panel is a $z - y$ cross–section of positions. The trajectories begin at the ○ symbols.

trajectories are similar to those from the 2D simulation in that, in the $x - z$ plane, they reveal updrafts that are fed by both lower and middle tropospheric inflow (much like trajectories A–a and E–e in Fig. 4.4) as well as inflowing lower and middle tropospheric air parcels that cross the line's position and often feed the surface cold pool (much like trajectories B–b, C–c, and D–d in Fig. 4.3). These similarities justify the basic scientific approach of this publication (i.e. to use 2D simulations to learn about the dynamics of quasi–2D systems). Although the discussions of Chapter 5 will emphasize the importance of transient accelerations and will point out differences between the transient components of the 2D and periodic–3D simulations, the present analysis also shows that, to first order, the quasi–stable characteristics and effects of the 2D and periodic–3D systems are the same. Notably, numerous previous studies have also demonstrated the similarity of 2D simulations of FFTS systems to their 3D counterparts in the real world and in numerical models [e.g. Hane (1973), Dudhia et al. (1987), Fovell and Ogura (1988), Rotunno et al. (1988)].

The main complication to the system's quasi–2D structure is that the convective updrafts are localized, and do not resemble the infinitely long (in $\hat{y}$) slabs of upward motion that occur in the 2D simulation. This has three important effects. The first is that the periodic–3D line never comprises entirely ascending or descending air; at any given time in the periodic–3D system, there exist convective cells in various stages of development, maturity, and decay. This is dynamically important because, whereas the 2D system presents an infinitely long temporally pulsing forcing to the mesoscale, the periodic–3D system presents a spatially inhomogeneous but temporally smooth forcing to the mesoscale. In a time series, while convection in the 2D simulation must be either "on" or "off", scattered convection in the periodic–3D simulation is always ongoing and its system–averaged mass fluxes are almost temporally invariant. As a result, the along–line averaged fields in the periodic–3D case are similar to, but much smoother than, those in the 2D case (cf. Figs 4.7 and 4.3). The second important effect is that the geometry of the w and buoyancy fields in individual 3D updrafts is different from that of the 2D updrafts. This is very important to the transient local accelerations, and is discussed in detail in Section 5.2. The third important effect of the localized updrafts is that air parcels can pass between the isolated updrafts of the periodic–3D line. Whereas in the 2D simulation the upper tropospheric storm–relative flow must become approximately stagnant on the system's upshear side, in 3D the upper level flow stagnation is very local (i.e. in Fig. 4.9 at $x = -8$ km, $y = 185$ km, at $x = -4$ km, $y = 215$ km, etc.), the pressure field favors acceleration of air into the channels between active updrafts (i.e. in Fig. 4.9 at $y = 200$ km, $y = 225$ km, and $y =$ 250 km), and the mean upper tropospheric mass flux across the convective line is approximately temporally invariant (not shown). Hence, the mean environmental flow in the 5–10 km AGL layer on the upshear side of the convective line is much stronger in 3D than in 2D (again, cf. Figs 4.7 and 4.3). In summary, the transient dynamics of the simulated periodic–3D FFLS system do differ somewhat from those of the 2D system, and these differences are discussed in Section 5.2; however, all caveats notwithstanding, from Figs. 4.7 and 4.8 it is clear that the periodic–3D system perturbs and overturns the environment in roughly the same way that the 2D system does. The nature of this overturning is discussed further in Section 6.2.

4.2 Maintenance of the front–fed LS system: destabilization of inflow by LS precipitation

As described in § 4.1, front–fed systems with leading precipitation can be long–lived and *quasi–stable.* Parker and Johnson (2000) noted that: "a fundamental question... regarding the longevity of LS cases [is] their persistence despite inflow of evaporatively cooled preline air into convective towers." If an inflow layer is relatively shallow, evaporation of precipitation falling into that layer would pseudo–adiabatically cool its air parcels, thereby adding convective inhibition with respect to the original sounding. However, an important result of the present study is that, because front–to–rear storm–relative inflow occurs over a relatively deep layer,[4] cooling also occurs over a relatively deep layer and this destabilizes the near–line sounding. Although later parts of this publication emphasize that many of the important dynamical processes in FFLS systems are transient (e.g. § 5.1), in the control simulation the near–line sounding is destabilized for most of the system's mature phase. As shown in Fig. 4.10, on average over a period of approximately 75 min., the near–

[4] The front–to–rear inflow layer is nearly 6 km deep in the present study. It was about 5.5 km deep in the mean profile presented by Parker and Johnson (2000), as can be inferred from their Fig. 12.

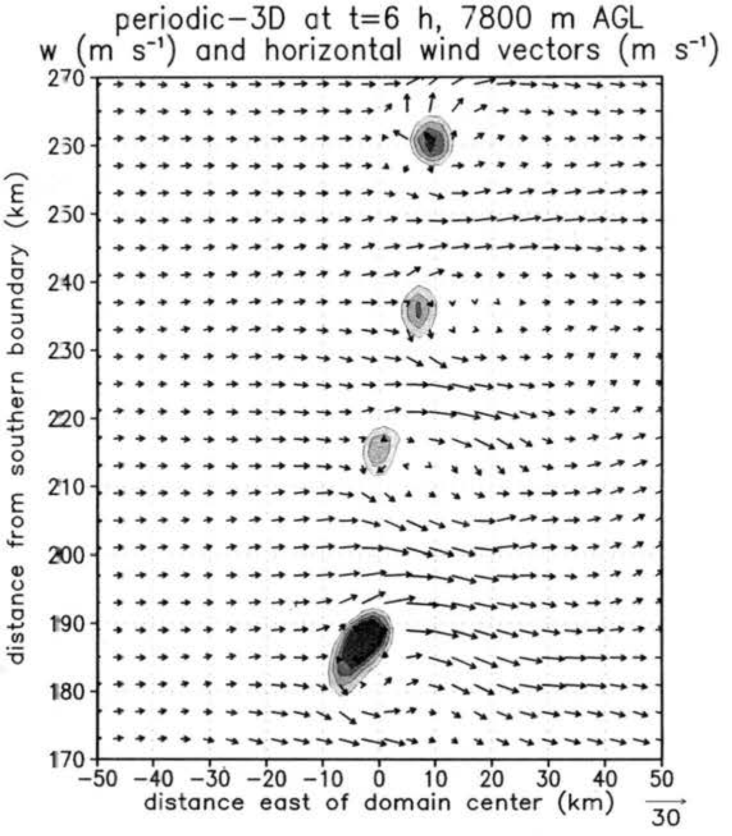

Figure 4.9: Vertical velocity (m s^{-1}) and horizontal wind vectors (m s^{-1}) for t = 6 h at 7800 m AGL in the periodic–3D FFLS simulation. Levels of shading for w are 5, 10, 15, and 20 m s^{-1}. Velocity vectors are scaled as shown.

line sounding is cooler and moister than the environment below about 550 hPa (approximately 4.5 km AGL). The temperature is most perturbed at approximately 720 hPa (approximately 2300 m AGL). Therefore, the lapse rate is steeper than that of the environment in the lower troposphere. The net effect is to diminish CIN and increase CAPE in the lower troposphere, which is to say that healthy updrafts can be easily triggered by the simulated system. Indeed, in some cases the near–line soundings even exhibit moist absolute instability (Bryan and Fritsch 2000).

Three mechanisms for destabilizing the near–line sounding suggest themselves. First, because θ increases with height in the base state (Fig. 4.10) , air that ascends and conserves its potential temperature will be cooler than the environment; in a large region of dry ascent, the lapse rate will thereby tend toward the adiabatic value. In addition, because θ_e decreases with height in the base state (i.e. it is potentially unstable, Fig. 4.11), lifting the layer to saturation will also destabilize it. Second, because θ_e decreases with height, the layer could be destabilized by evaporative cooling that increases with height. Since a given value for θ_e can correspond to an infinite number of temperature and humidity combinations, it may not be clear that the profile of θ_e in Fig. 4.11 necessarily implies that cooling the air to saturation will destabilize it. The base state's profile of wet bulb temperature in Fig. 4.12, however, reveals that evaporatively cooling the lower troposphere to saturation would increase the temperature lapse rate in the layer from approximately 880–700 hPa (approximately 600–2600 m AGL). Additionally, as is clear from Fig. 4.10, the lowest 50–70 hPa of the sounding were not chilled as much as the layer between about 880 and 700 hPa, such that the low levels were also destabilized somewhat. Third, because the minimum in θ' is quite close to the 0° C level (about 620 hPa or 3400 m AGL, see Figs. 2.2 and 4.10), it is likely that chilling owing to the melting of falling graupel is maximized aloft near the melting level, further increasing the lapse rate. The following text discusses these three mechanisms in turn.

A quick inspection of Fig. 4.11 reveals that at least part of the cooling must be associated with lifting. Indeed, at $x = +55$ km (the right hand side of Fig. 4.13), the inflowing air shows signs of ascent above 500 m AGL before it even penetrates the leading precipitation region (Fig. 4.11); for pseudo–adiabatic processes, the values of θ_e at some level can only be increased by vertical

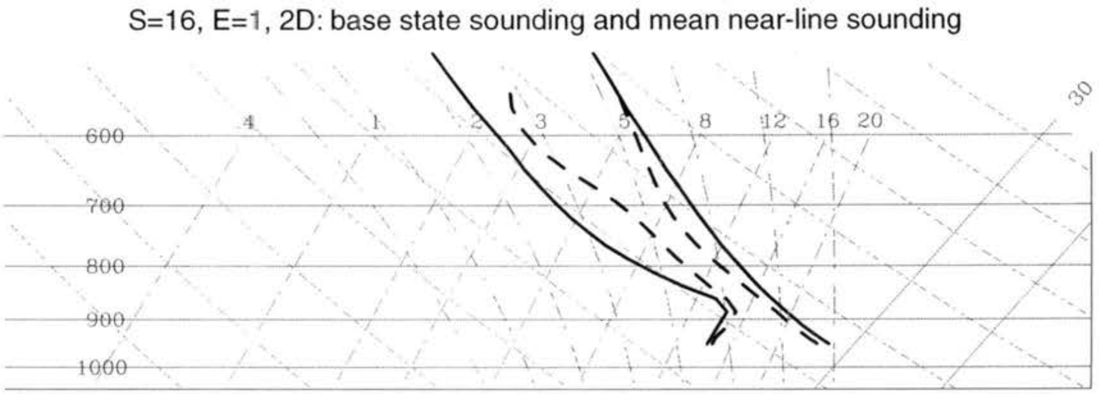

Figure 4.10: Skew-T ln-p diagram of the lower troposphere for base state initial condition (solid, cf. Fig. 2.2) and mean near–line sounding (dashed) for mature stage of S=16, E=1 simulation, averaged from 9600–14122 s. Values of θ' for the near–line sounding are given in the right–hand column of Table 4.1, part a.

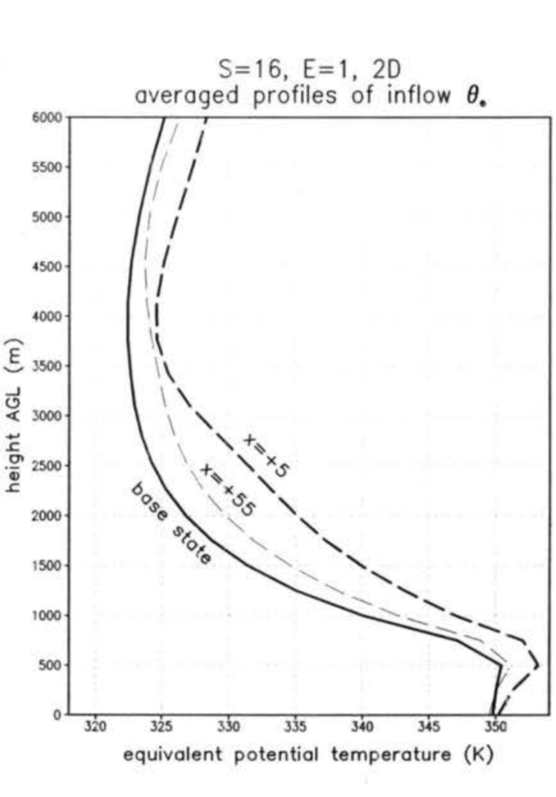

Figure 4.11: Mean profiles of equivalent potential temperature (K) for S=16, E=1, 2D simulation, t=9600–14122 s. Shown are the base state initial condition (heavy solid), the profile at $x = +55$ (light dashed), and the profile at $x = +5$ (heavy dashed). The location $x = +55$ corresponds to the right side of Fig. 4.13a, prior to inflow's penetration of the leading precipitation region. The location $x = +5$ corresponds to the left side of Fig. 4.13a, very near the edge of the surface cold pool and convective line.

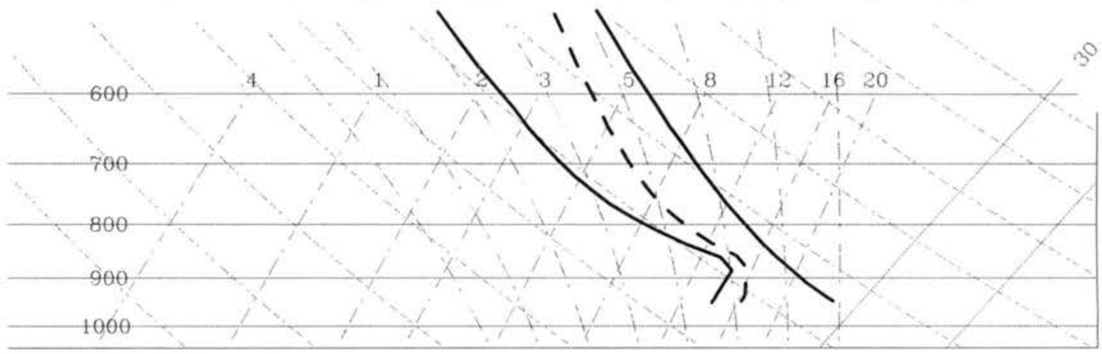

Figure 4.12: Skew-T ln-p diagram of the lower troposphere for base state initial condition's temperature and dewpoint (solid, cf. Figs. 2.2 and 4.10) and wet bulb temperature (dashed).

advection. Then, between $x = +55$ and $x = +5$ km, the inflowing air's profile of θ_e shows signs of additional ascent (Fig. 4.11).[5] The 9600–14122 s mean wind trajectories (i.e. streamlines) do indeed reveal that the inflowing air in the lower troposphere ascends on its way to the convective line (Fig. 4.13). Because the base state is stable ($d\theta/dz > 0$, see Fig. 2.2), adiabatic ascent implies local perturbations in θ following:

$$\frac{D\theta'}{Dt} = \frac{D\theta}{Dt} - \frac{D\theta_o}{Dt} = \dot{Q}_{diabatic} - w\frac{d\theta_o}{dz}. \qquad (4.1)$$

Inflowing air ascends over the lowest 1.5 km AGL in the 2D simulation and over the lowest 2.5 km AGL in the periodic–3D simulation (Fig. 4.13). However, it is difficult to infer the degree to which this ascent contributes to θ' in the near–line profile. Table 4.1 summarizes each term in (4.1) integrated over the length of the inflow trajectories in Fig. 4.13. For the 2D mean flow trajectories

[5] There remains the difficult problem of increased θ_e (greater than values in the original sounding) in the lowest 1 km AGL, which cannot be explained by advection in a purely θ_e–conservative system. As discussed by Iribarne and Godson (1981) and Emanuel (1994), precipitation falling into and evaporating in an unsaturated airmass can raise the air's θ_e. This is because, when the saturation process happens isobarically rather than via adiabatic ascent and moist descent, air does not do work to warm the liquid water and the latent heat required for vaporization is slightly less. Additionally, because this study used the full formulation for θ_e from Emanuel (1994), the specific heat of the liquid phase is included, and fallout of precipitation can locally increase θ_e in an air parcel (Fovell and Tan 1998). These processes account for some of the difference. Additionally, truncation errors and "overshooting" owing to the large vertical gradient in q_v contribute. Because the numerical model is not explicitly constrained to conserve θ_e, temperature and vapor content are uncoupled and can evolve in ways that may modify θ_e during processes that would normally be considered θ_e–conservative. Notably, Fovell and Tan (1998) found a very similar phenomenon in their squall line simulations (see their Fig. 3). A suitable question is: to what degree do the numerical sources for elevated θ_e increase CAPE for updraft air parcels? From analysis, it appears that downgradient turbulent mixing in the vicinity of the gust front and updrafts allow very little of this excess CAPE to be realized.

(Table 4.1, part a), perturbations owing to vertical displacement ($-\Delta\theta_c$ over the length of the trajectory) accounted for 50% or less of the total cooling along each trajectory, and actually contributed to warming above 2 km AGL. In contrast, ascent was quite important to the negative temperature perturbations in the periodic–3D simulation (Table 4.1, part b), accounting for as much as 110% of the change in θ' along the trajectories. Notably, many of the trajectories began with significant θ', which was partly due to ascent and was partly due to the fact that the trajectories above 1.5 km AGL began within the leading precipitation and had already been chilled by evaporation and melting (Fig. 4.13).

Why does such dramatic ascent occur within and ahead of the leading precipitation region? As shown in Fig. 4.14, the upward accelerations are primarily attributable to ACCB, and in turn the upward–directed ACCB is attributable to the vertical gradient in P'B. The P'B field owes its existence to the surface cold pool, which is west of the domain depicted in Fig. 4.14, and to the region of strong negative buoyancy centered around 2200 m AGL within the leading precipitation region (Fig. 4.14). This negatively buoyant region aloft exists in part because of persistent evaporation and melting in the region. Therefore, although ascent accounts for a significant part of the cooling along air parcel's trajectories, it is proper to say that the presence of the pre–line precipitation favors this ascent because the chilling that it induces yields a buoyant pressure field that is favorable for upward accelerations as air parcels flow into the leading precipitation region. Alternately, because buoyancy is arbitrarily defined with respect to whatever base state is chosen, we can conceive of the "base state" as a mass field that is in hydrostatic balance with the pressure field in the leading precipitation region. In this case, inflowing air is less dense than the "base state" mass field, and ascends as a result. In either case, the point is to highlight that the leading precipitation itself helps give birth to the ascent in the leading precipitation region.[6]

Although ascent is undoubtedly important, it is clear that above 2 km AGL in the 2D simulation, evaporation and melting must have accounted for most of the negative θ' (Fig. 4.13a and Table 4.1, part a). In addition, as this publication goes on to argue in § 5.1, many of the important

[6] Of course, very near the convective line, the main surface cold pool is also locally important in forcing lower tropospheric air parcels to ascend.

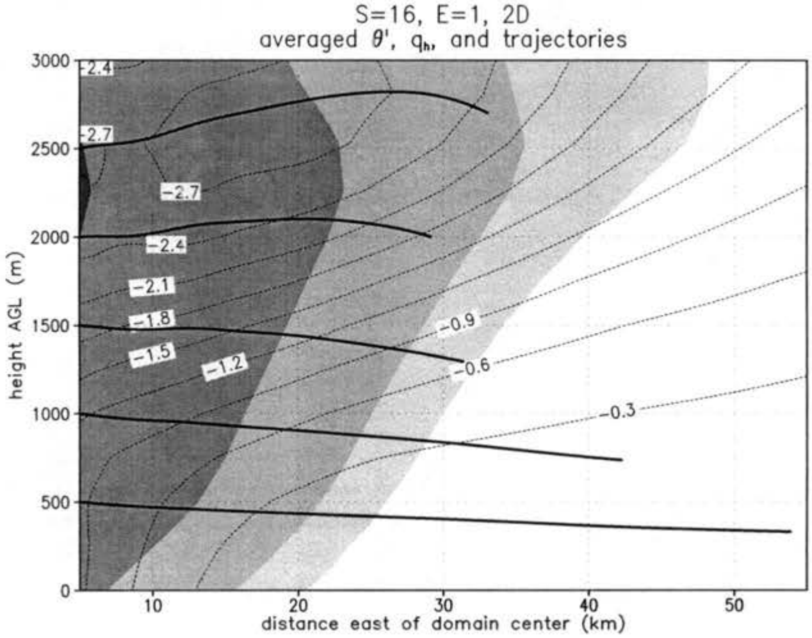

(a)

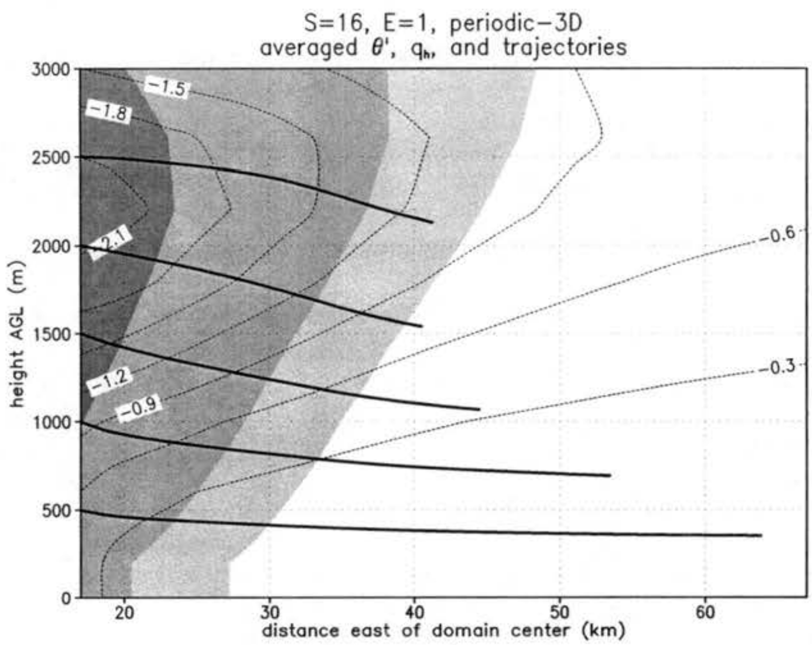

(b)

Figure 4.13: Mean hydrometeor mixing ratio (shaded), potential temperature perturbation (contoured, interval=0.3 K), and trajectories for S=16, E=1 simulations. a) for 2D simulation, averaged from 9600–14122 s. b) for periodic–3D simulation, averaged in $\hat{y}$ and from 18000–22200 s. Levels of shading are 0.005, 0.02, 0.08, and 1.28 g kg^{-1}, and are the same in both panels. The trajectories follow the mean flow throughout the time intervals for each case. Data for the plotted trajectories are given in Table 4.1, parts a and b.

Table 4.1: Data for trajectories that compose destabilized near–line soundings in S=16, E=1, 2D and periodic–3D simulations. Part a: trajectories computed for the mean flow field for 2D simulation, averaged from 9600–14122 s (cf. Fig. 4.13a). Part b: trajectories computed for the mean flow field for periodic–3D simulation, averaged in $\hat{y}$ and from 18000–22200 s (cf. Fig. 4.13b). Part c: forward trajectories computed in the evolving flow field of periodic–3D simulation (cf. Fig. 4.15). The data columns are: z_i (m), the initial parcel height, z_f (m), the final parcel height, $\Delta\theta'$ (K), the change in the potential temperature perturbation over the trajectory's duration, $-\Delta\theta_o$ (K), the change in the potential temperature perturbation attributable to ascent over the trajectory's duration, $\Sigma(\dot{\theta}_M + \dot{\theta}_E)$ (K), the change in the potential temperature perturbation attributable to evaporation and melting over the trajectory's duration, θ'_f (K), the parcel's final potential temperature perturbation with respect to the base state.

	trajectories	z_i	z_f	$\Delta\theta'$	$-\Delta\theta_o$	$\Sigma(\dot{\theta}_M + \dot{\theta}_E)$	θ'_f
a)	2D mean 9600–14122 s	331	500	-0.9	-0.2	-0.7	-0.9
		736	1000	-1.0	-0.5	-0.6	-1.2
		1295	1500	-1.2	-0.5	-0.8	-1.9
		2001	2000	-1.2	+0.0	-0.8	-2.5
		2703	2500	-0.4	+0.6	-1.0	-2.7
b)	periodic–3D mean 18000–22200 s	354	500	-0.5	-0.1	-0.4	-0.6
		694	1000	-0.9	-0.5	-0.4	-1.0
		1069	1500	-1.3	-0.9	-0.4	-1.6
		1539	2000	-1.4	-1.2	-0.2	-2.1
		2131	2500	-1.0	-1.1	+0.1	-2.1
c)	periodic–3D evolving flow 0–10800 s	200	300	-1.1	-0.1	-1.0	-1.1
		1000	1204	-1.9	-0.4	-1.5	-1.9
		1400	1417	-2.1	-0.0	-2.1	-2.1
		2202	2301	-2.7	-0.3	-2.4	-2.7
		3021	2893	-2.0	+0.4	-2.4	-2.0

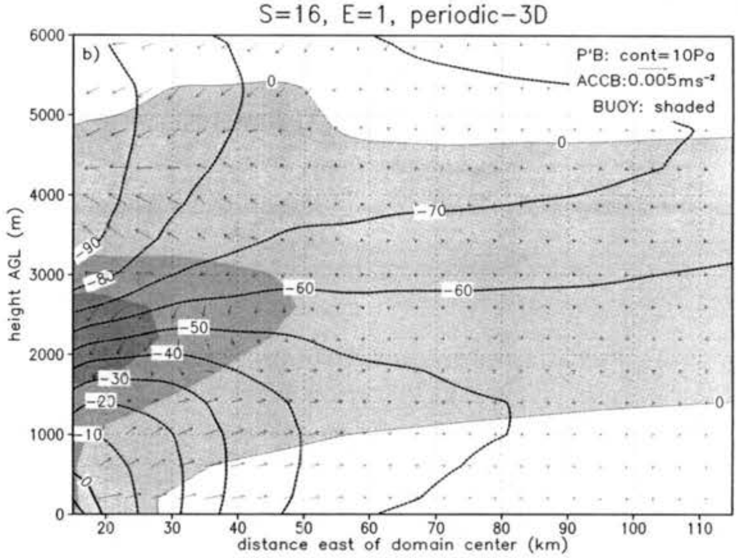

Figure 4.14: Buoyant components of the acceleration and pressure fields for S=16, E=1, periodic–3D simulation, averaged in $\hat{y}$ and from 18000–22200 s. $BUOY$ is shaded with levels: -0.04, -0.02, and 0 m s^{-2} (white/unshaded values are positively buoyant). $P'B$ is shown by heavy contours, $ACCB$ is shown by vectors. See Fig. 4.13 for mean air parcel trajectories and distribution of hydrometeors.

processes in FFLS systems are transient, and hence individual air parcels in the temporally evolving flow field do not generally follow the streamlines in Fig. 4.13. An example of this is depicted in Fig. 4.15, in which the inflowing air parcels that compose a destabilized near–line sounding in the periodic–3D simulation have scarcely ascended at all (see their actual displacements in Table 4.1, part c). As shown in Table 4.1, part c, the cooling that occurs along these time–dependent trajectories is significant, and is almost entirely attributable to evaporation and melting. This is not to say that most of the inflow trajectories are horizontal or that phase changes are the predominant chilling mechanism along most time–dependent trajectories. However, the contribution from evaporation and melting is indeed important on average, and predominant in some examples.

The mean hydrometeor mass field in Fig. 4.13a is almost entirely composed of rain and graupel (Fig. 4.16). Graupel predominates above the melting level[7] , which is just above 3 km AGL

[7] In nature, snow aggregates are probably present in significant concentrations near the melting level, and could play a vital part in the melting budget. In the present simulations (in which microphysics are parameterized), snow is advected forward quasi–horizontally from the convective line and composes the leading anvil aloft. As snow particles in this region settle downward and aggregate, they are "auto–converted" into the graupel category owing to their increasing size (in this respect, the graupel category is an alias for precipitation–sized ice in the leading precipitation region). Therefore,

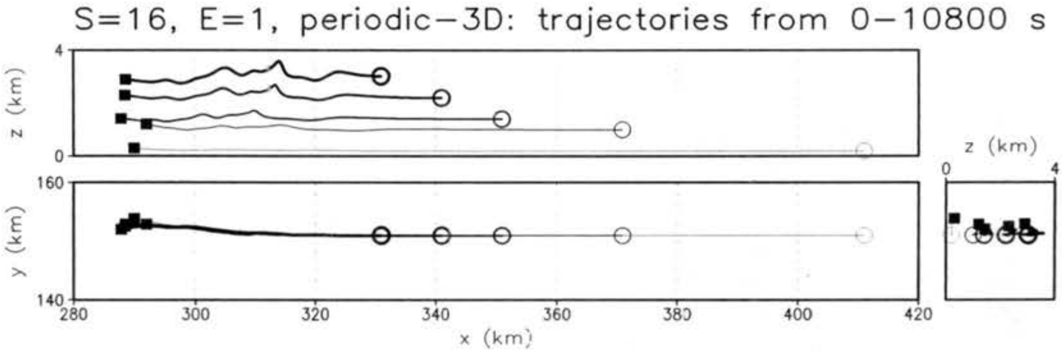

Figure 4.15: "Shadow" depiction of forward trajectories computed in the evolving flow field of S=16, E=1, periodic–3D simulation. These are "best match" forward trajectories which approximately compose a near–line sounding at $t = 10800$ s. Data points for this near–line sounding are shown in Table 4.1, part c. The central panel of this figure is an $x - y$ plan view of trajectory positions, the top panel is an $x - z$ cross–section of trajectory positions, and the right panel is a $z - y$ cross–section of positions. The trajectories begin at the ○ symbols and end at the filled □ symbols. The trajectories' thicknesses vary in order to assist in differentiating them. The thicknesses have no other meaning.

(Fig. 4.16b), whereas rain predominates below about 2.5 km AGL (Fig. 4.16a). Between 2.5 and 3 km AGL there is a zone in which much of the falling graupel melts (Fig. 4.16). Both melting of graupel and evaporation of rain contribute significantly to the chilling such that, for the lower tropospheric part of the leading precipitation region, (4.1) can more appropriately be written:

$$\frac{D\theta'}{Dt} \approx \left(\frac{D\theta}{Dt}\right)_{melting} + \left(\frac{D\theta}{Dt}\right)_{evaporation} - w\frac{d\theta_o}{dz}. \tag{4.2}$$

For a steady state (which the temporal mean nearly is), we can rewrite the melting and evaporation sources in terms of the vertical advection of rain and graupel using the method that follows.

The full 2D equation for the conservation of graupel mass as the graupel falls below the melting level is:

$$\frac{\partial m_g}{\partial t} + u\frac{\partial m_g}{\partial x} + (w - v_{tg})\frac{\partial m_g}{\partial z} = -M, \tag{4.3}$$

wherein v_{tg} is the mass–weighted (terminal) fallspeed of the graupel and M is the rate of melting. In the mean ("steady") state, $\partial m_g/\partial t = 0$ and $|v_{tg}| >> |w|$. Additionally, because $|v_{tg}| \sim |u|$ and

although snow probably contributes non–trivially to the melting budget in nature, it does not in the model simulations. However, given snow particles' small fallspeeds, even if significant snow existed near the melting level it would likely be advected back toward the convective line by the lower and middle tropospheric flow (as described in the previous section), such that the zone of significant melting/cooling wouldn't extend much farther ahead of the line.

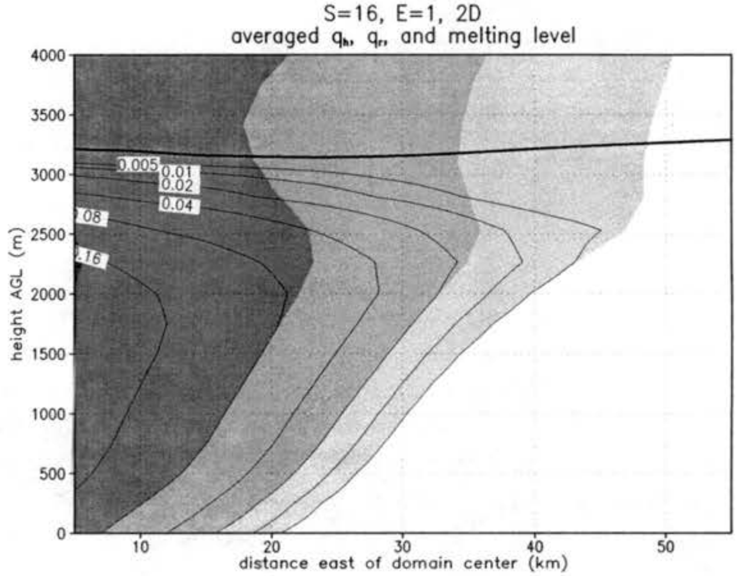

(a)

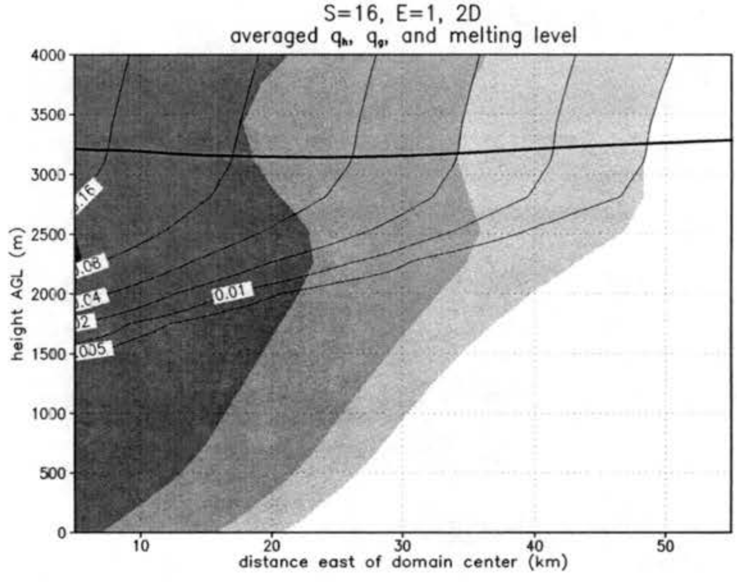

(b)

Figure 4.16: Mean hydrometeor mixing ratio (levels of shading are 0.005, 0.02, 0.08, and 1.28 g kg^{-1}) and 0° C isotherm (bold contour) for 2D simulation, averaged from 9600–14122 s, along with: a) rain mixing ratio (light contours, g kg^{-1}) and b) graupel mixing ratio (light contours, g kg^{-1}).

$|\partial m_g/\partial z| >> |\partial m_g/\partial x|$ in the mean state, (4.3) can be approximated:

$$-v_{tg}\frac{\partial m_g}{\partial z} = -M. \tag{4.4}$$

Therefore, rewriting (4.4) per unit volume:

$$\frac{M}{V} = v_{tg}\,\frac{\partial}{\partial z}\left(\frac{m_g}{V}\right) = v_{tg}\,\frac{\partial}{\partial z}\left(\rho_a q_g\right), \tag{4.5}$$

wherein ρ_a is the density of the air. In like manner, the equation for rain mass falling into unsaturated air below the melting level is:

$$\frac{\partial m_r}{\partial t} + u\frac{\partial m_r}{\partial x} + \left(w - v_{tr}\right)\frac{\partial m_r}{\partial z} = M - E, \tag{4.6}$$

wherein E is the rate of evaporation. Following the prior manipulations, then, (4.6) becomes (for the steady state, per unit volume):

$$\frac{E}{V} = v_{tr}\,\frac{\partial}{\partial z}\left(\frac{m_r}{V}\right) + \frac{M}{V} = v_{tr}\,\frac{\partial}{\partial z}\left(\rho_a q_r\right) + v_{tg}\,\frac{\partial}{\partial z}\left(\rho_a q_g\right). \tag{4.7}$$

Equations (4.5) and (4.7) are useful because they allow us to compute the steady state cooling rates attributable to the melting of graupel and the evaporation of rain water (these terms are by far the largest among the phase change sources and sinks below the melting level):

$$\left(\frac{D\theta}{Dt}\right)_{melting} = -\frac{L_{sl}}{c_p m_a}M = -\frac{L_{sl}}{c_p}\frac{1}{\rho_a}\frac{M}{V} = -\frac{L_{sl}}{c_p}\frac{1}{\rho_a}\left[v_{tg}\,\frac{\partial}{\partial z}\left(\rho_a q_g\right)\right]; \tag{4.8}$$

$$\left(\frac{D\theta}{Dt}\right)_{evaporation} = -\frac{L_{lv}}{c_p m_a}E = -\frac{L_{lv}}{c_p}\frac{1}{\rho_a}\frac{E}{V} = -\frac{L_{lv}}{c_p}\frac{1}{\rho_a}\left[v_{tr}\,\frac{\partial}{\partial z}\left(\rho_a q_r\right) + v_{tg}\,\frac{\partial}{\partial z}\left(\rho_a q_g\right)\right]. \tag{4.9}$$

This study uses these forms in (4.2) to compute the comparative magnitudes of the melting, evaporative, and ascent sources for θ'; these are shown in Fig. 4.17.

Obviously, cooling need not embody destabilization: it is cooling that increases with height that destabilizes the near–line sounding. As seen in Fig. 4.17, all three components contribute significantly to destabilization in some part of the 2D simulation's leading precipitation region. Notably, in the 2D simulation the near–line environment is characterized by subsident (cf. Fig. 4.13a) warming that increases with height (Fig. 4.17a), such that the evaporation and melting terms must

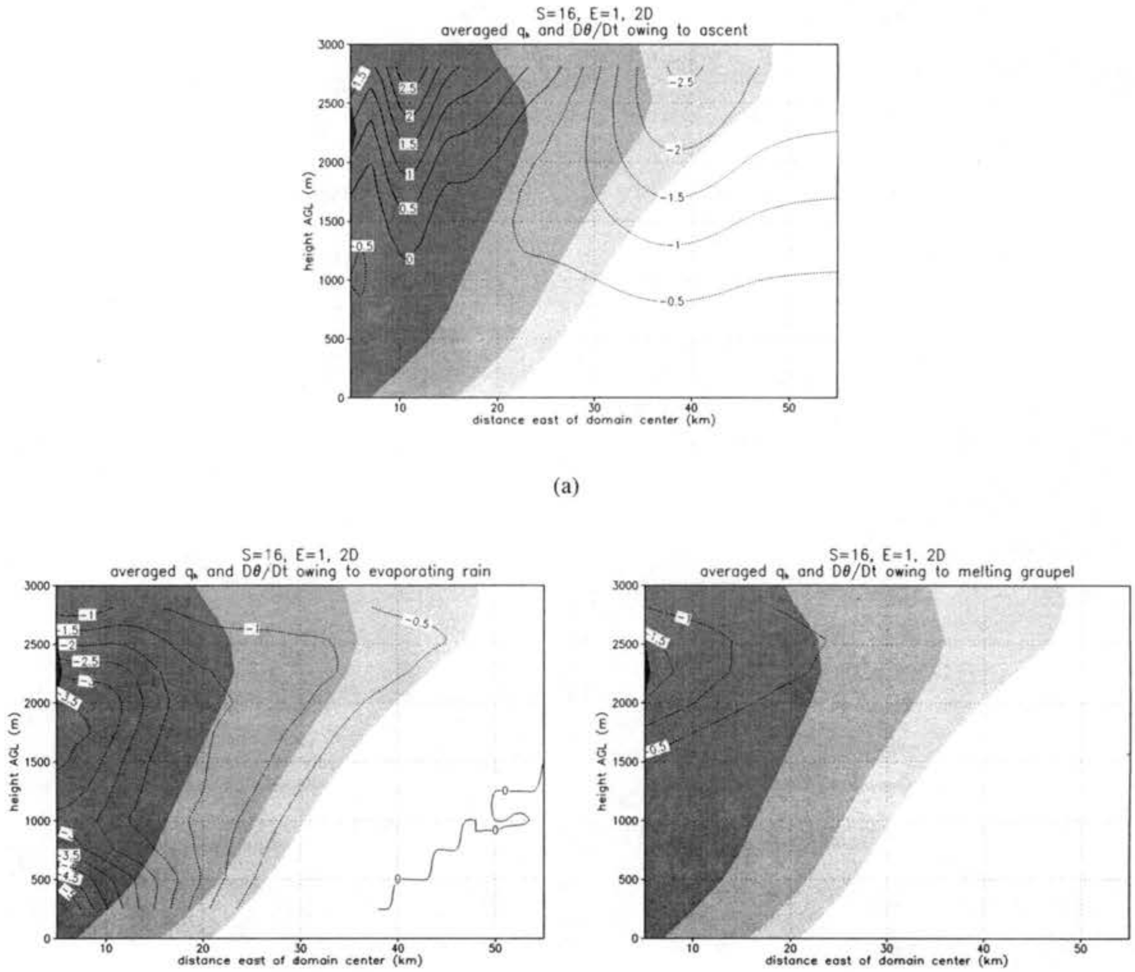

(a)

(b)

(c)

Figure 4.17: Mean hydrometeor mixing ratio (levels of shading are 0.005, 0.02, 0.08, and 1.28 g kg^{-1}) for 2D simulation, averaged from 9600–14122 s, along with: a) warming/cooling rate owing to mean descent/ascent (contours, K h^{-1}), b) heating/chilling rate owing to evaporation of falling rain [as computed from eq. (4.8), contours, K h^{-1}], and c) heating/chilling rate owing to melting of falling graupel [as computed from eq. (4.9), contours, K h^{-1}]. The curves are truncated at the upper and lower edges because the computation involved a vertical derivative.

compensate for it if the inflowing air is to remain or become increasingly destabilized.[8] Although the magnitude of the melting source is somewhat smaller than those associated with evaporation or ascent (mostly owing to the fact that $L_{sl} << L_{lv}$), it provides chilling that is maximized aloft and that occurs in the region of subsiding air (Fig. 4.17c), i.e. just where it is needed most. The melting, in tandem with the evaporation (Fig. 4.17b), contributes to a profile of chilling that increases with height from about 1 to 2.5 km AGL. Notably, Fig. 4.17b implies that the lowest 1 km of the inflow layer ought to be stabilized by decreasing evaporation with height near the convective line. The detrimental effect of this process is minimized because the inflow in the lowest 1 km AGL is moving westward rapidly, and therefore doesn't spend much time in the region of significant chilling. Clearly, the way that the cooling is partitioned between melting and evaporation is a function of the height of the melting level; in much warmer soundings, the level of maximum chilling will be higher, in much cooler soundings, the level of maximum chilling will be lower. It may therefore be that this destabilization process in nature is somewhat seasonal.[9]

Fig. 4.17 suggests two plausible interpretations for the near–line destabilization process. The first is that most of the destabilization occurs to the east of x=30 km owing to ascent, after which the phase changes more or less offset the stabilization owing to descent; this interpretation is consistent with the negatively buoyant descent of air owing to cooling. The second is that the couplet of ascent and descent provides relatively little mean destabilization over the course of the inflow trajectories, and the vertical profile of evaporation and melting plays the key role in increasing the lapse rates to the west of x=30 km. The data in Table 4.1 are consistent with either interpretation. As shown by the values of $\Delta\theta'$ in Table 4.1, in all three examples the cooling along the trajectories increases with height over the lowest 2 km AGL. For the 2D simulation (Table 4.1, part a), in which a relatively small amount of destabilization happens along the trajectories, neither ascent nor phase changes are clearly the predominant contributor to the destabilized ($\partial\theta'/\partial z < 0$) near–line sounding. On average in the periodic–3D simulation (Table 4.1, part b), ascent is the predominant

[8] To some degree, this may therefore resemble the subsidence and corresponding sublimation, melting, and evaporation in the *transition zone* of FFTS systems, as discussed, e.g., by Biggerstaff and Houze (1991).

[9] Notably, Parker and Johnson (2000) only studied LS systems that occurred in May, although LS MCSs have been observed in other months as well.

contributor to destabilization. For the group of time–dependent trajectories from the periodic–3D simulation (Fig. 4.15 and Table 4.1, part c), evaporation and melting are the predominant contributors to destabilization.

It is fairly easy to understand that melting which is maximized aloft can destabilize a sounding. Why does evaporative cooling destabilize a layer of inflowing air? Firstly, if θ_e decreases with height then, if the entire layer were saturated by local evaporation, it would be absolutely unstable. Of course, this does not guarantee that the layer will be destabilized when precipitation falls into it, but it provides the possibility that it could be via this process. Of additional importance is the fact that, as shown in Fig. 4.10 (or, alternately, in Fig. 2.2), the relative humidity of the base state decreases with height above the surface mixed layer. Because evaporation proceeds more rapidly in air with lower relative humidity [recall the numerator of (2.1)], a column of air from the environment would be destabilized upon encountering vertically uniform q_h. Thirdly, as can be seen in Fig. 4.16a, the rain water mixing ratio generally increases with height in the lowest 2 km AGL of the leading precipitation region. This is partly because the precipitation evaporates as it falls from above, and partly because the front–to–rear storm–relative flow advects hydrometeors back toward the convective line as they fall through the lower troposphere. And finally, because the storm–relative wind speeds decrease with height, air parcels at higher altitudes spend more time within the leading precipitation, and hence have longer to be chilled. These four factors together mean that inflowing air can be cooled to lower temperatures with increasing height, and that the evaporative chilling profile will increase with height because the relative humidity of the inflowing air decreases with height, q_h increases with height, and the Lagrangian time scale increases with height.[10]

In summary, leading precipitation provides two beneficial effects, both of which tend to destabilize the near–line sounding. The leading precipitation does cool the inflowing air, as Parker and Johnson (2000) originally speculated, but it does so in a way that is not detrimental to the sys-

[10] Notably, this sort of destabilization bears some resemblance to the removal of a capping inversion by virga, as discussed by Tripoli and Cotton (1989a). It may also be of some importance for the air that flows inward through precipitation in hurricanes.

tem's longevity. First, the leading precipitation melts and evaporates as it falls into the inflow, rendering cooling that increases with height over the lowest 2-2.5 km AGL. Secondly, as widespread evaporation and melting ensue, they lead to a pressure field that induces upward accelerations on inflowing air parcels in and ahead of the leading precipitation region. Because θ_e decreases with height in the lower troposphere and because the air parcels' vertical displacements often increase with height, this process also destabilizes the near–line profile as the cooled inflowing air parcels arrive there. Therefore, the leading precipitation region helps to foster continued development of healthy convection because the destabilization that it provides overwhelms any stabilization from gravity wave–induced subsidence.

Chapter 5

DYNAMICS AND KINEMATICS OF SIMULATED CONVECTIVE LINES WITH LEADING PRECIPITATION

Having described the properties of the temporally averaged FFLS simulations, the text now turns to their temporally varying parts. These transients prove to be very important to the production of an overturning updraft and leading precipitation. This chapter presents analyses of their dynamics using the framework outlined in Chapter 3. Section 5.1 considers the 2D control simulation. Then, Section 5.2 considers complications in the 3D case.

5.1 A typical updraft cycle in a mature front–fed LS system

Keeping in mind the typical pressure anomalies associated with cold pools and convection in a sheared environment (Figs. 3.1 and 3.3), this section documents the evolution of the components of the pressure field for a typical updraft cycle and the resultant accelerations that account for three representative air parcel trajectories from the 2D control FFLS simulation. During the period of interest, 9601–11862 s (approximately 160–198 min), an updraft occurs, followed by a suppressed period and finally by a second updraft. As shown in Fig. 5.1, three air parcels (△, ○, and □) that approach the convective region with very similar trajectories and pass through the exact same point ($x = -1$ km, $z = 730$ m AGL) at different times (△ at $t = 10196$ s, ○ at $t = 10315$ s, and □ at 11148 s) follow markedly different trajectories through and away from the convective region. Parcel △ ascends in the first updraft, whereas ○ arrives about 2 minutes later and does not. A suppressed period ensues, in which no inflowing parcels ascend in a deep updraft. Parcel □ then arrives just as the second updraft forms, and ascends and overturns in it. The proceeding discussion explains the basic accelerations that affect each parcel, and the reasons why some air parcels ascend in deep convective updrafts while others do not.

5.1.1 Two–dimensional air parcel accelerations

By inspecting the temporally averaged fields in Fig. 5.1, it is impossible to determine why some air parcels ascend in the deep updrafts (i.e. △ and □) while others do not (i.e. ○). This is a key point that bears repeating. *The essential dynamics that govern air parcels' accelerations in the convective region cannot be faithfully represented by long term temporally averaged fields. Although periodic, the accelerations are transient and are lost when averaged over a full active/supressed cycle.* Instead, in order to gain insight into these transient dynamics, this study investigated accelerations on individual air parcels.

This section assesses parcels' accelerations by using averages over time periods of approximately 4–8 minutes. This is a similar tactic to that used by Fovell and Dailey (1995) and Fovell and Tan (1998), who found that they could capture multicells' essential periodic behavior by analyzing their data at 3–8 minute intervals. Although averaging over time scales even as short as 4 minutes removes some amount of detail, the main shape of the transient signal is still well–approximated and the averaging enables the presentation of a reasonable number of figures to illustrate the discussion. During each averaging window, each plotted parcel was predominantly being accelerated in one particular direction. Table 5.1 displays the △, ○, and □ (cf. Fig. 5.1) parcels' starting and ending velocities for each averaging period discussed in this section.

Between 9601 and 9958 s, both △ and ○ approach the system's outflow boundary and gust front, which is located at $x \approx -4$ km (Fig. 5.2a). During this time period both air parcels are decelerated (Table 5.1) owing to the eastward–directed pressure gradient acceleration (Fig. 5.2b). The horizontal pressure gradient, in turn, is almost entirely attributable to P'B (Fig. 5.2c, much as in Fig. 3.1A), although the gradient in P'DNL contributes a very small amount (Fig. 5.2d, much as in Fig. 3.1D). The △ and ○ parcels do not experience significant vertical accelerations during this time period (Table 5.1). Notably, from 9601–9958 s, the cold pool isn't producing appreciable

S=16, E=1 from 9601–11862 s

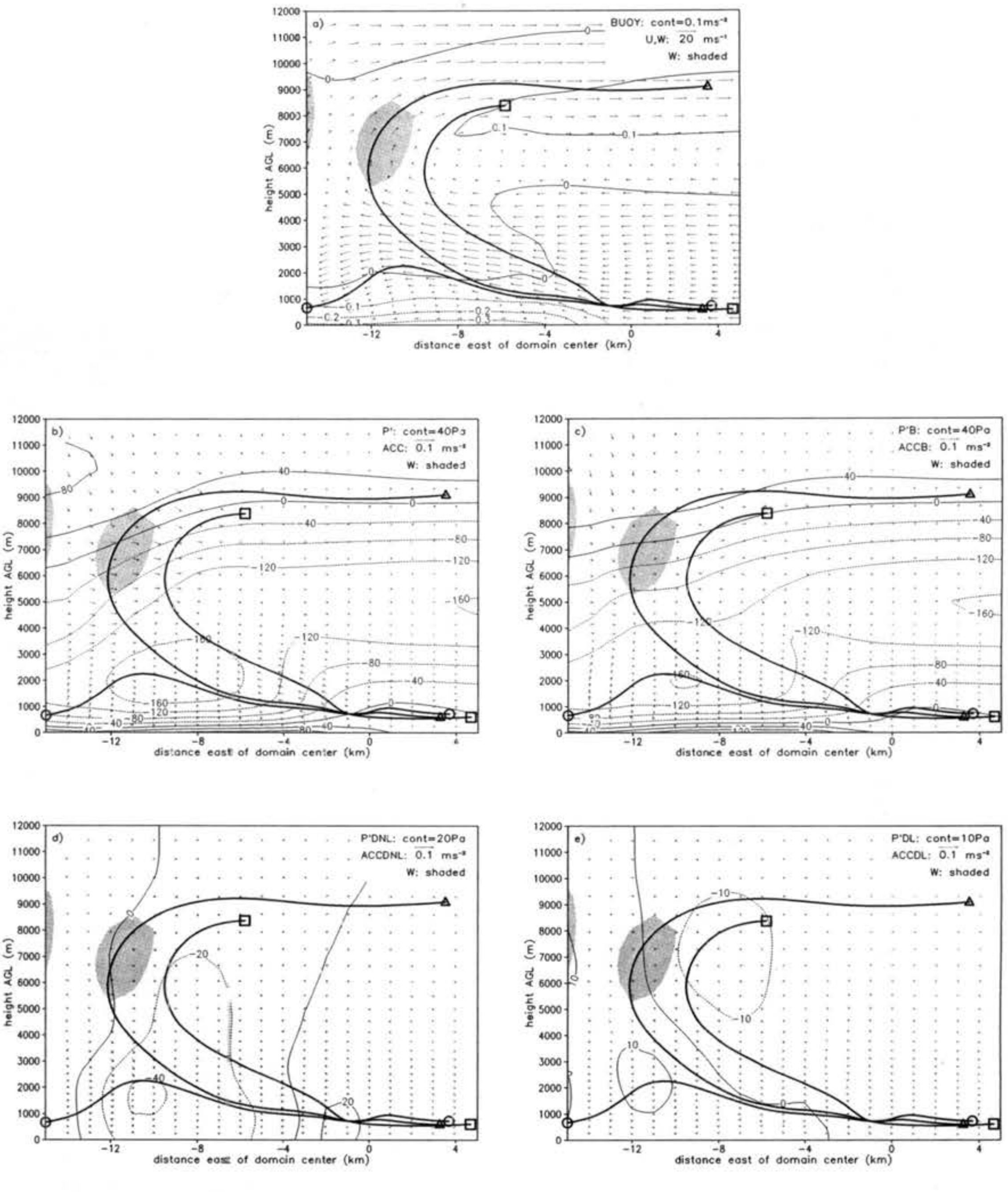

Figure 5.1: Mean velocities, perturbation pressures, and acceleration terms for simulation S=16, E=1 from 9601–11862 s. a) $BUOY$ contoured, u and w vectors. b) P' contoured, ACC vectors. c) $P'B$ contoured, $ACCB$ vectors. d) $P'DNL$ contoured, $ACCDNL$ vectors. e) $P'DL$ contoured, $ACCDL$ vectors. Vertical velocity shaded in all panels: levels of shading are 5 and 10 m s^{-1}. Three representative air parcel trajectories (△, ○, and □) are plotted as bold curves; segments of these trajectories are analyzed in Figs. 5.2–5.9. Contour intervals and vector scales are shown for each panel, and vary among panels. Terms are defined in § 2.2.3.

Table 5.1: Velocities (m s^{-1}) of the air parcels in Fig. 5.1 (△, ○, and □) at the beginning and ending times of the averaging periods used in this section. "NC" indicates no computation of a parcel's velocity because it was far from the region of interest.

	△		○		□	
time (s)	u (m s^{-1})	w (m s^{-1})	u (m s^{-1})	w (m s^{-1})	u (m s^{-1})	w (m s^{-1})
9601	-13.2	+0.3	-12.8	+0.3	NC	NC
9958	-4.6	+0.0	-3.9	+0.2	NC	NC
10196	-8.7	+0.7	-5.8	-1.3	NC	NC
10672	-17.4	+9.2	-16.3	+3.7	-10.5	-0.5
10910	-6.6	+13.1	-14.6	+2.2	-13.5	+0.2
11148	+13.8	+9.3	-12.2	-6.3	-8.9	+1.9
11505	+16.7	-1.1	NC	NC	-22.4	+9.8
11862	NC	NC	NC	NC	+13.9	+11.7

vertical motions along the outflow boundary and gust front, and there is not an active surface–based updraft (Fig. 5.2a).

From 9958 through 10196 s, both △ and ○ move relatively slowly (Table 5.1 and Fig. 5.3). A new updraft and attendant shallow cloud have developed above the outflow boundary (Fig. 5.3a), and there is an attendant positive buoyancy anomaly centered at $x = -4$ km, $z = 2000$ m AGL. Associated with the new maximum in buoyancy there exists a newly–developed minimum in P'B just below the center of the buoyancy anomaly (Fig. 5.3c, much as in Fig. 3.1B), and this P'B minimum imparts significant westward accelerations upon air parcels to its east. Air parcel ○ is slightly too far from the P'B minimum to be accelerated much by it (Fig. 5.3c); between 9958 and 10196 s, ○ merely continues to slowly move westward and to be accelerated downward owing to its small degree of negative buoyancy (having ascended slightly between 9601 and 9958 s). Meanwhile, △, which is a small distance west of ○, has begun to be lifted and accelerated rearward by ACCB (Fig. 5.3c). Hence, despite their similar velocities at 9958 s (Table 5.1), △ and ○ are accelerated to different degrees owing to their different positions with respect to the outflow boundary and its developing updraft and cloud. By the end of the time period at 10196 s, △ is approximately 1 km west of ○; this "head start" will become important in the parcels' near futures. Notably, in addition to the fresh updraft at the gust front, a deeper updraft has developed far behind the gust front, at $x \approx -14$ km. This updraft, although it does not yet include △ or ○,

S=16, E=1 from 9601–9958 s

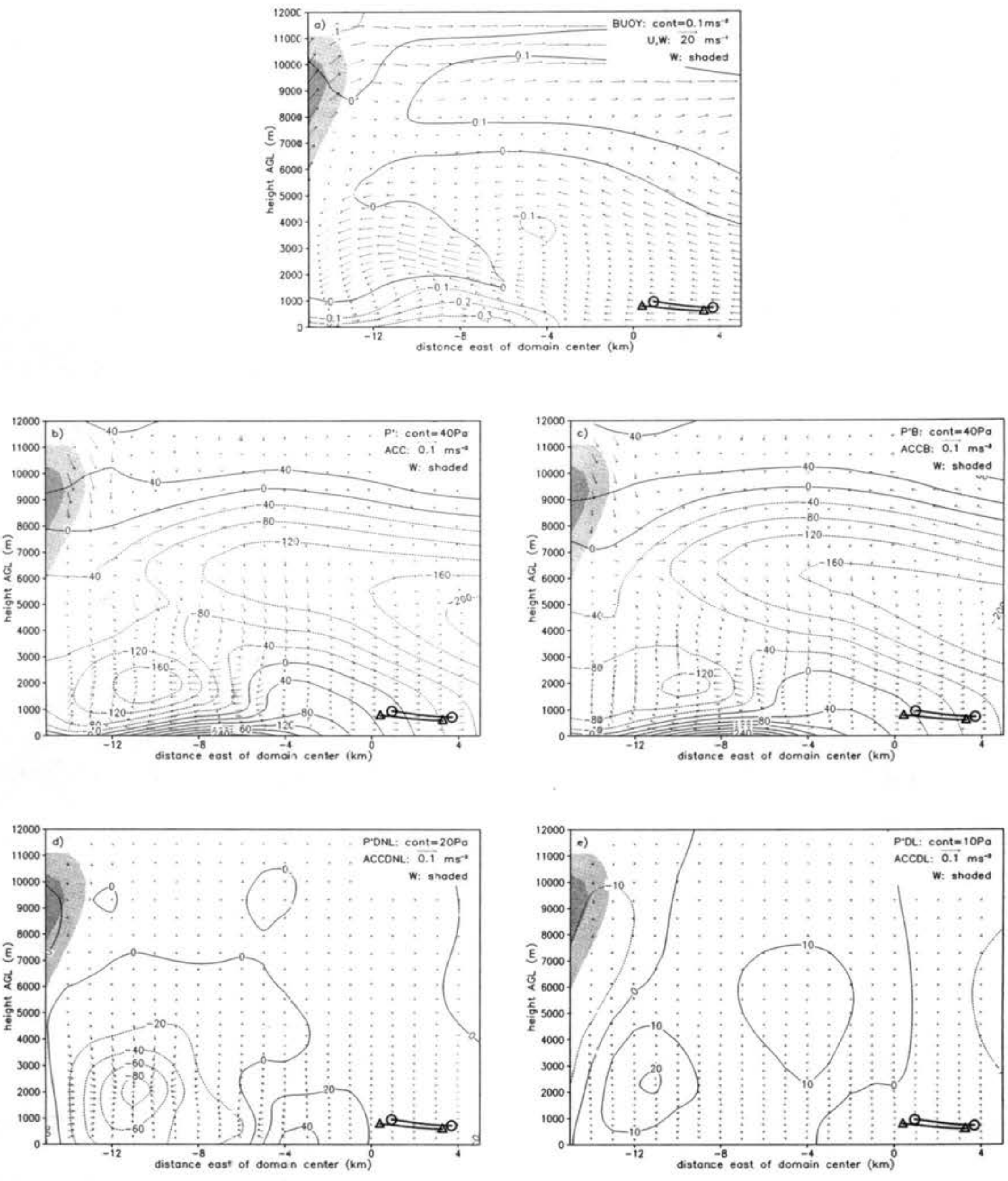

Figure 5.2: Mean velocities, perturbation pressures, and acceleration terms for simulation S=16, E=1 from 9601–9958 s. a) $BUOY$ contoured, u and w vectors. b) P' contoured, ACC vectors. c) $P'B$ contoured, $ACCB$ vectors. d) $P'DNL$ contoured, $ACCDNL$ vectors. e) $P'DL$ contoured, $ACCDL$ vectors. Vertical velocity shaded in all panels: levels of shading are 5 and 10 m s^{-1}. Segments of the three representative air parcel trajectories from Fig. 5.1 are plotted as bold curves. Parcels' symbols ($\triangle$, $\bigcirc$, and $\square$) are plotted to indicate their positions at the starting and ending times of the figure. Contour intervals and vector scales are shown for each panel, and vary among panels. Terms are defined in § 2.2.3.

does modify the local pressure field and thereby affects the △ and ◯ trajectories.

Between 10196 and 10672 s, both △ and ◯ are accelerated strongly rearward (Table 5.1). During this time period △ is also accelerated upward significantly, whereas ◯ receives a much smaller net upward acceleration. Early in this span of time, both parcels are accelerated upward by the vertical gradient in P'B near the edge of the outflow and rearward by the horizontal pressure gradient that is due to P'B and P'DNL near the cold pool's nose (Fig. 5.4c and d, much as in Fig. 3.1A and D). Throughout the period, and especially toward its end, the parcels are also accelerated rearward and upward toward the minimum in P'B centered at $x = -8$ km, $z = 2000$ m AGL (Fig. 5.4c) that, in turn, owes its existence to the maximum in buoyancy that is centered at $x = -8$ km, $z = 6000$ m AGL (Fig. 5.4a), much as in Fig. 3.1B. The reason that △ is accelerated upward so much more than ◯ between 10196 and 10672 s is that, given its more westward position, it encounters the gradient in P'B sooner. In addition, toward the end of the time period, △ also becomes positively buoyant (Fig. 5.4a), which further increases its upward ACCB. Notably, as of 10672 s there is no reason to suspect that ◯ won't follow roughly the same path as △.

By 10672 s, □ has finally entered the region of interest (Fig. 5.5), although it isn't accelerated much as it flows toward the outflow boundary and gust front (Table 5.1). Air parcel △ continues to be accelerated upward (Table 5.1), especially toward the end of the time period owing to its increasing buoyancy (Fig. 5.5a and c). As △ begins to ascend rapidly in the main updraft, it is accelerated strongly eastward by the horizontal pressure gradient which largely comprises the gradients in P'DL (Fig. 5.5e), owing to the environmental shear as in Fig. 3.1C, and in P'B, owing to the mesoscale structure of the buoyancy field as in Fig. 3.1G. Notably, updraft parcels on the eastern side of the updraft are also accelerated downshear by the horizontal gradient in P'DNL (Fig. 5.5d). It is difficult to determine from Fig. 5.5d whether the process depicted in Fig. 3.1F or in Fig. 3.3H predominates, and there is no clean way to mathematically partition between the two. Given that the atmosphere does not discriminate between the two sources for the vortical flow field, it would be haphazard to attempt to separate them. For the time period 10672–10910 s, ACCB, ACCDNL, and ACCDL all contribute to the downshear accelerations of air in the updraft. Meanwhile, al-

S=16, E=1 from 9958–10196 s

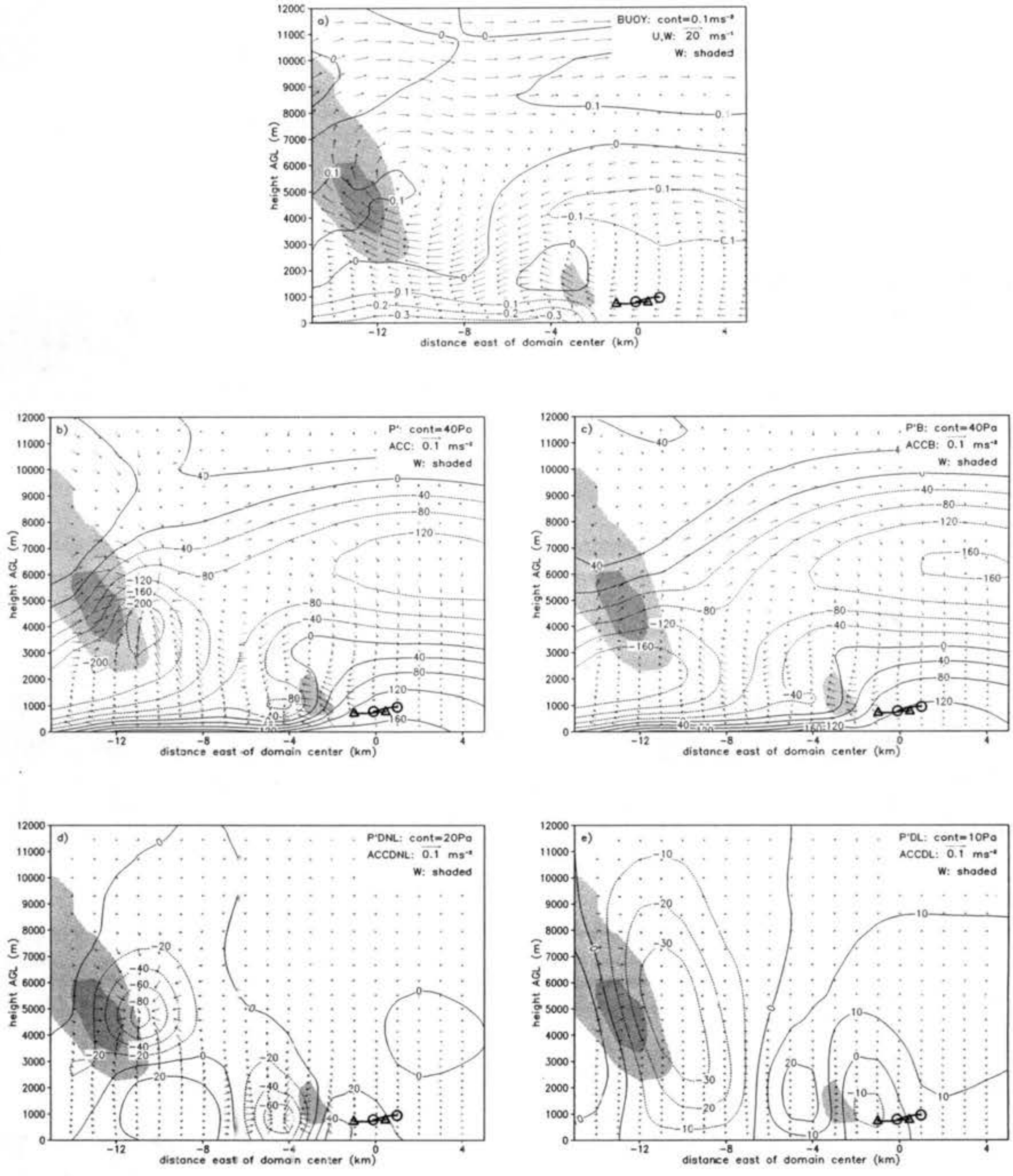

Figure 5.3: Mean velocities, perturbation pressures, and acceleration terms for simulation S=16, E=1 from 9958–10196 s. a) $BUOY$ contoured, u and w vectors. b) P' contoured, ACC vectors. c) $P'B$ contoured, $ACCB$ vectors. d) $P'DNL$ contoured, $ACCDNL$ vectors. e) $P'DL$ contoured, $ACCDL$ vectors. Vertical velocity shaded in all panels: levels of shading are 5 and 10 m s^{-1}. Segments of the three representative air parcel trajectories from Fig. 5.1 are plotted as bold curves. Parcels' symbols ($\triangle$, $\bigcirc$, and $\square$) are plotted to indicate their positions at the starting and ending times of the figure. Contour intervals and vector scales are shown for each panel, and vary among panels. Terms are defined in § 2.2.3.

S=16, E=1 from 10196–10672 s

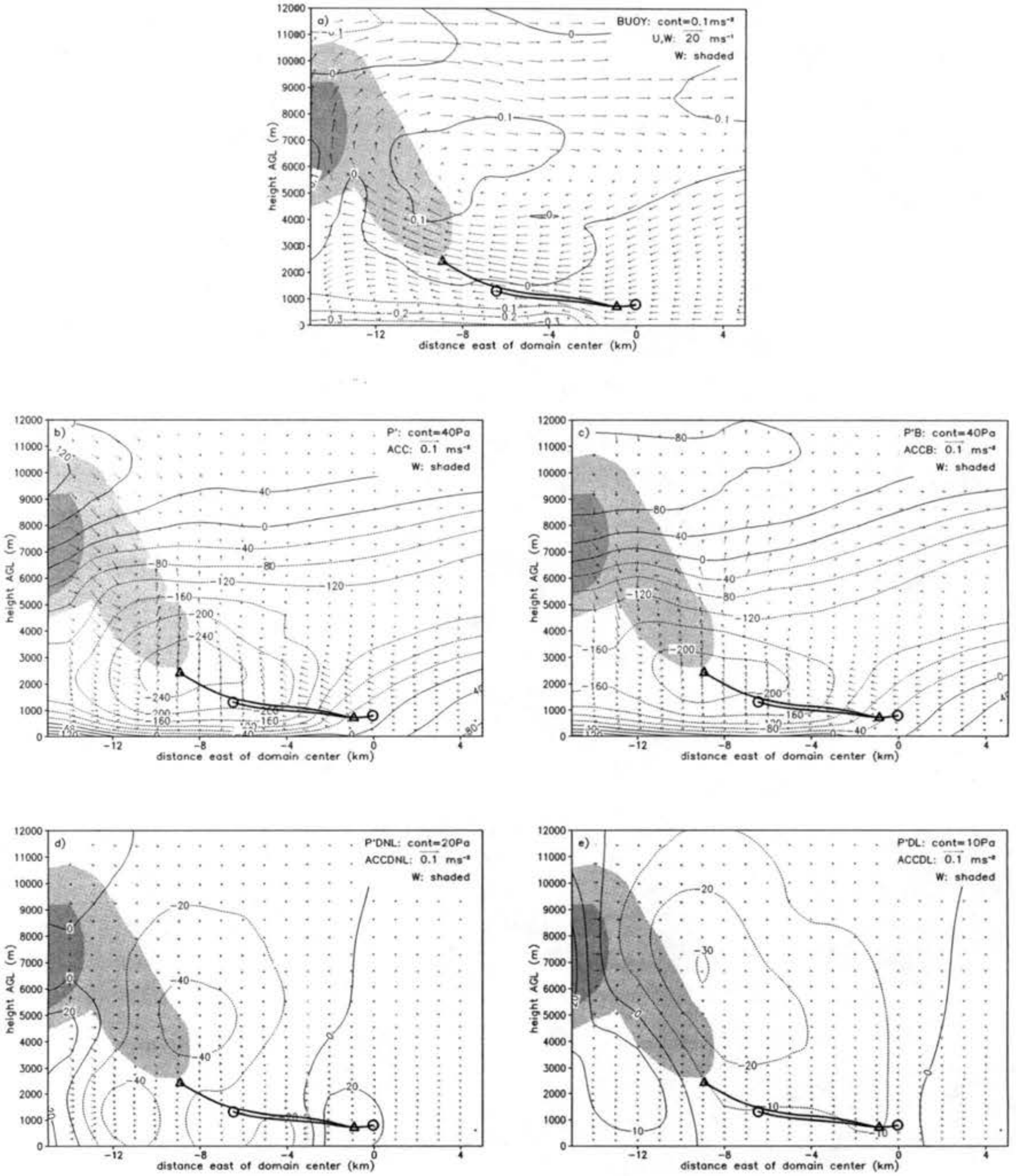

Figure 5.4: Mean velocities, perturbation pressures, and acceleration terms for simulation S=16, E=1 from 10196–10672 s. a) $BUOY$ contoured, u and w vectors. b) P' contoured, ACC vectors. c) $P'B$ contoured, $ACCB$ vectors. d) $P'DNL$ contoured, $ACCDNL$ vectors. e) $P'DL$ contoured, $ACCDL$ vectors. Vertical velocity shaded in all panels: levels of shading are 5 and 10 m s^{-1}. Segments of the three representative air parcel trajectories from Fig. 5.1 are plotted as bold curves. Parcels' symbols (△, ○, and □) are plotted to indicate their positions at the starting and ending times of the figure. Contour intervals and vector scales are shown for each panel, and vary among panels. Terms are defined in § 2.2.3.

though roughly following the path originally traced out by △, ◯ receives no additional net upward acceleration between 10672 and 10910 s (Table 5.1). One reason that is evident in (Fig. 5.5a) is that ◯ does not become significantly buoyant. The ◯ parcel isn't being accelerated downward much; rather, it is suffering from a lack of upward acceleration, and so it does not turn sharply upward and participate in the deep updraft during this time period. At this point it will suffice to say that ◯ is slightly negatively buoyant; a discussion of the processes that differentiate △ from ◯ appears later in the text.

From 10910 through 11148 s, □ is decelerated and lifted slightly (Table 5.1), much as △ and ◯ were between 9601 and 9958 s (Fig. 5.2). However, in the case of □, the deceleration is dominated by ACCDNL rather than ACCB (Fig. 5.6 c and d). It is difficult to predict whether ACCB or ACCDNL will be larger for a given cycle; their relative magnitudes are related to the chaotic details of the cold pool's shape and the low–level wind field near the gust front. During this period, △ is completing its ascent through the updraft, and continues to be strongly accelerated downshear. The updraft is weakening at this time, and from Fig. 5.6a it appears that △ was one of the last air parcels to join the updraft before it was separated from the inflowing airstream below 5 km AGL. Because the updraft has weakened and $\partial w/\partial x$ has decreased [recall (3.2) and (3.3)], the magnitudes of P'DNL and P'DL on its flanks have also weakened (cf. Fig. 5.6 d and e versus Fig. 5.5 d and e). Hence, although ACCDL continues to contribute somewhat (Fig. 5.6e), △ is now primarily accelerated downshear by the horizontal gradient in P'B (Fig. 5.6c), which is largely attributale to the mesoscale buoyancy structure (Fig. 5.6a, much as in Fig. 3.1G). In the mean time, ◯ undergoes a significant change in that it is acclerated strongly downward and begins to descend (Table 5.1, Fig. 5.6a). This downward acceleration is entirely due to ACCB (Fig. 5.6c), and, because the vertical gradient in P'B implies upward accelerations, it is clear that ◯ is accelerated downward because of its negative buoyancy (cf. Fig. 5.6a and c). It is finally clear by 11148 s that, despite their nearly identical origins and similar inflow trajectories, △ and ◯ will have quite different fates and will not end up anywhere near one another at later times. This highlights the large degree of transience that governs accelerations in the updraft region.

S=16, E=1 from 10672–10910 s

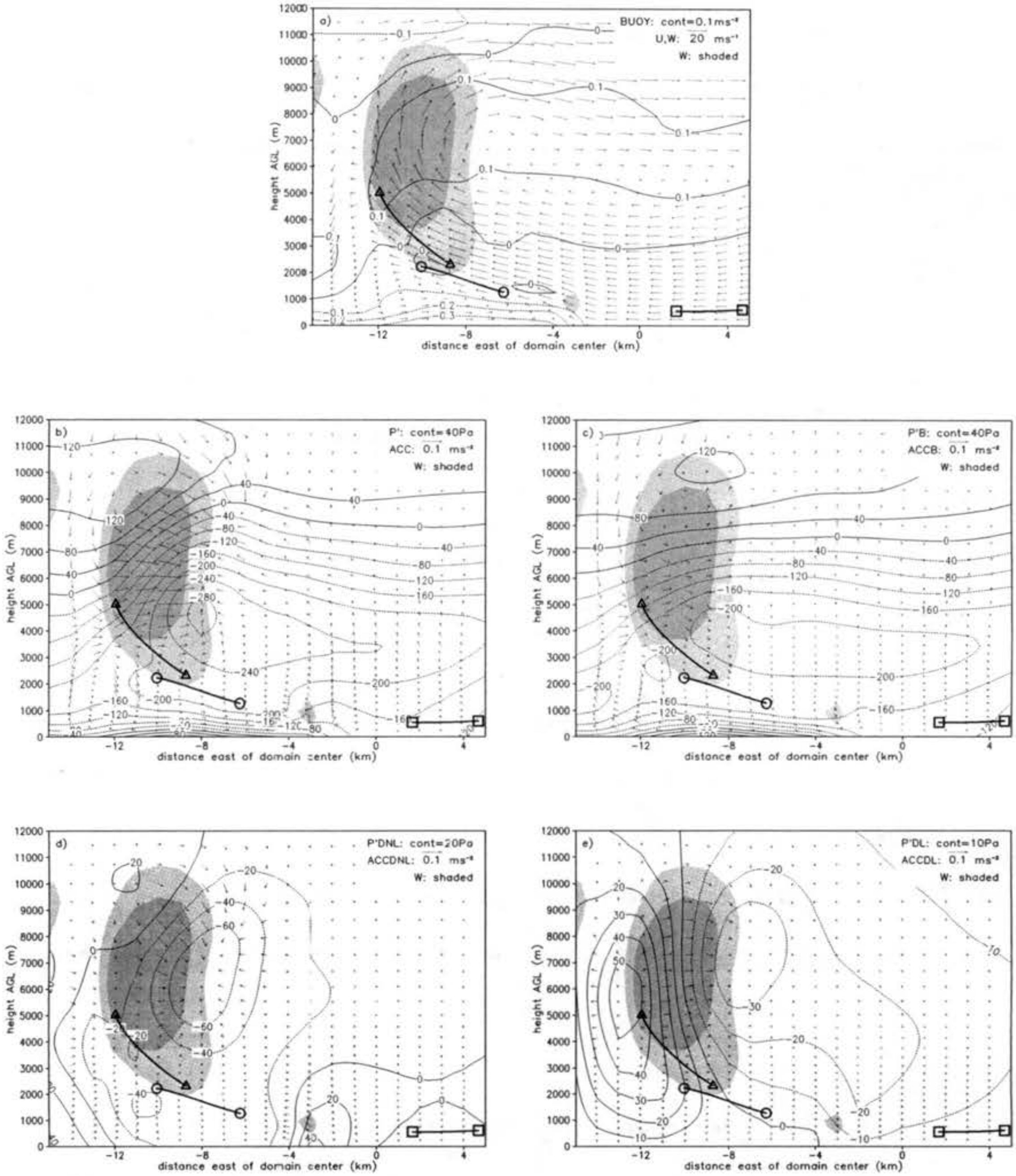

Figure 5.5: Mean velocities, perturbation pressures, and acceleration terms for simulation S=16, E=1 from 10672–10910 s. a) $BUOY$ contoured, u and w vectors. b) P' contoured, ACC vectors. c) $P'B$ contoured, $ACCB$ vectors. d) $P'DNL$ contoured, $ACCDNL$ vectors. e) $P'DL$ contoured, $ACCDL$ vectors. Vertical velocity shaded in all panels: levels of shading are 5 and 10 m s^{-1}. Segments of the three representative air parcel trajectories from Fig. 5.1 are plotted as bold curves. Parcels' symbols ($\triangle$, $\bigcirc$, and $\square$) are plotted to indicate their positions at the starting and ending times of the figure. Contour intervals and vector scales are shown for each panel, and vary among panels. Terms are defined in § 2.2.3.

Why is ○ accelerated downward into the cold pool while △ ascends in the updraft? As shown in Fig. 5.7c and d, ○ begins to experience precipitation drag long before it is positively buoyant [i.e. before it has reached its level of free convection (LFC)]. By 10910 s, ○ has neared its LFC but it no longer has a significant positive w (Fig. 5.7e and f). This is attributable to the downward accelerations imposed on it both by its negative buoyancy and by precipitation drag (Fig. 5.7c–f). Parcel ○'s relatively small w implies that it will take a longer time for the parcel to attain its LFC, and that downward accelerations will have more time to act as the parcel moves laterally into the precipitation core. By 11029 s, ○ is moving downward owing to the previous downward accelerations from both negative buoyancy and precipitation drag (Fig. 5.7g and h). From Fig. 5.7g, it appears that ○ is at last neutrally buoyant. However, Fig. 5.7h reveals that the parcel is still being accelerated downward by hydrometeor drag as it enters into the heaviest precipitation. Hereafter, ○ continues to descend, owing to its negative w, and indeed is accelerated downward by hydrometeor loading and by decreasing buoyancy (although not shown, as the parcel descends and warms its relative humidity decreases, hence it evaporates liquid and cools). In contrast to ○, as △ enters the main precipitation core at 10672 s, it continues to possess an appreciably positive w and has already started to become positively buoyant (i.e. has reached its LFC, cf. Fig. 5.7a and b). From 10791 s onward, △ has sufficient positive buoyancy to overcome the precipitation drag, and it is accelerated upward in the main updraft (Fig. 5.7c–h).

Between 11148 and 11505 s, the old updraft is completely cut off from the low–level inflow and weakens to $w < 10$ m s^{-1} (Fig. 5.8a). During this period △ ends its ascent, being accelerated downward by the vertical gradient in P'B (Fig. 5.8c), and moves eastward with a rear–to–front storm–relative velocity. As described in § 2.2.4, it carries its total water content with it and will contribute to the leading precipitation region that exists east of the convective region in the mature FFLS system. Air parcel ○ is no longer accelerated much after its downward acceleration during the last period, and it merely continues to flow rearward and descend slightly within the cold pool as it departs the region of interest. Meanwhile, □ is accelerated upward and rearward during the 11148–11505 s window (Table 5.1). The processes governing □ at this time are quite similar to

S=16, E=1 from 10910–11148 s

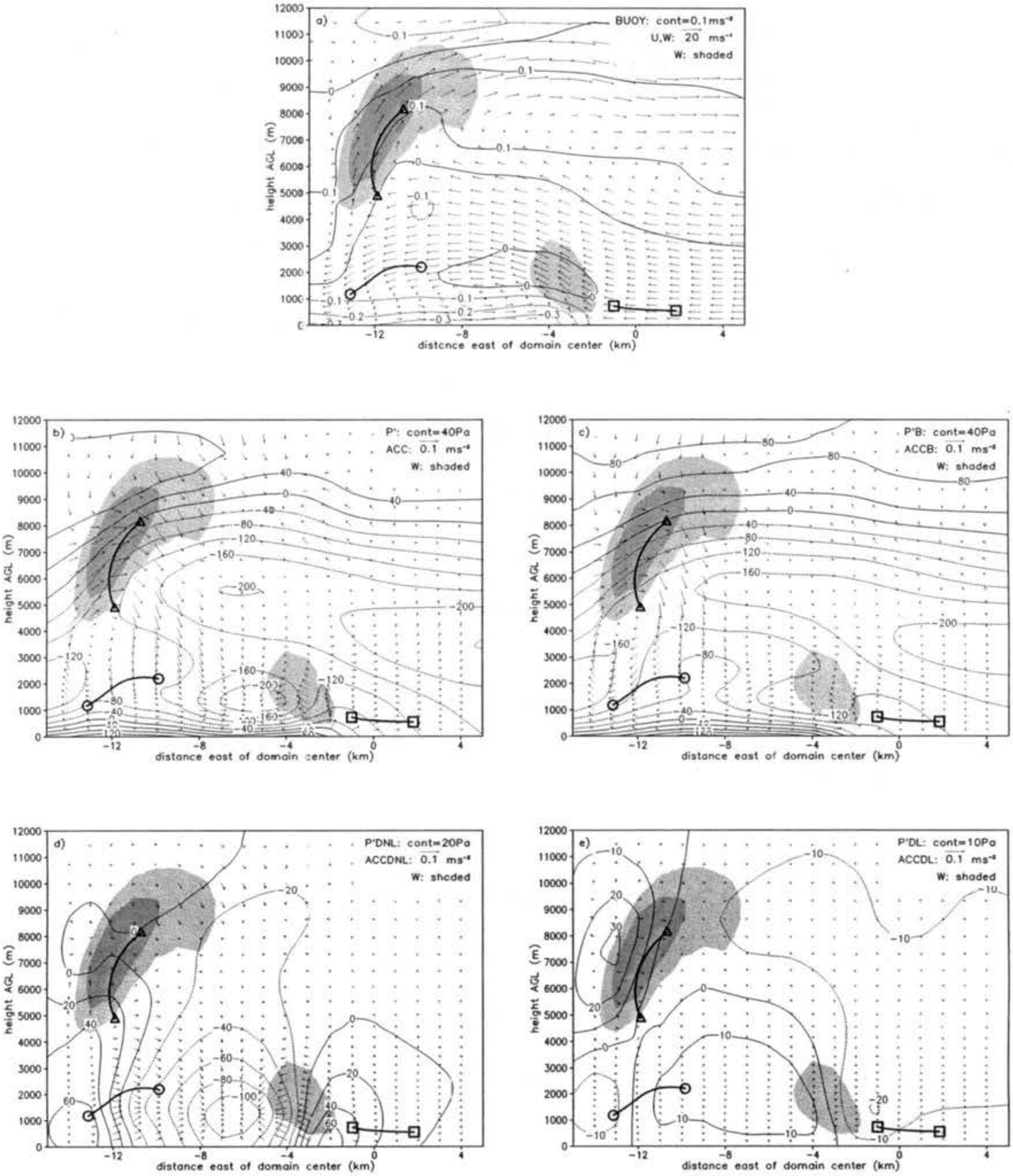

Figure 5.6: Mean velocities, perturbation pressures, and acceleration terms for simulation S=16, E=1 from 10910–11148 s. a) $BUOY$ contoured, u and w vectors. b) P' contoured, ACC vectors. c) $P'B$ contoured, $ACCB$ vectors. d) $P'DNL$ contoured, $ACCDNL$ vectors. e) $P'DL$ contoured, $ACCDL$ vectors. Vertical velocity shaded in all panels: levels of shading are 5 and 10 m s^{-1}. Segments of the three representative air parcel trajectories from Fig. 5.1 are plotted as bold curves. Parcels' symbols ($\triangle$, $\bigcirc$, and $\square$) are plotted to indicate their positions at the starting and ending times of the figure. Contour intervals and vector scales are shown for each panel, and vary among panels. Terms are defined in § 2.2.3.

S=16, E=1 from 10672–11029 s

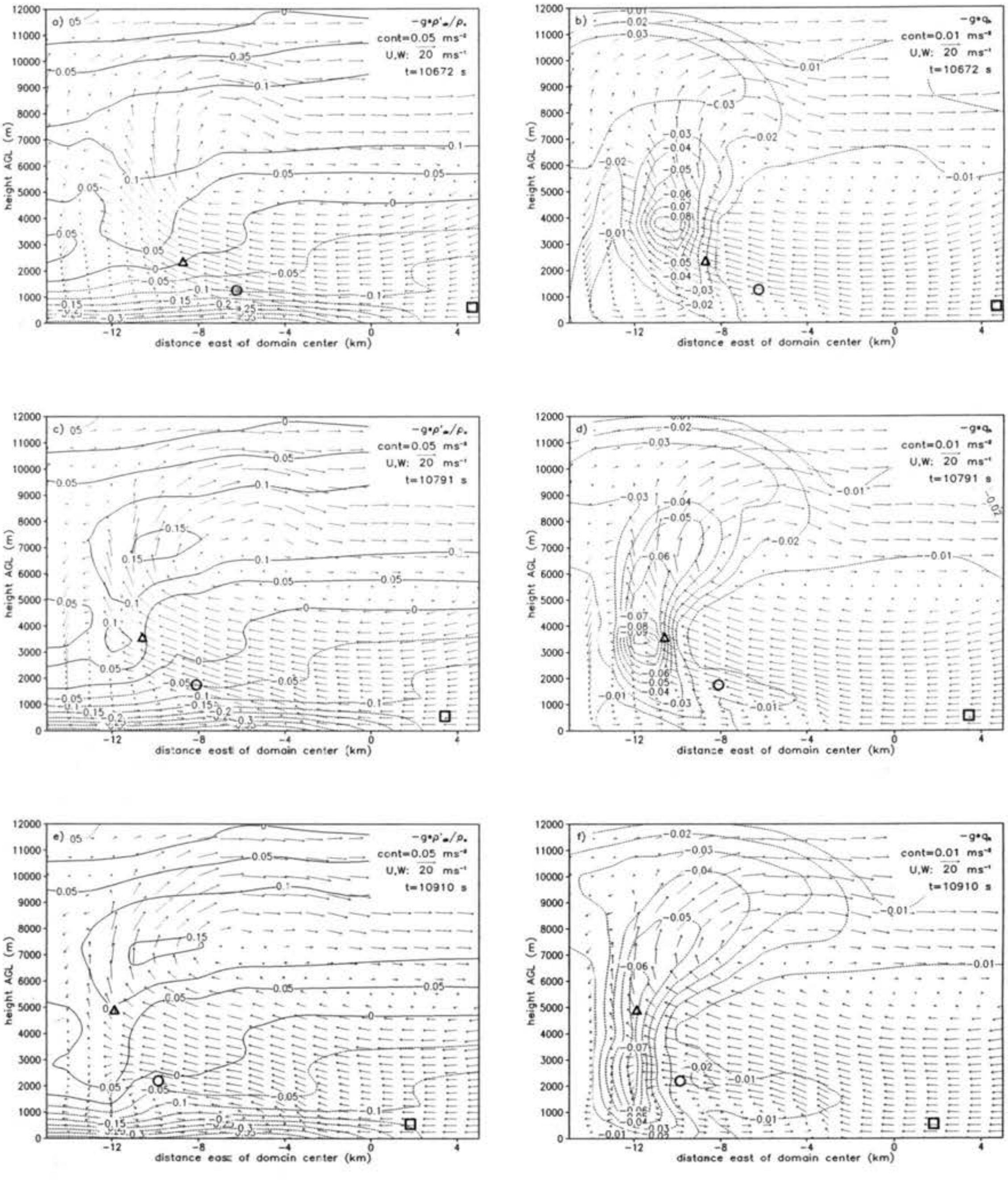

Figure 5.7: Velocities and components of buoyancy for simulation S=16, E=1 from 10672–11029 s. Buoyancy owing to perturbation in air density is shown in a), c), e), and g). Buoyancy owing to hydrometeor loading is shown in b), d), f), and h). Panels a) and b) are for $t = 10672$ s; panels c) and d) are for $t = 10791$ s; panels e) and f) are for $t = 10910$ s; panels g) and h) are for $t = 11029$ s. Parcels' symbols (△, ○, and □) are plotted to indicate their positions at the times of each panel.

S=16, E=1 from 10672–11029 s

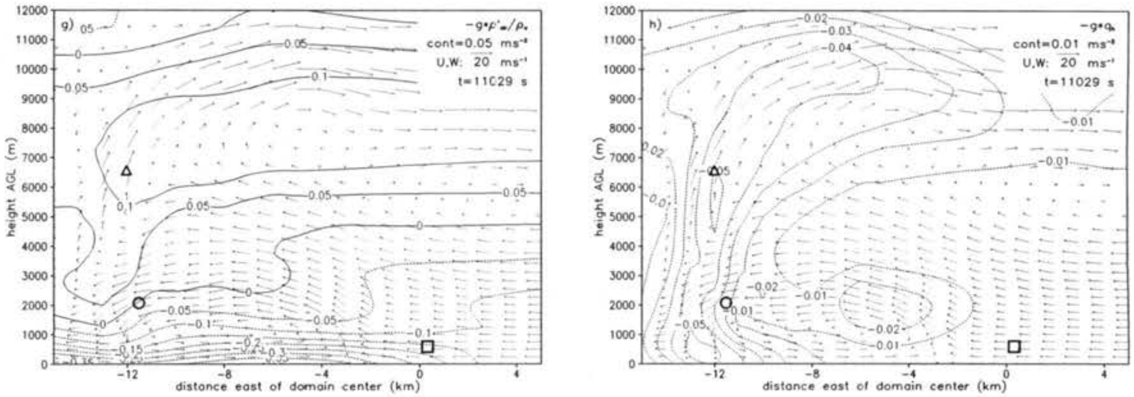

Figure 5.7: *Continued*

those that previously governed the upward and rearward accelerations of △ between 9958 and 10672 s (Figs. 5.3 and 5.4). A minimum in P'B has formed above the cold pool head (Fig. 5.8c) owing to a positive buoyancy anomaly associated with a new cloudy updraft (Fig. 5.8a). Air parcel □ is initially accelerated rearward toward this minimum in P'B and is accelerated upward as it also becomes buoyant within the cloudy updraft (Fig. 5.8a). However, in addition to this, P'DNL also contributes to □'s rearward acceleration, and hinders its ascent by providing a non–trivial downward acceleration (Fig. 5.8d). Why does such a strong minimum in P'DNL affect □ between 11148 and 11505 s when it was not present when △ approached and ascended over the cold pool? The reason is that the previous updraft (i.e. △'s updraft) has just produced a strong surge of outflow, some of which (like ○) moves westward/rearward and some of which moves eastward/forward (note the strong low–level westerlies from $x = -10$ to $x = -3$ km in Figs. 5.6a and 5.8a) rendering a region of strong horizontal vorticity and a dynamic pressure minimum as in Fig. 3.1D. Such an anomaly in P'DNL did occur as △ and ○ approached the gust front between 9601 and 9958 s (Fig. 5.2d); however, the parcels weren't far enough west to be affected by it. By the time △ and ○ began to ascend over the cold pool (9958–10672 s, Figs. 5.3 and 5.4), the active downdrafts had dissipated and the low–level minimum in P'DNL was no longer evident. In contrast, □ is one of the first/earliest air parcels to join the new updraft that is forming between 11148 and 11505 s, and therefore it is far enough westward to be affected by the P'DNL owing to strong downdrafts produced from the cycle that included △ and ○. Noting the close similarity of Fig. 5.2 to Fig. 5.8, with the caveat that the system and gust front have moved 2–3 km eastward, it is likely that □'s trajectory between 11148 and 11505 s would correspond to a trajectory extending approximately from $x = -4$ km, $z = 1000$ m AGL to $x = -10$ km, $z = 3500$ m AGL in Fig. 5.2. The similarity of Fig. 5.2 to Fig. 5.8 further demonstrates the quasi–stable periodic nature of the mature FFLS system. Meanwhile, the discussion of this section underscores the importance of transient accelerations in determining air parcel trajectories.

The accelerations on air parcel □ from 11505–11862 s are included in Table 5.1 and depicted in Fig. 5.9 for the sake of completeness. The parcel is accelerated upward slightly owing to its buoyancy and is accelerated strongly downshear, as in the prior updraft cycle, owing to the downshear contributions of ACCB, ACCDNL, and ACCDL. The reader can refer to the prior discussion of the time period 10672–10910 s for more details about the processes that govern these accelerations.

5.1.2 Summary of a typical updraft cycle

Updrafts in the FFLS simulations are alternately produced and suppressed. The local pressure and buoyancy fields follow similar cycles, and therefore the accelerations that affect air parcels in the convective region are also periodic. The general cycle is as follows. 1) Early in the lifetime of a new updraft, lifting at the edge of the cold pool is enhanced by ACCB and ACCDNL (Fig. 5.10a); this enhancement is largely due to a surge of outflow from the previous convective cycle, which strengthens the cold pool and intensifies the convergence at the gust front. Air parcels are decelerated as they approach the gust front, providing an extended period of time for the upward accelerations to impart positive w to the inflowing air parcels. Once air parcels have ascended over the outflow boundary, they are accelerated strongly rearward owing to the horizontal gradients in P'DNL and P'B. Often, the horizontal ACCB is attributable to a P'B minimum below a developing cloud. 2) Air parcels are accelerated upward toward their LFCs, and this upward acceleration is

S=16, E=1 from 11148–11505 s

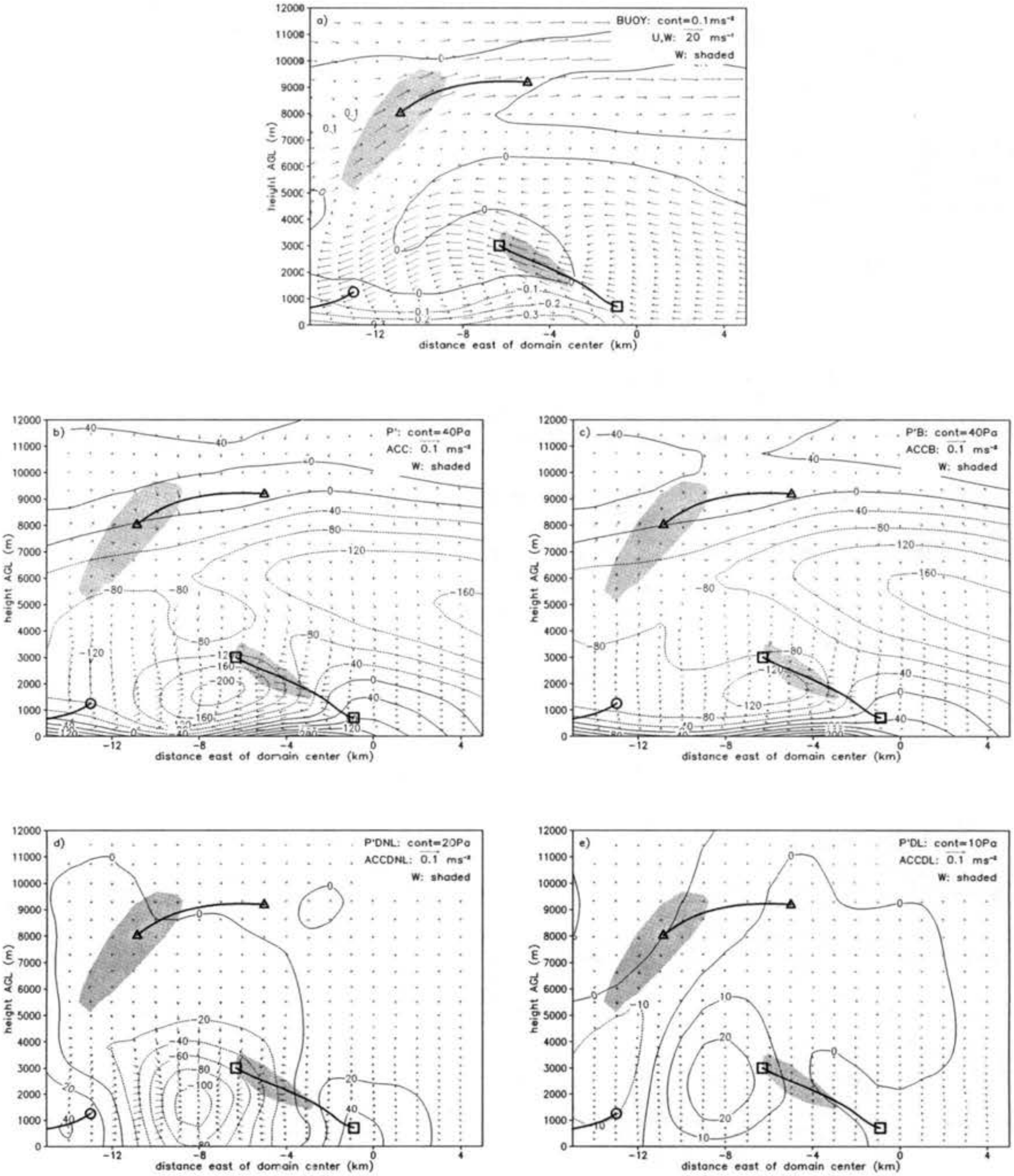

Figure 5.8: Mean velocities, perturbation pressures, and acceleration terms for simulation S=16, E=1 from 11148–11505 s. a) $BUOY$ contoured, u and w vectors. b) P' contoured, ACC vectors. c) $P'B$ contoured, $ACCB$ vectors. d) $P'DNL$ contoured, $ACCDNL$ vectors. e) $P'DL$ contoured, $ACCDL$ vectors. Vertical velocity shaded in all panels: levels of shading are 5 and 10 m s^{-1}. Segments of the three representative air parcel trajectories from Fig. 5.1 are plotted as bold curves. Parcels' symbols (△, ○, and □) are plotted to indicate their positions at the starting and ending times of the figure. Contour intervals and vector scales are shown for each panel, and vary among panels. Terms are defined in § 2.2.3.

S=16, E=1 from 11505–11862 s

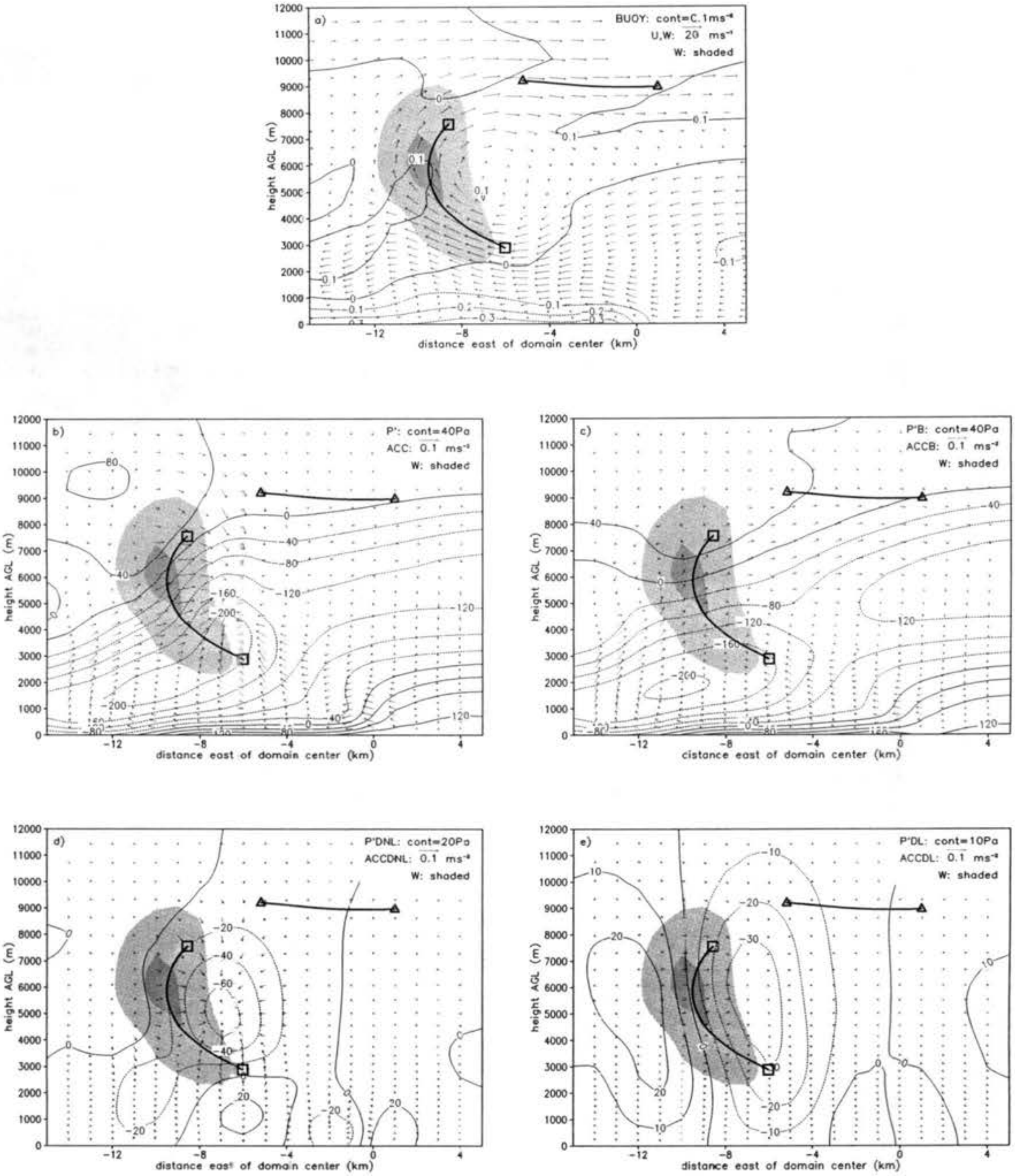

Figure 5.9: Mean velocities, perturbation pressures, and acceleration terms for simulation S=16, E=1 from 11505–11862 s. a) $BUOY$ contoured, u and w vectors. b) P' contoured, ACC vectors. c) $P'B$ contoured, $ACCB$ vectors. d) $P'DNL$ contoured, $ACCDNL$ vectors. e) $P'DL$ contoured, $ACCDL$ vectors. Vertical velocity shaded in all panels: levels of shading are 5 and 10 m s^{-1}. Segments of the three representative air parcel trajectories from Fig. 5.1 are plotted as bold curves. Parcels' symbols (△, ○, and □) are plotted to indicate their positions at the starting and ending times of the figure. Contour intervals and vector scales are shown for each panel, and vary among panels. Terms are defined in § 2.2.3.

largely due to the vertical gradient in P'B at the edge of the cold pool. In some sense, this is how cold pools lift air parcels. As the updraft develops at low levels, a downshear–directed ACCDL helps to provide more erect trajectories (the dashed arrow in Fig. 5.10a). The more erect updraft allows air to spend more time in the zone of upward acceleration, and decreases the magnitude of the minimum in P'DNL over the cold pool head (the weakening of the old downdrafts also is relevant to this decrease). During the active phase of the multicell, many air parcels are lifted to their LFCs in this way (e.g. △), participate in the main updraft, and are accelerated downshear by some combination of ACCB, ACCDNL, and ACCDL (Fig. 5.10b). The system deviates from the classical trailing precipitation model in that cloud and precipitation particles are carried forward from the convective updraft owing to air parcels' large net downshear accelerations. Therefore, as the convective updrafts life span progresses, some precipitation begins to fall in advance of the updraft's position. 3) Eventually there is a point of cut–off, when inflowing air parcels experience downward accelerations owing to hydrometeor loading as they approach the updraft (e.g. ○). As their vertical velocities decrease or become negative, they require longer and longer times to reach an LFC, and eventually move almost horizontally and accumulate downward acceleration until they descend (Fig. 5.10c). At this point, the multicell is suppressed, and no additional inflowing air parcels join the updraft. Meanwhile, the inflowing air parcels that have been strongly accelerated downward compose a downdraft and surge of outflow that strengthens the cold pool. Once the newly cut–off updraft has decayed and the precipitation curtain has dissipated sufficiently, the stage is once again set for phase 1 (i.e. for air parcel □, or panel a of Fig. 5.10).

The present simulations fall within the broad population of convective lines that are generally multicellular and exhibit periodic behavior. Yang and Houze (1995) attributed this periodic behavior to gravity waves forced by a quasi–steady gust front updraft; there is little evidence to support this conceptual model in the present analysis. In contrast, Fovell and Tan (1998) simulated an unsteady gust front updraft and attributed the convection's periodic behavior to a cut–off mechanism whereby each new buoyant updraft "[sows] the seeds of its own demise" by producing subsidence on its flanks, thereby supressing the gust front updraft and detaching the cell from it.

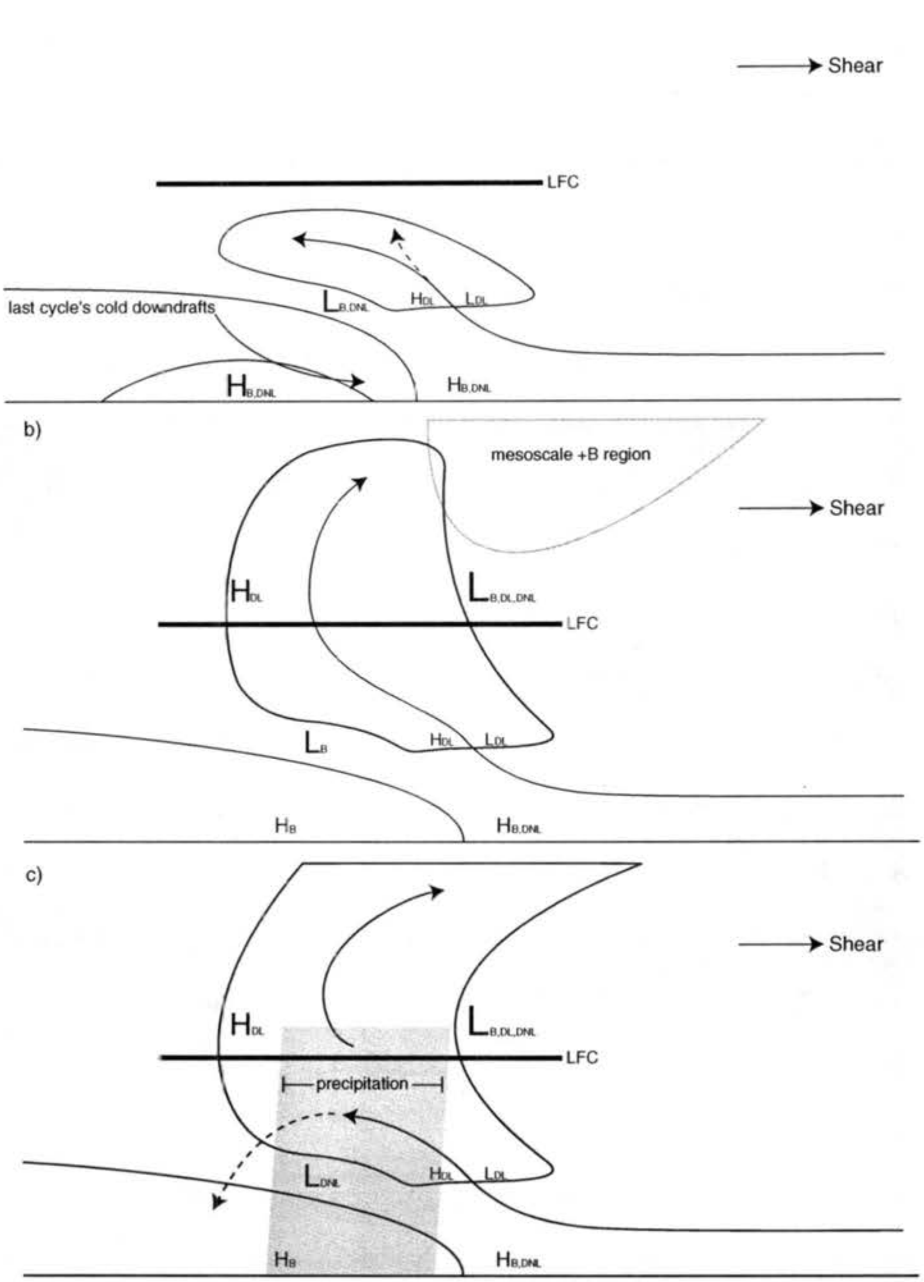

Figure 5.10: Schematic depiction of the FFLS multicellular cycle. a) development of a fresh updraft at the outflow boundary/gust front. b) maturation of the overturning updraft. c) the updraft is cut off from the inflow by precipitation. The cold pool and cloud outlines are shown schematically, along with typical airstreams. The level of free convection (LFC) and orientation of the deep tropospheric shear vector are also shown. In panel b, the shaded region represents the mesoscale region of positive buoyancy associated with the line–leading cloudiness. In panel c, the shaded region represents the newly developed convective precipitation cascade. Pressure maxima and minima are shown with "H" and "L" characters: their sizes indicate approximate magnitudes and their subscripts indicate the pressure components to which they are attributed. The vertical scale is expanded somewhat below the LFC and contracted somewhat above the LFC.

Lin et al. (1998) and Lin and Joyce (2001) provided a refinement to this idea by suggesting that the middle tropospheric flow controls the speed at which active cells are advected away from the gust front updraft, and therefore the period with which new convection can be regenerated.

Although Lin et al. (1998) and Lin and Joyce (2001) have effectively demonstrated the robustness of their conceptual model by employing a wide variety of idealized simulations and tests, an advective mechanism is somewhat difficult to reconcile with the present results, which focus on the dynamics that affect individual air parcels. Notably, in the simulation discussed above, the air parcels move through the maxima in w. This implies that the forcing for an updraft is somewhat more persistent than an individual parcel's Lagrangian timescale, and that air parcels move through this forcing and are caused to execute their characteristic updraft trajectories. The present results suggest that the period of the simulated FFLS multicells is probably at least partly related to the mid–level wind [as suggested by Lin et al. (1998) and Lin and Joyce (2001)] because the mid–level wind determines the translational speed of the updraft forcing (although this study did not include rigorous tests to confirm this). However, the dynamics that govern individual air parcels' trajectories need not have any obvious relationship to the mid–level wind. In addition, because of the cut–off mechanism discussed above, the multicell's time scale must also be strongly related to the intrinsic time scales required for the production of precipitation and cold downdrafts by convective clouds in the environment, which are likely a complicated function of the thermodynamic and kinematic profiles.

The multicell process in the simulations, described above, seems akin to that proposed by Fovell and Tan (1998) in that inflowing air parcels which are spatially and temporally proximate may experience vastly different outcomes based on the evolving forcing. And in turn, as suggested by Fovell and Tan (1998), the temporal evolution of the forcing is a result of the convection itself. However, in the present simulations, the cut–off mechanism appears to be related to precipitation processes; by contrast, the subsidence that Fovell and Tan (1998) implicated on cells' flanks was difficult to detect in the analysis. An interesting aspect of the present simulations is that air parcels overturn in the deep updrafts, yet the updraft forcing itself moves rearward with respect to the gust front. As a result, the developing updrafts and precipitation cores in the FFLS simulations still move rearward, much as in the systems studied by Fovell and Tan (1998), despite the fact that the mesoscale structure of the system is quite different. The fact that the overturning updraft is not situated directly above the gust front, but develops 5–10 km behind it, also makes the simulated system very interesting in the light of the arguments for deep lifting at gust fronts advanced by Rotunno et al. (1988). Section 6.1 addresses that issue.

5.2 Accelerations in 3D simulations of front–fed LS systems

This publication has not yet addressed the dynamics of the periodic–3D systems. An important and recurring question among dynamicists and numerical modelers is the degree to which 2D systems capture the essential physical processes of 3D systems. To this end, because the important dynamics in the updraft region are transient, it is not sufficient merely to note the similarity of the mean wind and condensate fields from the 2D and periodic–3D simulations (i.e. the similarity of Figs. 4.3 and 4.7, as was discussed in § 4.1). Although, it was not possible to conduct an exhaustive study of the 3D simulations, this section considers two significant updrafts from the periodic–3D control simulation and relates them to a foundation provided by previous studies.

After 6 hours (21600 s) of the control (S=16, E=1) periodic–3D simulation, the system has attained a quasi–stable FFLS configuration. As for the 2D simulations, Gauss–Seidel relaxation provided P'B, P'DL, and P'DNL over the entire 3D domain at this time. This section considers a relatively weak updraft (Fig. 5.11), whose characteristics are quite similar to those discussed for the 2D simulations in § 5.1, and a relatively strong updraft (Fig. 5.12), whose characteristics are somewhat different. Notably, the processes that govern the horizontal deceleration and upward acceleration of inflowing air parcels as they approach the gust front are very well–approximated by the 2D case. Although the surface cold pool in the periodic–3D simulations is not homogeneous, it still presents a nearly north–south barrier to the inflow air, whose velocity is very nearly due easterly. As a result of the cold pool's quasi–two–dimensionality, its associated P'B and P'DNL fields are also quasi–2D, and the basic air parcel accelerations in the vicinity of the outflow boundary/gust front can be explained almost entirely by resorting to the arguments in § 5.1.

In contrast, however, the system's updrafts are distinctly 3D. Due to the inhomogeneities in the surface cold pool, buoyant updrafts are initiated at individual points where the vertical accelerations produced by the cold pool are somewhat enhanced; this stands in contrast to the infinitely long (in $\hat{y}$) updrafts produced in 2D simulations. Of course, this process also initiates updrafts at different times along the length of the line because the inhomogeneities also contribute to along–line phase shifts in the periodic process described in § 5.1. As a result of these effects, it is exceedingly uncommon for slab–like updrafts to develop in the periodic–3D simulations.

Occasionally, the periodic–3D system produces a relatively weak updraft (Fig. 5.11) whose shape and characteristic w closely correspond to those of the 2D simulations (as in § 5.1). The 3D updraft in Fig. 5.11 resembles the 2D case in that the radius of curvature for the overturning updraft is fairly small (Fig. 5.11a) and in that ACCB, ACCDNL, and ACCDL all contribute to parcels' downshear accelerations throughout most of the updraft (Fig. 5.11c–e). Furthermore, as in 2D, for this updraft ACCB is largely attributable to the mesoscale horizontal buoyancy gradient (Fig. 5.11a,c) and ACCDNL is largely attributable to the minimum in P'DNL that forms on the downshear side of the updraft (Fig. 5.11d). Therefore, for weaker updrafts such as this, the basic 2D understanding developed in § 5.1 seems to be highly applicable.

However, most of the active updrafts produced by the periodic–3D system are considerably stronger than those in the 2D case (i.e. they more closely resemble Fig. 5.12 than Fig. 5.11). Schlesinger (1984) discussed physical reasons for this. One obvious cause can be traced to the much larger upward ACCB in 3D than in 2D (cf. Fig. 5.12 versus figures in § 5.1). As described in the beginning of § 3.1, in the limit of 1–D equation (3.1) reduces to a statement of hydrostatic balance for a given vertical profile of buoyancy. However, for that same vertical profile of buoyancy (3.1) implies that, for 2D cases, p'_B has horizontal structure in one dimension, and for 3D cases, p'_B has horizontal structure in two dimensions. For a boundary value problem, greater dimensionality implies weaker maxima and minima. In the 1D hydrostatic limit, the gradient in p'_B exactly opposes the buoyancy field, and no vertical accelerations are produced. With each added dimension, the ver-

S=16, E=1, for y=249 km at 21600 s

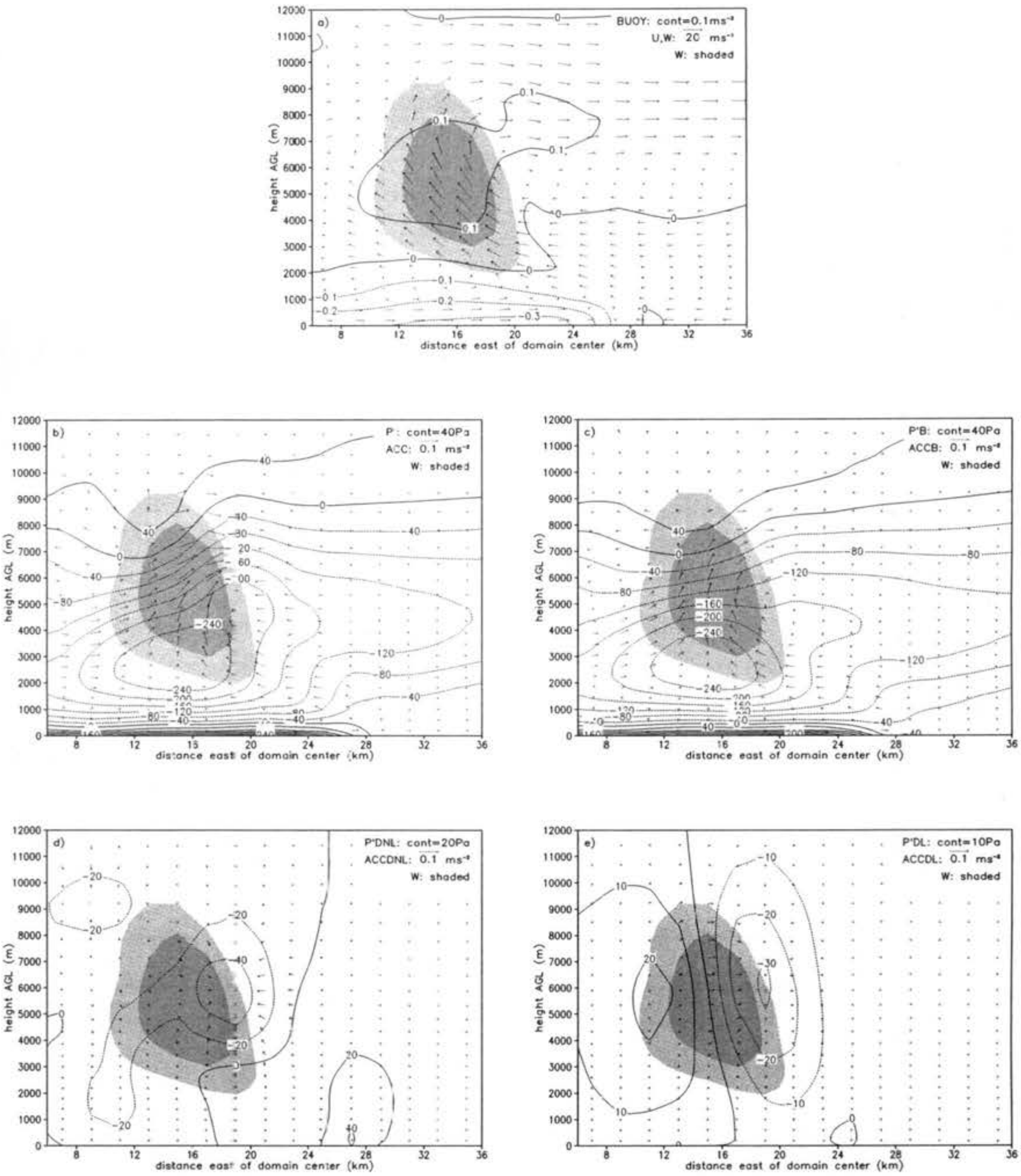

Figure 5.11: Mean velocities, perturbation pressures, and acceleration terms for periodic–3D simulation S=16, E=1, for y=249 km at 21600 s. a) $BUOY$ contoured, u and w vectors. b) P' contoured, ACC vectors. c) $P'B$ contoured, $ACCB$ vectors. d) $P'DNL$ contoured, $ACCDNL$ vectors. e) $P'DL$ contoured, $ACCDL$ vectors. Vertical velocity shaded in all panels: levels of shading are 5 and 10 m s^{-1}. Contour intervals and vector scales are shown for each panel, and vary among panels. Terms are defined in § 2.2.3.

S=16, E=1, for y=167 km at 21600 s

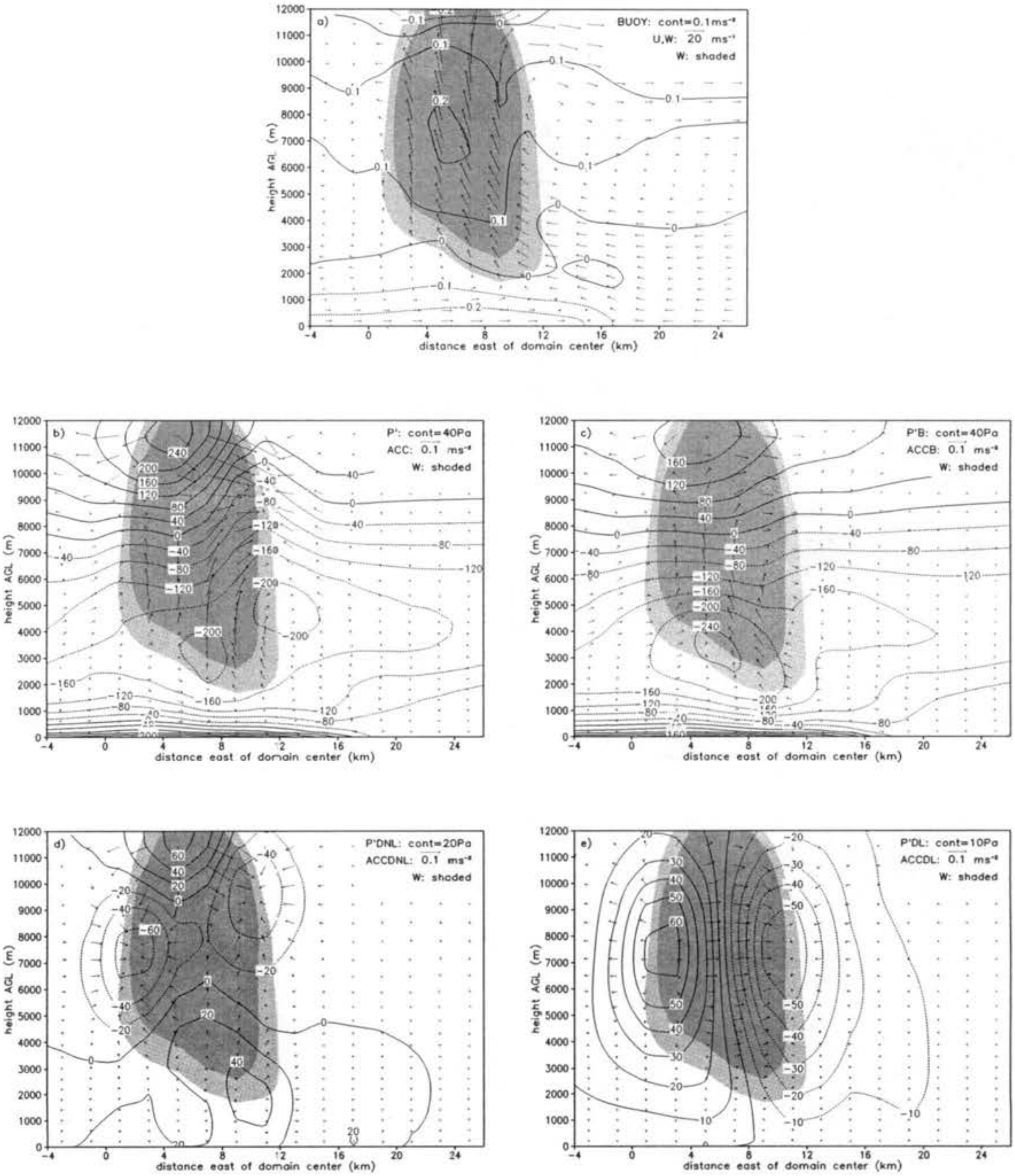

Figure 5.12: Mean velocities, perturbation pressures, and acceleration terms for periodic–3D simulation S=16, E=1, for y=167 km at 21600 s. a) $BUOY$ contoured, u and w vectors. b) P' contoured, ACC vectors. c) $P'B$ contoured, $ACCB$ vectors. d) $P'DNL$ contoured, $ACCDNL$ vectors. e) $P'DL$ contoured, $ACCDL$ vectors. Vertical velocity shaded in all panels: levels of shading are 5 and 10 m s^{-1}. Contour intervals and vector scales are shown for each panel, and vary among panels. Terms are defined in § 2.2.3.

tical gradient in p'_B opposes less of the buoyancy field. Following Soong and Ogura (1973), Yau (1979), and Schlesinger (1984), in 2D the p'_B field cancels about $\frac{1}{2} - \frac{2}{3}$ of the buoyancy force, while in 3D the p'_B field cancels about $\frac{1}{4} - \frac{1}{3}$ of the buoyancy force (in the 1D hydrostatic limit, 100% is cancelled). As might be anticipated, this yields a positive feedback. A greater upward ACCB in 3D yields a stronger updraft, which in turn implies a greater total condensation rate and therefore additional updraft buoyancy. Hence, most 3D updrafts have considerably larger magnitudes for buoyancy, w, and upward ACCB (cf. Fig. 5.12 versus figures in § 5.1).

The effects of increased updraft strength upon accelerations are evident in Fig. 5.12. Owing to the large and generally unopposed updraft buoyancy, ACCB within the strong 3D updraft is nearly vertical (Fig. 5.12c), and accounts for a comparatively small downshear acceleration (owing to the mesoscale buoyancy gradients) which is localized to the updraft's extreme downshear edge. Because the updraft is nearly vertical, and the radius of flow curvature on the downshear side is quite large, a minimum in P'DNL is not specifically favored on the updraft's downshear side (Fig. 5.12d). Instead, a quasi–symmetrical pair of P'DNL minima occur, much as in Fig. 3.1E. Hence, ACCDNL doesn't contribute any appreciable downshear acceleration to updraft air throughout most of the depth of the updraft. Indeed, the main signature of ACCDNL is forcing for cloud–top divergence owing to a pressure maximum in the deceleration zone at the top of the updraft. As might be anticipated for a stronger updraft, the downshear ACCDL is much larger (Fig. 5.12e), and accounts for almost all of the downshear accelerations imposed on air parcels that ascend in the updraft. It should be emphasized, however, that in extremely strong updrafts the parcel timescale is correspondingly shorter, so that the enhanced ACCDL has less time to act. The net result is that the updraft is erect throughout most of its depth, and the bulk of the downshear accelerations experienced by updraft air parcels occur very near the updraft's top (Fig. 5.12b), where the parcels are moving upward much less rapidly and where all three components of horizontal acceleration contribute in tandem.

Although more detailed analyses could certainly further differentiate 2D from 3D dynamics, much of this was already covered by Schlesinger (1984), and will not be repeated here. A fair question is to ask whether the detailed discussion of § 5.1 was truly warranted given the apparent dissimilarity of most 2D updrafts from those in the periodic–3D simulations. Although this section did not show a similarly detailed temporal analysis for the 3D simulations, the important overarching insights from § 5.1 are unchanged in 3D. In particular, the 3D simulations exhibit updrafts in which the air parcels overturn owing to a combination of ACCB, ACCDNL, and ACCDL, rendering a leading precipitation zone. More importantly, the 3D simulations exhibit similar periodic behavior to the 2D simulations, and for very similar reasons (the updraft–cutoff–outflow cycle described in the summary of § 5.1). Therefore, this section stands together with § 5.1 as a fairly comprehensive description of the air parcel accelerations and periodic behaviors of updrafts in both the 2D and periodic–3D FFLS systems.

Chapter 6

APPLICABILITY OF SQUALL LINE THEORY TO CONVECTIVE LINES WITH LEADING PRECIPITATION

Much theoretical work on squall lines has been published, although most of it evolved from studies of FFTS systems. Section 6.1 compares the parcel acceleration analysis of FFLS systems (i.e. Chapters 3 and 5) to Rotunno et al. (1988)'s horizontal vorticity theory for squall lines. Section 6.2 then notes the similarities of the FFLS mean circulations to one of Liu and Moncrieff (1996)'s theoretical models; this is convenient, because it provides an opportunity to discuss the meaning of the steady state. Section 6.3 provides a final note about the possible applicability of gravity wave theory to the present simulations.

6.1 RKW theory: an acceleration–based perspective

Horizontal vorticity framework and the RKW interpretation

The theory for long–lived squall lines proposed by Rotunno et al. (1988), and often called "RKW theory" after the names of its authors, invokes a balance of horizontal vorticity to explain the character and evolution of updrafts in 2D squall lines. It is widely applied, and its omission from a paper on squall line dynamics would be conspicuous. To begin, recall that the $\hat{x}$ and $\hat{z}$ components of (2.9) for an invsicid, irrotational 2D flow are:

$$\frac{Du}{Dt} = -\frac{1}{\rho_o}\frac{\partial p'}{\partial x}, \tag{6.1}$$

$$\frac{Dw}{Dt} = -\frac{1}{\rho_o}\frac{\partial p'}{\partial z} + B, \tag{6.2}$$

wherein $B \equiv -g\rho'/\rho_o$. Cross–differentiating $\partial/\partial z$(6.1) – $\partial/\partial x$(6.2) then produces a prognostic equation for horizontal vorticity in 2D:

$$\frac{D}{Dt}\left(\frac{\partial u}{\partial z} - \frac{\partial w}{\partial z}\right) = \frac{D\eta}{Dt} = -\eta\left(\frac{\partial u}{\partial x} + \frac{\partial w}{\partial z}\right) - \frac{\partial B}{\partial x} + \frac{1}{\rho_o^2}\frac{d\rho_o}{dz}\frac{\partial p'}{\partial x}. \tag{6.3}$$

The third term on the right–hand–side of (6.3), involving the vertical gradient of the base state density, was small in every instance investigated for this study, so it will be neglected. In addition, the first term on the right–hand–side of (6.3), involving the convergence or divergence of horizontal vorticity, was almost always an order of magnitude smaller than the second term, which involves generation by horizontal buoyancy gradients. Not only is it generally true that $|\eta \cdot \mathrm{div}| << |\partial B/\partial x|$, but also the shape of the $\partial B/\partial x$ field far more closely resembles the shape of the $D\eta/Dt$ field during times when $D\eta/Dt$ is non–trivial. Accordingly, to a very good approximation the governing vorticity dynamics for 2D simulations are described by:

$$\frac{D\eta}{Dt} \approx -\frac{\partial B}{\partial x}. \tag{6.4}$$

The primary interpretations of Rotunno et al. (1988) follow from (6.4). Although this exceedingly simple equation apparently omits many of the complicated processes involved in convection, it is a good approximation to (6.3), which was derived from first principles with several reasonable assumptions. Rotunno et al. (1988) argued that a balance between the environment's low–level vertical wind shear and the strength of the surface cold pool determines whether air parcels in systems' updrafts ascend vertically or in trajectories that curl forward or rearward. The basis for their claim is that, from (6.4), inflowing air has some characteristic η associated with the sheared background state, and then gains or loses some additional η on passing through a horizontal buoyancy gradient as it approaches and ascends over the cold pool. Accordingly, the vertical wind shear and the cold pool strength directly contribute to an air parcel's final η.

Problems with a horizontal vorticity framework and the RKW interpretation

Various authors have pointed out shortcomings of the Rotunno et al. (1988) local balance interpretation, especially that it omits system–scale vorticity generation (Lafore and Moncrieff 1989) and omits contributions from water loading and warming (Nicholls et al. 1988). Nevertheless, these arguments should not be taken as indictments of the correctness of (6.3) and its approximation (6.4). Rather, these arguments concern sources and sinks for horizontal vorticity that are not local to the interface of the inflow with an outflow boundary. They do not significantly undermine the application of RKW theory in an undisturbed environment.

However, a serious difficulty with the approach given by (6.3) and (6.4), and embodied by RKW theory, is that an individual air parcel's vorticity does not uniquely determine its velocity. Hence, although (6.4) is an accurate depiction of an air parcel's vorticity dynamics, the Rotunno et al. (1988) parcel–based interpretation is dubious because individual parcels' vorticities do not unambiguously determine the shapes of their trajectories (and hence the tilt of an updraft). Notably, if a fluid flow is nondivergent, both the velocity components and the vorticity can be expressed in terms of a streamfunction, ψ:

$$u = \frac{\partial \psi}{\partial z}, \tag{6.5}$$

$$w = -\frac{\partial \psi}{\partial x}, \tag{6.6}$$

$$\eta = \frac{\partial^2 \psi}{\partial x^2} + \frac{\partial^2 \psi}{\partial z^2}. \tag{6.7}$$

So, by globally predicting η in an Eulerian framework with (6.4), one could then retrieve the full velocity field by applying (6.5)–(6.7) with appropriate boundary conditions. However, there is no analogous way to solve for the velocity of an individual parcel in the Lagrangian framework. Therefore, (6.4) cannot describe the shape of an updraft parcel's trajectory unless it is integrated over a large domain and then used to solve for local velocity components. Because of the importance of air parcels' paths to this publication (recall § 2.2.4), the following section reinterprets RKW theory in terms of air parcels' accelerations as they pass near an outflow boundary and are lifted.

Acceleration vs. horizontal vorticity frameworks for developing convective systems

According to RKW theory, the strength and tilt of an updraft are functions of the balance between the strength of the lower tropospheric wind shear and the strength of a surface cold pool. From an acceleration point of view, this balance occurs primarily between the ACCB and ACCDL components associated with the cold pool and low–level shear (terms A and C, respectively, in Fig. 3.1), with an additional contribution from P'DNL owing to the cold pool's circulation (term D in Fig. 3.1). In this way of thinking, an air parcel's u and w as it ascends above 3 km AGL is determined by the integrated accelerations experienced below 3 km AGL. Therefore, the interaction between the cold pool and the low–level wind shear should have an important effect on the tilting of air parcel trajectories in the lower and middle troposphere, which is the basic claim of RKW theory.

Four additional simulation, under special circumstances, provided a simple test of the applicability of RKW theory to developing convective systems with leading precipitation. Each 2D simulation was set up as described in § 2.1.4 and then run for 30 minutes with all moist processes disabled, in order to allow the initial cold pool perturbation to establish a circulation and assume a realistic shape. Thereafter, the simulations included moist processes. The following analyses then concerned the first few convective cells that developed. This enabled an investigation of the basic physics of the convective initiation process without the complicating effects of a mature system that perturbs the wind and thermal fields. The control environment for this experiment was the same as for the control FFLS simulation described in § 2.1.4, and is here called S=16, LLS*1, CP=–3.2. The first variation was a simulation in which the 3–10 km wind shear was removed; it is called S=0, LLS*1, CP=–3.2. The second variation was a simulation in which the low–level wind shear was doubled; it is called S=16, LLS*2, CP=–3.2. The third variation was a simulation in which the strength of the initial cold pool was tripled; it is called S=16, LLS*1, CP=–9.6.

Notably, the CP=–9.6 variation failed to produce deep convective cells. Instead, it produced a quasi–steady shallow updraft that tilted strongly rearward just above the surface outflow boundary (Fig. 6.1a). The downshear–directed ACCDL associated with lower tropospheric wind shear (Fig. 6.1e, note that vectors for ACCDL are exaggerated by a factor of 5) was insufficient to counteract the significant upshear acceleration provided by the cold pool's ACCB and ACCDNL (Fig. 6.1c,d). Eventually, as parcels moved rearward over the cold pool nose, they were accelerated strongly downward owing to their negative buoyancy (Fig. 6.1c) and to the vertical gradient in P'DNL (Fig. 6.1d). The net acceleration vectors (Fig. 6.1b) make it fairly clear that, in this case, inflow air parcels have very little chance to attain their LFCs. This is in accordance with RKW theory, which predicts that a strong cold pool will baroclinically generate excessive negative η in inflowing air, and therefore will not produce deep upright lifting in the absence of significant positive environmental η. However, because vorticity does not uniquely determine an air parcel's velocity, it is more physical to say instead that ACCB and ACCDNL overwhelmed ACCDL.

For the simulations that produced deep convection, the tilt of updraft parcels' trajectories was roughly consistent with the balance between the lower tropospheric wind shear and the surface cold pool strength, as predicted by RKW theory. The control and S=0 simulations (both with LLS*1) produced fairly erect updraft trajectories (Fig. 6.2a,b), whereas the LLS*2 simulation produced updraft trajectories that tilted more strongly downshear (Fig. 6.2c). The primary reason for this is the increased ACCDL provided by the enhanced lower tropospheric shear in the LLS*2 simulation. At the peak of their first low–level updrafts, the control and S=0 simulations are almost identical kinematically owing to their identical lower tropospheric wind profiles (not shown). The net downshear ACC in the LLS*2 simulation, by contrast, is larger and this increase in almost entirely attributable to the enhanced ACCDL (cf. Fig. 6.3 vs. Fig. 6.4, especially panels e). As they ascend into the middle troposphere, the updrafts in the LLS*2 simulation become weaker than those in the control simulation. This has an important effect, and will be discussed shortly.

Despite the obvious sensitivity to the lower tropospheric shear, processes below 3 km AGL don't completely determine the updrafts' tilts. The vertical wind shear in the 3–10 km AGL layer also plays a role, as seen by contrasting the overturning trajectories of the control simulation (Fig. 6.2a) with those from the S=0 simulation, many of which are nearly vertical or tilt slightly upshear (Fig. 6.2b). The reason for the stronger downshear accelerations in the control simulation, as compared to the S=0 simulation, is the ACCDL attributable to the updraft's interaction with the 3–10 km AGL environmental shear. Notably, once their updrafts penetrate into the 3–10 km layer, non–linearities begin to cause the control and S=0 simulations to diverge (cf. Figs. 6.5 and 6.6). The updrafts in the S=0 simulations are generally stronger due to decreased turbulent mixing (this

S=16, LLS*1, CP=–9.6, 1799 s

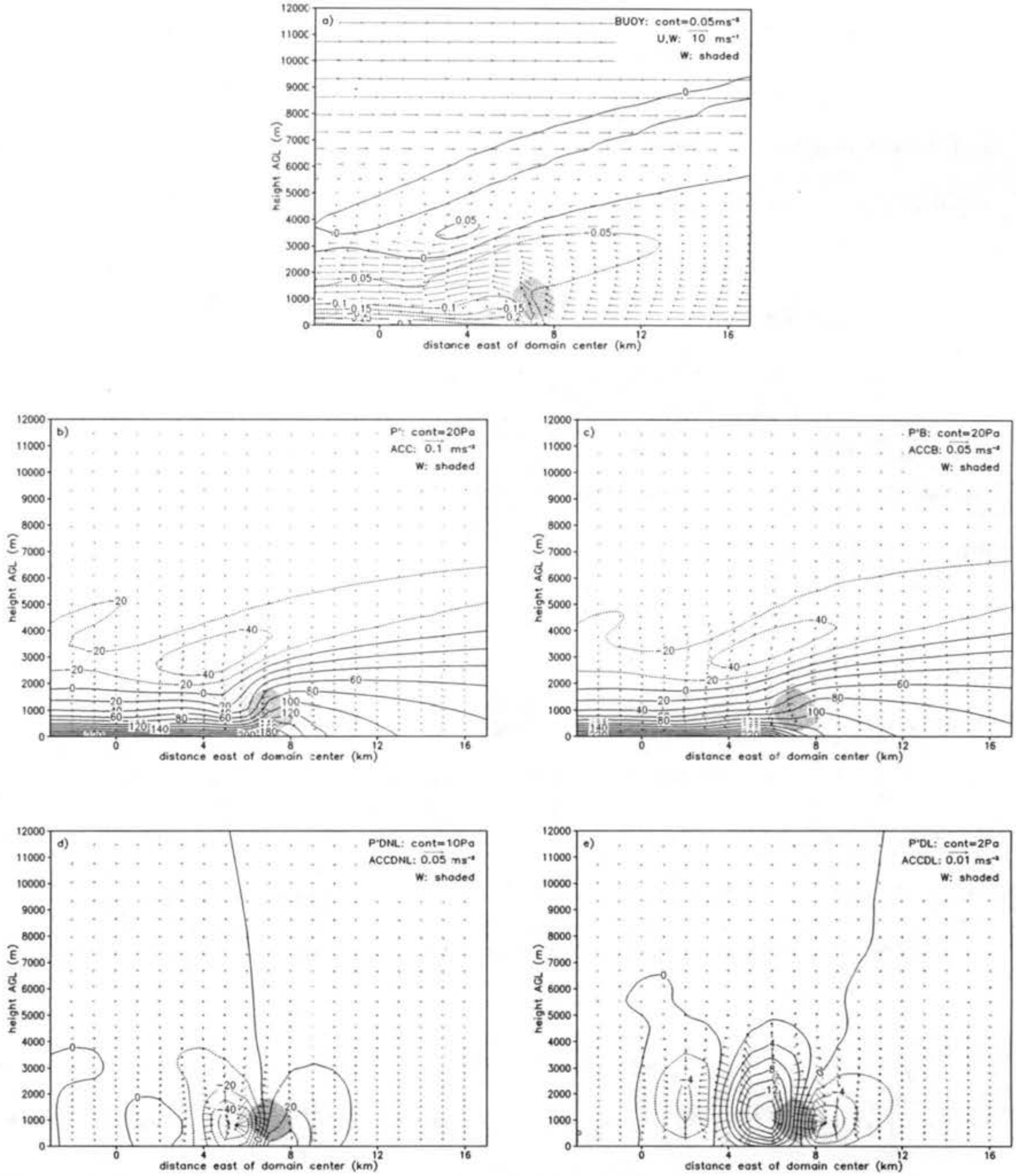

Figure 6.1: Mean velocities, perturbation pressures, and acceleration terms for simulation S=16, LLS*1, CP=–9.6, 1799 s. a) $BUOY$ contoured, u and w vectors. b) P' contoured, ACC vectors. c) $P'B$ contoured, $ACCB$ vectors. d) $P'DNL$ contoured, $ACCDNL$ vectors. e) $P'DL$ contoured, $ACCDL$ vectors. Vertical velocity shaded in all panels: levels of shading are 3 and 6 m s^{-1}. Contour intervals and vector scales are shown for each panel, and vary among panels. Terms are defined in § 2.2.3.

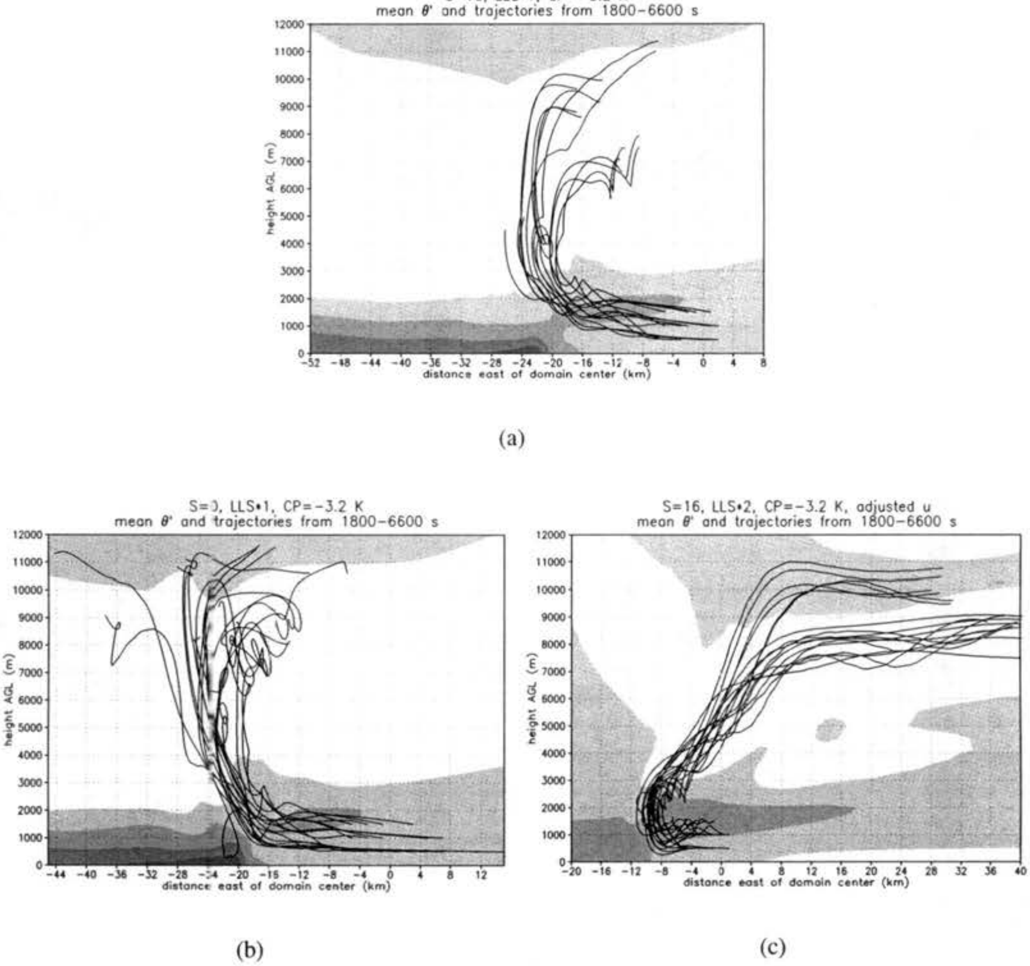

Figure 6.2: Temporally averaged perturbation potential temperature (shaded, levels are –3, –2, –1, and 0 K) and updraft trajectories for a) control simulation, b) S=0 experiment, c) LLS*2 experiment.

S=16, LLS*1, CP=–3.2 at 3822 s

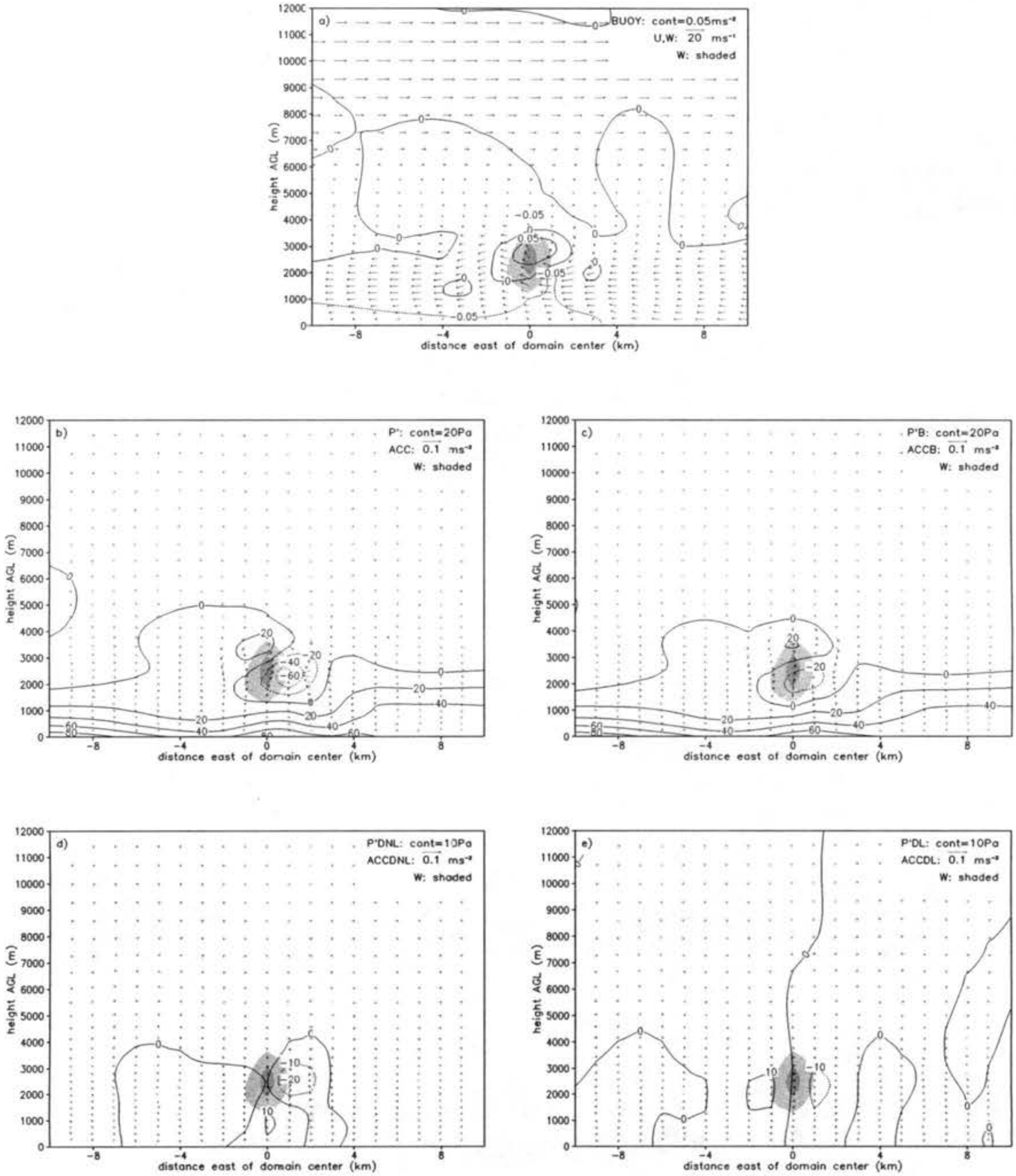

Figure 6.3: Velocities, perturbation pressures, and acceleration terms for simulation S=16, LLS*1, CP=–3.2 at 3822 s. a) $BUOY$ contoured, u and w vectors. b) P' contoured, ACC vectors. c) $P'B$ contoured, $ACCB$ vectors. d) $P'DNL$ contoured, $ACCDNL$ vectors. e) $P'DL$ contoured, $ACCDL$ vectors. Vertical velocity shaded in all panels: levels of shading are 3 and 6 m s^{-1}. Contour intervals and vector scales are shown for each panel, and vary among panels. Terms are defined in § 2.2.3.

S=16, LLS*2, CP=–3.2 at 3108 s

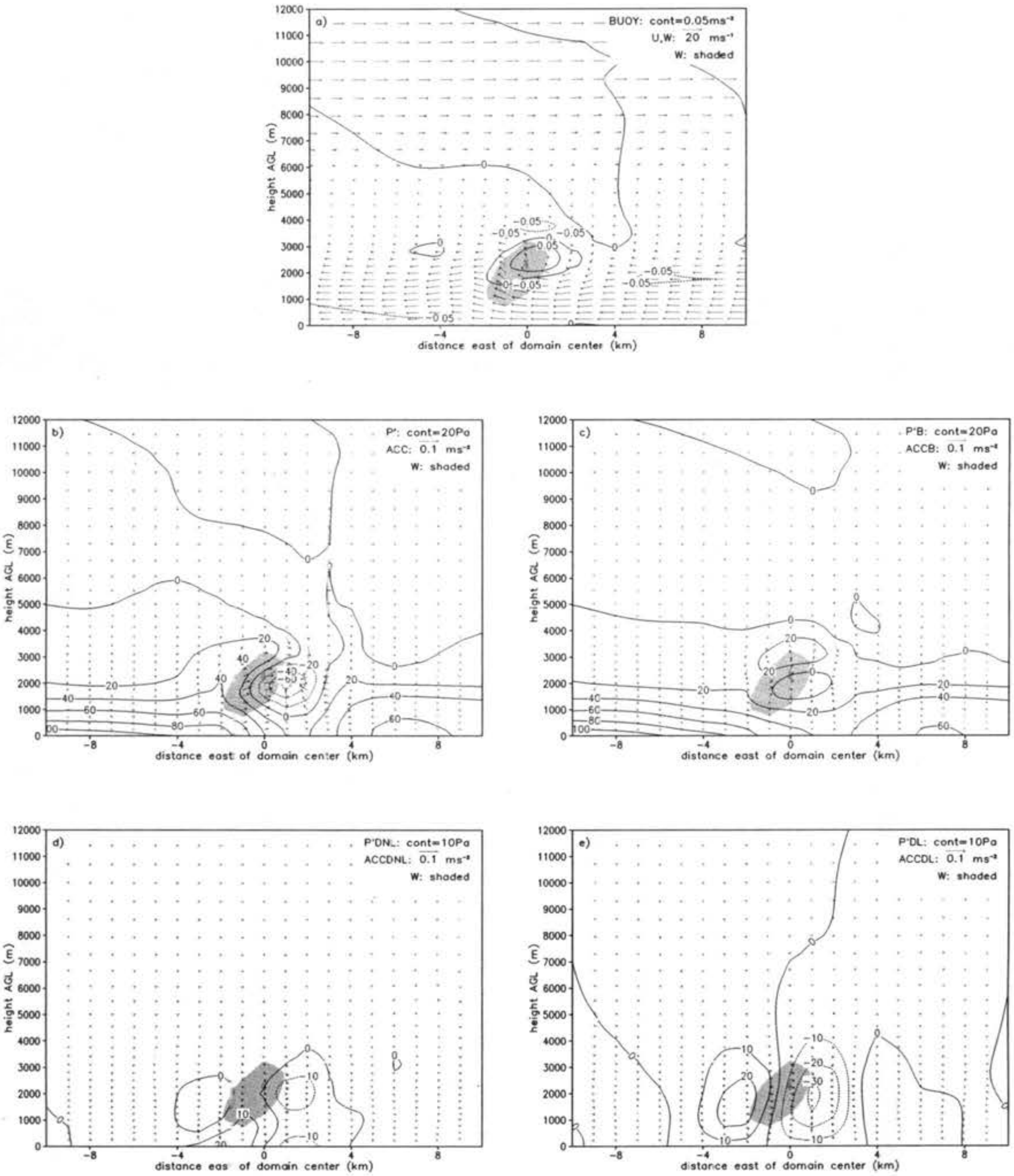

Figure 6.4: Velocities, perturbation pressures, and acceleration terms for simulation S=16, LLS*2, CP=–3.2 at 3108 s. a) $BUOY$ contoured, u and w vectors. b) P' contoured, ACC vectors. c) $P'B$ contoured, $ACCB$ vectors. d) $P'DNL$ contoured, $ACCDNL$ vectors. e) $P'DL$ contoured, $ACCDL$ vectors. Vertical velocity shaded in all panels: levels of shading are 3 and 6 m s^{-1}. Contour intervals and vector scales are shown for each panel, and vary among panels. Terms are defined in § 2.2.3.

is discussed in the next paragraph) and therefore the S=0 convection begins to perturb its environment more quickly, making simple graphical comparisons challenging. Nevertheless, Figs. 6.5 and 6.6 fairly accurately portray the basic differences. Above 3 km AGL, the downshear–directed ACCDL is much smaller in the S=0 run than in the control run (cf. Figs. 6.5e and 6.6e). However, ACCDNL compensates for this (cf. Figs. 6.5d and 6.6d) because the stronger updraft in the S=0 simulation implies greater horizontal vorticity on the updraft's eastern side.[1] This makes the total downshear ACC for the S=0 updraft quite close to that of the control run (cf. Figs. 6.5b and 6.6b). Even so, because of the weaker updrafts in the control run, the downshear accelerations have longer to act and therefore the integrated downshear accelerations are larger. Because ACCDL is the only downshear–directed acceleration component that is larger in the control simulation than in the S=0 simulation, the greater downshear tilt of the control run's updrafts is attributable to the contribution from ACCDL (owing to the greater environmental shear). For the sake of completeness, it should be noted that it is even more difficult to compare the accelerations in an active mature updraft from the LLS*2 case with those in the control case because the two simulations produce updrafts which deviate from one another so strongly in the lower troposphere. However, the accelerations in the 3–10 km AGL layer are qualitatively similar in the LLS*2 and control simulations (both with S=16), although the strength of the updraft in the LLS*2 simulation is weaker still (not shown).

As mentioned previously, when the updraft in the S=0 simulation ascends into the 3–10 km layer, it becomes stronger than that in the control simulation (compare the progressions in Fig. 6.7 and Fig. 6.8). This is largely attributable to a decrease in mixing. Without undergoing the lengthy derivation, the 2D prognostic equation for turbulence kinetic energy, $TKE(\equiv \overline{u'^2 + w'^2}/2)$, is [e.g. from Stull (1988)]:

$$\frac{\partial}{\partial t}\, TKE = -\overline{u'w'}\,\frac{\partial \bar{u}}{\partial z} + \overline{w'\theta_v'}\,\frac{g}{\bar{\theta}_v} - \text{transport} - \text{dissipation}. \tag{6.8}$$

All other things being equal, the first term on the right hand side of (6.8) causes the generation of

[1] P'DNL is not as strongly minimized on the western side because the flow is less vertical there owing to a front–to–rear airstream in the 2–4 km AGL layer (Fig. 6.6a). This front–to–rear flow stream comprises air parcels that did not attain their LFCs between the two pulses evident in Fig. 6.6 (one at $x = -20$ km, $z = 2.5$ km AGL, and the other at $x = -21$ km, $z = 5.5$ km AGL).

S=16, LLS*1, CP=–3.2, 4536 s

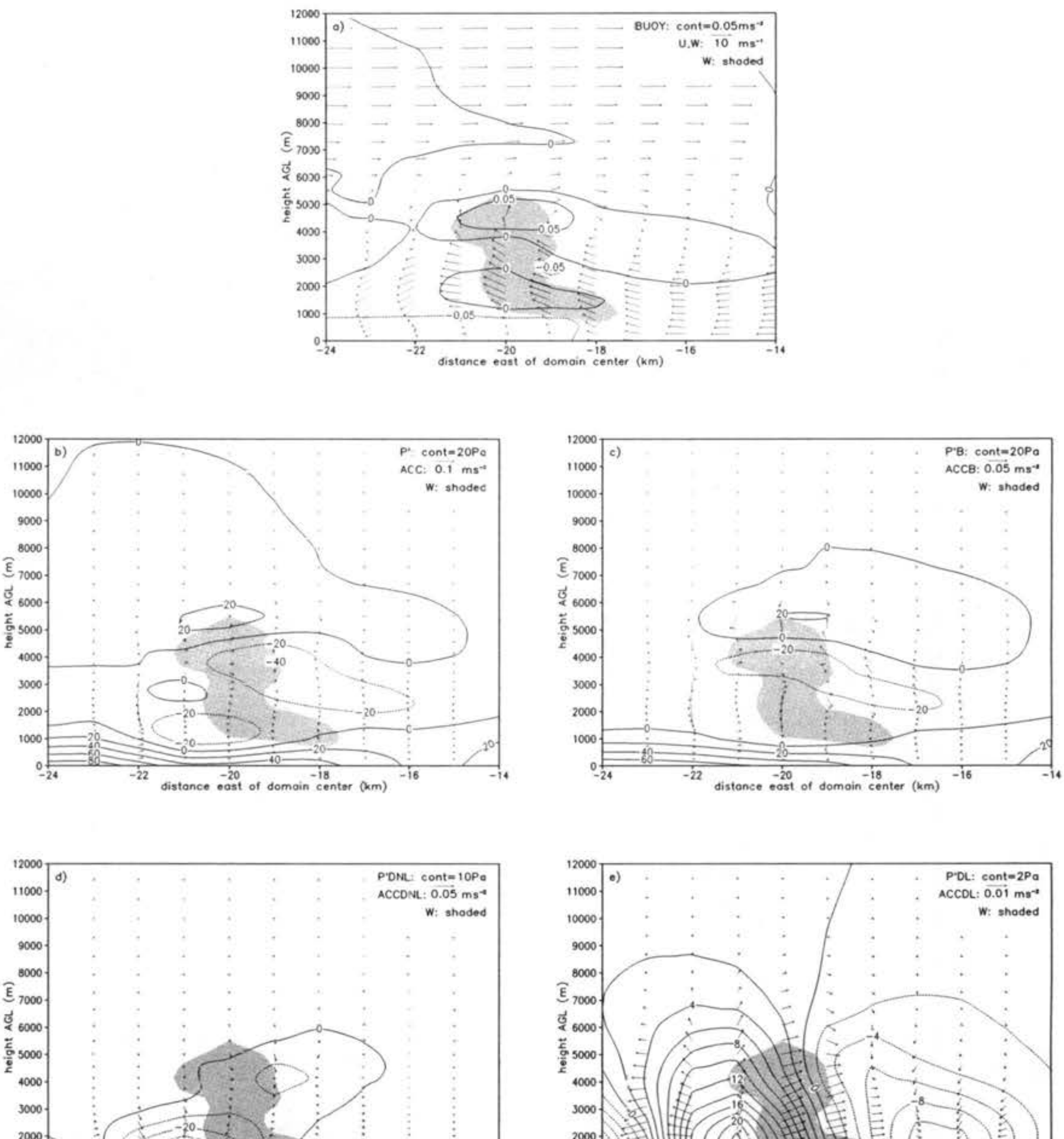

Figure 6.5: Mean velocities, perturbation pressures, and acceleration terms for simulation S=16, LLS*1, CP=–3.2, 4536 s. a) $BUOY$ contoured, u and w vectors. b) P' contoured, ACC vectors. c) $P'B$ contoured, $ACCB$ vectors. d) $P'DNL$ contoured, $ACCDNL$ vectors. e) $P'DL$ contoured, $ACCDL$ vectors. Vertical velocity shaded in all panels: levels of shading are 5 and 10 m s^{-1}. Contour intervals and vector scales are shown for each panel, and vary among panels. Terms are defined in § 2.2.3.

S=0, LLS*1, CP=–3.2, 4536 s

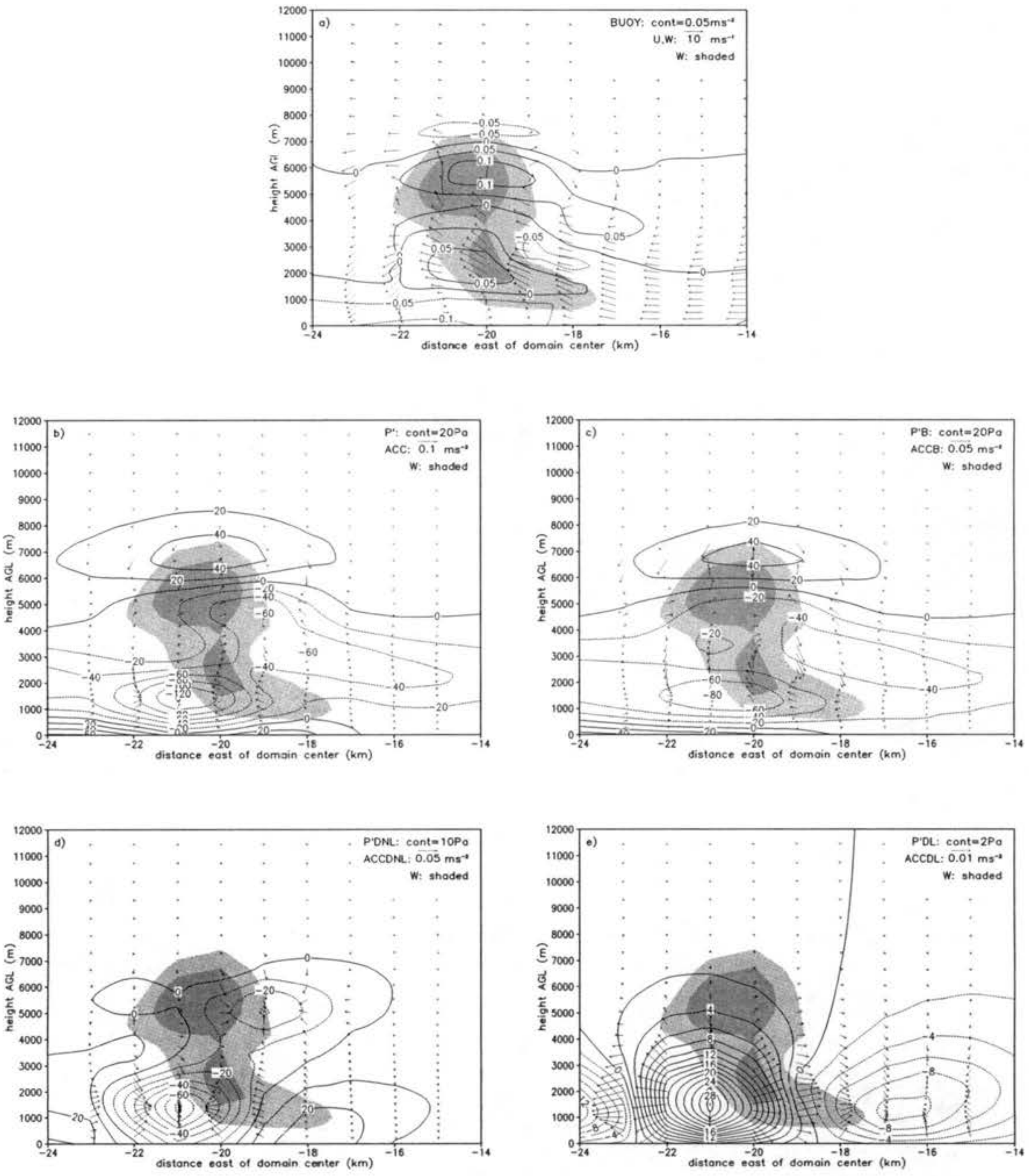

Figure 6.6: Mean velocities, perturbation pressures, and acceleration terms for simulation S=0, LLS*1, CP=–3.2, 4536 s. a) $BUOY$ contoured, u and w vectors. b) P' contoured, ACC vectors. c) $P'B$ contoured, $ACCB$ vectors. d) $P'DNL$ contoured, $ACCDNL$ vectors. e) $P'DL$ contoured, $ACCDL$ vectors. Vertical velocity shaded in all panels: levels of shading are 5 and 10 m s^{-1}. Contour intervals and vector scales are shown for each panel, and vary among panels. Terms are defined in § 2.2.3.

more turbulence in a fluid with increased vertical wind shear.[2] Turbulent mixing is detrimental to updraft strength because it constantly introduces dry environmental air into the saturated updraft, facilitating evaporative and sublimative cooling, and because it provides a deceleration to the updraft embodied by[3] :

$$\left(\frac{\partial w}{\partial t}\right)_{turbulent} = -u'\frac{\partial w'}{\partial x}. \tag{6.9}$$

Hence, to summarize the previous two paragraphs, the effect of vertical wind shear is dual. Firstly, stronger wind shear provides a substantial increase in the downshear–directed ACCDL. And secondly, increased wind shear weakens updrafts via mixing, thereby providing a longer time over which the downshear accelerations are applied.

The important downshear ACCDL owing to wind shear in the middle troposphere is not accounted for by RKW theory. The mean value of η in the control updraft *does* increase with respect to that in the S=0 simulation (cf. Figs. 6.7 and Fig. 6.8) as it ascends in the middle troposphere, although this is partly masked by the vorticity couplet that flanks the updrafts. The only thing in (6.4) that can account for the enhanced η of the control simulation's updraft core is mixing (i.e. non–linear advection) of η from the midlevels of the environment.[4] Of course this is clearly a local process, not related to the low–level shear and cold pool (and therefore contrary to RKW theory). The horizontal vorticity perspective also presents a difficulty because air parcels on both flanks of the updraft plume execute very similar trajectories through the depth of the troposphere (see Fig. 6.2) despite the fact that parcels on opposite sides of the updraft possess opposite–signed horizontal vorticity (Figs. 6.7 and 6.8) as a result of baroclinic generation by the buoyant updraft itself. This points yet again to the problem of trying to infer velocities from an air parcel's η. As this section has argued, the most physical way to understand the process is via accelerations, which are different in the control and S=0 simulations wholly because of environmental differences above

[2] Because the model's sub–gridscale mixing is a function of TKE, this is a good way to understand both the physical and numerical problem.

[3] Notably, in the simulations this turbulent drag effect was parameterized on the resolved scales as a function of TKE.

[4] It may not apparent that "mixing" is present in (6.4). However, because we presume (6.4) to be valid on all scales above the inertial subrange, on larger scales "mixing" really refers to unresolved advection [which nevertheless obeys (6.4)].

S=16, LLS*1, CP=–3.2

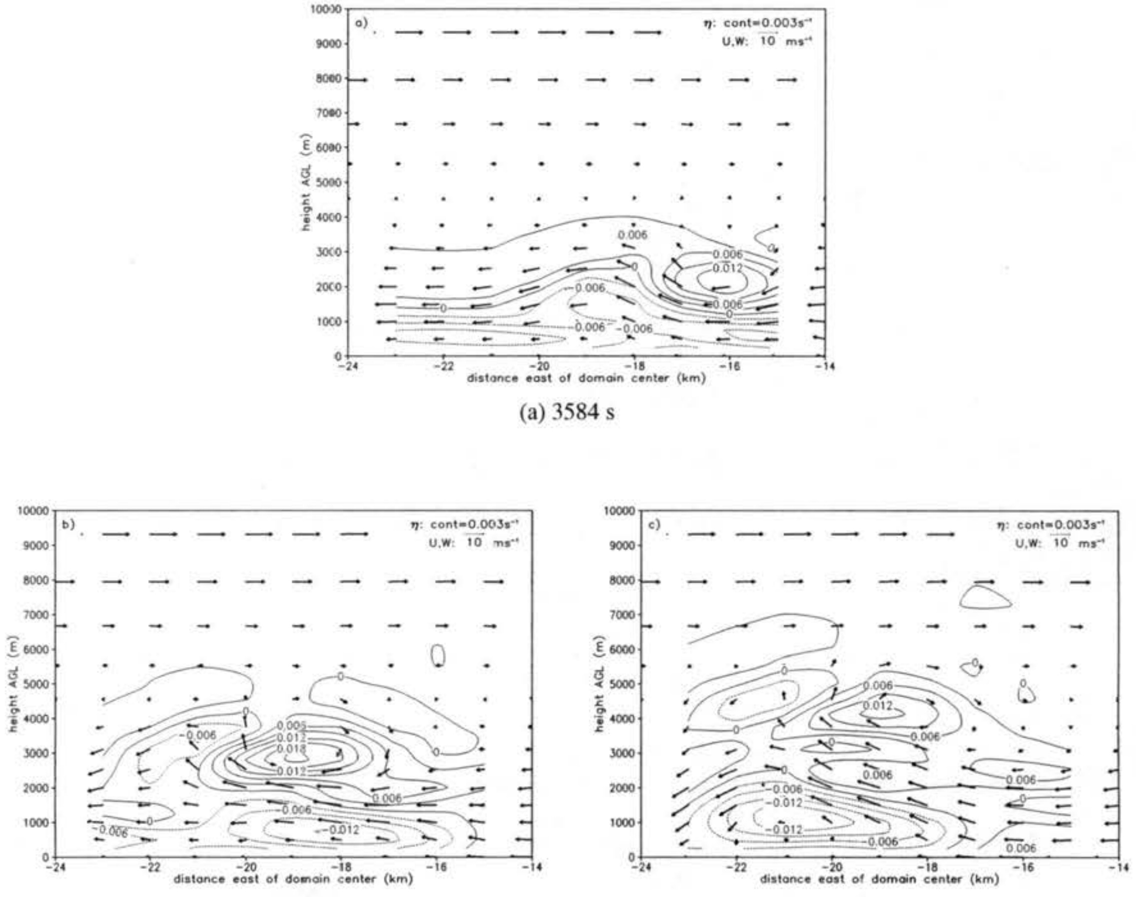

(a) 3584 s

(b) 4060 s

(c) 4536 s

Figure 6.7: Horizontal vorticity (contoured, interval=3 $\times$ 10^{-3} s^{-1}) and velocity vectors (ms^{-1}, scaled as shown) for the control simulation. a) at 3584 s, b) at 4060 s, c) at 4536 s.

3 km AGL. Section 7.1 again takes up the basic tenets of RKW theory, and further addresses the importance of the 3–10 km wind shear from a macroscale (rather than a parcel) perspective.

6.2 Comparison of the front–fed LS system's mean flow to 2D theoretical flow models

Chapter 5 argued that the convective transients in the simulated FFLS systems are very dynamically important, and are very different from the mean state. It is now appropriate to ask:

S=0, LLS*1, CP=–3.2

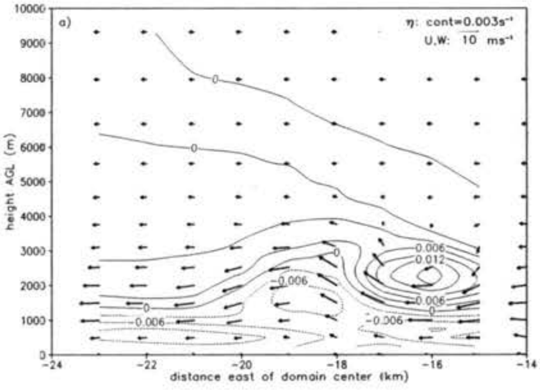

(a) 3584 s

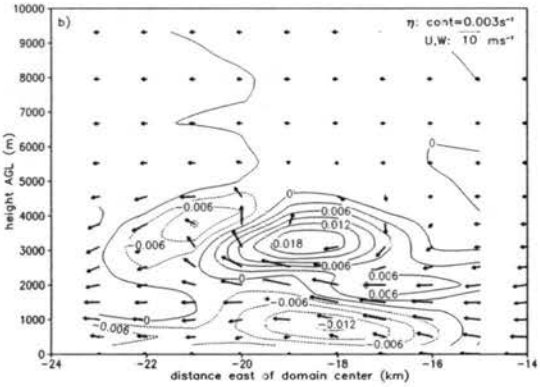

(b) 4060 s

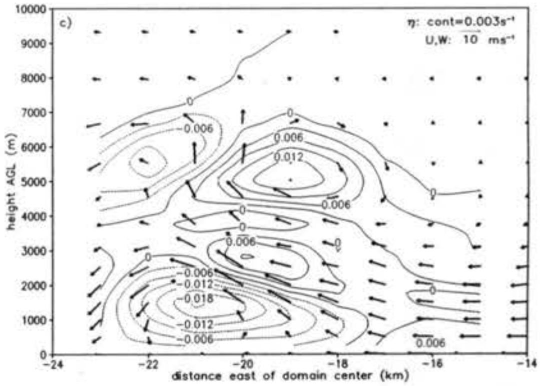

(c) 4536 s

Figure 6.8: Horizontal vorticity (contoured, interval=3 $\times$ 10^{-3} s^{-1}) and velocity vectors (ms^{-1}, scaled as shown) for the S=0 experiment. a) at 3584 s, b) at 4060 s, c) at 4536 s.

what, then, does the mean state represent?

As introduced in § 1.2, Moncrieff and various coauthors have produced analytic steady–state solutions for the flow structures of density currents and squall lines [e.g. Moncrieff (1992), Liu and Moncrieff (1996)]. Convective lines with trailing precipitation are known to have a temporally averaged line-perpendicular structure similar to that in Fig. 1.10. In contrast, the temporally averaged airflow structure of the simulated quasi–2D FFLS systems (e.g. Fig. 4.3) bears great resemblance to the Liu and Moncrieff (1996) analytic density current models depicted in Fig. 1.11. This result is interesting because, according to Dr. Mitchell Moncrieff (personal communication), FFLS MCSs are probably the only convective phenomena that possess such a structure. The steady state analytic models also provide beneficial insight into the mesoscale momentum fluxes by organized convection, and have the positive attribute that they predict different organizational modes for different system speeds (largely consistent with the interpretation of the FFLS to FFTS transition in Section 7.2). This section describes the qualitative similarities between the simulated FFLS systems and Liu and Moncrieff (1996)'s analytic solutions. Thereafter, it describes physically why the mean state exists and what it implies about the convection's effect on the environmental flow. In a sense, as inspired by, Moncrieff and Klinker (1997), this is a discussion about how FFLS systems ought to be parameterized.

For the times depicted in Figs. 4.3 and 4.7, the line–perpendicular system speeds were 2.0 m s^{-1} for the 2D simulation and 2.4 m s^{-1} for the periodic–3D simulation. In other words, the wind vectors in Figs. 4.3 and 4.7 are approximately storm–relative. Both plots (Figs. 4.3 and 4.7) depict mean states. However, in the 2D simulation the "along–line mean" for the infinitely long line is temporally varying. In contrast, for the periodic–3D simulation the along–line mean is approximately temporally invariant because the convective line always possesses a statistically similar distribution of active convective cells and inactive gaps (see, for example, Fig. 4.6). As described in § 4.1, air can flow through the periodic–3D line; therefore, its mean state does not exhibit a stagnation zone on the system's upshear side. However, its other mean state flow features are quite similar to those of the 2D case. For brevity, this section only addresses the mean state of the 2D simulations; these arguments also apply to periodic–3D FFLS systems with the notable exception that there are no stagnation zones on the 3D systems' upshear sides.

The mean flow in the 2D simulations comprises an overturning updraft (Fig. 4.3). Interestingly, trajectory and streamline analyses reveal that although lower tropospheric air parcels participate in the deep updrafts of the temporally varying flow (e.g. Fig. 4.4), in the mean state the overturning updraft is decoupled from the lower troposphere (Fig. 6.9). Inflowing air below approximately 3 km AGL rises slightly as it nears the surface outflow (whose head is marked by a small patch of stagnant storm–relative air), then moves rearward in a relatively uninterrupted band (Fig. 6.9).[5] The center of curvature for the overturning flow branch is at about 6.5 km AGL, and the overturning updraft therefore comprises air that flows westward into the system between about 3 and 6.5 km AGL (Fig. 6.9). The outflow from the overturning updraft in the 2D simulations is between about 6.5 and 11 km AGL, above which a rear–to–front airstream exists which is nearly decoupled from the overturning draft (Fig. 6.9). The final interesting phenomenon, as initally described in § 4.1, is a region of storm–relative stagnation in the middle and upper troposphere on the upshear side of the FFLS system.[6] The correspondence of these flow branches and stagnation zones to the analytic model shown in Fig. 1.11a is quite clear. Additionally, if we ignore the flow above 11 km AGL, which is ostensibly decoupled from the other drafts, we can think of the storm–relative flow fields below 11 km AGL as corresponding to those shown in Fig. 1.11b. With respect to Liu and Moncrieff (1996)'s notation (as in Fig. 1.11a,b), $h_o \approx 3$ km (the critical streamline's height), $h^* \approx 6.5$ km (the height off the overturning draft's axis), and $H \approx 11$ km (the depth of the flow regime).

One consistent interpretation for the circulations in Figs. 1.11a and 6.9 is that they embody the steady state obtained by pulling a rigid box, with solid barriers representing the stagnation zones, through a fluid at some constant speed, c (Fig. 6.10). It is therefore perhaps surprising that a fluid flow varying dramatically in time (owing to the presence of alternately active and suppressed

[5] The lack of deep mean ascent for the lower tropospheric air reflects the averaging of both up and downdrafts there; these up and downdrafts can be inferred individually from the mass fluxes in Fig. 4.5.

[6] "Stagnation" is embodied by the disorganized streamlines to the west of x=-20 km and between about 5.5 and 11 km AGL in Fig. 6.9.

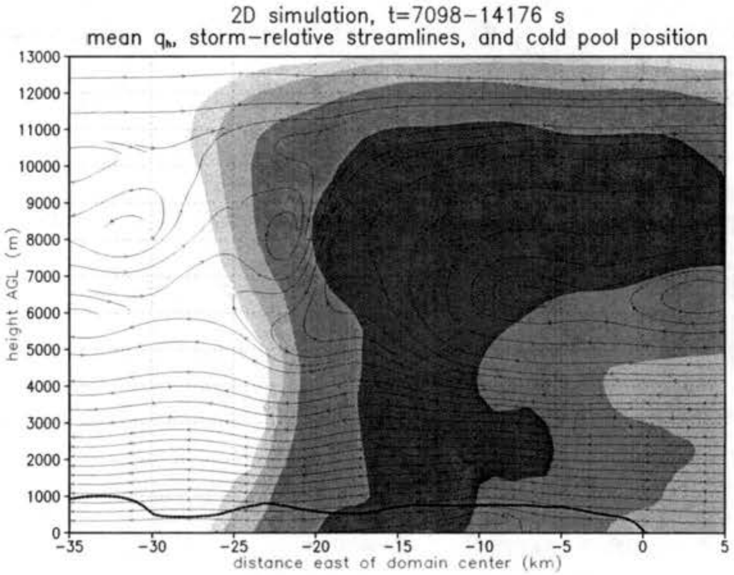

Figure 6.9: Mean hydrometeor mixing ratio (levels of shading are 0.02, 0.08, 0.32, and 1.28 g kg^{-1}), streamlines for mean storm–relative flow field, and mean surface cold pool position (heavy contour, which is the θ' = –3K isopleth) for the 2D control simulation, averaged from t=7098–14176 s.

convection), and periodically involving a great deal of latent heating, can exhibit a steady state in the same way that the very simple "rigid box" experiment would. Although, because of its highly temporally varying behavior, it is quite correct to say that the 2D FFLS system has no true steady state, the system does indeed perturb its environment in a mean sense (i.e. Fig. 6.9) much as the rigid box does.[7] In the real atmosphere there are no rigid boxes, and it must therefore be the pressure field that accounts for the appropriate accelerations and stagnation points for air that flows through the system [recall equation (2.8)]. In short, the transient convection perturbs the pressure field in a way that gives rise to the mean ("steady") flow fields in Fig. 6.9. The following text describes the FFLS steady state from the perspective of the mean flow, and then discusses the role of the transients.

Taking ($\rho\mathbf{u}\cdot$) the inviscid, irrotational form of (2.8) yields a kinetic energy equation:

$$\rho \frac{D}{Dt}\left(\frac{\mathbf{u}\cdot\mathbf{u}}{2}\right) = -\mathbf{u}\cdot\nabla p - \rho w g. \tag{6.10}$$

[7] This may be easier to understand in the periodic–3D case, for which the along–line mean does not vary with time. In this case, the mesoscale far field does not experience the 3D system as temporally varying.

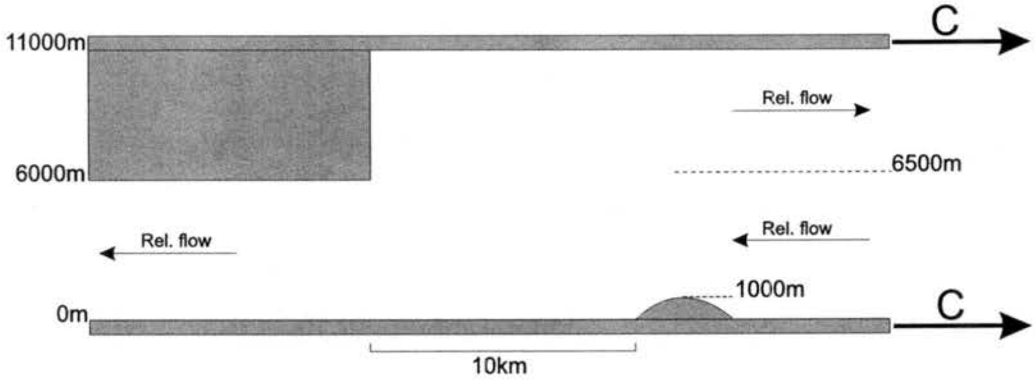

Figure 6.10: Schematic illustration of a rigid box that, when pulled through a fluid, would generate comparable circulations to the mean state produced by the 2D control simulation.

For a steady state, $\partial/\partial t = 0$, so that $D/Dt = \mathbf{u} \cdot \boldsymbol{\nabla}$, and (6.10) can be written:

$$\rho \frac{D}{Dt}\left(\frac{\mathbf{u} \cdot \mathbf{u}}{2}\right) = -\frac{Dp}{Dt} - \rho g \frac{Dz}{Dt}. \tag{6.11}$$

Therefore, by integrating along a Lagrangian trajectory and assuming incompressibility ($D\rho/Dt = 0$), (6.11) gives:

$$\rho \frac{\mathbf{u} \cdot \mathbf{u}}{2} + p + \rho g z = \text{constant}. \tag{6.12}$$

This is Bernoulli's equation, which is valid along a streamline in a steady state flow field. A special simplification for (6.12) is that of hydrostatic balance, in which case:

$$\frac{\partial p}{\partial z} = -\rho g, \tag{6.13}$$

and we are left with:

$$\frac{\partial}{\partial z}\left(\frac{1}{2}\rho\, \mathbf{u} \cdot \mathbf{u}\right) = 0. \tag{6.14}$$

In words, for the special case of a hydrostatic steady state, kinetic energy is conserved along an ascending streamline. This is relevant to the FFLS system because the inflow above 3 km AGL exhibited very little convective available potential energy (CAPE); depending upon the method of computation, the overturning flow branch had between 0 and 14 J kg^{-1} of CAPE. According to (6.14), however, the mean flow field's overturning updraft can exist and be maintained without CAPE owing solely to the kinetic energy of the inflowing air. Therefore, although the deep, transient overturning updrafts do indeed release CAPE, the temporally averaged flow fields do not necessarily require it. Additionally, (6.12) also reveals that, in the simplified steady state, kinetic energy and pressure perturbations change along a streamline in a compensating way. This is a manifestation of the pressure gradient acceleration: as air following the steady state streamlines crosses isobars toward lower pressure it is accelerated (or, toward higher pressure it is decelerated), hence the first two terms of (6.12) maintain a dynamic balance with one another. As a result, the mean pressure field can be regarded as both being entirely consistent with the mean flow field and as mechanically maintaining the mean flow field.

To a high degree this relationship is evident in the mean state pressure and wind fields of the 2D simulation (Fig. 6.11). The stagnation zone on the system's upshear side is roughly coincident with a region of maximized pressure and comparatively weak horizontal pressure gradient (Fig. 6.11). The dynamic balance implied by (6.12) is also evident: as the air following the streamlines in the overturning draft crosses isobars toward higher pressure it slows (this slowing is embodied by the spreading of the streamlines in Fig. 6.11; also recall Fig. 4.3). Because the steady state pressure field mechanically determines the steady state flow field, as suggested above, we can consider the pressure field to act much like the solid barriers in the rigid box experiment (recall Fig. 6.10). The storm–relative flow field impinges on the steady state pressure field (or the rigid box) and what results is a mean flow field that satisfies (6.12), subject to its simplifications. Therefore, an appropriate question is: what gives rise to the steady state pressure field? The answer lies with the transient convective overturning.

As is discussed in Chapter 3, individual convective updrafts perturb the pressure field owing both to their wind perturbations and to their attendant buoyancy fields. In time, a succession of convective updrafts generates a region of positive buoyancy in the middle and upper troposphere (Fig. 6.12a). This occurs largely because of the latent heating owing to phase changes. The transient convective updrafts embody intense localized heating. On longer time scales, however, the leading precipitation region is at least as important. Buoyant air parcels and their total water content are detrained from the updrafts and move forward into the pre–line anvil and precipitation plume (recall

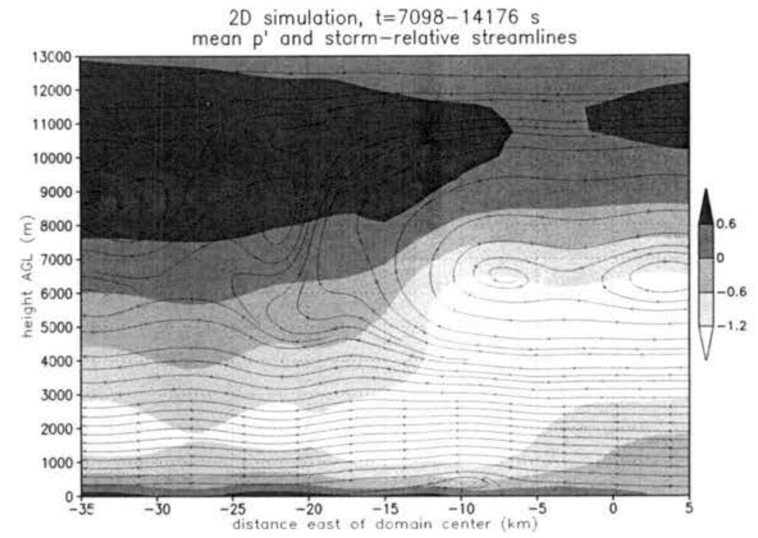

Figure 6.11: Mean pressure perturbation (hPa, shaded as shown) and streamlines for mean storm–relative flow field as in Fig. 6.9 for the 2D control simulation, averaged from t=7098–14176 s.

Section 2.2.4). In addition to carrying their perturbed, comparatively high temperatures with them, these air parcels may also experience a small amount of additional heating owing to deposition of vapor onto ice crystals and snow in the stratiform region [as described in FFTS systems by Rutledge and Houze (1987)]. As a result, a mesoscale region of buoyant middle and upper tropospheric air develops on the downshear side of the convective line in time (i.e. east of x=–15 km in Fig. 6.12a). Notably, however, the middle and upper troposphere have also been warmed on the upshear side of the convective system. The pressure field associated with a positive buoyancy anomaly causes subsidence nearby (for an illustration of this, see Fig. 3.1, B and G), which generally will propogate away as a gravity wave. However, when the heating is long–lived, the subsidence instead takes the form of a buoyancy bore because the local pressure field favors continual forcing for descent (until the local heating is removed). For the 2D simulation, the result of this buoyancy bore—or "wave of depression"—is net descent of the air on the upshear side of the convective line, with concomitant warming. Therefore, the long–lived convective and stratiform heating in the upper troposphere comprise a buoyancy anomaly on the downshear side of the convective line and generate a buoyancy anomaly on the upshear side of the convective line owing to propagating subisdence.

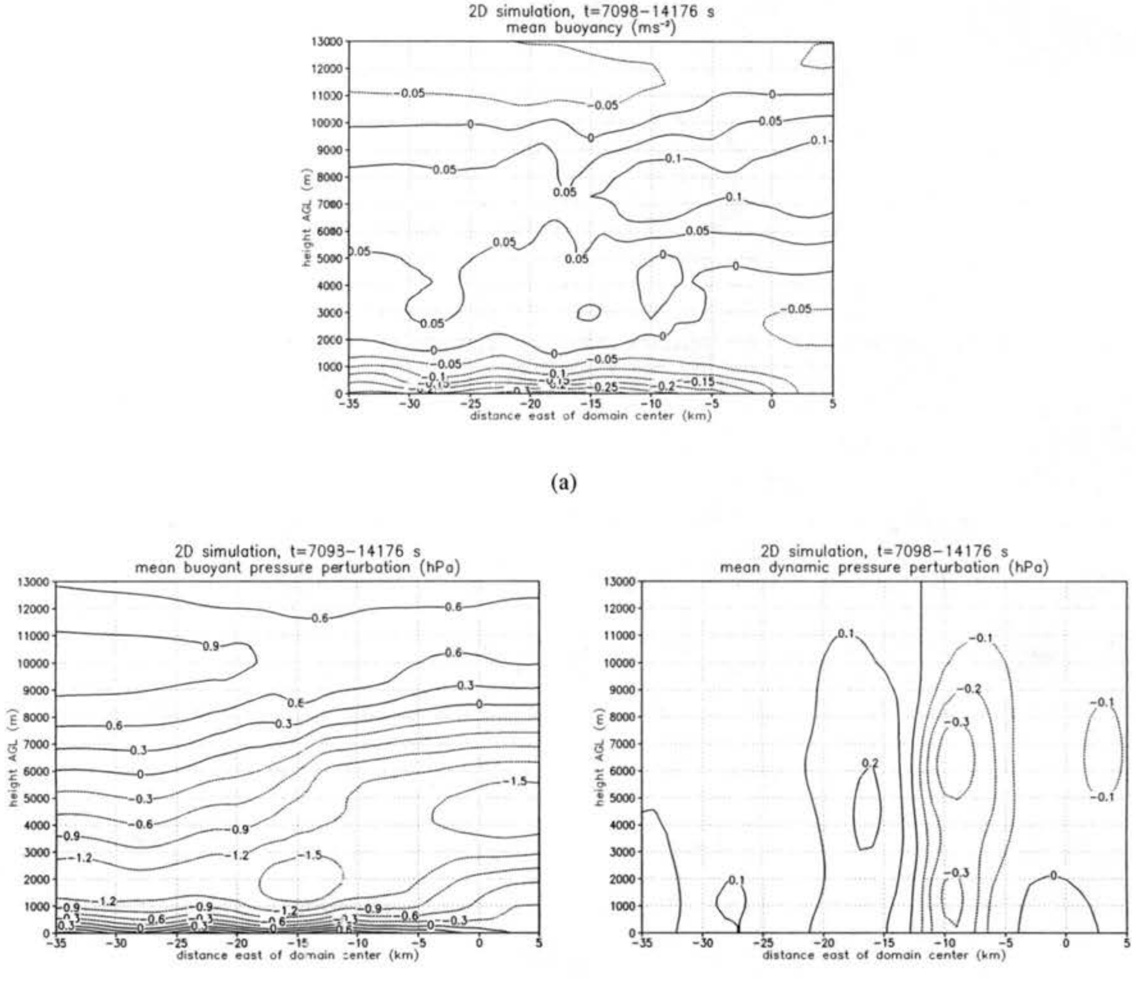

(a)

(b)

(c)

Figure 6.12: Averages from t=7098–14176 s of the 2D control simulation: a) buoyancy ($-g\ \rho'/\rho_o$, m s^{-2}), b) buoyant pressure perturbation (P'B, hPa), and c) dynamic pressure perturbation (P'D, hPa).

It is clear from Fig. 6.12b that the buoyant component of the pressure field (P'B) predominates in the 2D simulation's mean state. Hence, it is accurate to say that the convective transients predominantly perturb the mesoscale pressure field toward its steady state values by introducing latent heating periodically, which in turn also generates compensating subsidence in the nearby environment. It may be unclear why the transient heating should generate a steady state pressure field. The reason is that P'B responds to the distribution of buoyancy, not the instantaneous heating rate. The convection perturbs the buoyancy field on some time scale, in competition with which acoustic and gravity waves disperse the buoyancy perturbations on some other time scales. Accordingly, it is a simple rate problem; if the convection heats the local troposphere at about the same rate that the acoustic and gravity waves disperse the heating, a temporally noisy but nevertheless quasi–steady buoyancy field can result. By extension, the perturbation pressure field, which is largely attributable to P'B, can also be quasi–steady on long time scales. The pressure fields will asymptotically approach this steady state with time, or at least until the rate of convective heating changes.

There is also a small dynamic component to the perturbation pressure field (P'D, Fig. 6.12c). This can be attributed to both the effects of a mean updraft within a vertically sheared base state (for an illustration of this, see Fig. 3.1 C) and the nonlinear effect of the curvature of the mean overturning updraft (for an illustration of this, see Fig. 3.1 F). These effects yield much smaller magnitudes for P'D than for P'B. However, P'D does play a role in accelerating air parcels downshear in the mean updraft. Notably, the dynamic pressure perturbations will not be significant in the temporal mean if they are only associated with transient updrafts. Therefore, it is perhaps more appropriate to envision them as being consistent with the mean flow field that evolves as a result of the buoyant pressure perturbations. In that respect, the transient convective overturning renders a quasi–steady pressure field (a "rigid box") almost exclusively owing to the persistent (although periodic) warming of a large region of the troposphere via latent hating and propagating subsidence.

This section has described the mean state, its basic properties, and how the transient convective elements help the mean state to come about. The remaining question is then: what does the mean state represent? Individual air parcels in the temporally evolving flow do not follow the mean flow streamlines. Moreover, the mean flow streamlines don't describe the phenomena that convection scientists typically study, i.e. the transient deep convective up and downdrafts. An elegant interpretation for the mean state is that it represents the net effects of an appropriate mesoscale parameterization for the convective scale transients. As discussed above, the primary effect of the transients on the far field is felt through the persistent mesoscale pressure perturbations, which arise largely as a result of the local heating owing to the deep convective overturning. Therefore, on the mesoscale, the appropriate parameterization of the 2D FFLS system's heating and momentum fluxes would yield the mean state's pressure fields and steady wind fields (e.g. as in Fig. 6.11). As an FFLS system moves across a domain, its net effect on the environment is to tranform the base state wind profile into the post–line wind profile (as depicted in Fig. 6.13). It is relatively easy to see how a steady state model such as in Fig. 1.11b can depict this change to the environment. It is perhaps less clear that Fig. 1.11b can accurately describe the appropriate stabilization of the environment given the analytic model's neglect of the transient convection and its consumption of lower tropospheric CAPE. Although somewhat cursory, one interpretation of (6.12) is that the steady state pressure field that is dynamically and mechanically consistent with the steady state flow field is also the appropriate P'B field due to the mesoscale distribution of buoyancy. On mesoscale temporal and spatial scales, the environment responds to the convection via the mesoscale P'B field. Therefore, in capturing the appropriate mean pressure and wind responses the analytic models implicitly also capture the appropriate mesoscale buoyancy perturbations. There are plans to continue considering this problem in collaboration with Dr. Moncrieff.

6.3 A word about gravity waves and squall lines

Cram et al. (1992) used numerical simulations to demonstrate that the prefrontal squall line of 18 June 1978 could be understood to propagate as an internal gravity wave. In reviewing the pertinent literature, Cram et al. emphasized the wave–CISK theory for squall line propagation and maintenance, in which an n=2 (that is, having one full wavelength within the troposphere) internal

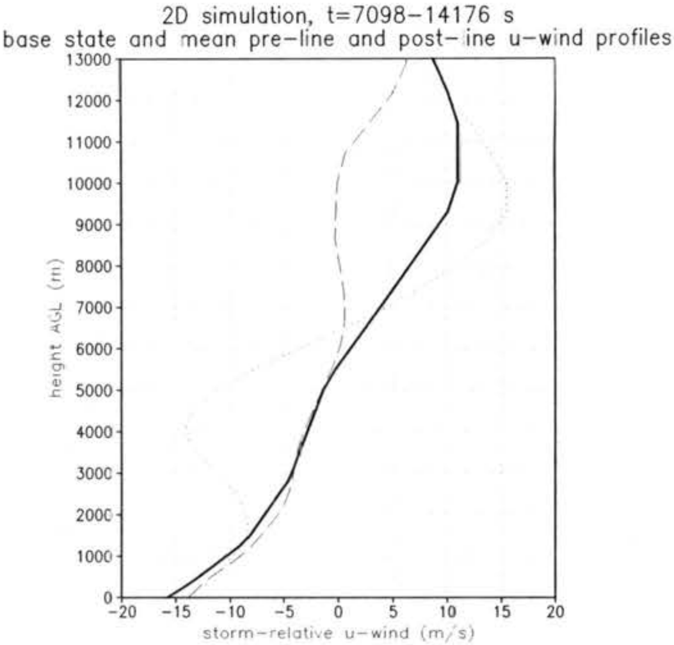

Figure 6.13: Vertical profiles of the storm–relative u–wind from the base state (heavy solid curve), 20 km east of the mean convective line's position (i.e. the right hand side of Fig. 6.9, dotted curve), and 20 km west of the mean convective line's position (i.e. the left hand side of Fig. 6.9, dashed curve) for the 2D control simulation, averaged from t=7098–14176 s.

gravity wave can phase with the convection and provide continual forcing for it, while simultaneously being reinforced by it. For cases in which wave–CISK occurs, the speed of the squall line or convective system is determined by the speed of the internal gravity waves' forcing [of course, the presence of the convection may also affect the speed of the wave, as noted by Cram et al. (1992)]. Cram et al. pointed out that, "convection excites many scales of gravity waves, none of which will necessarily phase–lock with the convection." In other words, the wave–CISK process is by no means guaranteed when deep convective storms and internal gravity waves coexist. However, the absence of a true wave–CISK process does not mean that gravity wave dynamics are irrelevant to the structure and evolution of a squall line. Dr. William Cotton (personal communication) has suggested that in almost all convective systems, a great deal of the transient signal may be understood to comprise gravity waves. Examples of this approach to organized convective studies include the analyses performed by Tripoli and Cotton (1989b) and Schmidt and Cotton (1990).

Clearly, the gravity wave approach to understanding convective dynamics is quite different from the parcel acceleration perspective utilized in Chapter 5. To what degree can the FFLS structure in the present simulations be explained in terms of gravity waves? A rigorous answer to that question is beyond the scope of this publication. Nevertheless, it seems clear that the lower tropospheric ascent in the leading precipitation region of the present simulations could be explained as resulting from n=2 gravity waves or an n=2 buoyancy bore, whose characteristic pressure field corresponds to that in Figure 4.14. However, this is likely not an example of wave–CISK because the convection resides near the edge of the surface outflow, not in the broad region of n=2 lower tropospheric ascent. Nevertheless, these kinds of non–finite mode gravity waves account for most of a convective system's effects on the far field, as suggested in the previous section. And, as shown by Nicholls et al. (1991), Mapes (1993), and Fovell (2002), the n=2 mode of lower tropospheric ascent can condition the atmosphere for additional convection and aid in its initiation.

It is also possible that the basic structure of the mean overturning FFLS updraft could be understood as an n=1 (that is, having one half wavelength within the troposphere) roll–type gravity wave, with the transience of the multicellular system reflecting the effects of higher frequency gravity wave modes; the present study did not include analyses to substantiate this claim[8] . In particular, in the strongly sheared environment of the FFLS simulations, gravity wave behavior may be somewhat unique. Nachamkin and Cotton (2000) discussed the fact that vertical wind shear contributes to a tilted heat source, which affects the direction of gravity wave propagation as originally established by Pandya and Durran (1996). The tilt of the heated region in the present FFLS simulations suggests that gravity waves would preferentially propagate forward into the pre–line region, where they could have an effect on the local wind and temperature fields. However, because gravity waves propagate owing to their buoyant pressure fields, it would also seem that some components of the local convective circulation and its transient accelerations, which are attributable to the dynamic pressure field, fall outside the range of gravity wave theory. Perhaps future studies will be able to clarify the role of gravity waves in FFLS as well as other convective systems.

[8] As mentioned in Section 5.1.1, analyses of the present simulations did not support Yang and Houze (1995)'s hypothesized role for the gust front updraft in generating high frequency gravity waves that controlled the multicellular period.

Chapter 7

OTHER QUASI–2D LINEAR CONVECTIVE MODES: SENSITIVITIES, EVOLUTION, AND DYNAMICS

7.1 System evolution and the environment: basic sensitivities

One obvious benefit to using a numerical model is the ability to perform controlled simulations in which only one parameter is varied. With regard to squall lines and convective systems, this topic has already been covered at length. Pertinent and important studies of convective systems' sensitivity to their environments include those by Hane (1973), Thorpe et al. (1982), Dudhia et al. (1987), Nicholls et al. (1988), Rotunno et al. (1988), and Szeto and Cho (1994). Because this is well–trodden ground, this study did not duplicate the prior experiments. This section discusses several sensitivity tests whose purpose is to help elucidate the dynamics of the simulated FFLS systems, not to demonstrate the full breadth of convective modes that are possible. The first part of this section returns to RKW theory and addresses it using a simple test in which the evaporation rate and 3–10 km shear vary. The second part of this section addresses a few of the basic sensitivities of the periodic–3D simulations. Although this may, in part, overlap with some of the previous studies listed above, the results are included here in order to show the robustness of the FFLS structure and the basic effects of variations to the typical FFLS environment.

7.1.1 RKW theory encore: evaporation rate and deep layer shear in 2D simulations

As was explained in § 6.1, although a surface cold pool's strength with respect to the lower tropospheric environmental shear is indeed relevant to updraft dynamics (Rotunno et al. 1988), the wind profile in the 3–10 km AGL layer is also important. This section addresses the gross effects of the basic dynamics that Section 6.1 described, rendering a broader perspective on how deep layer shear affects the mesoscale organization of a convective system rather than an individual air parcel. A matrix of nine 2D simulations used the three wind profiles shown in Fig. 2.3 ("S=16", "S=10", and "S=4") along with three multiplicative factors ("E=2", "E=1", and "E=0.5") for the evaporation rate as described in § 2.1.3. The resulting system structures are shown via Hovmoller diagrams in Fig. 7.1.

All of the simulated systems initially produced downshear–tilted updrafts and leading precipitation. And, with the exception of the simulation with the strongest shear and lowest evaporation rate ("S=16, E=0.5"), all of the simulated systems eventually evolved from their initial FFLS structure into a FFTS structure (Fig. 7.1). Not surprisingly, given the basic dynamics discussed in § 6.1, simulated systems in stronger deep layer wind shear maintained their leading precipitation regions longer (in Fig. 7.1, deep layer shear increases from left to right), and simulated systems with larger evaporation rates evolved toward TS structure more rapidly (in Fig. 7.1, evaporation rate increases from bottom to top). Because the lower tropospheric wind profile was not varied in these experiments, it seems clear that the determination of LS vs. TS system structure is more complicated than what Rotunno et al. (1988) envisioned. The simulated structures are nicely stratified by the 3–10 km wind shear: for the E=0.5 simulations, S=16 produced a long–lived FFLS structure, S=4 produced a long–lived FFTS system, and S=10 produced a hybrid.

Although it isn't feasible to individually analyze and compare large numbers of individual trajectories from these simulations, it is possible to extract the mean behaviors of groups of trajectories. Each simulation included 1000 air parcels, launched into the lowest 2 km of the inflowing airstream, spaced such that they arrived at the convective region regularly throughout the systems' mature periods. In each case, between 220 and 455 of the parcels ascended in a convective updraft. Tables 7.1–7.6 summarize the mean integrated front–to–rear and rear–to–front accelerations on these updraft air parcels. This kind of separation is useful because most of the updraft trajectories, both individually and when averaged as a group, attained their maximum rearward velocities near

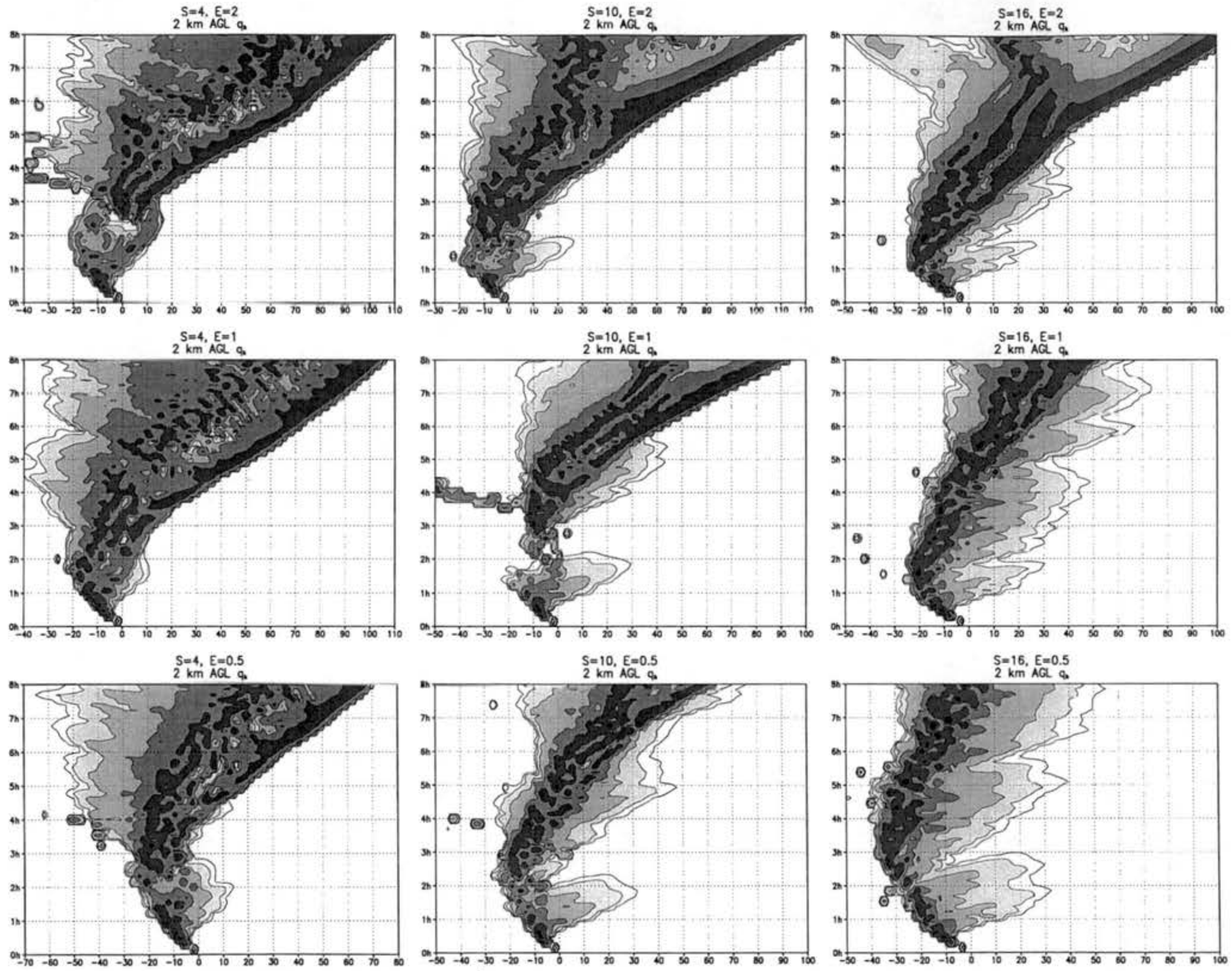

Figure 7.1: Matrix of Hovmoller diagrams depicting 2 km AGL hydrometeor mixing ratio (from t=0–8 h) for 3–10 km shear (S) = 4, 10, 16 and evaporation rate factor (E) = 0.5, 1, 2. Levels of shading are 0.005, 0.02, 0.08, 0.32, 1.28, and 5.12 g kg^{-1}. The front–fed LS control run is S=16, E=1.

3 km AGL. This coincides nicely with the isolation of the 3–10 km wind shear magnitude in this experiment, and suggests that the problem indeed has two distinct dynamical parts as proposed in Section 6.1: 1) an RKW–like interaction between the cold pool's ACCB+ACCDNL and the low-level wind profile's induced ACCDL, and 2) downshear accelerations in the 3–10 km AGL layer owing to ACCDL (and also contributions by ACCB and ACCDNL, as discussed in § 5.1 and § 6.1). Notably, although this publication has argued that the important accelerations within convective systems are, by nature, transient (as in § 5.1), the analysis in this chapter averages numerous trajectories that individually ascended in updrafts and experienced these transient accelerations; this is the most physically relevant way to average a temporally varying convective system.

All of the simulations began with identical wind profiles below 3 km AGL. Therefore, for all 9 simulations, the mean initial u–velocities of the updraft parcels was about the same, roughly –7 m s^{-1} (Table 7.1). The mean rearward parcel accelerations were primarily sensitive to the evaporation rate, with increasing net rearward accelerations for higher evporation rates (Table 7.2). The reason for this relationship is that greater evaporation rates render stronger surface cold pools, which in turn imply greater rearward ACCB and ACCDNL, as described in § 6.1. There was also a weak sensitivity of the mean rearward accelerations to the 3–10 km shear vector (Table 7.2). It is more difficult to assess the dynamics of this relationship because, as previously mentioned, the rearward accelerations occur almost entirely below 3 km AGL. Section 6.1 discussed the role of shear in facilitating turbulent mixing and evaporation in the middle and upper troposphere. In addition, because the updraft trajectories in the S=4 simulations do not strongly overturn, rearward–tilted systems occur which drop most of their precipitation on the same side of the gust front as the pre-existing cold pool, whereas FFLS systems in the S=16 simulations drop a significant fraction of their precipitation on the leading side of the gust front, away from the pre–existing surface cold pool. As a result of these factors, in the E=0.5–1 experiments, the S=16 systems are far less effective at reinforcing their own cold pools than are the S=4 systems; this, in turn, somewhat weakens the ACCB and ACCDNL associated with the outflow.

On average, once the air parcels reach 3 km AGL, they have attained their maximum rear-

Table 7.1: Mean initial u–velocities (m s^{-1}) of updraft parcels in each of the nine shear/evaporation experiments.

	S=4	S=10	S=16
E=2	-7.7	-7.4	-6.5
E=1	-7.1	-7.3	-7.1
E=0.5	-6.9	-7.0	-6.6

Table 7.2: Mean rearward u–velocity changes (m s^{-1}) of updraft parcels in each of the nine shear/evaporation experiments.

	S=4	S=10	S=16
E=2	-8.2	-10.9	-7.9
E=1	-7.5	-4.5	-2.1
E=0.5	-5.3	-4.5	-1.9

Table 7.3: Mean forward u–velocity changes (m s^{-1}) of updraft parcels in each of the nine shear/evaporation experiments.

	S=4	S=10	S=16
E=2	9.4	22.5	29.0
E=1	10.3	19.4	21.7
E=0.5	9.9	18.5	22.0

Table 7.4: Mean final u–velocities (m s^{-1}) of updraft parcels in each of the nine shear/evaporation experiments.

	S=4	S=10	S=16
E=2	-5.6	4.6	13.3
E=1	-4.4	6.2	13.4
E=0.5	-3.2	6.6	14.3

Table 7.5: Mean gust front translational speeds (m s^{-1}) in each of the nine shear/evaporation experiments.

	S=4	S=10	S=16
E=2	3.2	3.2	5.8
E=1	3.4	1.1	3.9
E=0.5	0.9	0.7	2.0

Table 7.6: Mean final storm–relative u–velocities (m s^{-1}) of updraft parcels in each of the nine shear/evaporation experiments.

	S=4	S=10	S=16
E=2	-8.8	1.4	7.5
E=1	-7.8	5.1	9.5
E=0.5	-4.1	5.9	12.3

ward velocities and are ascending into a region of rear–to–front acceleration. As should be expected based on the discussions in § 5.1 and § 6.1, these forward accelerations are almost entirely attributable to the deep layer wind shear. In other words, although there is a very weak sensitivity to the evaporation rate, the net rear–to–front acceleration of the updraft parcels is by far more sensitive to the 3–10 km shear magnitude (Table 7.3). The large sensitivity to the 3–10 km wind shear is due to the importance of the base state wind shear to P'DL and ACCDL [recall equation (3.2)]. As described in § 5.1, ACCB and ACCDNL often also help to contribute in the direction toward which ACCDL causes the cloud to tilt. The weak sensitivity to evaporation rate apparently exists because stronger surface cold pools tend to produce marginally stronger updrafts, and P'DL in turn is also a function of the horizontal gradient in w within the updraft (i.e. for a given updraft width, P'DL is a function of the updraft's strength).

Although the lower tropospheric rearward accelerations are sensitive to the evaporation rate, the upper tropospheric forward accelerations are even more strongly sensitive to the 3–10 km wind shear. As a result, the mean final u–velocities of the updraft parcels in the nine simulations were grouped almost entirely based on the deep layer shear (Table 7.4). The distribution of integrated accelerations, and hence final u–velocities, was broad (from +2.8 m s^{-1} for the S=4 cases to +20.8 m s^{-1} for the S=16 cases) and cannot be explained by RKW theory.

In what respect is cold pool strength important to the current experiment, then? Because surface outflow behaves roughly like a density current (Charba 1974), its speed is proportional to its depth and temperature perturbation (in a word, its "strength"). Therefore, in the matrix of nine simulations, the system's eastward speeds increased with increasing evaporation rate (Table 7.5). From this perspective, the cold pool strength is important because it determines the system speed, which in turn determines the final storm–relative velocities for air parcels with a given ground–relative u velocity. As a result, the final mean storm–relative line–perpendicular parcel velocities are sensitive to both the evaporation rate and the 3–10 km AGL wind shear (Table 7.6). Section 2.2.4 argued that the mean final storm–relative u of individual air parcels contributes to the development of either a leading or trailing precipitation region, and the data from Table 7.6 and Fig. 7.1 bear this out. Notably, the system speeds given in Table 7.5 are averages over the entire 8 hours of each simulation; most of the systems accelerated later in their lifetimes, which is consistent with increasingly rearward storm–relative parcel velocities and hence the systems' evolutions from LS toward TS structure. Section 7.2 gives additional attention to the dynamics of this transition from LS to TS.

7.1.2 Sensitivities in periodic–3D simulations

As mentioned in the preamble to Section 7.1, this chapter is not meant to catalogue the full breadth of possible convective structures in this study. Rather, it describes several tests that demonstrate the robustness and basic sensitivities of the periodic–3D FFLS simulations. There were few surprises from these sensitivity experiments; the large body of previous work on modeled squall lines provided fairly accurate expectations. This subsection compares the mature convective system structures from six variations to the original periodic–3D FFLS control simulation. All of the systems have attained a quasi–stable state by $t = 6$ h, making comparisons appropriate at that time. The criteria for comparison (Table 7.7) are the horizontal shapes of the systems' mean 0–10 km AGL total hydrometeor mixing ratio (Figs. 7.2–7.5), and their cold pools' along–line averaged minimum in θ', domain–averaged total hydrometeor mixing ratios, domain–averaged vertical velocities, and horizontally averaged "enstrophy" (actually, $|\zeta|$) at 5.9 km AGL.

The first experiment had increased CAPE of 3394 J kg^{-1} (cf. Table 2.2), attained by decreasing θ_{trop} to 335 K and T_{trop} to 211 K in the base state sounding (cf. Table 2.1). This modification didn't change the basic system structure very much (cf. Figs. 7.2 and 7.3a). However, the updrafts generally were stronger (Table 2.1). This enabled the system to produce more hydrometeor

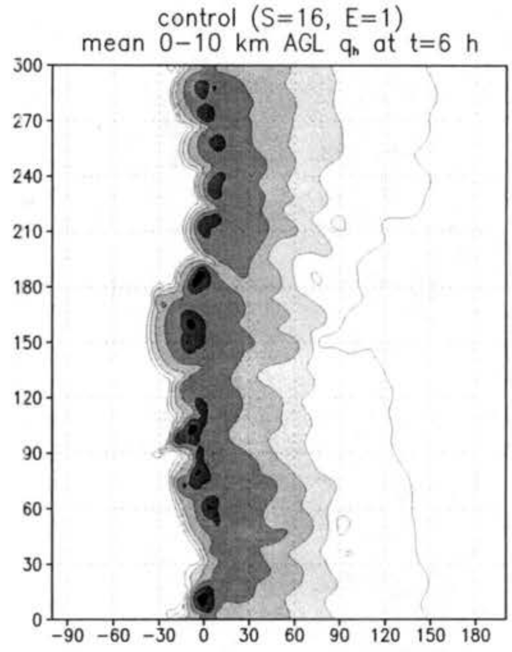

Figure 7.2: Mean hydrometeor mixing ratio from 0–10 km AGL at 6 h for periodic–3D control simulation. Levels of shading are 0.005, 0.02, 0.08, 0.32, 1.28, and 5.12 g kg^{-1}.

Table 7.7: Summary of spatially averaged variables at t = 6 h for the seven sensitivity experiments. The details of each simulation are described in the text. Column 2: along–line averaged minimum in θ' (K). Column 3: domain averaged hydrometeor mixing ratio. Column 4: domain averaged vertical velocity (m s^{-1}). Column 5: horizontally averaged absolute value of vertical vorticity at 5.9 km AGL (s^{-1}).

simulation	$\overline{\theta'_{min}}^{y}$ @ sfc	$\overline{q_h}^{x,y,z}$	$\overline{w}^{x,y,z}$	$\overline{\lvert\zeta\rvert}^{x,y}$ @ 5.9 km
control	-6.2 K	5.0 $\times 10^{-5}$	0.012 m s^{-1}	8.3 $\times 10^{-5}$ s^{-1}
increased CAPE	-7.8 K	8.1 $\times 10^{-5}$	0.021 m s^{-1}	1.0 $\times 10^{-4}$ s^{-1}
decreased CAPE	-4.8 K	2.3 $\times 10^{-5}$	0.011 m s^{-1}	6.0 $\times 10^{-5}$ s^{-1}
increased shear	-6.6 K	5.6 $\times 10^{-5}$	0.006 m s^{-1}	1.2 $\times 10^{-4}$ s^{-1}
decreased shear	-6.9 K	4.5 $\times 10^{-5}$	0.018 m s^{-1}	3.1 $\times 10^{-5}$ s^{-1}
moistened mid–levels	-5.4 K	6.2 $\times 10^{-5}$	0.018 m s^{-1}	7.9 $\times 10^{-5}$ s^{-1}
dried mid–levels	-6.9 K	3.9 $\times 10^{-5}$	0.010 m s^{-1}	8.1 $\times 10^{-5}$ s^{-1}

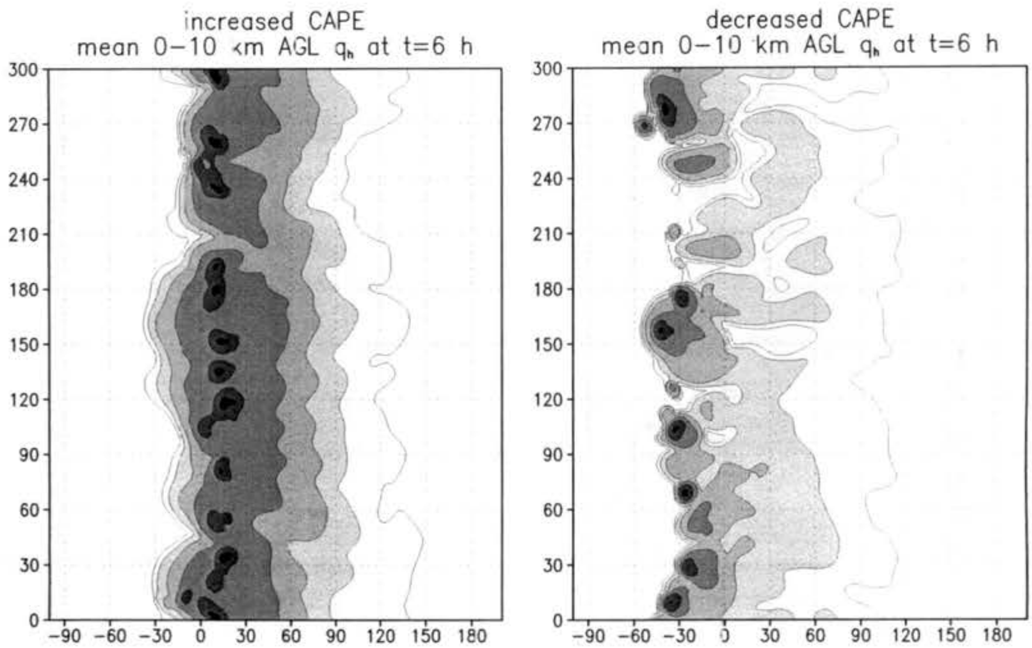

(a)

(b)

Figure 7.3: Mean hydrometeor mixing ratio from 0–10 km AGL at 6 h for periodic–3D simulations: a) increased CAPE, b) decreased CAPE. Levels of shading are 0.005, 0.02, 0.08, 0.32, 1.28, and 5.12 g kg^{-1}.

mass which, in turn, contributed to more net evaporation and colder surface outflow (Table 2.1). The mean enstrophy along the convective line also increased owing to the stronger w, which tilted the mean environmental wind shear into couplets of positive and negative vorticity flanking the updrafts.

The second experiment had decreased CAPE of 1644 J kg^{-1} (cf. Table 2.2), attained by increasing θ_{trop} to 345 K and T_{trop} to 217 K in the base state sounding (cf. Table 2.1). This modification had the opposite effect of increased CAPE. Vertical velocities were decreased, which in turn decreased the hydrometeor mass, surface cold pool, and enstrophy that the system produced. What resulted, as shown in Fig. 7.3b, was a similar skeletal structure for the simulated system, but with fewer intense convective cells and a much less contiguous leading precipitation region. This may seem surprising given that $\overline{w}$ was not much smaller than in the control simulation (Table 2.1). The lower troposphere in the decreased CAPE experiment wasn't altered much by the changes to

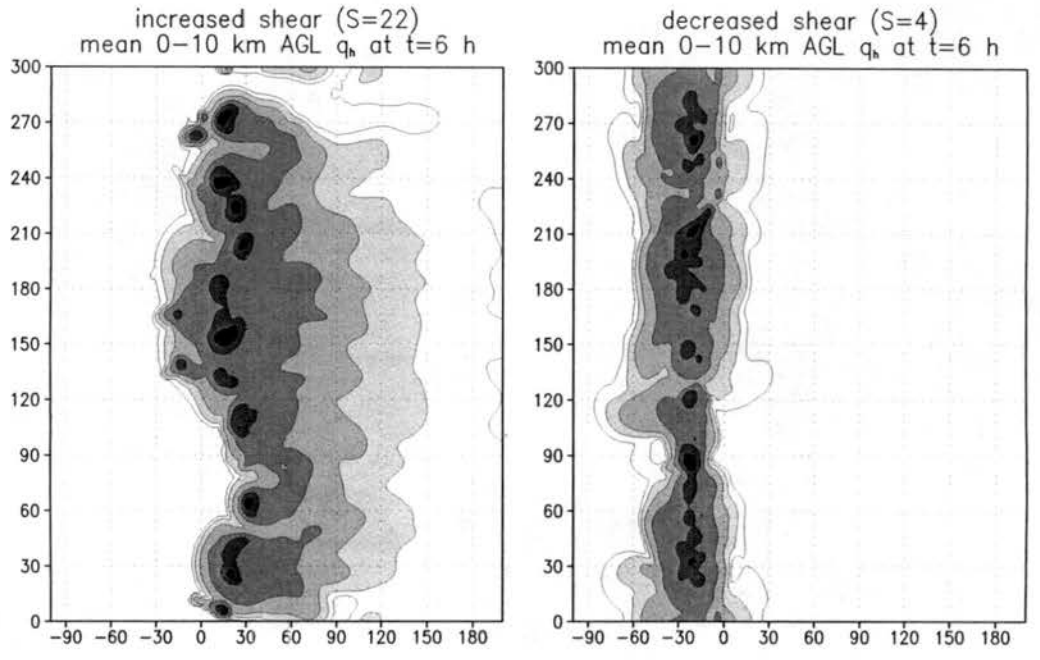

(a) (b)

Figure 7.4: Mean hydrometeor mixing ratio from 0–10 km AGL at 6 h for periodic–3D simulations: a) increased 3–10 km shear, b) decreased 3–10 km shear. Levels of shading are 0.005, 0.02, 0.08, 0.32, 1.28, and 5.12 g kg^{-1}.

the sounding; this was intended to ensure a basic similarity in the low level processes among the control and high and low CAPE experiments. As a result, updraft air parcels in the low CAPE experiment were accelerated upward in the lower troposphere and attained values of w similar to those in the control experiment. However, in the middle and upper troposphere, the updrafts in the low CAPE experiment were siginificantly weaker (not shown) owing to the comparatively small upward accelerations provided by buoyancy as compared to the detrimental effects of mixing and water loading.

The third experiment had increased 3–10 km wind shear (22 m s^{-1}). Although the vertical wind profile is not shown, the reader can infer its shape from Fig. 2.3. The most obvious effect of the increased windshear was to decrease the mean w on the domain. As discussed in § 6.1, strong vertical shear tends to weaken updrafts' intensities by favoring enhanced mixing and entrainment. However, more important than this effect was the role of strong shear in producing several strong,

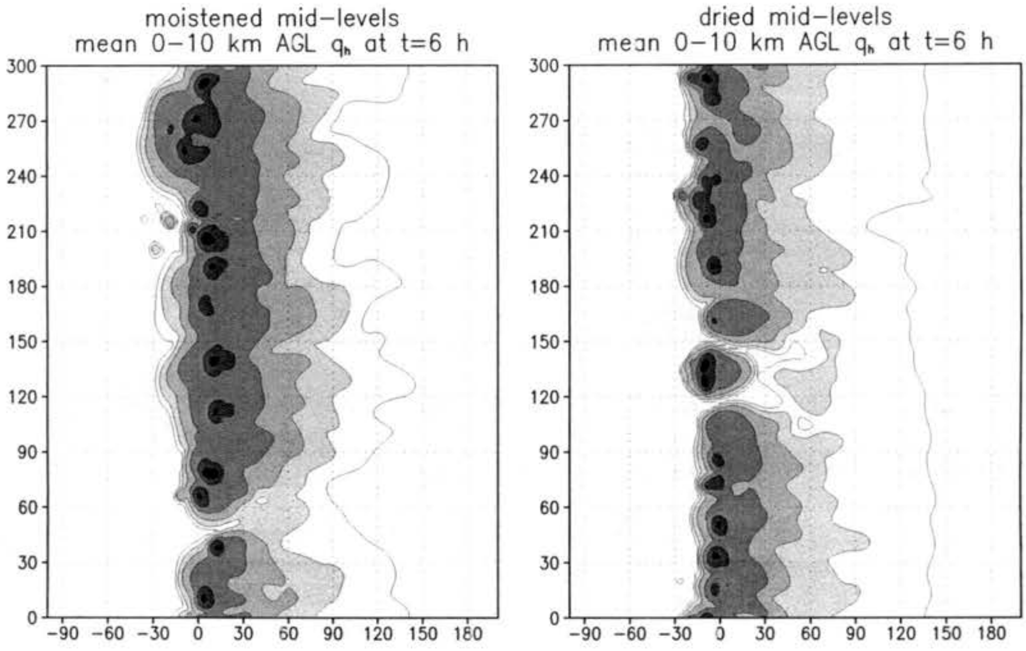

(a) (b)

Figure 7.5: Mean hydrometeor mixing ratio from 0–10 km AGL at 6 h for periodic–3D simulations: a) increased middle tropospheric humidity, b) decreased middle tropospheric humidity. Levels of shading are 0.005, 0.02, 0.08, 0.32, 1.28, and 5.12 g kg^{-1}.

quasi–supercellular updrafts (note the increased mean enstrophy in Table 7.7). Indeed, $\overline{w_+|\zeta|}^{x,y}$ (a sort of mean, unsigned updraft helicity) at 5.9 km AGL in the increased shear simulation was nearly a factor of two larger than that in the control simulation. When averaged separately, the mean upward velocity (w_+) in the high shear simulation was almost identical to that of the control simulation (0.076 vs. 0.073 m s^{-1}), which is consistent with their relatively similar cold pool strengths and hydrometeor loads (Table 2.1).[1] However, the mean downward velocity (w_-) was much larger in the high shear simulation than in the control run (–0.073 vs. –0.059 m s^{-1}). As has been discussed, increased shear implies increased turbulent mixing, which in turn implies a larger source of mid–level evaporative cooling for downdrafts. Additionally, as reviewed by Markowski (2002), supercellular storms are known to produce dynamically driven downdrafts, which might

[1] As discussed by Lilly (1986), helical updrafts are less susceptible to turbulent dissipation than ordinary updrafts, which may tend to offset the detrimental effect of the increased shear somewhat.

also account for part of this discrepancy. Finally, because of the embedded quasi–supercellular elements, the system structure in the high shear simulation is somewhat less linear and contains several larger, stronger convective cells (Fig. 7.4a).

The fourth experiment decreased the 3–10 km wind shear, using the S=4 profile shown in Fig. 2.3. As seen in Fig. 7.4b, by 6 hours this did not lead to a TS system the way that it did in the 2D simulations (see Fig. 7.1), but rather an LS/TS hybrid; it continued to evolve toward TS structure and realized it later (not shown). Perhaps this different behavior in weaker shear explains the anecdotal observations (by members of Dr. Richard Johnson's mesoscale research group) that long linear convective systems often have both FFLS and FFTS segments. The cold pool strength and hydrometeor load for the decreased shear run were fairly similar to the control simulation, which may seem surprising given the larger mean w (Table 7.7). As for the increased shear case, however, the change in $\overline{w}$ was largely attributable to the differences in downdraft strength; in this case, the updrafts were of similar strength but the downdrafts were weaker. As has been discussed, decreased shear implies decreased turbulent mixing, which in turn implies a smaller source of mid–level evaporative cooling for downdrafts; as a result, the domain averaged w was increased. The lower $\overline{q_h}$ is due to the relatively small horizontal dispersion of hydrometeors by the system (as in Fig. 7.4); much of the condensate fell directly to the ground through the unsheared updraft, rather than being carried forward by updraft parcels that had been accelerated downshear, as in the control and stronger shear simulations. Not surprisingly, given the weaker middle and upper tropospheric shear, the mean enstrophy owing to tilting was greatly decreased (Table 7.7).

The fifth and sixth experiments alternately increased the base state's minimum relative humidity, r_{min}, to 0.5 and decreased it to 0.2 (cf. Table 2.1), which respectively moistened and dried the sounding's middle and upper troposphere without altering the CAPE of the surface–based air parcels. As expected, because a certain amount of mixing occurs on the periphery of the updrafts, dryer middle tropospheric air promotes weaker updrafts and stronger downdrafts and cold pools, while the opposite is true of moister middle tropospheric air (Table 7.7). In addition, given the stronger updrafts and moister mid–levels, it isn't surprising that the domain's hydrometeor content is increased in the moistened simulation; and, once again, the opposite is true. The middle tropospheric humidity did not significantly alter the convective line's mean enstrophy, probably because the low–level tilting processes weren't affected much by the humidity of the middle and upper troposphere. The basic structure of the convective system also wasn't changed much by the varying mid–level humidity (Fig. 7.5), except that perhaps the precipitation shield in the dryer simulation was slightly less contiguous owing to evaporation and sublimation, as expected.

Summary of sensitivities in periodic–3D simulations

As has been found by many previous scientists, the 3D convective system simulations are sensitive to CAPE, shear, and humidity. The surface cold pool's strength is a function of the convection's intensity (and the accompanying rate of hydrometeor production) and the humidity of the middle and upper troposphere. CAPE has an obvious effect on updraft strength, as does humidity. The sensitivity of updrafts' and downdrafts' strengths to the deep layer shear is somewhat more complicated because, at the high end of the shear spectrum, shear may again become beneficial to updraft strength as quasi–supercellular convection occurs. The tendency of individual convective updrafts to produce flanking vorticity couplets via tilting can be enhanced either by increasing the deep layer shear or by enhancing the updraft strength via increased CAPE. Finally, the basic structure of the control FFLS simulation didn't change much during the sensitivity tests with the exception that, as the deep layer shear decreases below some critical value (not identified), systems become LS/TS hybrids and evolve toward TS structure. This is an important result: *for moderate to large values of deep layer wind shear, the FFLS structure is a robust periodic–3D structure, and exists over a reasonably broad thermodynamic parameter space.*

7.2 Evolution from front–fed LS structure to front–fed TS structure

As was discussed in Section 7.1, almost all of the simulated 2D systems (and the periodic–3D systems in weaker deep layer shear) eventually evolve toward a FFTS structure. Szeto and Cho (1994) have discussed this physical process in some detail, and their work serves as the foundation for the discussion that follows. Szeto and Cho (1994) found in their simulations that a meso–γ (Orlanski 1975) pressure minimum occurred just to the rear of convective lines owing to both buoyant and dynamic contributions (Fig. 7.6). This pressure minimum was central to the rapid evolution of a fairly upright convective line into a well–developed TS system. Szeto and Cho (1994) explained that this low pressure center initiated a positive feedback mechanism, whereby inflowing air was accelerated rearward toward the pressure minimum, which rendered a more rearward tilt to the updraft trajectories, which in turn tended to reinforce the pressure minimum both thermally and dynamically. Their interpretation of this sequence as a "self–accelerating process" is consistent with the results of the current simulations.

Data from the control (S=16, E=1) and S=10, E=0.5 simulations are presented in Figs. 7.7 and 7.8. In both simulations, the low–level outflow boundaries begin to move eastward more rapidly around $t = 4$ h (Figs. 7.7b,c and 7.8b,c), and thereafter the systems evolve toward TS structure (Figs. 7.7a and 7.8a). Neither system stops producing leading precipitation immediately. However, with time the horizontal gradients in q_h decrease on the systems' trailing edges and increase on their leading edges. These are symptoms that fewer updraft parcels are carrying water forward from the convective line and more are carrying water rearward and contributing to a trailing precipitation region. Notably, in each case this transition around $t = 4$ h takes place without a significant increase in the temperature perturbation of the outflow (Figs. 7.7b and 7.8b). However, as suggested by Szeto and Cho (1994), the onset of this evolution appears to be well–correlated with decreasing pressure in the lower and middle troposphere to the rear of the outflow boundary (Figs. 7.7c and 7.8c). The minima in pressure precede the increases in the cold pools' θ' by 5–15 min, and appear to be fairly well correlated with the onset and acceleration of the systems' LS–TS transitions.

Szeto and Cho (1994) did not dispute the significance of the cold pool to system evolution; rather, they clarified that: "...the intensification of the cold pool is partly due to the upshear development of the system...". The cold pool's strength is still very important to a system's speed and, as in § 5.1, the cold pool plays a central role in the dynamics affecting air parcels near the outflow boundary. It is difficult to separate the effects of cold pool intensification from those of the middle

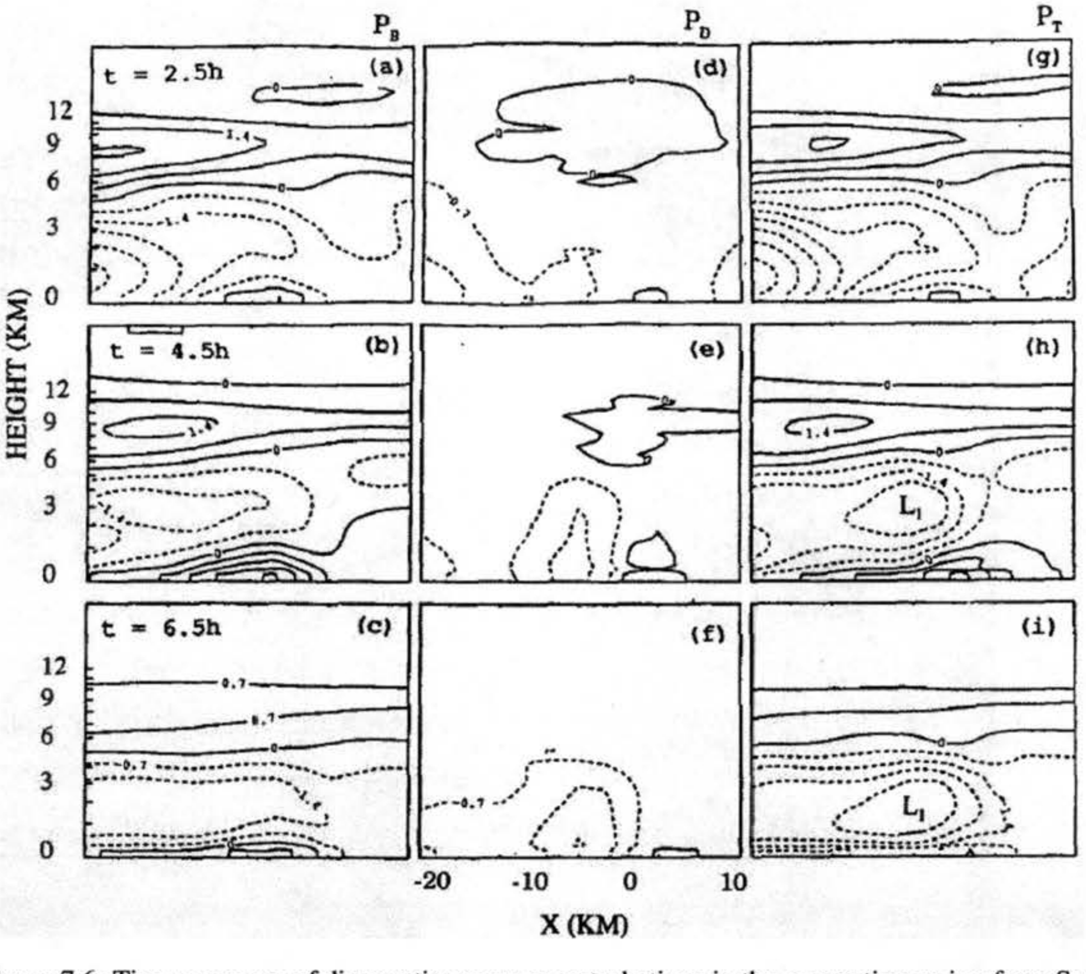

Figure 7.6: Time sequence of diagnostic pressure perturbations in the convective region from Szeto and Cho (1994): (a)–(c) buoyancy partial pressure, (d)–(f) dynamic partial pressure, and (g)–(i) total pressure perturbations. Contour interval is 0.7 hPa, and x ranges from –20 km to 10 km with x=0 located at the gust front.

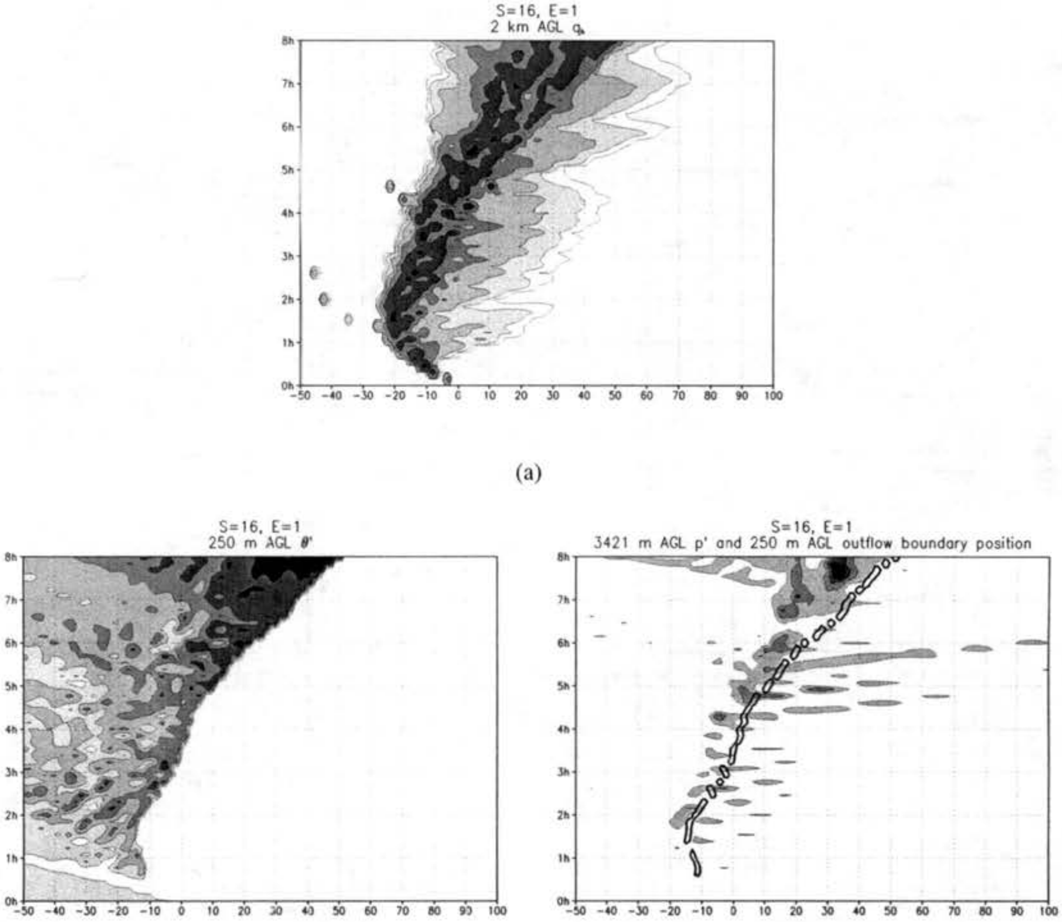

(a)

(b)

(c)

Figure 7.7: Hovmoller diagrams (from t=0–8 h) for S=16, E=1 simulation depicting a) 2 km AGL hydrometeor mixing ratio (levels of shading are 0.005, 0.02, 0.08, 0.32, 1.28, and 5.12 g kg^{-1}), b) 250 m AGL θ' (levels of shading are –3, –5, –7, –9, and –11 K), c) 3421 m AGL p' (levels of shading are –2, –3, –4, and –5 hPa) and position of the outflow boundary at 250 m AGL (heavy contour is the $\partial\theta/\partial x = 0.002$ K m^{-1} isopleth).

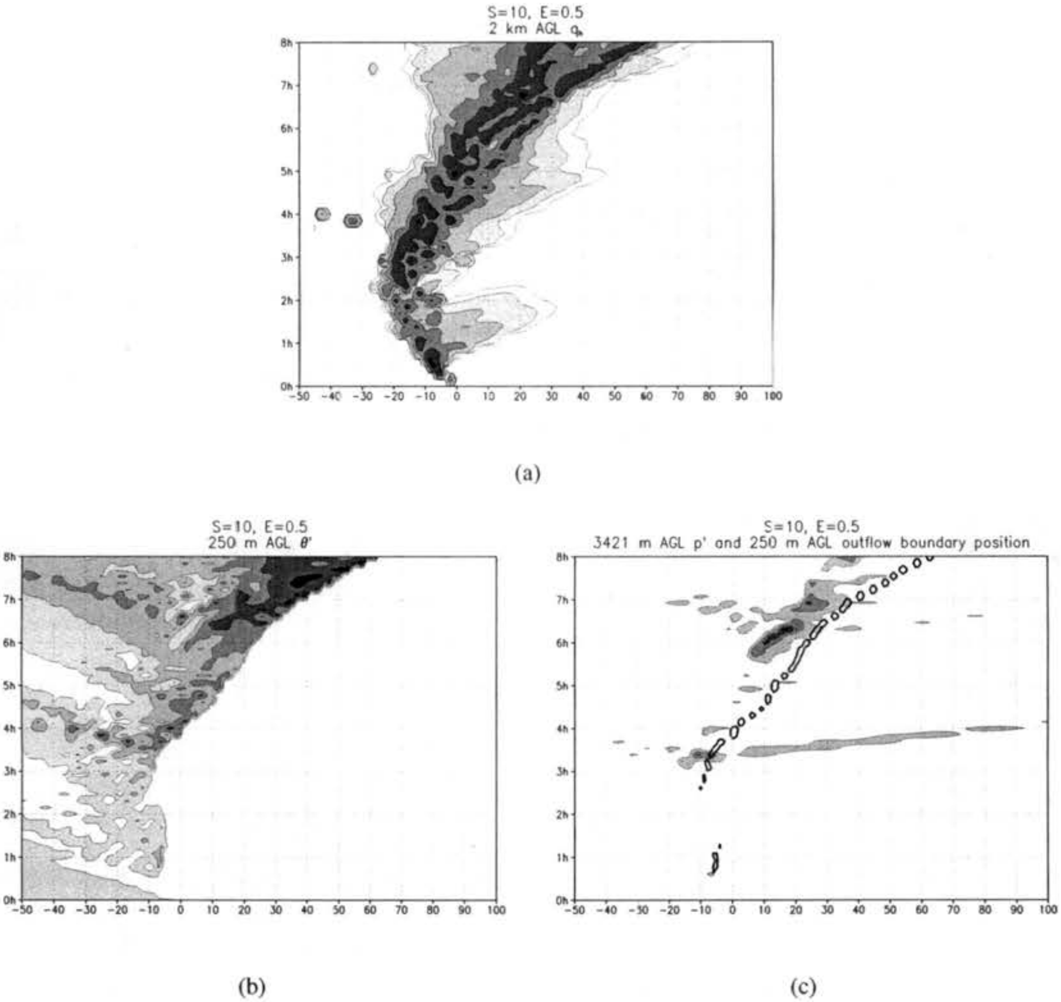

Figure 7.8: Hovmoller diagrams (from t=0–8 h) for S=10, E=0.5 simulation depicting a) 2 km AGL hydrometeor mixing ratio (levels of shading are 0.005, 0.02, 0.08, 0.32, 1.28, and 5.12 g kg^{-1}), b) 250 m AGL θ' (levels of shading are –3, –5, –7, –9, and –11 K), c) 3421 m AGL p' (levels of shading are –2, –3, –4, and –5 hPa) and position of the outflow boundary at 250 m AGL (heavy contour is the $\partial\theta/\partial x = 0.002$ K m^{-1} isopleth).

tropospheric pressure minima in Figs. 7.7 and 7.8. Without trying to reproduce the work already completed by Szeto and Cho (1994), it is worthwhile to consider briefly the components of the pressure minimum and their effects for the S=16, E=1 simulation at $t = 27300$ s (≈ 7.6 h, Fig. 7.9), at which time p' aft of the outflow boundary is exceedingly large (Fig. 7.7c). In order to make it easier to compare the Hovmoller diagrams in Fig. 7.7 with the vertical cross sections in Fig. 7.9, a cross–section of the S=16, E=1 system's hydrometeor and wind fields at $t = 27300$ s appears in Fig. 7.10.

As compared to the quasi–stable FFLS phase of the S=16, E=1 system (e.g. at t =10672–10910 s, Fig. 5.5), the pressure field is far more perturbed (Fig. 7.9b), the convective updraft is far less erect (Fig. 7.9a), and the cold pool is somewhat stronger (Fig. 7.9a). Much as was diagnosed by Szeto and Cho (1994), the pressure minimum to the rear of the primary convective cell has significant contributions from both P'B and P'D (specifically, P'DNL). Above approximately 5 km AGL in the updraft, the net ACC remains downshear (Fig. 7.9b). However, Fig. 7.9a reveals that most of the air in the updraft is not ascending very far above 5 km AGL because the updraft comprises air parcels with very large rearward velocities (in places, $u < 30$ m s^{-1}). Additionally, the net ACC vectors are nearly horizontal above 5 km AGL owing to the strong downward ACCDNL, such that air parcels ascending above 5 km do not gain any additional vertical momentum. As a result of these effects, inflowing air parcels move through the upward forcing very quickly and then proceed rearward within a plume of quasi–horizontal flow (i.e. at $x = 26$ to $x = 33$ km, $z = 3$ to $z = 7$ km AGL in Fig. 7.9a). Why is the magnitude of u' so much larger at $t = 27300$ s than it was earlier in the system's lifetime? After it has ascended the gust front/outflow boundary, inflowing air is accelerated very strongly rearward toward the minimum in P' (this process begins prior to Fig. 7.9). Near the outflow boundary, the enhanced rearward ACCB owing to the stronger cold pool also contributes (i.e. at $x = 43$ to $x = 46$ km, $z = 0.5$ to $z = 3$ km AGL in Fig. 7.9c). In comparison to the quasi–stable FFLS stage (again, recall Fig. 5.5), at $t = 27300$ s, the P'B field has become nearly symmetric and P'DNL is now minimized on the upshear side of the primary updraft. These significant differences do not occur over one updraft cycle. Rather, they represent

S=16, E=1 at 27300 s ($\approx$ 7.6 h)

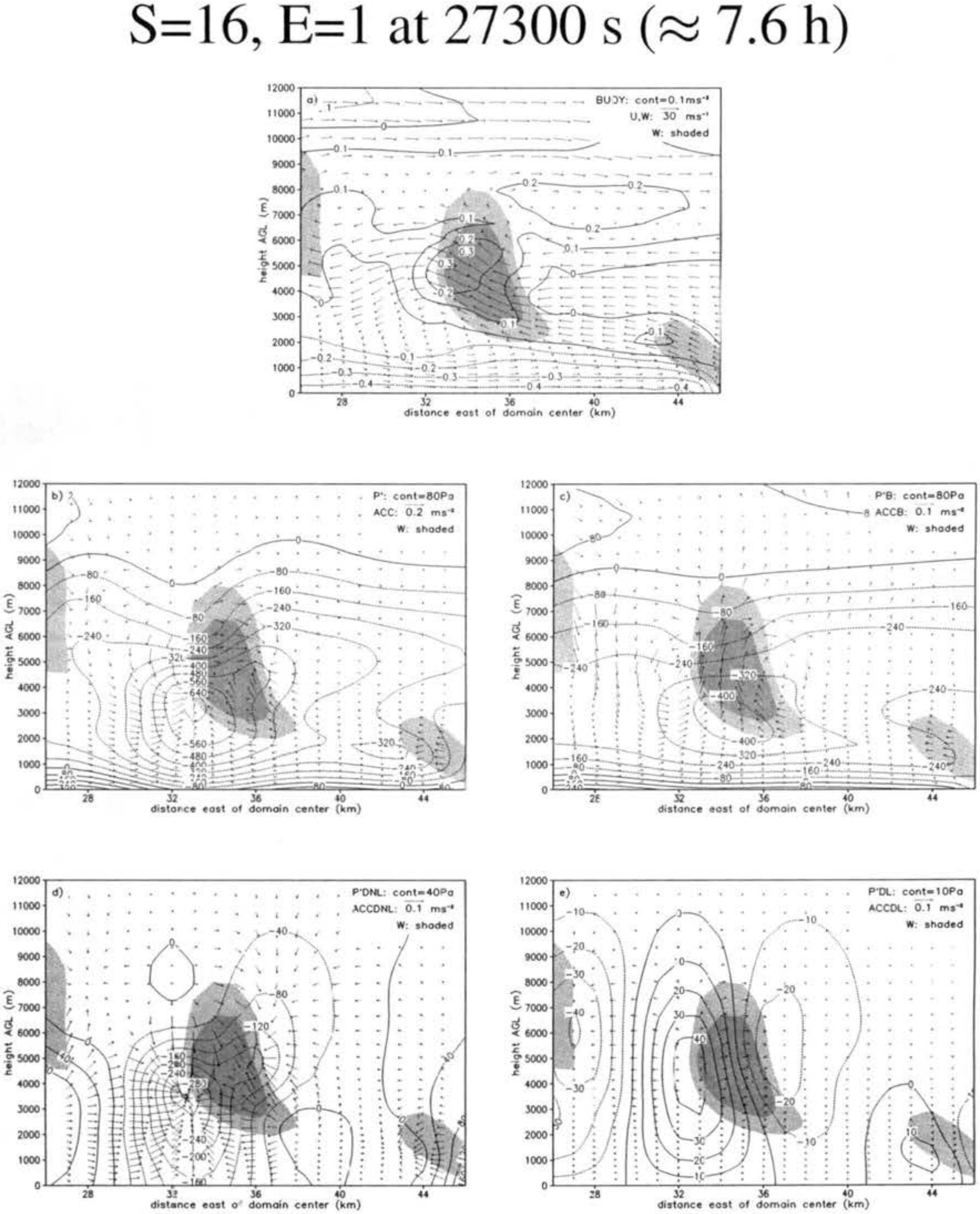

Figure 7.9: Velocities, perturbation pressures, and acceleration terms for simulation S=16, E=1 at 27300 s ($\approx$ 7.6 h). a) $BUOY$ contoured, u and w vectors. b) P' contoured, ACC vectors. c) $P'B$ contoured, $ACCB$ vectors. d) $P'DNL$ contoured, $ACCDNL$ vectors. e) $P'DL$ contoured, $ACCDL$ vectors. Vertical velocity shaded in all panels: levels of shading are 5 and 10 m s^{-1}. Contour intervals and vector scales are shown for each panel, and vary among panels. Terms are defined in § 2.2.3.

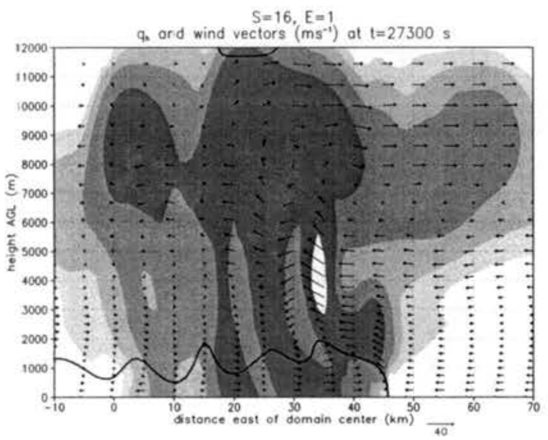

Figure 7.10: Total hydrometeor mixing ratio (levels of shading are 0.02, 0.08, 0.32, 1.28, and 5.12 g kg^{-1}) and wind vectors (m s^{-1}, scaled as shown) for the S=16, E=1 simulation at t =27300 s ($\approx$ 7.6 h). The θ'=–4.5 K isopleth is also plotted to show the cold pool's position.

accumulations of the Szeto and Cho (1994) feedback mechanism. As updrafts gradually begin to tilt more rearward with height (as opposed to the erect overturning updrafts of the quasi–stable FFLS stage), the minimum in P'B shifts rearward beneath the sloping patch of updraft buoyancy and the minimum in P'DNL begins to favor the vorticity zone between the rearward tilting updrafts and the rear–to–front flow in the surface outflow. In turn, more heated air is detrained and moves rearward from the updrafts, which begins to cancel the mesoscale gradient in P'B that once accelerated air forward. In the modeling study of Szeto and Cho (1994) this transition was "abrupt"; in the present simulations it takes more time, largely because the strong deep layer wind shear continues to render downshear ACCDL for developing updrafts. Nevertheless, as Figs. 7.7 and 7.8 show, significant changes in system speed and organization can occur on relatively short time scales.

As has been mentioned (recall Fig. 7.1), nearly every 2D FFLS simulation eventually evolved toward TS structure. This suggests that, although the parameter space in which 2D FFLS systems can occur is fairly broad (Section 7.1), the parameter space in which an FFLS system can be indefinitely long–lived (like its FFTS cousin) is quite small, if such a combination of parameters even exists at all (indeed, this study did not happen upon it). This has implications for the mean MCS lifetimes reported by Parker and Johnson (2000), who found that LS systems were much shorter–lived than TS systems on average. Because Parker and Johnson (2000) classified systems based upon their predominant organizational modes, they classified as TS any long–lived systems that had significant LS phases but evolved toward and persisted with TS structure for longer periods of time. The present study suggests that this transition is common and dynamically favored. Parker and Johnson (2000) found that 30% of the LS systems that they studied evolved into TS systems while 65% remained with LS structures until they decayed. This may mean that the relatively short mean lifetimes for LS systems reported by Parker and Johnson (2000) were symptoms that most of the longer–lived systems in their population evolved into a TS structure, and hence were not classified as LS in their study. Notably, however, the periodic–3D FFLS simulations in the present study were much more robust; only in experiments with extremely weak deep layer wind shear did the 3D systems evolve toward TS structure within the first 10 hours of simulation. Assuming that the Szeto and Cho (1994) hypothesis accurately describes the LS–TS transition, the greater resistance of 3D systems to this process is attributable to the generally smaller pressure perturbations that occur aft of their convective cells owing to the limited along–line extent of the individual convective eddies. Until more detailed case studies can be performed, it will remain unclear to what degree real world FFLS systems are 3D. Reflectivity data for the FFLS systems studied by Parker and Johnson (2000, e.g. their Fig. 6) did reveal individual cells along the systems' convective lines which, in a moderate–high shear regime, can imply a fairly large degree of local three–dimensionality (recall § 5.2 and § 7.1.2).

7.3 Dynamics of front–fed TS and rear–fed LS structures

In case studies, Parker and Johnson (2000) and Pettet (2001) noted the "mirror image" resemblance of several rear–fed LS (RFLS) systems to front–fed TS (FFTS) systems. Additionally, Parker et al. (2001) noted some gross similarities in their patterns of cloud–to–ground lightning. However, given the relatively coarse observational data that were used for those studies, it was unclear to those authors how similar were the dynamics of RFLS and FFTS systems. This section compares and contrasts the basic mesoscale features that occur in simulated 2D FFTS and RFLS systems, which occur at opposite ends of a surface cold pool for a given wind profile. Although it does not present a detailed analysis of the transient updrafts' dynamics (the importance of which was emphasized in earlier discussions), it describes them qualitatively in terms of their similarity to the FFLS structure and the basic physical principles which govern their differences. The reader may wish to return to the theoretical and quantitative underpinnings of this discussion in Chapter 3.

The mean environmental wind profiles for midlatitude FFTS systems generally possess a predominantly line–perpendicular wind shear vector directed from rear–to–front [e.g. Parker and Johnson (2000)'s Fig. 12]. The same is also true of the three RFLS case studies presented by Parker and Johnson (2000) and Pettet (2001). The difference, of course, is that the convective line is on an FFTS system's downshear side, but on an RFLS system's upshear side. As an additional caveat, the wind profiles from Parker and Johnson (2000)'s case (their Fig. 16) and at least one of the soundings from Pettet (2001)'s work (her Fig. 5.4a) show lower tropospheric jet profiles for RFLS cases, with reverse shear thereabove, hereafter abbreviated as "RFLS–jet".[2] The present study addressed the basic dynamics of convective systems in these three flow regimes by incorporating three simulations using the simple wind profiles in Fig. 7.11. Although the wind profiles in Fig. 7.11 are highly idealized, they are useful because they permit a more controlled experiment. They meet the basic criterion for the orientation of the shear vector with respect to the outflow boundary [as inferred from the Parker and Johnson (2000) and Pettet (2001) studies], and yet the FFTS and RFLS profiles are identical to one another in the troposphere (to within an added constant). This set–up completely isolated the role of the lower tropospheric shear vector's orientation with respect to the outflow boundary. A simultaneous simulation of both an FFTS system on a cold pool's eastern edge and an RFLS system on that cold pool's western edge (not shown) confirmed the correctness of this approach. The simulations with the RFLS–jet profile included an additional simple reverse shear layer above 3 km AGL, in order to address the possible importance of the middle and upper tropospheric shear in RFLS–jet cases.

Although the Hovmoller diagrams of 2 km AGL q_h (Fig. 7.12)[3] provide only limited in-

[2] Parker and Johnson (2000) noted that a similar jet profile in a rear–fed system was also identified by Fritsch et al. (1994).

[3] Note that the homogeneous regions of hydrometeor content that dissipate with time in both cases are symptoms of the artificial cold pool trigger's presence. Because the mixing ratio in the cold pool was unmodified, its high relative humidity and very weak local ascent combined to saturate the layer for awhile. This had no apparent impact on the

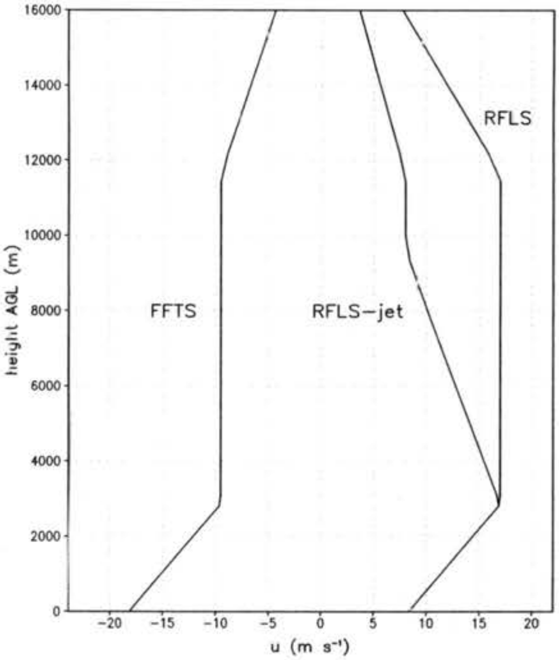

Figure 7.11: Profiles of u–wind used in the FFTS and RFLS experiments.

sight into the actual structures and dynamics of the RFLS and FFTS convective systems, they are important in that they bridge the gap between the base scan radar data investigated by Parker and Johnson (2000) and the present simulations. The horizontal shape and evolution of the 2D simulations summarized in Fig. 7.12 dovetail nicely with the quasi–2D structures that Parker and Johnson (2000) documented. As mentioned in Section 4.1, whereas surface rainfall rates > 1 mm h^{-1} extend only 20–25 km ahead of the convection in the FFLS simulations, they extend on the order of 100 km from the convective regions in the RFLS and FFTS simulations. Much as explained in Section 4.1, this is a symptom of basic differences in the system–scale flow structure; whereas the FFLS simulations possess strong storm–relative inflow within their stratiform precipitation regions, Fig. 7.13 shows that the FFTS and RFLS systems possess deep slanted conveyors that transport hydrometeors away from their convective lines throughout most of the troposphere, with little or no flow toward the convective line therein.

simulated convective systems. Additionally, some fine scale structures appear in Fig. 7.12; these occur largely because in 2D, with a fairly stationary gust front/outflow boundary, standing waves develop above the cold pool in the stratiform precipitation regions.

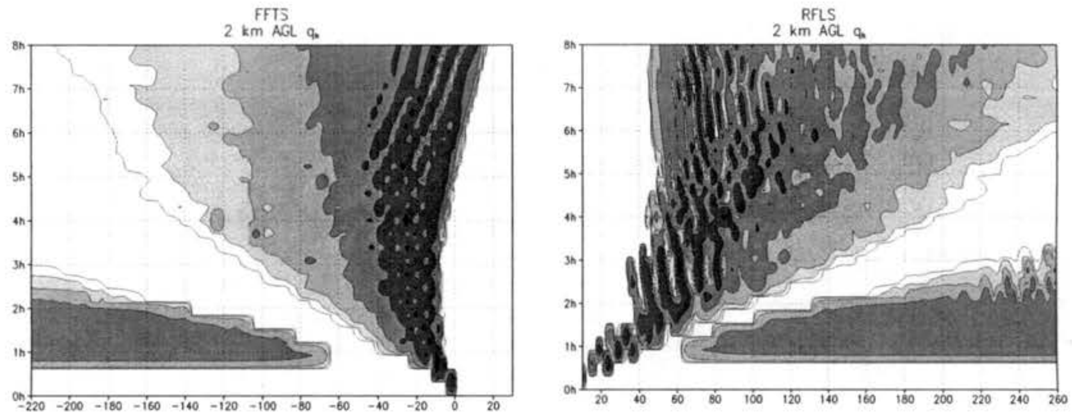

(a) (b)

Figure 7.12: Hovmoller diagram depicting 2 km AGL hydrometeor mixing ratio (from t=0–8 h) for a) FFTS and b) RFLS simulations. Levels of shading are 0.005, 0.02, 0.08, 0.32, 1.28, and 5.12 g kg^{-1}. See footnote 3 for discussion of the homogeneous regions of hydrometeor content that dissipate with time in both cases.

In many respects, the Hovmoller diagrams of q_h for the FFTS and RFLS simulations do indeed have mirror image similarity (Fig. 7.12). However, the vertical cross sections through the FFTS and RFLS systems reveal important differences (Fig. 7.13).[4] The updrafts in the FFTS simulation are, on average, stronger than those in the RFLS simulation. Indeed, it is difficult to see any mean upward motion for the RFLS case in Fig. 7.13b. The dynamical reasons for this are discussed shortly. As a result of the stronger updrafts and mesoscale ascent in the FFTS system, the vertically integrated hydrometeor content is much greater than in the RFLS simulation (cf. Fig. 7.13a and b), even though their 2 km AGL q_h Hovmoller diagrams look fairly similar to one another. Implicit in the greater condensate load for the FFTS system is that more latent heating has occurred, and hence the stratiform precipitation region contains more buoyancy (not shown). A symptom of this buoyancy is that the mesoscale quasi–hydrostatic P'B field is more perturbed in the FFTS system: the midlevel minimum in p' is about 1 hPa lower than that in the RFLS system, and the cloud top maximum in p' is about 1 hPa higher than that in the RFLS system (cf. Fig. 7.13a

[4] This demonstrates one drawback of Parker and Johnson (2000)'s base scan radar survey. Systems that look similar to one another in a plan view of reflectivity may have very different vertical structures and kinematic fields.

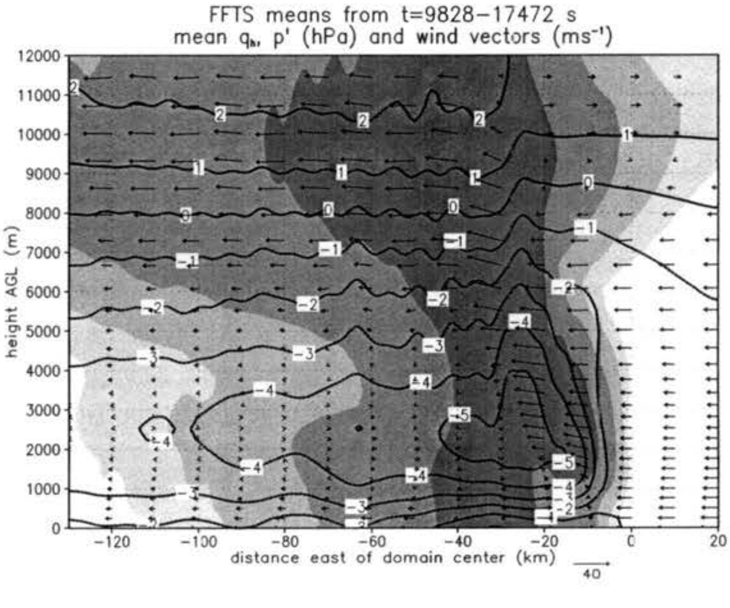

(a)

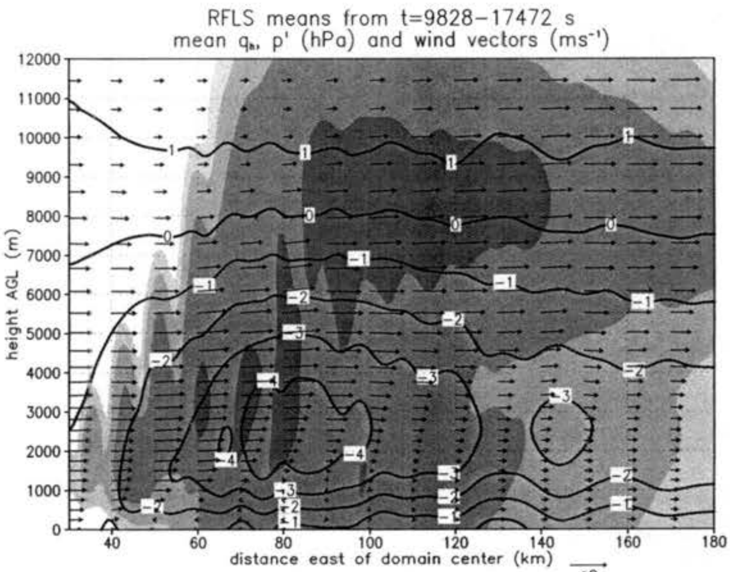

(b)

Figure 7.13: Mean total hydrometeor mixing ratio (levels of shading are 0.02, 0.08, 0.32, 1.28, and 5.12 g kg^{-1}), pressure pertubation (contours, hPa), and ground–relative wind vectors (m s^{-1}, scaled as shown) for a) FFTS and b) RFLS simulations.

and b). It is also dynamically important that the horizontal pressure gradient around 2–3 km AGL at the systems' leading edges is much larger in the FFTS than in the RFLS simulation (cf. Fig. 7.13a $x = -20$ to $x = 0$ km vs. Fig. 7.13b $x = 30$ to $x = 70$ km). The temporally averaged pressure perturbations in Fig. 7.13 are almost entirely attributable to P'B (not shown). Whereas the lack of strong localized w and the broad shallow slope of the q_h field in the RFLS system (Fig. 7.13b) imply gradual ascent as air moves forward, with a concomitant quasi–horizontal buoyancy field, the localized maxima in w and the erect column of maximized q_h in the FFTS system imply steeper ascent of the rearward flow, with a concomitant increase in the slope of the buoyancy field. Hence, the sharp gradient in p' for the FFTS case is largely attributable to the more erect buoyancy field of its ascending airstream.

Because the only initial difference between the FFTS and RFLS simulations is the side of the cold pool on which the convection is initiated, it is fairly easy to describe the dynamical differences between the simulations in the early going. In Rotunno et al. (1988)'s way of thinking, η of the environmental air parcels and $D\eta/Dt$ owing to the cold pool are opposite–signed for the FFTS system, but same signed for the RFLS system [recall equation (6.3)]. Or, more appropriately (following § 6.1), for the FFTS case the downshear ACCDL for a gust front updraft opposes the rearward ACCB and ACCDNL owing to the cold pool's pressure field, whereas for the RFLS case ACCDL acts in the same direction as ACCB and ACCDNL. After 1092 s (18.2 min), the initial updrafts produced in the two simulations are quite different from one another (Fig. 7.14). By this time, the FFTS system has produced a healthy updraft (with $w > 16$ m s^{-1}) that extends upward to approximately 5 km AGL (Fig. 7.14a). Meanwhile, the RFLS simulation has produced a weak updraft ($w < 4$ m s^{-1}) that slopes strongly downshear and has little vertical extent (Fig. 7.14b). Much as shown by Moncrieff and Liu (1999), the edge of the cold pool in much steeper on its downshear (i.e. Fig. 7.14a) than on its upshear (i.e. Fig. 7.14b) side.

To understand why the simulations are so different by $t = 1092$ s, it is useful to analyze the accelerations in the early going, at $t = 119$ s (Figs. 7.15 and 7.16). In both cases, ACCB is initially almost identical (Figs. 7.15c and 7.16c), as it should be given the two simulations identical initial cold pool shapes and strengths. The upward ACCB at the edge of the cold pool increases with height over the lowest 1 km AGL, and this renders a maximum in w at approximately 1.5 km AGL as inflowing air parcels move through the forcing (Figs. 7.15a and 7.16a). In the presence of a mean shear, this causes P'DL to be most perturbed around 1.5 km AGL [recall eq. (3.2) and see Figs. 7.15e and 7.16e]. In both simulations, this induces an eastward ACCDL that increases with height at and on the warm side of the outflow boundary. This renders a more erect cold air nose in the FFTS simulation and a more sloped cold air nose in the RFLS simulation. In time, the slope of the cold air's nose then feeds back into the process because the steeper outflow boundary in the FFTS case produces deeper lifting via ACCB than does the shallow wedge of cold air in the RFLS case. Additionally, the vertical profile of convergence at the gust front (decreasing with height in the FFTS case, increasing with height in the RFLS case) renders different vertical profiles of P'DNL at the FFTS and RFLS gust fronts (Figs. 7.15d and 7.16d). Because P'DNL decreases with height at the gust front in the FFTS simulation it provides an additional upward ACCDNL that doesn't occur in the RFLS simulation (cf. Figs. 7.15d at x = 2–4 km vs. 7.16d). Finally, as the more erect outflow boundary in the FFTS simulation produces a stronger gust front updraft, P'DL increases and the downshear ACCDL further assists the updraft's development by giving air parcels more upright trajectories and allowing them to spend more time in the zone of deep upward forcing as they move rearward through it. In contrast, any contribution from ACCDL in the RFLS simulation will only accelerate the air parcels more strongly forward. These accumulated differences in ACCDL, ACCB, and ACCDNL result in the huge disparity between the FFTS and RFLS simulations by t = 1092 s (Fig. 7.14).

The Hovmoller diagram of 2 km AGL q_h for the RFLS–jet simulation was incredibly similar to that for the base RFLS case (Fig. 7.17). And, because their 0–3 km wind profiles were identical and the convection in both simulations was initiated on the upshear side of the initial cold pool, their low–level dynamics and evolution in the early going were almost identical (not shown). However, the temporally averaged vertical cross section through the mature RFLS–jet system (Fig. 7.18) reveals that its structure lies somewhere between the RFLS and "mirror image" FFTS extremes.

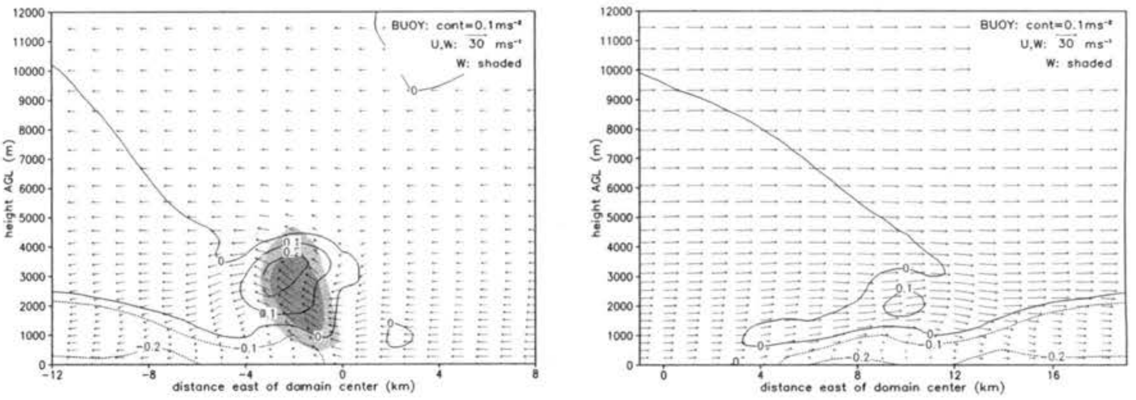

(a) FFTS (b) RFLS

Figure 7.14: Buoyancy and wind vectors at t = 1092 s for a) FFTS and b) RFLS simulations. Vertical velocity shaded at 5 and 10 m s^{-1}. Contour intervals and vector scales are shown for each panel.

In particular, the mean w is slightly larger in the RFLS–jet simulation, the hydrometeor content is greater and the pressure field is correspondingly more perturbed. Although a deep plume of significant w is still not evident in Fig. 7.18, the q_h field is more erect, and analysis of the RFLS–jet system's temporally varying fields revealed that individual updrafts were indeed more erect. The only difference between the RFLS and RFLS–jet simulations is the addition of the reverse shear aloft in the RFLS–jet environment. Therefore, the clear dynamical reason for the more upright structure in the RFLS–jet system is the westward ACCDL owing to the existence of easterly shear above 3 km AGL, along with some of the higher order feedbacks that were discussed in Section 3. In a sense, then, the front–to–rear ACCDL aloft compensates in part for the rear–to–front ACCDL in low levels. Given the observations of jet profiles by Parker and Johnson (2000) and Pettet (2001), the middle and upper tropospheric ACCDL may be an important dynamical component in rendering fairly upright convection in real–world RFLS systems such as documented by Pettet (2001).

Notably, both Parker and Johnson (2000) and Pettet (2001) found that the highest–θ_e rear–to–front inflow for some RFLS systems was not rooted in a surface mixed layer. Because these systems were mostly nocturnal, the near–surface boundary layer was generally stable, and the systems updrafts were likely ingesting air from the remnants of the previous day's convectively mixed

FFTS at 119 s

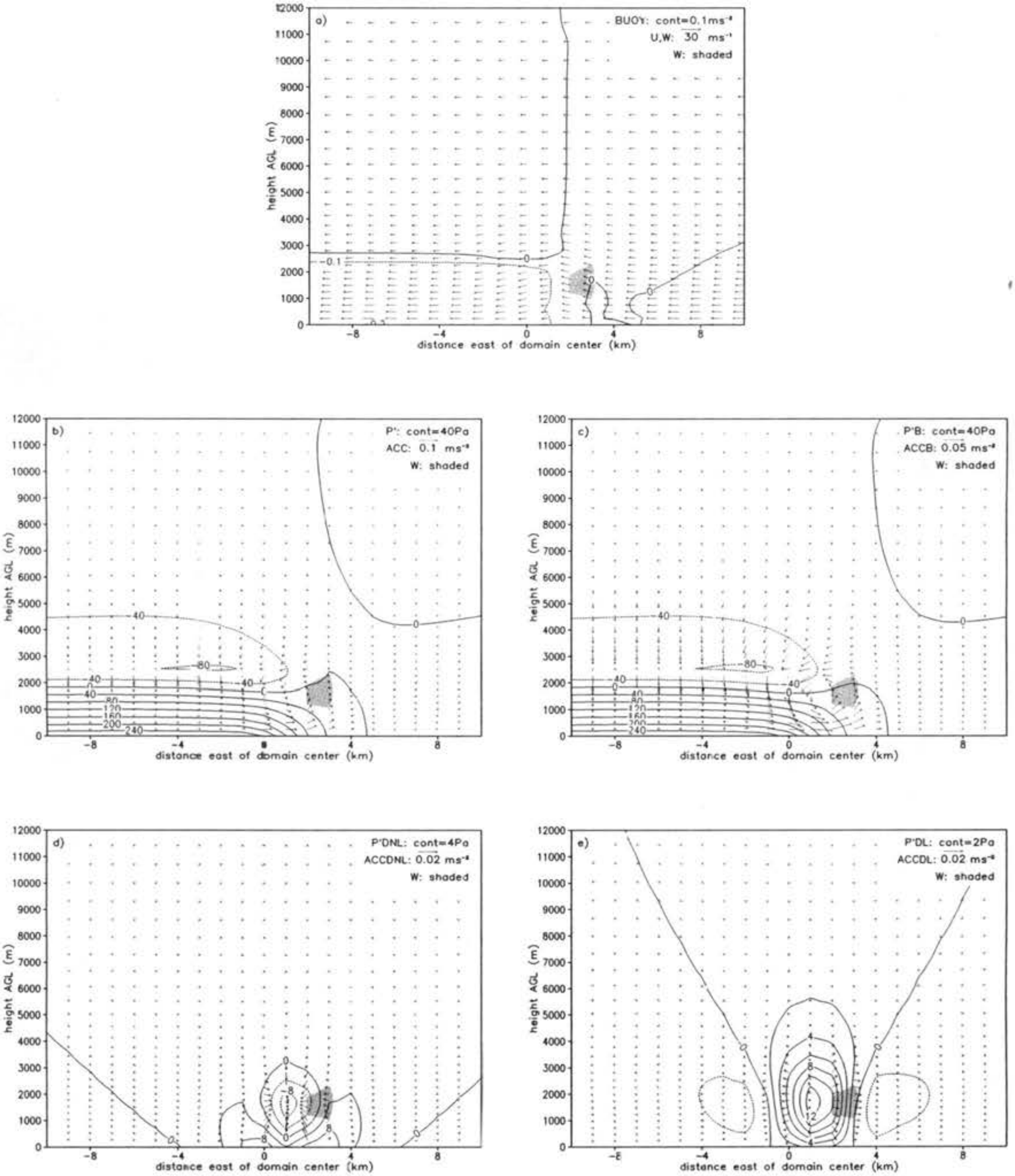

Figure 7.15: Velocities, perturbation pressures, and acceleration terms for simulation FFTS at 119 s. a) $BUOY$ contoured, u and w vectors. b) P' contoured, ACC vectors. c) $P'B$ contoured, $ACCB$ vectors. d) $P'DNL$ contoured, $ACCDNL$ vectors. e) $P'DL$ contoured, $ACCDL$ vectors. Vertical velocity shaded in all panels: levels of shading are 3 and 6 m s^{-1}. Contour intervals and vector scales are shown for each panel, and vary among panels. Terms are defined in § 2.2.3.

RFLS at 119 s

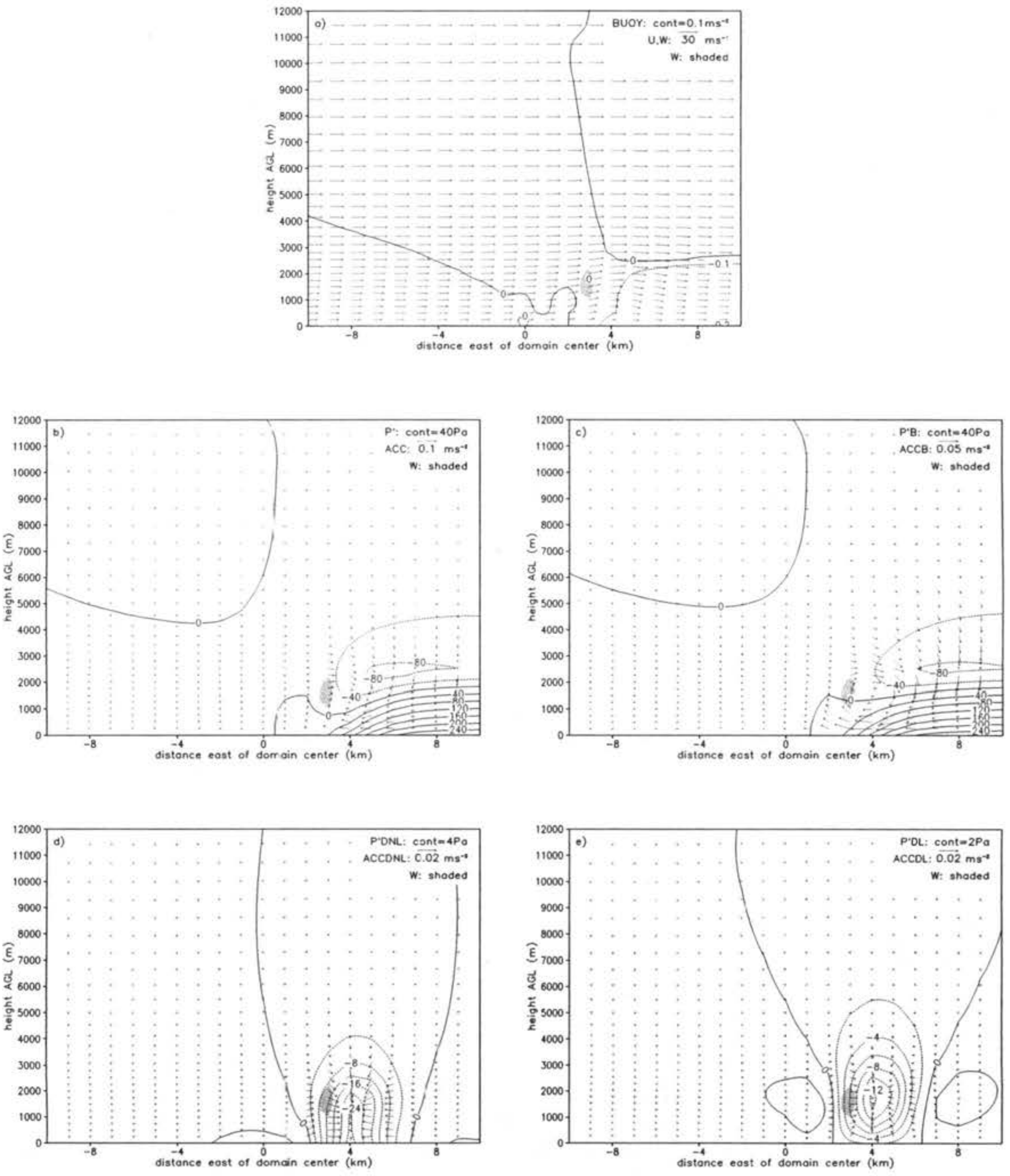

Figure 7.16: Velocities, perturbation pressures, and acceleration terms for simulation RFLS at 119 s. a) $BUOY$ contoured, u and w vectors. b) P' contoured, ACC vectors. c) $P'B$ contoured, $ACCB$ vectors. d) $P'DNL$ contoured, $ACCDNL$ vectors. e) $P'DL$ contoured, $ACCDL$ vectors. Vertical velocity shaded in all panels: levels of shading are 3 and 6 m s^{-1}. Contour intervals and vector scales are shown for each panel, and vary among panels. Terms are defined in § 2.2.3.

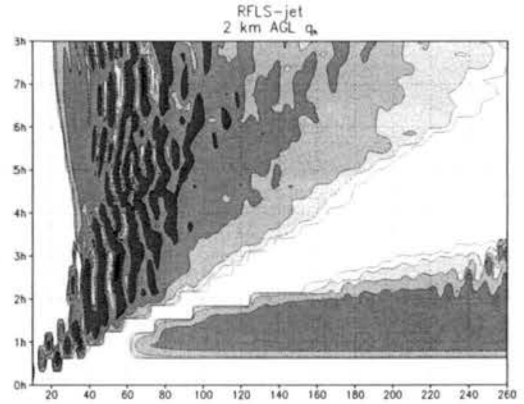

Figure 7.17: Hovmoller diagram depicting 2 km AGL hydrometeor mixing ratio (from t=0–8 h) for RFLS–jet simulation. Levels of shading are 0.005, 0.02, 0.08, 0.32, 1.28, and 5.12 g kg^{-1}.

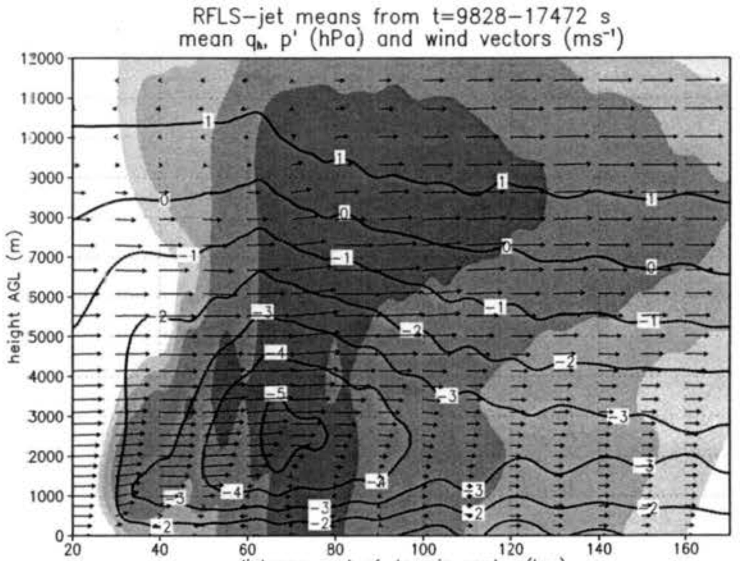

Figure 7.18: Mean total hydrometeor mixing ratio (levels of shading are 0.02, 0.08, 0.32, 1.28, and 5.12 g kg^{-1}), pressure pertubation (contours, hPa), and wind vectors (m s^{-1}, scaled as shown) for RFLS–jet simulation.

boundary layer. In addition, horizontal transports by a low–level jet could further increase the local θ_e above the nocturnal stable layer. Such scenarios are somewhat too complicated for the idealized modeling approach of the present study. However, this is not to say that elevated θ_e maxima aren't important to the basic processes of RFLS systems. One possibility is that elevated rear inflow into RFLS systems can partly escape the large downshear ACCB and ACCDNL that the cold pool imposes on the near surface inflowing air. As suggested by Pettet (2001), additional studies with fine scale thermodynamic observations and dual–Doppler radar data are needed to resolve the local details of this potentially important process. Numerical simulations of RFLS systems using more realistic midlatitude nocturnal boundary layers would also more shed light on the problem.

Chapter 8

CONCLUDING REMARKS

8.1 Synthesis of FFLS structure and dynamics

Chapters 4 – 7 discussed the basic quasi–stable and periodic structures of simulated convective lines with leading precipitation (FFLS systems). The mesoscale, along–line and temporally averaged fields in the 2D and periodic–3D simulations were quite similar to one another. Although this publication emphasized the importance of the transient accelerations on updraft air parcels, the systems also have important persistent effects on their mesoscale environments. Firstly, the systems provide destabilization to inflowing lower and middle tropospheric air because they impose a profile of chilling by evaporation and melting that increases with height, and because they perturb their pre–line pressure fields in a way that favors ascent; this allows the FFLS structure to be quasi–stable over long periods of time (3 h in 2D, $>$ 6 h in 3D). Secondly, owing to a persistent pressure minimum that occurs on the line–leading side of the systems in the middle troposphere (owing to the buoyancy of the leading precipitation region and to the curvature of the overturning mean updraft), the system contributes to the development of a front–to–rear middle tropospheric inflow jet. In turn, this mid–level jet constitutes a decrease in the lower tropospheric vertical wind shear and an increase in the upper tropospheric wind shear. As a result, the mesoscale quasi–stable flow field feeds back into the transient accelerations via horizontal gradients in non–linear part of the dynamic pressure perturbation (P'DNL) owing to ascent within the persistent perturbation wind shear.

Fundamental transient dynamical processes force updraft parcels downshear by some combination of buoyant, dynamic linear, and dynamic non–linear accelerations (ACCB, ACCDL, and ACCDNL, respectively). The downshear–directed ACCB is attributable to the downshear tilt of the buoyant updrafts and to the mesoscale gradients in buoyancy associated with the FFLS system itself. The downshear–directed ACCDL is attributable to the presence of an updraft in shear. The downshear–directed ACCDNL is attributable to the curvature of the updraft itself and to the presence of the updraft in a profile with perturbed vertical shear. The integrated effects of the these downshear accelerations are overturning updraft trajectories, with air parcels carrying their total water content into the pre–line region, where they begin to compose a leading precipitation region. Eventually, for each updraft cycle there is a point of cut–off when inflowing air parcels experience downward accelerations owing to hydrometeor loading as they approach the updraft. The production of a strong downdraft then intensifies the surface outflow and thereby sets the stage for the next convective cycle. So long as the mesoscale pressure field remains in its quasi–stable configuration, this process occurs periodically and comprises an FFLS multicellular convective system. The period for the multicellular oscillations is apparently determined by the speed with which the forcing is advected by the mean flow, as well as the time required for convective cells to produce precipitation and downdrafts.

8.2 Indicated future work

This publication has described results from idealized numerical simulations. Undoubtedly, we need studies with observational data to verify the details presented in the text more rigorously and to learn more about the near–line environments in real–world FFLS systems. In particular, dual–Doppler radar analyses of the wind field along with spatially fine rawinsonde observations are needed to carry out the kind of analyses presented in this publication. Unfortunately, such measurements are not on the near horizon for non–classical convective systems. Until such a time as our community can mount a field campaign to make these kinds of high resolution observations, real–world case studies will be restricted to operational data, which are sparse at best.

In the mean time, additional numerical studies of non–classical convective systems may bear fruit, despite the philosophical drawbacks to simulating systems for which detailed measurements have not yet been made. Certainly, future studies could attempt less idealized simulations of FFLS systems, including line–end effects, Coriolis accelerations, radiation, and surface fluxes. Following this suggestion to its logical end, scientists could also attempt to simulate real–world FFLS case studies. As well, given the importance of melting and evaporation in destabilizing the inflowing air (§ 4.2), more detailed studies of the systems' sensitivity to the model's microphysical parameterization (i.e. beyond simple variations in evaporation rate, graupel fallspeed, etc.) would be worthwhile. In this study, the structure and evolution of systems in moderate and high shear regimes were sensitive to the pattern of convective initiation. This appears to be fertile ground for future research: the wide variety of convective triggers in the atmosphere may in part account for the numerous convective structures and evolutionary pathways that we commonly observe. Additionally, as discussed in Section 7.1.2, the FFLS convective regime appears to border or overlap the supercellular regime. A fuller understanding of the FFLS–supercell continuum would be of interest to forecasters and warning meteorologists, who often must make decisions between tornado and severe thunderstorm watches and warnings based on sparse data. Along slightly different lines, Section 6.3 also provides some ideas for analysis of the presence and dynamical importance of gravity waves in FFLS systems.

Finally, a great deal of latitude for experimentation and discovery still remains with respect to the similarities and differences among the convective modes identified by Parker and Johnson (2000). This study did not address convective lines with parallel precipitation. Parker et al. (2001) found some interesting lightning characteristics in these systems, suggesting that they may have some unique dynamical and microphysical features. There is good reason to believe that they can be represented in idealized 3D simulations, and future work to this end might would likely be worthwhile. Additionally, Parker (2001) found from simple simulations that the geometry of linear convective systems could have important effects on how gravity waves destabilized the environment in a resting base state. Later simulations with mean flow, however, exhibited more complicated behavior, and the experiment was tabled. Nevertheless, these kinds of simple idealized simulations have the potential to reveal low–hanging fruit, and are worthy of future consideration.

8.3 Summary

This work utilized the Advanced Regional Prediction System (ARPS) to simulate convective lines with leading precipitation. Using a typical mid–latitide MCS environment and a mean wind profile from archetypal cases, the model simulated a front–fed convective line with leading precipitation (FFLS). Primary findings include:

- In both 2D and periodic–3D simulations, the FFLS systems were quasi–stable, with inflowing air passing through pre–line precipitation and ascending in convective cells that developed periodically.
- The 2D FFLS system's mean flow corresponded extremely well with an analytic density current model developed by Liu and Moncrieff (1996). Its effects on the environment can be partly understood using this analytic model.
- Inflowing air was destabilized by lifting and by the vertical profile of evaporation and melting as it passed through the line–leading precipitation region. This process helped to maintain the simulated FFLS systems.
- In purely 2D simulations, the leading precipitation region almost entirely comprises air parcels that have ascended in the convective updrafts. In 3D simulations, however, upper tropospheric environmental air is able to flow between convective updrafts and into the pre–line region.
- Periodic–3D simulations of FFLS systems are somewhat more complicated than 2D simulations, largely because they render localized 3D, rather than slab–symmetric 2D, convective updrafts. The updrafts in the 3D simulations are stronger and more erect, but the general system properties of the 3D and 2D systems are still quite similar to one another.
- The accelerations causing inflowing air parcels to ascend and overturn in deep convective updrafts are transient, and can't be realistically extrapolated from temporally averaged fields. Inflowing air in the lower troposphere is periodically lifted by the buoyant and dynamic pressure field near the outflow boundary and gust front. During active phases of the multicellular system, the vertical

pressure gradient lifts the air to its level of free convection (LFC); thereafter, the horizontal gradients in the buoyant, linear dynamic, and non–linear dynamic pressure fields all contribute to the downshear accelerations of air parcels in the system updrafts. During the suppressed phases of the multicellular system, inflowing air cannot attain its LFC above the outflow boundary owing to negative buoyancy.

- The period at which fresh convection is initiated, develops, and decays appears to be related to a precipitation cut–off mechanism, whereby developing precipitation on the downshear side of updrafts periodically falls into the inflowing airstream and causes it to be negatively buoyant owing to evaporative chilling and water loading.
- The conceptual squall line model of Rotunno et al. (1988, "RKW theory") is inadequate in situations with deep vertical wind shear. It also provides little physical insight into the velocities and trajectories of air parcels, which this publication has argued to be important to system structure.
- The simulated convective systems exhibited well–known sensitivities to the evaporation rate and to environmental paramaters such as wind shear, CAPE, and humidity. Importantly, the sensitivity tests revealed that the periodic–3D FFLS structure is relatively robust, and can occur over a fairly large parameter space in regimes with moderate–to–strong shear.
- Rear–fed systems with leading precipitation (RFLS) are indeed quite similar to front–fed systems with trailing precipitation (FFTS). However, the downshear accelerations owing to the horizontal gradient in the linear dynamic pressure field cause the FFTS updrafts to be much more erect than those in the RFLS systems.
- All of the simulated 2D FFLS systems evolved toward an FFTS structure, owing to intensification of their outflows and the eventual develpoment of a post–line mid-level pressure minimum as described by Szeto and Cho (1994). The periodic–3D simulations produced much longer–lived FFLS systems, in part because they did not develop such large post–line pressure minima.

This study represents a first attempt to understand the basic dynamics of convective lines with leading precipitation. Future work with high resolution data and more sophisticated numerical simulations will help in further evaluating and expanding on these conclusions.

BIBLIOGRAPHY

Biggerstaff, M. I., and R. A. Houze, Jr., 1991: Kinematic and precipitation structure of the 10–11 June 1985 squall line. *Mon. Wea. Rev.*, **119**, 3034–3065.

Blanchard, D. O., 1990: Mesoscale convective patterns of the southern High Plains. *Bull. Amer. Meteor. Soc.*, **71**, 994–1005.

Bluestein, H. B., and M. H. Jain, 1985: Formation of mesoscale lines of precipitation: Severe squall lines in Oklahoma during the spring. *J. Atmos. Sci.*, **42**, 1711–1732.

Bryan, G. H., and M. J. Fritsch, 2000: Moist absolute instability: The sixth static stability state. *Bull. Amer. Meteor. Soc.*, **81**, 1207–1230.

Charba, J., 1974: Application of gravity current model to analysis of squall–line gust front. *Mon. Wea. Rev.*, **102**, 140–156.

Cram, J. M., R. A. Pielke, and W. R. Cotton, 1992: Numerical simulation and analysis of a prefrontal squall line. Part II: Propagation of the squall line as an internal gravity wave. *J. Atmos. Sci.*, **49**, 209–225.

Doswell, C. A., III, H. E. Brooks, and R. A. Maddox, 1996: Flash flood forecasting: An ingredients–based methodology. *Wea. Forecasting*, **11**, 560–581.

Dudhia, J., M. W. Moncrieff, and D. W. K. So, 1987: The two–dimensional of West African squall lines. *Quart. J. Roy. Meteor. Soc.*, **113**, 121–146.

Durran, D. R., and J. B. Klemp, 1983: A compressible model for the simulation of moist mountain waves. *Mon. Wea. Rev.*, **111**, 2341–2361.

Eitzen, Z. A., 2001: Simulation and parameterization of vertically propagating convectively generated gravity waves. Ph.D. dissertation, Colorado State University, 203 pp. [Available from Department of Atmospheric Science, Colorado State University, Fort Collins, CO, 80523-1371.]

Emanuel, K. A., 1994: *Atmospheric Convection.* Oxford Univ. Press, 580 pp.

Fankhauser, J. C., G. M. Barnes, and M. A. LeMone, 1992: Structure of a midlatitude squall line formed in strong unidirectional shear. *Mon. Wea. Rev.*, **120**, 237–260.

Fovell, R. G., 2002: Upstream influence of numerically simulated squall–line storms. *Mon. Wea. Rev.*, **126**, 551–577.

Fovell, R. G., and P. S. Dailey, 1995: The temporal behavior of numerically simulated multicell–type storms. Part I: Modes of behavior. *J. Atmos. Sci.*, **52**, 2073–2095.

Fovell, R. G., and Y. Ogura, 1988: Numerical simulation of a midlatitude squall line in two dimensions. *J. Atmos. Sci.*, **45**, 3846–3879.

Fovell, R. G., and P.-H. Tan, 1998: The temporal behavior of numerically simulated multicell–type storms. Part II: The convective cell life cycle and cell regeneration. *Mon. Wea. Rev.*, **126**, 551–577.

Fritsch, J. M., J. D. Murphy, and J. S. Kain, 1994: Warm-core vortex amplification over land. *J. Atmos. Sci.*, **51**, 1780–1807.

Grady, R. L., and J. Verlinde, 1997: Triple–Doppler analysis of a discretely propagating, long–lived, High Plains squall line. *J. Atmos. Sci.*, **54**, 2729–2748.

Gray, M. E. B., 2000: Characteristics of numerically simulated mesoscale convective systems and their application to parameterization. *J. Atmos. Sci.*, **57**, 3953–3970.

Hane, C. E., 1973: The squall line thunderstorm: Numerical experimentation. *J. Atmos. Sci.*, **30**, 1672–1690.

Houze, R. A., Jr., and E. N. Rappaport, 1984: Air motions and precipitation structure of an early summer squall line over the eastern tropical Atlantic. *J. Atmos. Sci.*, **41**, 553–574.

Houze, R. A., Jr., S. A. Rutledge, M. I. Biggerstaff, and B. F. Smull, 1989: Interpretation of Doppler weather radar displays of midlatitude mesoscale convective systems. *Bull. Amer. Meteor. Soc.*, **70**, 608–619.

Houze, R. A., Jr., B. F. Smull, and P. Dodge, 1990: Mesoscale organization of springtime rainstorms in Oklahoma. *Mon. Wea. Rev.*, **118**, 613–654.

Iribarne, J. V., and W. L. Godson, Eds., 1981: *Atmospheric Thermodynamics*. D. Reidel Publishing, 259 pp.

Johnson, R. H., and M. D. Parker, 2001: Mesoscale convective systems and floods: A review. Preprints, *Symposium on Precipitation Extremes: Prediction, Impacts, and Responses*, Albuquerque, NM, Amer. Meteor. Soc., 102–106.

Kessinger, C. J., P. S. Ray, and C. E. Hane, 1987: The Oklahoma squall line of 19 May 1977. Part I: A multiple Doppler analysis of convective and stratiform structure. *J. Atmos. Sci.*, **44**, 2840–2864.

Kessler, E., 1969: On the distribution and continuity of water substance in atmospheric circulations. *Meteor. Monogr.*, No. 32, Amer. Meteor. Soc., 1–84.

Klemp, J. B., and R. B. Wilhelmson, 1978: The simulation of three-dimensional convective storm dynamics. *J. Atmos. Sci.*, **35**, 1070–1096.

Lafore, J.-P., and M. W. Moncrieff, 1989: A numerical investigation of the organization and interaction of the convective and stratiform regions of tropical squall lines. *J. Atmos. Sci.*, **46**, 521–544.

LeMone, M. A., 1983: Momentum transport by a line of cumulonimbus. *J. Atmos. Sci.*, **51**, 281–305.

Lilly, D. K., 1986: The structure, energetics and propagation of rotating convective storms. Part II: Helicity and storm stabilization. *J. Atmos. Sci.*, **43**, 126–140.

Lin, Y.-L., R. L. Deal, and M. S. Kulie, 1998: Mechanisms of cell regeneration, development, and propagation within a two–dimensional multicell storm. *J. Atmos. Sci.*, **55**, 1867–1886.

Lin, Y.-L., R. D. Farley, and H. D. Orville, 1983: Bulk parameterization of the snow field in a cloud model. *J. Climate Appl. Meteor.*, **22**, 1065–1092.

Lin, Y.-L., and L. E. Joyce, 2001: A further study of the mechanisms of cell regeneration, propagation, and development within two–dimensional multicell storms. *J. Atmos. Sci.*, **58**, 2957–2988.

Liu, C., and M. W. Moncrieff, 1996: A numerical study of the effects of ambient flow and shear on density currents. *Mon. Wea. Rev.*, **124**, 2282–2303.

Mapes, B. E., 1993: Gregarious tropical convection. *J. Atmos. Sci.*, **50**, 2026–2037.

Markowski, P. M., 2002: Hook echoes and rear–flank downdrafts: A review. *Mon. Wea. Rev.*, **130**, 852–876.

Moncrieff, M. W., 1992: Organized convective systems: Archetypal dynamical models, mass and momentum flux theory, and parameterization. *Quart. J. Roy. Meteor. Soc.*, **118**, 819–850.

Moncrieff, M. W., and E. Klinker, 1997: Organized convective systems in the tropical western Pacific as a process in general circulation models: A TOGA COARE case–study. *Quart. J. Roy. Meteor. Soc.*, **123**, 805–827.

Moncrieff, M. W., and C. Liu, 1999: Convective initiation by density currents: Role of convergence, shear, and dynamical organization. *Mon. Wea. Rev.*, **127**, 2455–2464.

Nachamkin, J. E., and W. R. Cotton, 2000: Interactions between a developing mesoscale convective system and its environment. Part I: Numerical simulation. *Mon. Wea. Rev.*, **128**, 1225–1244.

Nachamkin, J. E., R. L. McAnelly, and W. R. Cotton, 2000: Interactions between a developing mesoscale convective system and its environment. Part I: Observational analysis. *Mon. Wea. Rev.*, **128**, 1205–1224.

Newton, C. W., 1950: Structure and mechanism of the prefrontal squall line. *J. Meteor.*, **7**, 210–222.

Newton, C. W., and J. C. Fankhauser, 1964: On the movements of convective storms, with emphasis on size discrimination in relation to water–budget requirements. *J. Appl. Meteor.*, **3**, 651–668.

Nicholls, M. E., R. H. Johnson, and W. R. Cotton, 1988: The sensitivity of two–dimensional simulations of tropical squall lines to environmental profiles. *J. Atmos. Sci.*, **45**, 3625–3649.

Nicholls, M. E., R. A. Pielke, and W. R. Cotton, 1991: Thermally forced gravity waves in an atmosphere at rest. *J. Atmos. Sci.*, **48**, 1869–1884.

Ogura, Y., and M.-T. Liou, 1980: The structure of a midlatitude squall line: A case study. *J. Atmos. Sci.*, **37**, 553–567.

Ogura, Y., and T. Takahashi, 1971: Numerical simulation of the life cycle of a thunderstorm cell. *Mon. Wea. Rev.*, **99**, 895–911.

Orlanski, I., 1975: A rational subdivision of scales for atmospheric processes. *Bull. Amer. Meteor. Soc.*, **56**, 527–530.

Orlanski, I., 1976: A simple boundary condition for unbounded hyperbolic flows. *J. Comput. Phys.*, **21**, 251–269.

Pandya, R. E., and D. R. Durran, 1996: The influence of convectively generated thermal forcing on the mesoscale circulation around squall lines. *J. Atmos. Sci.*, **53**, 2924–2951.

Parker, M. D., 2001: Simulated gravity waves produced by MCS–like heating profiles: MCS geometry and its effects on the environment. Preprints, *9th Conf. Mesoscale Processes*, Fort Lauderdale, FL, Amer. Meteor. Soc., 514–518.

Parker, M. D., and R. H. Johnson, 2000: Organizational modes of midlatitude mesoscale convective systems. *Mon. Wea. Rev.*, **128**, 3413–3436.

Parker, M. D., S. A. Rutledge, and R. H. Johnson, 2001: Cloud–to–ground lightning in linear mesoscale convective systems. *Mon. Wea. Rev.*, **129**, 1232–1242.

Pettet, C. R., 2001: Airflow and precipitation structure of two leading stratiform mesoscale convective systems. M.S. thesis, Department of Atmospheric Science, Colorado State University, 106 pp. [Available from Department of Atmospheric Science, Colorado State University, Fort Collins, CO, 80523-1371.]

Rotunno, R., J. B. Klemp, and M. L. Weisman, 1988: A theory for strong, long–lived squall lines. *J. Atmos. Sci.*, **45**, 463–485.

Rutledge, S. A., and R. A. Houze, Jr., 1987: A diagnostic modeling study of the trailing stratiform region of a midlatitude squall line. *J. Atmos. Sci.*, **44**, 2640–2656.

Rutledge, S. A., R. A. Houze, Jr., M. I. Biggerstaff, and T. Matejka, 1988: The Oklahoma-Kansas mesoscale convective system of 10–11 June 1985: Precipitation structure and single-Doppler radar analysis. *Mon. Wea. Rev.*, **116**, 1409–1430.

Schiesser, H. H., R. A. Houze, Jr., and H. Huntreiser, 1995: The mesoscale structure of severe precipitation systems in Switzerland. *Mon. Wea. Rev.*, **123**, 2070–2097.

Schlesinger, R. E., 1984: Effects of the perturbation pressure field in numerical models of unidirectionally sheared thuderstorm convection: Two versus three dimensions. *J. Atmos. Sci.*, **41**, 1571–1587.

Schmidt, J. M., and W. R. Cotton, 1990: Interactions between upper and lower tropospheric gravity waves on squall line structure and maintenance. *J. Atmos. Sci.*, **47**, 1205–1222.

Schultz, P., 1995: An explicit cloud physics parameterization for operational numerical weather prediction. *Mon. Wea. Rev.*, **123**, 3331–3343.

Seitter, K. L., and H.-L. Kuo, 1983: The dynamical structure of squall–line type thunderstorms. *J. Atmos. Sci.*, **40**, 2831–2854.

Smull, B. F., and R. A. Houze, Jr., 1985: A midlatitude squall line with a trailing region of stratiform rain: Radar and satellite observations. *Mon. Wea. Rev.*, **113**, 117–133.

Smull, B. F., and R. A. Houze, Jr., 1987a: Dual–Doppler radar analysis of a midlatitude squall line with a trailing region of stratiform rain. *J. Atmos. Sci.*, **44**, 2128–2148.

Smull, B. F., and R. A. Houze, Jr., 1987b Rear inflow in squall lines with trailing stratiform precipitation. *Mon. Wea. Rev.*, **115**, 2869–2889.

Soong, S.-T., and Y. Ogura, 1973: A comparison between axisymmetric and slab–symmetric cumulus cloud models. *J. Atmos. Sci.*, **30**, 879–893.

Stull, R. B., 1988: *An Introduction to Boundary Layer Meteorology*. Kulwer Academic Publishers, 666 pp.

Szeto, K. K., and H.-R. Cho, 1994: A numerical investigation of squall lines. Part II: The mechanics of evolution. *J. Atmos. Sci.*, **51**, 425–433.

Tao, W.-K., and J. Simpson, 1993: Goddard Cumulus Ensemble Model. Part I: Model description. *TAO*, **4**, 35–72.

Thorpe, A. J., M. J. Miller, and M. W. Moncrieff, 1982: Two–dimensional convection in non–constant shear: A model of midlatitude squall lines. *Quart. J. Roy. Meteor. Soc.*, **108**, 739–762.

Tripoli, G. J., and W. R. Cotton, 1989a: Numerical study of an observed orogenic mesoscale convective system. Part 1: Simulated genesis and comparison with observations. *Mon. Wea. Rev.*, **117**, 273–304.

Tripoli, G. J., and W. R. Cotton, 1989b: Numerical study of an observed orogenic mesoscale convective system. Part 2: Analysis of governing dynamics. *Mon. Wea. Rev.*, **117**, 305–328.

Weisman, M. L., and J. B. Klemp, 1982: The dependence of numerically simulated convective storms on vertical wind shear and buoyancy. *Mon. Wea. Rev.*, **110**, 504–520.

Weisman, M. L., J. B. Klemp, and R. Rotunno, 1988: Structure and evolution of numerically simulated squall lines. *J. Atmos. Sci.*, **45**, 1990–2013.

Weisman, M. L., W. C. Skamarock, and J. B. Klemp, 1997: The resolution dependence of explicitly modeled convective systems. *Mon. Wea. Rev.*, **125**, 527–548.

Xue, M., K. K. Droegemeier, and V. Wong, 2000: The Advanced Regional Prediction System (ARPS) - A multiscale nonhydrostatic atmospheric simulation and prediction tool. Part I: Model dynamics and verification. *Meteor. Atmos. Phys.*, **75**, 161–193.

Xue, M., K. K. Droegemeier, V. Wong, A. Shapiro, and K. Brewster, 1995: *Advanced Regional Prediction System version 4.0 users guide*. Center for the Analysis and Prediction of Storms, Norman, Oklahoma. [Available from ARPS Model Development Group, CAPS, University of Oklahoma, 100 East Boyd, Norman, OK 73019-0628.]

Xue, M., K. K. Droegemeier, V. Wong, A. Shapiro, K. Brewster, F. Carr, D. Weber, Y. Liu, and D.-H. Wang, 2001: The Advanced Regional Prediction System (ARPS) - A multiscale nonhydrostatic atmospheric simulation and prediction tool. Part II: Model physics and applications. *Meteor. Atmos. Phys.*, **76**, 134–165.

Yang, M.-J., and R. A. Houze, Jr., 1995: Multicell squall–line structure as a manifestation of vertically trapped gravity waves. *Mon. Wea. Rev.*, **123**, 641–661.

Yau, M. K., 1979: Perturbation pressure and cumulus convection. *J. Atmos. Sci.*, **36**, 690–694.

Zalesak, S. T., and S. L. Ossakow, 1980: Nonlinear, equatorial spread-F: spatially large bubbles resulting from large, horizontal-scale, initial perturbations. *J. Geophys. Res.*, **85**, 2131–2142.

Zipser, E. J., 1977: Mesoscale and convective-scale downdrafts as distinct components of squall-line structure. *Mon. Wea. Rev.*, **105**, 1541–1567.